School of Resource Science and Technology

Techniques For Improved 2-D Kirchhoff Prestack Depth Imaging

Christopher D Manuel

THIS THESIS IS PRESENTED AS PART OF THE REQUIREMENTS FOR

the award of the Degree of Doctor of Philosophy
of the Curtin University of Technology

November 2002

Declaration

This thesis contains no material which has been accepted for the award of any other degree or diploma in any university.

To the best of my knowledge and belief this thesis contains no material previously published by any other person except where due acknowledgment has been made.

Signature:_____

Date: 7/11/12

DEDICATION

To my wife Suzanne who has been a constant source
of strength for the duration of this journey.

ACKNOWLEDGMENTS

I would like to thank my supervisor, Professor Norm Uren, for his "motivational talks" and knowledge throughout the term of the research. I cannot thank him enough for his role as "editor-in-chief" during the preparation of the thesis. Special mention must also be made of Associate Professor Bruce Hartley who provided insight and support with various problems encountered in the research, including assistance with the generation of the synthetic data using his software.

Acknowledgment must also be given to Mr Murray Hill for the provision of computer support, to fellow PhD students for their constructive criticism and use as a "sounding-board" when required, and to all other staff and students in the Department of Exploration Geophysics for providing a friendly working environment.

I would also like to thank the Curtin Reservoir Geophysics Consortium (CRGC) and the Australian Petroleum Cooperative Research Centre (APCRC) for providing the funding needed for this research. In addition I would like to acknowledge the financial support of the Curtin University Postgraduate Scholarship scheme (CUPS) and the American Association of Petroleum Geologists (AAPG) for the provision of two Grants-In-Aid scholarships. Acknowledgement must also be given to the Australian National University for use of their supercomputer resources.

ABSTRACT

TECHNIQUES FOR IMPROVED 2-D KIRCHHOFF PRESTACK DEPTH IMAGING

The goal of oil and gas exploration using seismic methods is to accurately locate geological structures that could host such reserves. As the search for these resources tends towards more complex regions, it is necessary to develop methods to extract as much information as possible from the seismic data acquired. Prestack depth imaging is a seismic processing technique that has the capability to produce a realistic depth image of geological structures in complex situations. However, improvements to this technique are required to increase the accuracy of the final depth image and ensure that the targets are accurately located.

Although prestack depth imaging possesses the ability to produce a depth image of the Earth, it does have its disadvantages. Three problematic areas in depth imaging are: the computer run times (and hence costs) are excessively high; the success of depth migration is highly dependent upon the accuracy of the interval velocity model; and seismic multiples often obscure the primary reflection events representative of the subsurface geology. Velocity model building accounts for most of the effort in prestack depth imaging and is also responsible for the likelihood of success. However, the more effort that is expended on this process, the greater the cost of producing the required depth section. In addition, multiples remain a problem in complex depth imaging since many attenuation techniques are based assumptions that may only be approximately correct and in addition require a priori information.

The Kirchhoff method is considered to be the workhorse in industry for prestack depth imaging. It is a simple and flexible technique to implement, and usually produces acceptable images at a small fraction of the cost of the other depth migration methods. However, it is highly dependent on a method for calculating the traveltimes that are required for mapping data from the prestack domain to the output depth section. In addition, it is highly dependent on the accuracy of the interval velocity model. Multiples can also be problematic in complex geological scenarios.

To improve the quality of the depth section obtained from Kirchhoff depth imaging, these three issues are considered in this thesis.

This thesis took on the challenge of developing new techniques for (a) improving the accuracy and efficiency of traveltimes calculated for use in Kirchhoff prestack depth imaging, (b) building the interval velocity model, and (c) multiple attenuation in complex geological areas. Three new techniques were developed and tested using a variety of numerical models. A new traveltime computation method for simulating seismic multiple reflections was tested and compared with a Promax© finite-difference traveltime solver. The same method was also used to improve the computational efficiency whilst retaining traveltime accuracy. This was demonstrated by application to the well-known Marmousi velocity model and a velocity model obtained from analysis of data from the North West Shelf of Western Australia. A new interval velocity model building technique that utilises the information contained in multiple events was also implemented and tested successfully using a variety of numerical models. Finally, a new processing sequence for multiple attenuation in the prestack depth domain was designed and tested with promising results being observed.

Improved accuracy in the depth image can be obtained by combining the three techniques I have developed. These techniques enable this to be achieved by firstly improving traveltime accuracy and computation efficiency. These benefits are then combined with a more accurate interval velocity model and data with a minimal problematic multiple content to produce an accurate depth image. These new techniques for Kirchhoff depth imaging are capable of producing a depth section with improved accuracy, and with increased efficiency, that will aid in the process of seismic interpretation.

© Promax 2-D Version 1998.6 - Landmark Graphics Corporation

CONTENTS

Chapter 1

Introduction 1

1.1 Petroleum exploration 1

1.2 Need for the research 2

1.3 Proposed research 6

1.4 Structure of the thesis 7

Chapter 2

Imaging the Subsurface With Depth Migration 10

2.1 Commonly implemented depth migration techniques 12

2.1.1 The wave equation 13

2.1.2 Finite-difference migration using the one-way wave equation 14

2.1.3 Depth migration using the full acoustic wave equation 19

2.1.4 Kirchhoff depth migration 21

2.2 Methods for traveltime computation 30

2.2.1 The ray tracing method 31

2.2.2 The finite-difference method 33

2.3 Building the velocity model 35

2.4 Depth imaging - where to from here? 45

Chapter 3

Calculation of Traveltimes 48

3.1 Implementation of the finite-difference method 48

3.2 The generalised exploding reflector method 50

3.2.1 Method description 50

3.2.2 Simulation of seismic multiples 55

3.2.3 Multiple grid cell sizes 64

Chapter 4

Migration Velocity Analysis Using Seismic Multiples 87

4.1 Sensitivity of multiples to changes in velocity 87

4.2 Determination of interval velocity from multiples 90

4.3 Synthetic data testing 93

4.3.1 The effect of multiple periodicity in MVA 94

4.3.2 MVA using water-bottom multiples 104

4.3.3 MVA using interbed multiples 104

4.3.4 MVA where multiples interfere with primaries 110

4.3.5 MVA using multiples in the presence of dip 114

4.4 Summary 136

Chapter 5

Multiple Attenuation Using Migration Velocity Analysis 138

5.1 Multiple attenuation in the prestack depth domain 139

5.1.1 The need for multiple attenuation in depth imaging 139

5.1.2 Recent developments for multiple attenuation in the prestack depth domain 140

5.1.3 An alternative processing flow for multiple attenuation in the prestack depth domain 143

5.2 Treating multiples as noise in MVA 144

5.2.1 The role of average velocity 144

5.2.2 Separation of multiple and primary energy in a CIG 150

5.2.3 Inverse Kirchhoff PSDM - how is it performed? 159

5.3 Multiple attenuation where events interfere 172

5.4 Summary 178

Chapter 6

Conclusions and Recommendations 180

References 182

Appendix

Software Developed in the Thesis 196

A1 Numerical simulation of seismic multiples using the GERM 197

A2 Implementation of multiple grid cell sizes using the GERM 213

A3 Kirchhoff PSDM incorporating the GERM 229

A4 Migration velocity analysis – residual curvature method 237

A5 Coherency for residual curvature method 247

A6 Demigration for multiple attenuation 251

FIGURES

Figure 2.1 Poststack and prestack Kirchhoff depth migration 23

Figure 2.2 Constructive amplitude interference associated with 2-D Kirchhoff poststack depth migration 24

Figure 2.3 Problems with ray tracing 32

Figure 2.4 Reflector patterns when migrated with incorrect velocities 38

Figure 2.5 Common reflection point geometry for non-horizontal reflectors 43

Figure 3.1 The exploding reflector method 51

Figure 3.2 Two rays not predicted by the exploding reflector model 52

Figure 3.3 The generalised exploding reflector method 54

Figure 3.4 Implementation of the GERM to simulate primary reflection 57

Figure 3.5 Traveltime isochron maps associated with implementation of the GERM to simulate water-bottom multiples in horizontally layered media 59

Figure 3.6 Traveltime isochron maps associated with implementation of the GERM to simulate a S212R event in dipping media 60

Figure 3.7 A comparison of event arrival times from using the rugose boundary model 62

Figure 3.8 A comparison of event arrival times using the three layer model with dipping boundaries 63

Figure 3.9 Application of the generalised exploding reflector method to change the grid cell size 66

Figure 3.10 The field velocity model used for demonstrating how the GERM can be implemented with changing the grid cell size 68

Figure 3.11 Quantitative analysis of differences in traveltime using the simple field velocity model 70

Figure 3.12 Traveltime difference analysis for the simple field velocity model 72
Figure 3.13 Implementation of the GERM in PSDM of the field dataset 74
Figure 3.14 Run times for each test associated with the field dataset 75
Figure 3.15 The synthetic Marmousi velocity model generated by the Institut Francais du Petrole (IFP) 77
Figure 3.16 Quantitative analysis of differences in traveltime using the Marmousi velocity model 79
Figure 3.17 Traveltime difference analysis for the Marmousi model 80
Figure 3.18 Implementation of the GERM in PSDM of the Marmousi dataset 82
Figure 3.19 Run times for each test associated with the Marmousi dataset 85
Figure 4.1 Error in velocity is compounded as the distance of propagation increases 88
Figure 4.2 Multiple reverberation in a layered situation 92
Figure 4.3 Velocity models used for generating short-period and long-period surface peg-leg multiples 95
Figure 4.4 Shot 100 from each dataset created using different first layer thicknesses to vary the multiple periodicity 97
Figure 4.5 Common image gathers formed as a result of migrating a suite of shots from each dataset 98
Figure 4.6 γ-semblance analysis for each example obtained using Equation (2.18) 99
Figure 4.7 Interval parameter errors obtained when examining multiple periodicity in MVA 103
Figure 4.8 MVA using water-bottom multiples 105
Figure 4.9 MVA using interbed multiples 107
Figure 4.10 MVA where multiples and primary events interfere 111
Figure 4.11 MVA in the presence of dip 116
Figure 4.12 A comparison of γ-semblance methods 117

Figure 4.13 Trajectories on a CIG of the semblance analysis curves defined by the methods of Al-Yahya (1989) and Lee and Zhang (1992) 121
Figure 4.14 Three velocity models used for generating synthetic data where the multiple reverberations occur in a horizontal layer and the second layer was allowed to dip 122
Figure 4.15 Shot gathers and CIGs obtained where the second layer dip varied 124
Figure 4.16 γ-semblance analysis using Equation (2.20) where the second layer dip varied 125
Figure 4.17 Three velocity models used for generating synthetic data where the multiple reverberations occur within a dipping layer 128
Figure 4.18 Shot gathers and CIGs obtained where the first layer dip varied 129
Figure 4.19 γ-semblance analysis using Equation (2.20) where the first layer dip varied 130
Figure 4.20 Error analysis from performing MVA using multiples where the multiple reverberation occurs within a dipping layer 134
Figure 4.21 Multiple reverberation within a layer of differing dips 135
Figure 5.1 The West Shetlands line - selected image gathers 141
Figure 5.2 A proposed processing flow for multiple attenuation in the depth domain 145
Figure 5.3 Velocity model used to generate synthetic data for testing the proposed processing flow 148
Figure 5.4 CIGs obtained in the prestack depth domain after performing Kirchhoff PSDM with the average velocity of specific multiples 149
Figure 5.5 Results of performing τ-p transforms on the CIGs obtained after migrating with the average velocity of a specific multiple 152

Figure 5.6 τ-p transforms and reconstructed CIGs after rejecting all energy but the targeted multiple 154
Figure 5.7 The wavelet transform 156
Figure 5.8 Using the wavelet transform to predict multiple energy in a CIG 160
Figure 5.9 Determination of the total distance required for demigration in time 163
Figure 5.10 Demigration in depth of the original CIG and the CIG containing the isolated multiple energy from the τ-p transform 165
Figure 5.11 Demigration in time of the demigrated sections in depth 166
Figure 5.12 A comparison of pre-migrated and demigrated zero offset traces 168
Figure 5.13 Resultant CMP gathers after subtracting the demigrated isolated multiple energy from a CMP gather located at the MVA location 170
Figure 5.14 A comparison of zero offset traces from an original CMP gather located at the MVA location and the processed CMP gathers 171
Figure 5.15 Velocity model used to generate synthetic data containing events that interfere 173
Figure 5.16 Isolation of the S201R event in the τ-p domain where events in the CIG interfere 175
Figure 5.17 Demigration of the filtered CIG in the case where the problematic multiple interferes with other events 177

TABLES

Table 2.1: Solutions to the one-way wave equation 16

Table 4.1: Interval velocity and thickness summary based on MVA for long- and short-period multiples 102

Table 4.2: Results of MVA after using water-bottom multiples for interval parameter determination 106

Table 4.3: Results of MVA after using interbed multiples for interval parameter determination 109

Table 4.4: Results of MVA for the case where surface peg-leg multiples are interfering with primary events 113

Table 4.5: Results of MVA when two different γ-semblance methods were used for determining interval velocity and thickness 119

Table 4.6: Results of MVA using multiples where the multiple reverberations occurred in a horizontal layer but the second layer was allowed to dip 126

Table 4.7: Results of MVA using multiples where the multiple reverberations occur within a dipping layer 132

CHAPTER 1

INTRODUCTION

1.1 PETROLEUM EXPLORATION

The petroleum industry is of great importance to the Australian economy, contributing over eight billion dollars each year with half of this amount coming from Western Australia (Department of Minerals and Energy, 2001). The Australian Petroleum Production and Exploration Association (2001) stated that in 1999, approximately 800 million dollars was spent on petroleum exploration resulting in 51,900 line kilometres of acquired seismic data and approximately 244 kilometres of drilling, both onshore and offshore. Without successful exploration the Australian economy would be denied a significant component of its income. However, considering the expense of this exploration effort and the competitive commercial environment, it is necessary that new and improved cost effective methods are continually sought to ensure that maximum information is obtained from the data acquired.

The seismic method for petroleum exploration involves the release of energy near the surface of the Earth and the recording of the returning acoustic and elastic sound waves by sensors near the Earth's surface. By utilising the recorded reflection energy, an image of the subsurface geology is obtained. Based on such images, decisions are made on the locations of drilling operations in the search for oil and gas. Seismic multiples, which are the result of reverberation of sound waves in the subsurface, frequently mask the primary reflection events which are the principal source of information from which subsurface information is derived.

Sheriff (1994) describes *signal* as denoting any event on the seismic record from which we wish to obtain information. Everything else is considered as *noise*, including coherent events that interfere with the observation and measurement of signals. On the basis of this philosophy, multiple energy is usually considered to be coherent noise. Conventional seismic processing aims to remove multiple energy from the seismic record as early as possible in the processing sequence so that

information from the subsurface can be obtained from just the primary events. However, as with primaries, multiples also result from the reflection process and therefore may also carry information about the subsurface. Hence, when multiple events are attenuated, important information about the subsurface is potentially being discarded. Perhaps if the multiple energy were treated as signal rather than noise, more information might be extracted from the seismic data. This could result in a more accurate depth section.

A typical offshore well costs millions of dollars. For example, in permit WA-287-P on the North West Shelf of Western Australia, even though targets are shallow at depths of 1000-1550m, drilling costs are at least an estimated A$6 million per well (Petroleum Exploration Society of Australia, 2002). Costs of other wells have been much higher. High accuracy seismic imaging is essential to prevent such investment being wasted through incorrect drill-rig positioning. In addition, because of the high costs of acquiring and processing seismic data, it is important that the imaging be performed at minimum cost. An alternative way of looking at this issue is to consider the high cost of acquiring seismic data and how much of it is actually utilised to form the depth image. Conventional seismic processing discards quite a lot of data due to it being considered as noise. However, if the discarded data can provide information about the subsurface then it should be considered as signal and be utilised. This extra information could perhaps provide a means of obtaining a more accurate depth image than is presently possible.

1.2 NEED FOR THE RESEARCH

Depending on the quality of the input seismic data and the accuracy of the velocity model, depth migration is capable of creating a realistic depth image of geological structures, often placing hydrocarbon-bearing structures within tens of metres of their actual locations. This degree of spatial resolution is highly desirable, since drilling errors of even tens of metres can affect the economic outcome of a well (Gray, 1999). Prestack depth migration (PSDM) is the preferred method of producing a depth image in complex geological regions. Since seismic exploration is trending toward more complex, costly and challenging exploration targets, it is important that

the depth migration process be constantly improved to enable imaging in even more complex regions. However, it is necessary to identify current weaknesses in the method before improvements can be contemplated. Three such problematic areas in depth imaging are:

(a) Computer run times (and hence costs) are excessively high;
(b) The success of depth migration is highly dependent upon the accuracy of the velocity model; and
(c) Seismic multiples often obscure the primary reflection events representative of the subsurface geology.

With regard to the first problem, Kirchhoff depth migration usually produces acceptable images at a small fraction of the cost of the other depth migration methods (Gray et al., 2001). However, with the advent of parallel processing and increased disk space, run times and costs are being decreased. This is making even the full wavefield depth migration techniques economically feasible. However, for processing houses that have restricted access to such resources, the costs are still too high and even Kirchhoff depth imaging is considered to have significant run times. Decreasing the run time of Kirchhoff depth migration normally involves some form of trade-off with the amount of information that is to be used in the process. For example, the cell size used to digitise the velocity model may be made larger, fewer sources and receivers may be used in the migration, or the migration aperture used might be made smaller. However, all of these economies invariably serve to reduce the accuracy in the resultant depth section. Therefore, in this competitive world, it is desirable that a method be found (other than simply purchasing more expensive computing power) to enable the run time of Kirchhoff depth migration to be reduced whilst retaining an acceptable level of accuracy in the depth section.

The second problem deals with the accuracy required in the velocity model used for depth migration. The interval velocities used are averages of the actual Earth velocities, where the average is taken over some characteristic distance such as a wavelength. This allows depth migration to model seismic wave behaviour within the Earth much more accurately than time migration (Gray et al., 2001). The primary advantage of depth migration is that it normally produces a structurally correct depth

section provided the interval velocity model is correct. If there is error present in the velocity model then the resultant depth image will not be properly focussed. Any subsequent interpretations will thereby be made more difficult. While estimation of the imaging velocities needed for time migration is a routine task, estimating interval velocities for depth migration is a problem that continues to challenge the geophysicist. In fact, estimating the velocities to be used for depth migration is often much more challenging than the problem of migration itself, since the major tool available for estimating those velocities is to actually perform the migration (Gray et al., 2001).

Velocity estimation remains a fundamental imaging problem especially when the velocity of the subsurface varies laterally or possesses anisotropy. In such situations, the migration problem becomes even more difficult since most velocity determination techniques assume minimal lateral variation (Fagin, 1998). Therefore, any new method that can be used to estimate velocity more accurately is of extreme importance as it will ultimately lead to higher quality depth images. The conventional process for building a velocity model requires many iterations to converge on the most suitable model. In other words, depth migration often involves using an initial velocity model followed by a quantitative analysis of the degree of focussing in the depth image. The velocities are then updated and the process is repeated until a satisfactory result is obtained. In addition, for a successful depth migration, estimated velocities are normally required to be within 0.5 to 1% of the true velocities (Fagin, 1998). However, these percentages depend on the complexity of the velocity variation. A significant number of migration iterations is normally required to produce this accuracy. With these requirements it is obvious that a method that would reduce the number of iterations required to build the velocity model (and hence the time spent building the model), whilst still achieving a high degree of accuracy, is highly desirable. If this could be achieved then the cost and run time required to build the velocity model would be reduced. In addition, the large amount of user interaction normally required would also be reduced and then these saved resources might be devoted to solving other problems. Thus the benefits of achieving a more accurate velocity model in less time would have a flow-on effect to the whole exploration effort.

The third problem pertains to the presence of multiple reflections in the depth image. Seismic sections are interpreted on the assumption that a simple reflection (primary) occurs at each elastic (geological) boundary. Reflections at deeper geological structures occur at greater times on the seismic record. This is not valid when acoustic energy reverberates between two highly reflective boundaries before returning to the surface. Multiple reflections, due to the increased travel path (and hence travel times), will resemble primary reflections from greater depths. Due to the observed multiples not representing deep structure they normally need to be removed from a seismic section to enable a valid geological interpretation. Multiple reflections will occur in all sedimentary environments with their extent and amplitude depending on the reflectivity and absorption effects of the rock strata on the elastic wave. For example, multiple reflections are more dominant in the marine environment because the seawater-air interface has a reflectivity of approximately 0.97 (on a scale of 1.0 for full reflection and 0.0 for total transmission). Thus in the marine environment, 97% of the amplitude of the wave returning to the surface will again be transmitted back into the subsurface, to be reflected back again, recorded and so on. The problem is not quite as prevalent with land acquisition since a low velocity layer (unconsolidated sediments) will generally exist near the surface and substantially reduce the impact of the surface reflectivity (De Pledge, 1993).

Conventionally, an attempt is made to attenuate multiple energy as early as possible in the seismic processing sequence. However, it is normally the case that more than one method of attenuation must be used to target the variety of multiple types present in the data. An example of this is the North West Shelf of Western Australia where a highly reflective carbonate layer produces multiples of high amplitude. The most commonly used technique for multiple suppression there (especially in deep water areas) is F-K multiple attenuation. This is often combined with inner trace muting and either signature deconvolution, or predictive deconvolution, or both. This technique has not been very successful in areas where:

(a) The primary and multiple normal moveout (NMO) difference is small (this is the case in the high velocity carbonate wedge which extends over much of the North West Shelf area).

(b) The reverberation time of the multiple is long or non-periodic.

(c) The amplitude ratio of the primary energy to the multiple energy is low.

However, in shallower waters near the Western Australian coast, predictive deconvolution and spectral equalisation have worked well. In the areas where these multiple attenuation techniques are not so effective, the multiples need to be accurately identified or modelled to facilitate the proper application of multiple removal techniques (Ramsden et al., 1988).

The application of seismic depth imaging techniques assumes input data free of multiple energy. Unfortunately this assumption is generally invalid to some degree and the presence of multiple energy results in less clear images and incorrect amplitudes which hinder processing and interpretation (Hill et al., 1999). Much progress has been made in attenuating multiples, but as each new technique has a preferred range of applicability, each also has its limitations. It is often the case that several different techniques will be combined in commercial processing to target a particular multiple problem. This however can be costly in terms of time and money. In addition, most of these techniques rely on certain assumptions or prerequisites to perform optimally. Thus for particular cases, certain methods may or may not be good demultiple tools. Examples of inappropriate assumptions include: the geology may not be horizontally layered; there may not be enough velocity discrimination; or a method may not work at certain offsets. As a result multiples remain a problem, motivating the search for new demultiple techniques which can function with less a priori information, fewer restrictions and unrealistic assumptions, and can target more than one multiple type. Such methods (which would have to be highly versatile and flexible) would be of great benefit to the exploration industry as the need to find a specific attenuation method for a particular geological regime and multiple type would thereby be greatly reduced. More attention could then be devoted to other components of the processing sequence.

1.3 PROPOSED RESEARCH

The goal of the depth imaging process is to produce a high quality depth section that is representative of the subsurface geology. Common hindrances to this process include multiple content and excessive run times. With the idea in mind that

developments in a mature technology more often than not occur as a result of the culmination of several incremental advancements, the goal of this thesis is to investigate possible ways to improve the accuracy of the two dimensional depth image. It is proposed to work in two dimensions (2-D) rather than three dimensions (3-D) in a preliminary study due to the necessity of reducing sources of error which may occur when developing new concepts and because imaging is computationally expensive. Subsequent extension to 3-D would not be expected to be such a major step. The issue of anisotropy will not be touched upon here with respect to depth imaging as it is just as large as the topic of depth migration itself. Therefore, I will be assuming isotropic velocity variations with the issue of anisotropy being left for future research.

Kirchhoff PSDM is used to produce the depth section with traveltime computations comprising a significant proportion of the run time in this process. Conventionally, there is often a trade-off between run time and accuracy. If run time is to be decreased then accuracy must often be sacrificed in the depth image. Initially the possibility of decreasing the run time whilst retaining a significant degree of accuracy will be examined in improving the Kirchhoff depth imaging process. Secondly, I propose to investigate the possibility of using multiple energy as signal in order to produce a more accurate velocity model than is presently possible. Finally, I propose to consider these multiples as noise and analyse the process of migration velocity analysis (MVA - the method for building a velocity model in complex geological regions) as a possible method for attenuating these unwanted events. If these three goals are successfully achieved, even in part, then the depth imaging process will have been made more accurate, faster, and would have had significant multiple content removed. In other words, if successful, these three incremental advancements in technology will be a contribution to the ultimate goal of an improvement in image quality.

1.4 STRUCTURE OF THE THESIS

Chapter 2 will begin with a review of depth migration methods commonly employed by industry. A description of how each method operates will be given along with a discussion of the merits and drawbacks of each method. This will bring to light those

areas of the depth imaging process that might be improved. As a matter of interest, while using the Society of Exploration Geophysicists' digital cumulative search index (available online), 1621 references were found on the subject of migration. In addition to these 1621 references, 561 more were found to be associated with the subject of depth migration. With so much reference material available it is evident that, besides migration generally, depth migration alone is a widely researched area of interest and has many different issues related to it. Therefore, one must concentrate on improvements in only a subset of the depth migration field. The Kirchhoff method is addressed in this thesis since it is considered to be the workhorse of the industry. Given this widespread use of Kirchhoff migration by industry, it is worthwhile for a concerted effort to be made to develop and test improvements that could yield higher quality images in regions of complex geology. Kirchhoff depth migration requires an accurate interval velocity model and an accurate method for calculating traveltimes. The thesis will discuss the common methods for achieving these two goals and common pitfalls that these methods encounter. The findings from this review will be used to determine the areas where Kirchhoff PSDM might be improved.

Implementing Kirchhoff PSDM conventionally involves calculating the first arrival traveltime from each source to each receiver via all point scatterers in the subsurface (although calculation of later arrivals is becoming a more common occurrence). The accuracy of these traveltimes will determine the quality of the depth section produced. Chapter 3 analyses this computationally intensive and vitally important component of Kirchhoff PSDM. The generalised exploding reflector method is introduced as a possible method for providing improved accuracy in the depth section while not increasing the run time and hence cost of the procedure to any significant degree.

Chapter 4 explores the possibility of utilising multiple energy in the velocity model building process with the intention being to produce a more accurate velocity model than can be achieved at present. Conventionally, an attempt is made to attenuate multiple energy before the velocity model building process takes place. However, this essentially reduces the signal available to build the velocity model. Examples

will be studied to illustrate how multiples may be utilised in the velocity model building process.

The multiple energy which might be utilised, in finding different ways of improving accuracy in the velocity model building process, will still need to be attenuated at some stage. Methods of multiple attenuation will be explored in Chapter 5 with both the Radon and wavelet transforms being analysed as possible tools for achieving this goal. The possibility of using these tools in conjunction with MVA will be analysed. Chapter 6 summarises the developments made in the thesis and discusses possible consequences they may have for conventional Kirchhoff depth imaging.

CHAPTER 2

IMAGING THE SUBSURFACE WITH DEPTH MIGRATION

Depth migration[1] involves any migration process which properly handles vertical and lateral velocity variations and is not limited in dip (Sheriff, 1994). Although time migration may adequately handle simple velocity variations, in the more geologically complex regions the assumptions on which the process is based break down, and depth migration must be implemented. The most important feature that differentiates depth migration from time migration is that the former can more effectively account for lateral velocity variations. Changes in velocity, with all the attendant raypath bending, are accounted for in a depth migration. In contrast, time migration is usually associated with using straight, or laterally invariant, raypaths. Prestack depth migration (PSDM) is of benefit when events are non-hyperbolic and cannot be stacked along hyperbolic trajectories. From a geophysical standpoint, Fagin (1998) gives four reasons why one *may* expect improved imaging with depth migration, provided the velocity field is known with sufficient accuracy (the last two reasons are associated with PSDM only):

(a) *Vertical positioning* – depth migration will result in an image free of structural distortions related to lateral velocity variations that may cause time pull-ups and sags.

(b) *Lateral positioning* – depth migration places events in their correct lateral position due to raypath bending having been accounted for.

(c) *Resolution* – depth migration gives a higher resolution than time migration, both laterally and vertically, because it does not rely on hyperbolic moveout assumptions (however, it could be argued that a depth section has a lower vertical resolution than a time section due to time to depth stretching).

(d) *Velocity model derivation* – depth migration provides its own diagnostics for obtaining a velocity model. When reflections in an offset-depth gather (a product of PSDM) are flat, it implies that imaging with the velocity model yields an identical image at all offsets, which indicates a correct velocity model.

---

[1] *Depth migration* refers to the migration process only, whereas *depth imaging* refers to both the velocity model building and depth migration processes.

This discussion indicates the importance of an accurate velocity model in producing an accurate depth migrated image. Time migration cannot adequately account for the wavefield bending associated with subsurface velocity changes therefore the derivation of the velocity field required is less demanding. In contrast, depth migration requires a far more accurate velocity field for two main reasons:

(a) The results of depth migration are scaled in depth and so the velocity field must be geologically reasonable to satisfy the demands of depth conversion.

(b) The velocity field should be accurate enough to migrate amplitudes for a given reflection to the same depth at every offset position.

Velocity model building accounts for most of the effort in depth imaging and is also responsible for the likelihood of success. Hence, the ability to produce a velocity model with a higher degree of accuracy is of paramount importance.

Two other barriers to depth imaging include the computational effort required and data management (Fagin, 1998). The computational effort associated with depth imaging has decreased remarkably over the last two decades. In the early 1980's this factor limited the routine use of depth imaging to the 2-D poststack mode. However, full volume prestack depth imaging has recently become routine although this is limited to one or two types of migration. A significant burden that has arisen with prestack depth imaging has to do with the large data volumes involved. This is related to the need to handle prestack data both before and after imaging. Related to this are the large amounts of data that have to be accessed by the computer.

The purpose of this chapter is to review depth imaging methods that are commonly employed by industry. A brief description of how each method operates will be given along with a strong focus on the merits and drawbacks of each method. This will bring to light those areas of the depth imaging process that have potential for improvement. Initially I will be examining conventional depth migration implementations. Following this, techniques for calculating traveltimes will be discussed, since this is important for the depth migration component of depth imaging. Concluding the chapter is a discussion on the various methods for building the velocity model.

2.1 COMMONLY IMPLEMENTED DEPTH MIGRATION TECHNIQUES

The depth migration technique most frequently employed by the exploration industry is of the Kirchhoff type. This is due to its relative ease of implementation and low cost compared with full wavefield methods. However, with the advent of parallel processing and with computing resources becoming more affordable, full wavefield implementations are now in use as well. The aim of this section is to give a description of the common wavefield implementations such as finite-difference migration and full wave equation migration, and then to follow up with a discussion of Kirchhoff depth migration. Each depth migration method will be analysed to determine which method will be studied in this research.

Claerbout's imaging principle (Claerbout, 1976) is the basis for a series of depth migration techniques. It states that,

Reflectors exist in the Earth at places where the onset of the down-going wave is time coincident with an up-coming wave.

On the basis of this principle, reflection coefficients at points of interest can be obtained by the following steps:

(a) Propagate the down-going wavefield forward in time to these points.

(b) Extrapolate the data collected on the observation surface (up-coming wavefield) backward in time to the same points.

(c) Calculate the reflection coefficient at these points using both wavefields.

The main task for depth migration is to extrapolate waves in inhomogeneous media and the vehicle for doing this with Claerbout's imaging principle is the wave equation. Although Kirchhoff migration is not based on Claerbout's imaging principle, it is however derived from the wave equation.

Other methods for performing depth migration that are worth noting but won't be examined in detail in this review for the main reason that they are not commonly implemented in a depth migration regime are: (a) frequency domain migration, and (b) Born inversion. Frequency domain migration (Stolt, 1978; Gazdag, 1978) was introduced initially for poststack purposes and was strictly valid for vertical velocity variations at most. The method makes up for its lack of flexibility by being extremely fast. However, it is limited in its applicability as a depth migration because, even

though it is possible to extend the method to accommodate lateral velocity variations, the extension makes it one of the slowest methods (Gray, 2001).

Born inversion (Clayton and Stolt, 1981; Bleistein et al., 1985; Beylkin, 1985; Cohen et al., 1986; Bleistein et al., 1987; Bleistein, 1987) involves an inversion technique in which the velocity perturbation and reflectivities are recovered from the scattered waves which are separated from the incident waves using the "Born approximation". The Born inversion technique is established through a well-defined physical model of reflection seismology known as Born scattering. It uses Beylkin's Generalised Radon Transform (Beylkin, 1985), a straight forward inversion technique, to find an inverse operator. The inversion algorithm needs a reasonably smooth background velocity which may vary in any direction and true amplitude observation data. Perturbations in this background velocity are then sought (Zhao, 1996a). Born inversion will not be studied in this thesis since it is not widely implemented as a depth migration technique in industry.

2.1.1 THE WAVE EQUATION

Since the majority of depth migration techniques are based on the wave equation, it is useful to present the mathematical steps involved in transforming this equation to a form which is suitable for performing depth migration. The most common assumptions in deriving the wave equation in its most widely used form are that the medium is acoustic (only compressional waves exist) and that energy is propagated in one direction only (Bancroft, 1997). The usual form of the 2-D acoustic wave equation expressed with constant density is:

$$\left(\frac{\delta^2 P}{\delta x^2}\right)+\left(\frac{\delta^2 P}{\delta z^2}\right)=\frac{1}{c^2}\frac{\delta^2 P}{\delta t^2}, \tag{2.1}$$

where $P(x,z,t)$ is the solution to the acoustic wave equation in two dimensions, c is velocity, x is distance, and z is depth. Given the up-coming seismic wavefield $P(x,z=0,t)$, which is recorded at the surface, the goal is to determine the wavefield as it comes off each reflector, $P(x,z,t=0)$. This represents the migrated section. The wavefield $P(x,z,t)$ can be represented by its two dimensional Fourier transform $P(k_x,z,\omega)$ in the k_x-ω domain as:

$$P(x,z,t) = \iint P(k_x, z, \omega) e^{i(\omega t - k_x x)} dk_x d\omega \,, \tag{2.2}$$

where k_x is the horizontal wave number and ω is the angular frequency. Substituting (2.2) into (2.1) gives:

$$\frac{\delta^2 P}{\delta z^2} + \left[\frac{\omega^2}{c^2} - k_x^2 \right] P = 0 \,, \tag{2.3}$$

where $P=P(k_x,z,\omega)$. In addition,

$$k_z = \pm \sqrt{\frac{\omega^2}{c^2} - k_x^2} \,. \tag{2.4}$$

This is known as the dispersion relation. Substituting (2.4) into (2.3) gives:

$$\frac{\delta^2 P}{\delta z^2} + k_z^2 P = 0 \,. \tag{2.5}$$

Equation (2.5) has two solutions. If z is positive downwards, then the equation with the positive sign represents down-going waves and the equation with the negative sign represents up-coming waves:

$$P(k_x, z, \omega) = P(k_x, 0, \omega) e^{\pm i k_z z} \,. \tag{2.6}$$

This equation can also be represented as a first order differential wavefield where $P=P(k_x,z,\omega)$:

$$\frac{\delta P}{\delta z} = \pm i k_z P \,. \tag{2.7}$$

Subsequently,

$$P(k_x, z + \Delta z, \omega) = P(k_x, z, \omega) e^{\pm i k_z \Delta z} \,. \tag{2.8}$$

Equation (2.8) is the basis of Gazdag's (1978) phase-shift migration and is the basic equation for a series of migration methods based on one-way wave propagation (exploding reflector model). One such method is *finite-difference migration* and this will be examined next.

2.1.2 FINITE-DIFFERENCE MIGRATION USING THE ONE-WAY WAVE EQUATION

The one-way wave equation deals with the positive solution to the wave equation in Equation (2.7). Finite-difference methods for the solution of the one-way wave equation can be divided into two classes known as the *implicit* (Claerbout, 1976) and

explicit (Berkhout, 1985; Holberg, 1988; Hale, 1991; Nautiyal et al., 1993) methods. With the implicit method a system of equations must be solved to advance to the next time level (Golub and Ortega, 1992). The method is widely used to extrapolate seismic wavefields in depth because they are guaranteed to be stable. On the other hand, the explicit method is easy to code, and easily handles local velocity variations.

Implicit Method

Various levels of assumptions can be used to simplify the scalar wave equation, resulting in implementations with various levels of dip accuracy, often classified as 15°, 45°, and 65° finite-difference migrations. This type of finite-difference migration involves an implicit solution to the scalar wave equation, in other words, an indirect solution requiring an additional matrix inversion. An approximation to the positive square root of the *dispersion relation* (Equation (2.4)) is needed in order to solve the wave equation and implement it in a finite-difference migration scheme. Consider the dispersion relation for the up-coming wavefield being rewritten using the variables X and R:

$$X = \frac{ck_x}{\omega},$$

$$\text{and} \quad R = \sqrt{1 - X^2}\,. \tag{2.9}$$

The dispersion relation then becomes:

$$k_z = \frac{\omega}{c}\sqrt{1 - \frac{c^2 k_x^2}{\omega^2}} = \frac{\omega}{c}\sqrt{1 - X^2} = \frac{\omega}{c}R\,. \tag{2.10}$$

By applying an approximation formula to the dispersion equation, various solutions to the one-way wave equation can be obtained. One such approximation is the continued fraction expansion and results of using this are presented in Table 2.1. From this table, the 15° solution is expressed as:

$$\frac{\delta P}{\delta z} = i\left(\frac{\omega}{c} - \frac{ck_x^2}{2\omega}\right)P\,. \tag{2.11}$$

Applying the Fourier transform to Equation (2.11), the wavefield $P(k_x,z,\omega)$ can be inverse transformed from the horizontal wavenumber domain k_x, to the horizontal space domain x, by substituting the operator $(ik_x)^2 = \delta^2/\delta x^2$. The wavefield is now

Solution	Continued Fraction Expansion	Full Transform Mode (k_z)	Depth Domain ($\partial P/\partial z$)
5°	$R_0 = 1$	$\frac{\omega}{c}$	$i\left(\frac{\omega}{c}\right)P$
15°	$R_1 = 1 - \frac{X^2}{2}$	$\frac{\omega}{c} - \frac{ck_x^2}{2\omega}$	$i\left(\frac{\omega}{c} - \frac{ck_x^2}{2\omega}\right)P$
45°	$R_2 = \frac{4 - 3X^2}{4 - X^2}$	$\frac{\omega}{c}\left[\frac{\left(4\omega^2/c^2\right) - 3k_x^2}{\left(4\omega^2/c^2\right) - k_x^2}\right]$	$i\left(\frac{\omega}{c}\left[\frac{\left(4\omega^2/c^2\right) - 3k_x^2}{\left(4\omega^2/c^2\right) - k_x^2}\right]\right)P$
90°	$R = \sqrt{1 - X^2}$	$\sqrt{1 - \frac{c^2k_x^2}{\omega^2}}$	$i\sqrt{\frac{\omega^2}{c^2} - k_x^2}\ P$

Table 2.1: Solutions to the one-way wave equation (after Bancroft, 1997).

represented by $P(x,z,\omega)$.

$$\frac{\delta P}{\delta z} = \left[\frac{i\omega}{c} - \frac{c}{2i\omega} \frac{\delta^2}{\delta x^2} \right] P . \tag{2.12}$$

This equation cannot account for lateral velocity variations. However, Claerbout (1971) introduced a retardation term which can accommodate the phase-shift that results from a lateral velocity variation.

Explicit Method

The explicit finite-difference method extrapolates the wavefield by recursive application (depth-by-depth) of a convolutional filter in the x-ω domain (Berkhout, 1985; Holberg, 1988; Hale, 1991; Nautiyal et al., 1993). The basic idea is to consider the extrapolating operator $e^{ik_z \Delta z}$ (from Equation (2.8)) as a phase-shift operator for wave extrapolation from one depth level to the next. The operator which is obtained using a pre-defined frequency and velocity in a normalised k-ω domain, is transformed to the x-ω domain. For a general inhomogeneous medium with significant lateral velocity variations, downward continuation can be carried out conveniently in the x-ω domain using an x-dependent convolution of the waves and a filter which is the Fourier transform of the phase-shift operator (extrapolator). The processing begins by computing a table of phase-shift extrapolators for a typical range of normalised spatial frequencies. This is followed by extrapolation from one depth to the next with the key step being to solve a filter design problem as the accuracy of the explicit extrapolations is determined by the length of this filter. Lateral velocity variations are handled by letting the filter coefficients vary laterally as the value of normalised spatial frequency changes with velocity. Finally, the wavefield, P, at a depth level $z+\Delta z$ can be obtained by convolving its value at depth level z with the filter in the x-ω domain. The key problem with this method is to make the filter stable and many authors have tackled this aspect of the explicit finite-difference method (Berkhout, 1985; Holberg, 1988; Hale, 1991; Nautiyal et al., 1993).

The primary advantages of the explicit finite-difference method are that it can handle significant lateral velocity variations and can be easily extended for 3-D depth

migration. Implicit finite-difference migration has the advantage of stability but is limited to dealing with weak to moderate velocity variations. The implicit method also has the disadvantages of poor accuracy and significant frequency dispersion effects (Landmark, 1999). In addition, both methods have trouble imaging steep dips and have a major disadvantage in that they can't handle VSP and cross-hole surveys. They also have trouble handling irregular survey layouts which can prove to be a barrier when attempting to migrate large land datasets.

Implementation of the finite-difference migration technique in prestack depth mode is quite expensive and time consuming with the majority of the computation arising in the process of downward continuing the wavefield from the recording surface. If a larger migration aperture is needed, this aperture must be included as part of the entire calculation. In other words, the migration must include the aperture (output traces) at all depths, even if no energy is present at the recording surface at those trace locations. This simple fact typically results in an enormous number of extra calculations for finite-difference migration, and has so far made 3-D prestack migration of marine data by finite-difference methods economically uncompetitive compared to Kirchhoff methods (Gray et al., 2001).

Finite-difference migration using the one-way wave equation allows energy to propagate in the downward direction only. The method is limited by the assumptions made in deriving the one-way wave equation and, in particular, it is assumed that spatial derivatives of the velocity field can be ignored. However, such terms are significant in the presence of strong velocity contrasts. Furthermore, most finite-difference migration schemes that use the one-way wave equation contain a limit on the maximum dip of events which can be migrated properly. The one-way wave equation is also incapable by nature of producing correct amplitudes (Berkhout and Van Wulfften Palthe, 1979). Changes in amplitude for smooth and discontinuous velocity variations become important in the construction of prestack migration methods (Kosloff and Baysal, 1983). Being based on the one-way wave equation, only primary reflection and diffraction events are expected for the imaging process (although Eikonal or ray methods may not handle some diffractions). All non-primary events in the data such as multiples, refractions, and other wave types are

assumed to be removed before migration (Youn and Zhou, 2001). Another approach known as full wave equation migration propagates waves in the time direction and takes account of most of the drawbacks just mentioned for the one-way scheme. This method will be discussed shortly.

In summary, due to the finite-difference migration method not being particularly attractive in prestack mode, it will not be the technique of choice in this research. However, this discussion has highlighted two areas of PSDM generally that do need to be improved. The fact that the process is both time consuming and memory intensive implies that these areas need to be further considered in order to make the PSDM technique more cost-effective. Specific aspects of the PSDM process that cause it to be time consuming will be investigated in this thesis.

2.1.3 DEPTH MIGRATION USING THE FULL ACOUSTIC WAVE EQUATION

The use of the full acoustic wave equation has been implemented in poststack migration (Loewenthal and Mufti, 1983; McMechan, 1983; Baysal et al., 1983; Whitmore, 1983; Levin, 1984) and in prestack migration (Chang and McMechan, 1986; Sun and McMechan, 1986; Loewenthal and Hu, 1991). The fundamental idea of full wave equation migration is to apply the imaging principle (Claerbout 1971, 1976). Put simply, for a shot gather, the wavefield from the source is propagated forwards and the recorded wavefield is propagated backwards. A reflector image exists where these propagated wavefields are in phase. Loewenthal and Hu (1991) state that the early versions of full wave equation migration were implemented only for poststack depth migration where the whole stacked section is backward extrapolated in time, with half the velocity of the medium. All exploding reflectors are imaged at "time zero" which is referred to as the *imaging condition*. Each spatial grid point (treated as a scatterpoint) has a different excitation time, which is equal to the one-way traveltime from the source to that grid point. Each scatterpoint is imaged separately at its excitation (the "imaging time").

Chang and McMechan (1986) introduced the prestack depth implementation of full

wave equation migration using the excitation time imaging condition. To achieve an image at any scatterpoint, D in the x-z plane, three steps are used:

(a) Calculate the traveltime (or excitation time, t_{SD}) from the source to the scatterpoint (D). The excitation time can be obtained by any method of traveltime calculation such as ray tracing, by the Eikonal solution to the wave equation, or by using maximum amplitude criteria using the same full wave equation (Loewenthal and Hu, 1991).

(b) Extrapolate the entire observed wavefield backward through time to t_{SD} (backward propagation uses exactly the same equation as forward wave propagation but with reverse-time).

(c) Apply the imaging condition - obtain the amplitude of the extrapolated waves using the location of the scatterpoint and its specific excitation time and add it to the migration image panel at the same spatial point in the x-z plane.

A recent development in full wave equation migration has been made by Youn and Zhou (2001) in which multiples, transmitted, and refracted events are all treated as data instead of noise in order to increase the imaged reflector quality. This approach solves the two-way wave equation for both forward and backward propagation using a finite-difference technique. Thus it handles all types of acoustic waves such as reflection (primary and multiples), refraction, diffraction, transmission, and any combination of these waves. During the imaging, all these types of wavefields collapse at the boundaries where they are generated or altered. The results show accurate imaging of primaries and multiples with significant improvements over conventionally imaged sections. However, the method requires massive amounts of computing memory and extensive CPU time.

Full acoustic wave equation migration preserves the maximum information in the seismic record, and will accurately handle vertical and lateral velocity variations. However, a smoothed velocity model should be used in order to avoid scattered waves which may be generated from discontinuities in the velocity (Loewenthal et al., 1987). This type of migration can also handle dips up to and exceeding 90° and has no problem dealing with VSP or cross-hole survey configurations. However, the method does have the same problems with stability and numerical dispersion that

- control aliasing; and
- be an efficient interpolator.

The Kirchhoff migration method can be understood better from a 2-D physical standpoint. Given a source location, a receiver location, and a sample at time t on an unmigrated trace, the energy may have originated from any point in the Earth for which the total traveltime from source to the receiver via a scatterpoint located in the subsurface is t. In a constant velocity 2-D Earth, this locus of points is a semi-ellipse in two dimensions, with one focus at the source and the other at the receiver. In the zero offset case where the source and receiver are coincident, the semi-ellipse becomes a semi-circle. These are the only candidate reflector locations (Gray et al., 2001). If just a single spike existed on an unmigrated trace, migration has no choice but to spread the spike over the locus of all possible reflection points - the semi-circle for 2-D poststack migration (the zero offset case) (Figure 2.1(a)) or the ellipse for 2-D prestack migration (the non-zero offset case) (Figure 2.1(b)).

With respect to 2-D poststack migration, given a different sample, perhaps on a different unmigrated trace, migration would similarly spread that sample onto a semi-circle of its own. Kirchhoff migration works by repeating this process for all samples on all input unmigrated traces, summing each resulting semi-circle's contributions into the output image as it goes (Gray et al., 2001). The familiar destructive and constructive interference process observed in optics applies here with constructive interference occurring where a subsurface event exists. Figure 2.2 demonstrates this process for 2-D poststack migration. A similar situation could be visualised for the 2-D prestack method where semi-ellipses constructively and destructively interfere to give the migrated image.

The integral solution to the 2-D scalar acoustic wave equation consists of two terms: the *near-field* term which is proportional to $1/r$ and decays more rapidly with distance than the *far-field* term which is proportional to $1/\sqrt{r}$. The distance from a source to a receiver via the location of a scatterpoint in the subsurface defines 'r'. The first term is normally dropped in a practical implementation of the integral because its contribution is negligible when compared with the second term (Yilmaz,

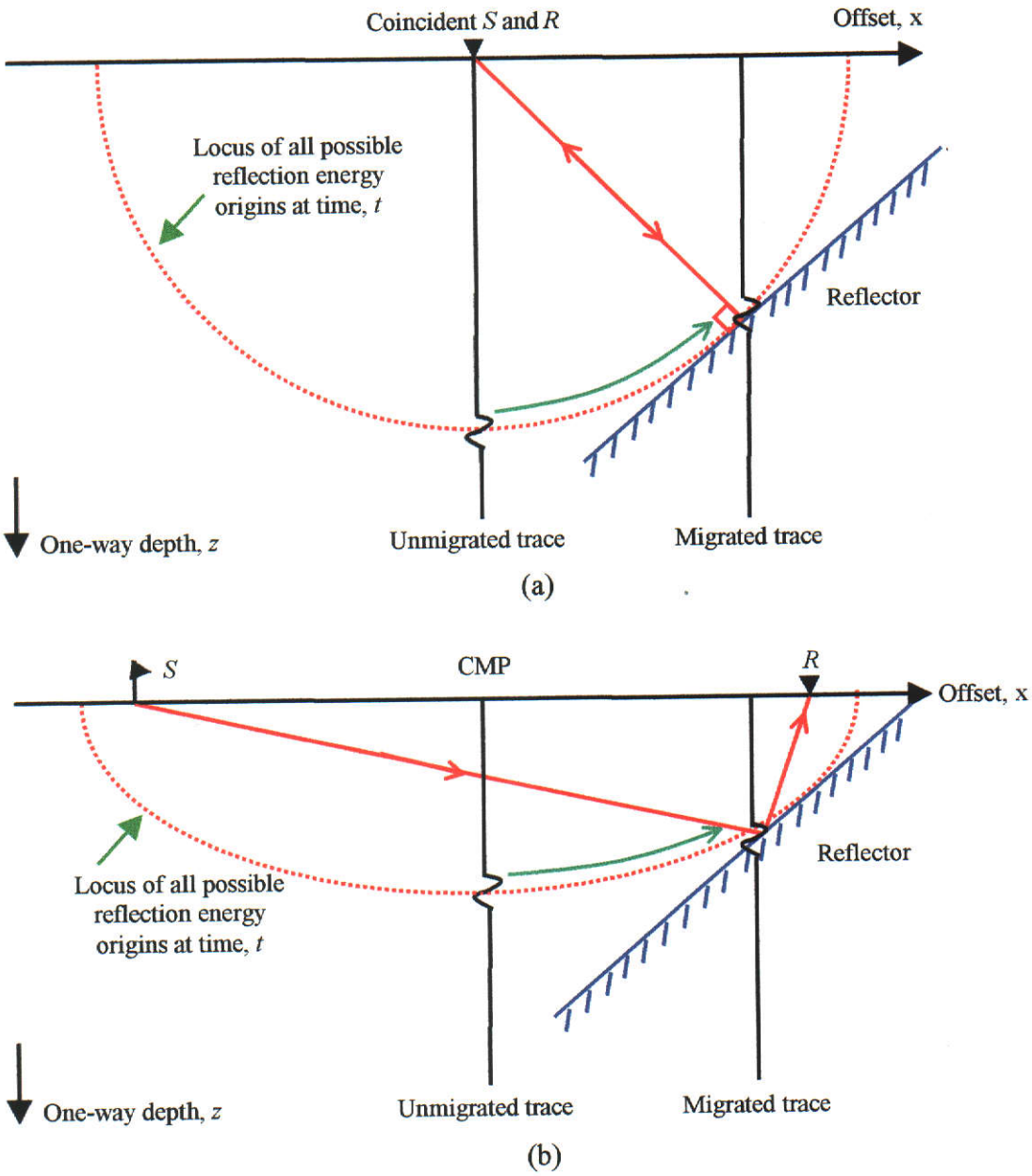

Figure 2.1: Poststack and prestack Kirchhoff depth migration. (a) Poststack - reflections with the same time could come from any position on a *semi-circle*. (b) Prestack - all possible reflection points lie on a *semi-ellipse* with the S and R locations being the foci (Bancroft, 1997).

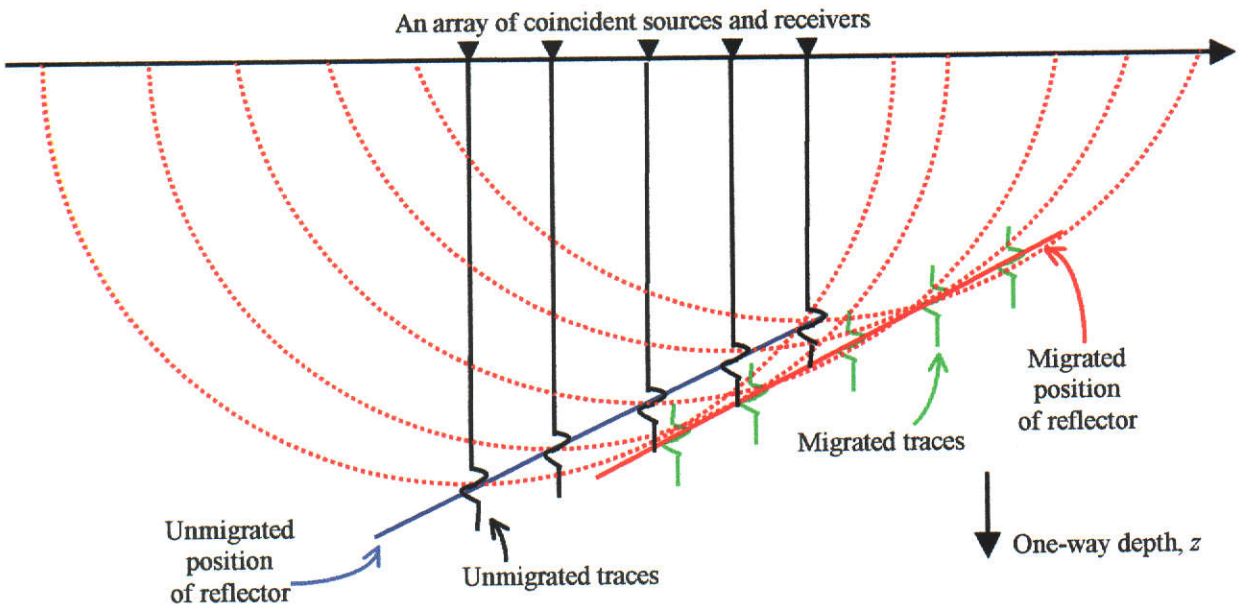

Figure 2.2: Constructive amplitude interference associated with 2-D Kirchhoff poststack depth migration. Each reflection event on a seismic trace spreads to all possible reflection points, the shape defining a semi-circle. Constructive interference of all semi-circles occurs where a subsurface event exists.

1987). However, this can be done only in the case of surface seismic - the near field contribution is significant when considering VSP and cross-well data. The two terms are evident in the following equation (Yilmaz, 1987):

$$P_m(x_m, z_m(x_m), 0) = \frac{1}{\pi}\int_{-\infty}^{\infty}\left[\frac{\cos\theta_{xz}}{r_{xz}}P_u(x_u, 0, t_u) + \frac{\cos\theta_{xz}}{\sqrt{cr_{xz}}}\frac{\partial^{1/2}}{\partial t^{1/2}}P_u(x_u, 0, t_u)\right]dx\,, \quad (2.13)$$

where: P_u and P_m are the unmigrated and migrated pressure fields respectively; x and z are the cartesian coordinates of the pressure wave location; $r_{xz}=(x_u,z_u)$ is the location of the unmigrated pressure event; c is the constant velocity of the medium above the reflector; $t_u=(t_m+r_{xz}/c)$ is the traveltime of the unmigrated pressure event (this is also known as the *advanced time* and is the time taken for the pressure event to travel in a straight line between the unmigrated and migrated locations); θ_{xz} is the angle subtended by the pressure wave location and the surface location of the coincident (zero offset case) source and receiver; and dx is the infinitesimal input trace spacing. Equation (2.13) indicates that what happens at a depth point (x_m,z_m) at time $t_m=0$, is determined by measurements made at all surface points, $(x_u,0)$, at a later time $t_u=r_{xz}/c$. Various parameters can be described as follows:

(a) $\cos\theta_{xz}$ is the 2-D *obliquity* factor which exists because the recordings of lateral signals are diminished in amplitude as the z-component decreases with an increase in angle to the normal. However, in the integral solution, this effect is compensated for when changing from an integral over the angle to an integral over a surface with a corresponding Jacobian.

(b) $1/\sqrt{cr_{xz}}$ is a 2-D true amplitude *scaling* or spreading factor that can be applied before or during the migration process. This is to take account of the loss of amplitude due to geometrical spreading for a source-receiver configuration.

(c) $\partial^{1/2}/\partial t^{1/2}$ is the 2-D *wavelet shaping* factor which is designed with a 45° constant phase spectrum and an amplitude spectrum proportional to the square root of frequency. It requires that a 2-D maximum phase-compensating filter be applied before the migration process in order to maintain wavelet compatibility with the original source wavelet.

Thus far I have described Kirchhoff migration by considering the location to which the energy on a seismic trace in the shot domain gets mapped. In the 2-D poststack case the energy gets spread out over a "semi-circle" whereas in the prestack case it is spread out over a "semi-ellipse". However, Kirchhoff migration can also be described in terms of "where did the energy at a scatterpoint position in the depth section come from?" Essentially, this energy is the result of summing all amplitudes that lie on a diffraction hyperbola with the apex defined at the scatterpoint position in x-z space. In Kirchhoff migration, how the diffraction curve used for summation is defined and what weights to apply (and when) become topics of considerable interest. For example, defining the diffraction curve as a hyperbola results in time migration. In a depth implementation, the diffraction shape is defined by estimating traveltimes from an interval velocity model, using ray tracing or by calculating wavefront positions by solving an expression such as the Eikonal equation. Traveltime maps relate the time (and optionally the amplitude) from each surface location to a region of points in the subsurface. Without considering amplitude, a simple way to achieve a structural image is to calculate the traveltimes along the ray path (source-scatterpoint-receiver) using an interval velocity model (in other words, wavefronts are being propagated and not waveforms). This is followed by migrating the amplitudes at the traveltimes to the position of the scatterpoint in the model. The final image at the scatterpoint can be obtained by stacking all contributions from all shots and receivers.

As with the depth migration methods discussed previously, there are also disadvantages associated with Kirchhoff migration. However, these can generally be overcome and coupling this fact with the advantages of the method makes it the most widely preferred type of PSDM used by industry. Firstly, Kirchhoff migration has two theoretical shortcomings. Almost all implementations make use of an asymptotic approximation that is valid only for large values of ωt (where ω is angular frequency and t is traveltime). This range of validity means that scatterpoints within several wavelengths of source or receiver locations will not be imaged correctly. At the very least, this high frequency approximation casts doubt on the ability of Kirchhoff migration to image accurately near the surface. However, in practice only the shallowest depths (within a few wavelengths of the source and receiver locations) are

affected by this approximation. Usually, even these locations are reasonably well imaged, albeit with some degradation of the amplitude and phase (Gray et al., 2001).

The second theoretical shortcoming arises from the fact that the Eikonal solution only calculates first arrival times. When the medium has highly contrasting velocity structures, several arrivals may be possible by different ray paths from any scatterpoint to a receiver array. When more than one arrival exists from a subsurface point, the first arrival may have a lower amplitude than later arrivals. Therefore, when only first arrivals are used for migration, a low amplitude or even blank image may be produced. This problem of a relative lack of accuracy has been attacked with some success by several approaches that maintain the flexibility of Kirchhoff migration. For example, Zhao et al. (1998) proposed a solution by developing a new method of calculating later arrival times and applying both first and later arrivals to a Kirchhoff diffraction mapping algorithm. It was shown that a substantial improvement could be achieved in migrated sections obtained in media with large velocity contrasts. An alternative solution was Gaussian Beam migration (da Costa et al., 1989; Lazaratos and Harris, 1990; Hill, 1990; 2001) which performs local decompositions of the source and receiver wavefields into beams which are subsequently directed back into the Earth using extremely accurate ray tracing. Several beams can emanate from a given surface location, each one corresponding to a different initial propagation direction. Each beam propagates independently of all the others along an individual "ray tube". These ray tubes can overlap so that energy can travel between image locations and source and receiver locations by more than one path. This allows Gaussian Beam migration to address the multipathing problem. Finally, Bevc (1997) applied standard Kirchhoff migration down to a depth many wavelengths below the recording surface. Within that restricted depth range, the method assumes that multipathing has not yet become a severe problem, so that Kirchhoff migration has been performed accurately. At that depth, the method computes a downward continued wavefield which is used for Kirchhoff migration within the next restricted range of depths. After several of these combined operations of migration and downward continuation, the process is complete. Bevc's (1997) method thus allows for multipathing by cascading together several steps of single path propagation.

Another disadvantage of Kirchhoff migration is that it doesn't compute correct amplitudes (Landmark, 1999). In theory, a diffraction hyperbola over which amplitude summation occurs extends to infinite time and distance. However, in practice truncated summation paths have to be dealt with. The spatial extent that the actual summation path spans (called the migration aperture) is measured in terms of the number of traces the path spans (Yilmaz, 1987). It is this finite aperture width that causes an incorrect amplitude to be obtained. A final disadvantage involves the occurrence of operator aliasing. This arises naturally for Kirchhoff migration which images by passing a diffraction surface over data without regard for their frequency content. As Abma et al. (1999) explain, the steep part of a diffraction surface can easily undersample the seismic wavelet as it passes over a flat portion of the unmigrated data. To overcome this problem, Gray (1992) and Lumley et al. (1994) proposed reducing the frequency content of the data encountered by the steep part of the diffraction surface. This approach is reported to work well but it adds a certain amount of complexity and expense to the migration.

The superior advantage of Kirchhoff migration compared with wavefield continuation migrations is that it is flexible in handling any type of survey layout. The Kirchhoff migration procedure involves an integration of the seismic wavefield along the recording surface, which in practice is cast as a discrete summation. Irregular sampling of the wavefield along the recording surface is easily handled by the discrete sum. In contrast, finite-difference and Fourier domain methods require regular sampling along the recording surface to take advantage of efficient finite-difference and fast Fourier transform operator implementations to process the wavefield. Since 3-D seismic data acquisition geometries often produce irregular trace spacings, the Kirchhoff migration method is currently the only practical approach to migrating 3-D prestack seismic data (Audebert et al., 1997). It is also commonplace with 2-D data for similar reasons.

A more striking difference between standard Kirchhoff migration and wavefield continuation methods can be seen in their treatment of migration aperture. Summing input traces over a diffraction curve or smearing input samples onto an output aperture is the major action of Kirchhoff migration. If a larger aperture is needed, an

individual trace swings into more output traces. On the other hand, as stated earlier, finite-difference migration downward continues entire wavefields from the recording surface. If a larger output aperture is needed, this aperture must be included as part of the entire calculation. This simple fact typically results in an enormous number of extra calculations for the wavefield continuation migration methods, and has so far made 3-D prestack finite-difference migration economically uncompetitive compared to the Kirchhoff method (Gray et al., 2001). In spite of greater imaging accuracy offered by other migration methods, Kirchhoff migration promises to remain a method of choice for prestack migration, especially in 3-D, for some time to come. This is because Kirchhoff migration is unique in its ability to migrate input traces selectively onto a pre-specified output volume, and this capability allows a target-oriented 3-D prestack migration to be performed hundreds of times faster by the Kirchhoff method than by competing methods (Gray and May, 1994).

Kirchhoff migration also has the ability to cope with steep dips up to and beyond 90° (i.e. turning ray energy). In addition it has great flexibility in balancing speed and accuracy and is able to handle vertical and laterally variant velocity fields quite well. As discussed previously, Kirchhoff migration is normally restricted to using the traveltimes calculated along one or a number of different paths. However, this restriction also provides Kirchhoff migration with one of its greatest strengths. It allows Kirchhoff migration with a laterally varying velocity field to run considerably faster than other methods while preserving its flexibility (Gray et al., 2001).

The Kirchhoff method is considered the workhorse in industry for prestack depth imaging. It is this common usage that designates the method as being the one where even a small improvement will have the widest impact. Prestack Kirchhoff depth imaging consists of three operations:

(a) Velocity model building;

(b) Traveltime computation; and

(c) Mapping seismic data from the shot domain to the depth domain.

The first two components are where significant improvements might be made which may ultimately lead to an improvement in the Kirchhoff depth migrated image. The depth migration process has been found to be highly sensitive to the velocity model

(Versteeg, 1993; 1994) hence any increase in accuracy of the model should be reflected in the depth migrated section. The accuracy of calculated traveltimes is also a factor that might be improved. Conventional traveltime solvers and velocity model building techniques will be reviewed in the following sections to enable specific problematic areas to be identified. These areas could provide avenues for research into the improvement of the quality of the Kirchhoff depth migrated section.

2.2 METHODS FOR TRAVELTIME COMPUTATION

The quality of depth sections obtained by performing Kirchhoff PSDM is dependent on the method of traveltime calculation. Two main approaches for traveltime calculation can be used in Kirchhoff migration. One such algorithm is ray tracing followed by interpolation of traveltimes onto the regular grid used in the migration. Another is based on solving the Eikonal equation directly on the regular grid. The Eikonal equation,

$$\left(\frac{\delta t}{\delta x}\right)^2 + \left(\frac{\delta t}{\delta z}\right)^2 = \frac{1}{c^2}\ , \tag{2.14}$$

has primarily been used to determine traveltimes along individual raypaths in a medium with acoustic velocity $c(x,z)$. Reshef and Kosloff (1986) and Vidale (1988) proposed using the Eikonal equation to compute traveltime fields directly on a regular grid. This was achieved by solving the Eikonal equation numerically, by finite-differences, at each grid point. Each grid cell formed by four grid points contains a constant velocity (Bancroft, 1997). The wavefronts in each box are assumed to be linear, and given the traveltimes at three grid points, the fourth can be computed. Computation of traveltimes at all grid points constitutes a "traveltime map".

The calculated traveltimes from a particular source to a particular receiver via a scatterpoint define points on a diffraction curve used for amplitude summation in PSDM. Hence, the more accurate the method for calculating these traveltimes, the more accurate the depth migrated section is likely to be.

2.2.1 THE RAY TRACING METHOD

Ray theory describes a variety of rays individually using Snell's law. Hence it is a flexible tool for understanding various types of waves. Ray theory plays an important role in dealing with inhomogeneous media in exploration seismology such as in traveltime tomography, seismic forward modelling, seismic inversion, and depth migration. The ray tracing method in seismology has been mathematically derived by Cerveny (1972) and since then it has been extensively applied in seismology and seismic exploration.

From a physical standpoint, ray tracing has been implemented in two main ways: ray-shooting or ray-bending. Ray-shooting is formulated as an initial value problem, where a raypath is given an initial take-off angle and starting position, then it is incrementally traced through the velocity model. A fan of rays may be traced, all emanating from the same source location and the ones that terminate sufficiently close to the desired receiver location are retained. The final ray is then found by interpolation between those nearest to the receiver position. On the other hand, ray-bending is formulated as a two-point boundary value problem where the source and receiver locations are specified. An initial guess of the path of the ray is constructed, followed by the algorithm iteratively perturbing the raypath until convergence is reached consistent with Fermat's principle of least time (Langan et al., 1985).

The primary advantage of ray tracing is its speed which makes it an efficient traveltime algorithm to use in Kirchhoff PSDM where the traveltime computation process can account for a large percentage of the run time. However, in practice ray tracing faces severe problems especially where complex velocity structures exist. When low velocity zones exist, it may not be possible to trace rays from all parts of the reflector to the receivers where energy is actually received. At these receivers ray tracing may cause artificial *shadow zones*. Sheriff (1994) defines a shadow zone as an area in which there is little penetration of waves, usually because of the velocity distribution (Figure 2.3(a)). However, it is known that waves may enter such zones by diffraction (ray tracing does not allow for diffraction or diffraction effects such as wavefront healing). In addition, when velocity models are complicated, the raypaths connecting the source to all receivers may be difficult to determine even if a dense

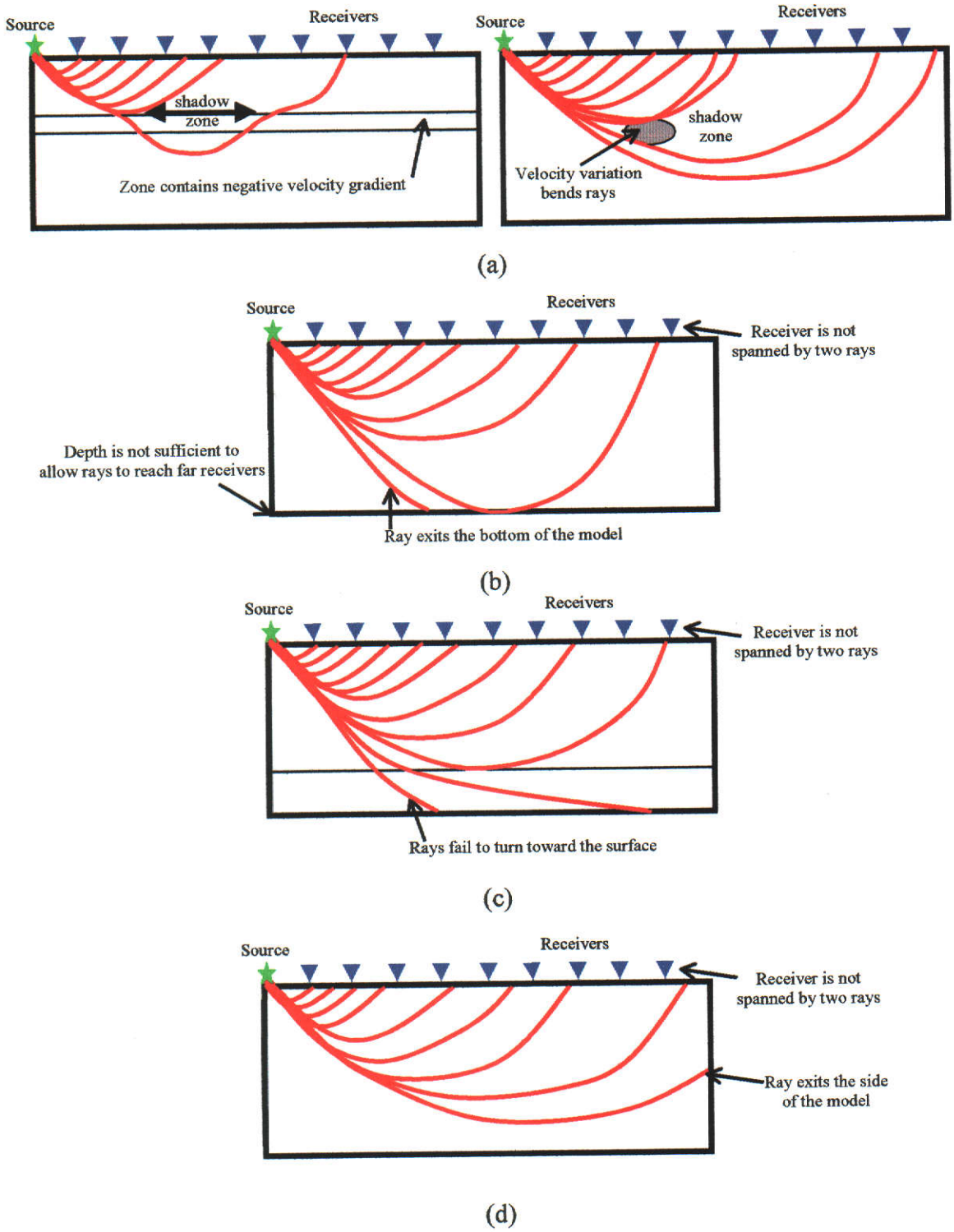

Figure 2.3: Problems with ray tracing.

(a) Velocity variations may cause shadow zones;

(b) The model is not deep enough to allow rays to reach the far receiver;

(c) The model may not have a positive gradient in the lower part;

(d) The far receiver is too close to the edge of the model and is not spanned by two rays (Landmark, 1999).

ray fan is used (which can be computationally expensive) (Thurber and Ellsworth, 1980). Further disadvantages can occur due to the size of the velocity model used for ray tracing. For example, the model may not be deep enough to allow rays to bend back sufficiently to reach the far receiver (Figure 2.3(b)). On the other hand, the model may not have a positive gradient in the lower part that means that the rays never return to the surface within the confines of the velocity model (Figure 2.3(c)). Alternatively, the far receiver may be too close to the edge of the model resulting in the situation where it is not spanned by two rays (Figure 2.3(d)). Iteration towards a correct solution is then impossible (Landmark, 1999). In addition, a shadow zone may occur due to fracturing or a change in fluids. However, the major drawback that reflection takes place from a single point for a given ray which makes it highly dependent on the local geometry of the reflecting surface. In reality, reflection effectively occurs from a region known as the *Fresnel zone*, with the overall effect being the consequence of constructive wave interference.

2.2.2 THE FINITE-DIFFERENCE METHOD

Solutions to wave propagation problems by using the finite-difference method have received considerable attention (Boore, 1972; Alford et al., 1974; Kelly et al., 1976; Vidale, 1990). This method is particularly attractive for structurally complex subsurface geometries because of the great difficulties encountered in obtaining analytical solutions in such situations. It may account for direct waves, primary reflected waves, and multiply reflected waves, head waves, diffracted waves, critically refracted waves, and wave penetration into ray-theoretical shadow zones (Kelly et al., 1976).

In recent years, finite-difference methods for the Eikonal equation were developed to replace ray tracing in applications such as first arrival time calculations. Vidale (1988, 1990) introduced a finite-difference method to solve the Eikonal equation. However, his method only accommodated outward wave propagation and failed in the presence of high velocity contrasts. To alleviate the problem, Qin et al. (1992) used an expanding grid configuration to improve Vidale's original algorithm. Cao and Greenhalgh (1994) produced a corner-node scheme that improved the accuracy of the calculation. Podvin and Lecomte (1991) introduced a method to propagate

traveltimes only and was based on an approximation to Huygens' principle and a local plane wave assumption. By applying Huygens' principle, the traveltime at a grid point can be obtained by picking the first arrival from the traveltimes of the waves coming from its neighbouring grid points. These points act as secondary Huygens' sources. This method can handle large contrasts in velocity however, the local plane wave assumption is not quite accurate without extra grid points near the source because the local plane wave fails to simulate the very curved wave fronts which appear in this region. Schneider et al. (1992) introduced a method based on a curved wavefront assumption which compensated for the disadvantages in the traveltime calculation caused by assuming plane waves near a source. In actual calculation, the curved wavefront is more accurate and stable compared with that which uses plane waves (Schneider et al., 1992). Zhao (1996b) generalised the techniques of Podvin and Lecomte (1991) while also incorporating the curved wavefront approach of Schneider et al. (1992) in order to improve the accuracy. The method allows for transmission, refraction, and diffraction of seismic waves with the arrival times being based on Fermat's principle of least time. However, the method does not consider wave amplitudes or wave shape. It can handle any geological shape or velocity contrast, utilises limited computer memory, and is computationally very fast, making it very cheap to run.

Traveltime mapping using a finite-difference method has the potential to handle large velocity contrasts (Zhao et al., 1998). It is also possible to avoid the shadow zone problem which is prevalent in ray tracing methods. However, the finite-difference method is restricted in accuracy by the grid cell size used in the computational scheme. The expense and computer requirements of these calculations rapidly become excessive as the number of grid cells is increased. This is due to the more complex geological models requiring smaller grid cell sizes in order to account for sudden velocity changes. This inevitably leads to increased costs. Conventionally, only one grid cell size is used to digitise the whole velocity model meaning that a compromise must be made between the run time (i.e. cost) and traveltime accuracy.

In summary, although it is very fast, ray tracing has the major disadvantage of losing traveltime accuracy in regions of complex velocity where PSDM is most often used.

Hence a finite-difference solution to the Eikonal equation is more commonly utilised. The major disadvantage when using this finite-difference method is the compromise that has to be made between traveltime accuracy and cost. This is an area upon which research could focus in order to provide an alternative solution to this compromise.

2.3 BUILDING THE VELOCITY MODEL

PSDM provides a powerful tool for performing velocity analysis due to its high sensitivity to the velocity error and its ability to image subsurface reflectors in the presence of severe lateral velocity gradients and large dips. However, in the exploration and appraisal of areas of complex and steeply dipping geology and limited well control, the derivation of an accurate and robust velocity model is still a challenging task. Velocity model building typically requires many iterations of computationally intensive PSDM which can be costly in terms of time and money. Hence, this is one region in which the velocity analysis technique could be improved. Versteeg (1993) states that in the early 1990's PSDM was expected to improve the accuracy and reliability of velocity estimation to the point where typical velocity errors would be 5% or less. This has still not generally happened and commonly results in persistent mis-ties, both horizontally and vertically, for wells drilled into structural targets. In practice, its frequent inability to predict accurate target locations does not represent an inherent failure of the method, but rather a shortcoming in the ability to perform velocity estimation. Therefore, to reap the full benefits of depth migration and its ability to position events in their true spatial locations, some effort has to be expended on constructing a good interval velocity model. The constantly improving quality of seismic data and increasing survey accuracy demand correspondingly high quality and accuracy for velocity models (Schultz, 1998). This means developing new techniques that can produce a better velocity model with lower velocity errors and in a minimal number of migration iterations. That is, a more accurate velocity model in less time.

Three common techniques that could be employed for building a velocity model to be used in depth imaging include forward modelling, reflection tomography, and migration velocity analysis (MVA). Forward modelling methods model the overlying, previously established, structure to predict the effects of structure on moveout. Two

techniques that rely on forward modelling to provide information for obtaining an image are the common focus point (CFP) method (Berkhout and Rietveld, 1994; Berkhout, 1996, 1997a,b; Thorbecke and Morton, 1997; Kabir and Verschuur, 1996, 2000) and coherency inversion (Landa et al., 1991). A third forward modelling method which is a variation on coherency inversion is stacking velocity inversion (Gerritsma, 1977; van der Made and van Riel, 1988; Toldi, 1989; Zijlstra et al., 1992). Reflection tomography (Bishop et al., 1985; Sherwood et al., 1986; Stork, 1992) is an approach to velocity analysis that has the ability to handle lateral velocity variations. The velocity of the medium is determined by minimising a misfit function that represents the deviation of traveltimes. The method has been implemented in association with migration as a means of generating accurate subsurface models, either from event curvature measurements (Etgen, 1990; Stork, 1992) or from migration velocities (Fowler, 1988). Reflection tomography makes few assumptions about the subsurface and potentially could handle some of the problems of the more traditional methods. However, it is inherently unstable (Tieman, 1995). In contrast, MVA can use the semblance method to measure residual moveouts and pick reflectors in the migrated domain in order to determine interval velocities. MVA can also apply a recursive procedure to estimate interval velocities. The approach is reputed to be more stable and less computationally intensive than reflection tomography. For this reason, it is the MVA technique that will be addressed in this research. It should also be simple to implement in a Kirchhoff PSDM algorithm.

Velocity estimation, CMP stacking, and migration are generally considered independent processes. However, they all have a common theoretical basis - the scalar wave equation (Yilmaz, 2001). Solution of this equation allows downward extrapolation of a seismic wavefield recorded at the Earth's surface. In turn, downward extrapolation provides a basis for common midpoint (CMP) stacking and migration (Clayton, 1978; Yilmaz and Claerbout, 1980). Since the processes of CMP stacking and migration require velocity information, they can also be used to obtain a velocity estimate (Taner and Koehler, 1969; Gardner et al., 1974). These concepts form the basis of the technique known as migration velocity analysis.

Migration velocity analysis is based on the principle that after migration with the correct velocity model, events in a common image gather (CIG) are aligned horizontally regardless of structure (Al-Yahya, 1989). A CIG is the result of collating seismic traces that image the same horizontal location. These traces are obtained from different migrated CMP gathers or shot profiles. When imaged correctly by using the correct model velocities, the image of the subsurface at a particular surface location from a range of offsets should be at the same depth regardless of the source position. An analogue is the alignment of reflections in a CMP gather after application of NMO and DMO with the correct velocity. However, the important difference between the post-migration CIG and the processed CMP gather is that the alignment of images in a CIG takes place regardless of structure - it depends only on having been migrated with the correct velocity. With an incorrect subsurface velocity model, events in a CIG will exhibit curvature as a function of offset. Lines et al. (1993) suggest that if an event curves upwards ("smile"), the migration velocity used is too slow and the depth imaging will yield depths that are too shallow. Conversely, if an event curves downwards ("frown"), the migration velocity used is too fast and the depth imaging will yield depths that are too deep (Figure 2.4). Al-Yahya (1989) notes that if the image of one reflector is aligned while the images of reflectors above it are not aligned, this means that some average velocity above the lower reflector is correct while the detailed interval velocities are not.

A variety of methods has appeared in the past decade that exploit this and other properties of migration. These include residual curvature analysis (RCA) (Al-Yahya, 1989) which exploits the event curvature property directly, stack power maximization (Shurtleff, 1984; Tieman, 1994), which exploits the event curvature property indirectly, and depth focussing analysis (DFA) (Yilmaz and Chambers, 1984) which exploits another property of migration altogether.

According to Liu (1997), MVA must address two issues to succeed:

(a) How to establish a criterion for knowing if a migration velocity is correct, and

(b) How to update the velocity if it is unacceptable.

To date, a variety of updating formulas have been developed. However, these formulas degrade with increasing complexity of media because of the rough

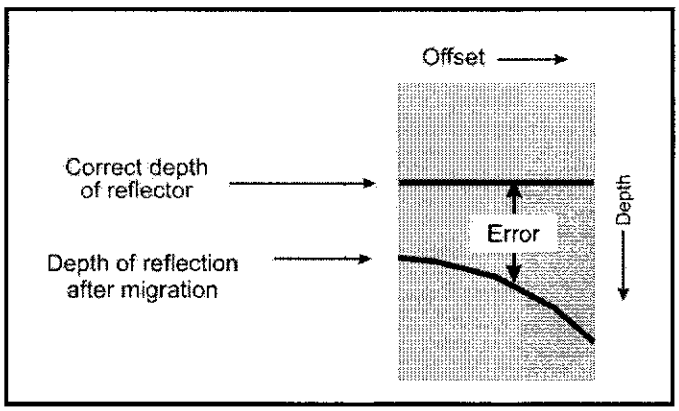

(a)

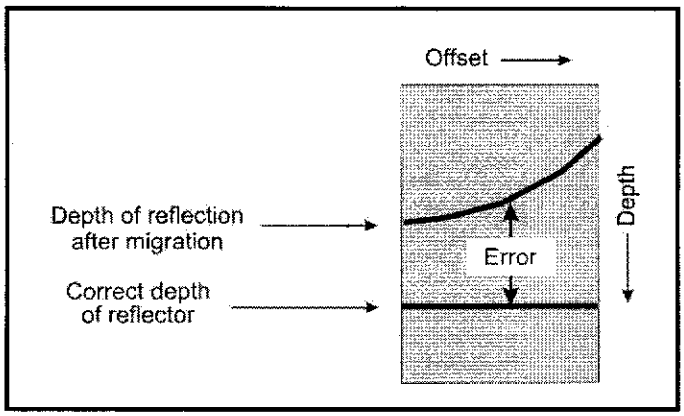

(b)

Figure 2.4: Reflector patterns when migrated with incorrect velocities.

(a) Migration velocity greater than the model velocity;

(b) Migration velocity less than the model velocity (Fagin, 1998).

approximations used to estimate velocity (such as lateral velocity homogeneity, small offsets, and small dips). Another concern with the majority of MVA methods is that they require many runs of computationally intensive PSDM (Kim et al., 1996).

Although iteration is generally helpful in obtaining a more accurate velocity model, there is a need to find an MVA technique that can reduce the required number of iterations without compromising the accuracy.

Stacking Power Methods

Stacking power methods for estimating velocity involve prestack migrating the data with a suite of constant velocities (Schleicher et al., 1991). Velocity interpretation is based on picking amplitude maxima at a given location against velocity and time. The velocity interpretation is assumed to produce the *rms* velocity in migrated time and space. This MVA technique has been implemented with a Kirchhoff algorithm (Sattlegger, 1975) and an F-K algorithm (Fowler, 1984). When constant velocity migration is followed by stacking, the method closely resembles the constant velocity NMO and stacking approach used in conventional velocity analysis. However, the cost of migration is much greater than NMO analysis and thus restricts the feasibility of the stacking power method.

Depth Focussing Analysis

Depth focussing analysis (DFA) is a technique that is essentially based on stacking power to measure velocity error. The wave equation is used to propagate the wavefield recorded at the surface down into the subsurface. The downward continued data will then appear as if they had been recorded at this depth at time zero (Mackay and Abma, 1992). When the migration velocity is equal to the medium velocity, the associated reflector will focus best at zero offset and with a zero time difference between the time of the migrated event and the time at which downward continuation began. By interpreting the non-zero times at which focussing actually occurs, the migration velocities can be updated iteratively (Liu, 1997).

This concept was first introduced by Doherty and Claerbout (1976) who worked with single CMP gathers to carry out velocity estimation from unstacked seismic data.

Yilmaz and Chambers (1984) extended their approach to include more than one CMP gather in each analysis. This allowed proper treatment of dipping events. Jeannot et al. (1986) generalised this method to PSDM in the form of DFA by determining the focussed depth in the process of downward continuation. Mackay and Abma (1989) then showed how the DFA data volume could be used to form a well focussed seismic section. The new section, the 'focal surface image', estimates the result of PSDM using the updated velocities. The formula they introduced for updating velocity was:

$$V_\tau = V_m \frac{z_m + \delta}{z_m}, \tag{2.15}$$

where z_m = migrated depth, V_τ = updated velocity, V_m = migration velocity, and δ = half the difference between the focussing and migrated depths. This formula is valid for horizontal reflectors, small offset angles, and constant velocities. Kim and Gonzalez (1991) presented the Kirchhoff integral approach to DFA which is advantageous over other DFA methods since the flexibility of the Kirchhoff integral allows one to compute just the zero offset trace at each depth point. The effects of lateral velocity variations have received less attention, although MacKay and Abma (1992, 1993) have discussed the effects of a linear velocity variation on the results of focussing analysis.

It has been shown that DFA *can* provide a focussed seismic section. However, there are disadvantages (Lee and Zhang, 1992):

(a) It requires several iterations of prestack migration.

(b) Conventionally it is based on finite-difference migration which is relatively slow and dip limited. However, the Kirchhoff approach has been implemented enabling greater flexibility.

(c) It is based only on stacking power which can be an ambiguous measure of local velocity error.

Residual Curvature Analysis

Residual curvature analysis (RCA) utilises differences in imaged depth in a CIG to provide information for updating the velocity iteratively. Al-Yahya (1989) discussed

RCA by iterative shot profile migration. Two methods for determining interval velocity were introduced: the search method and the iterative method. The search method involves searching the velocity space by migrating with several velocities to determine what velocity function aligns all events in the CIG. Semblance methods can be used to check the alignment. However, for accurate velocity estimation, the number of velocities needed to be scanned is very large which means that the cost can be high due to the increased number of migrations necessary. The interval velocities are obtained from the velocities used in migration by a method similar to the Dix equation for layered media (Dix, 1955). In Al-Yahya's (1989) iterative approach, the data are migrated once and a residual average velocity is estimated, which has to be converted to a residual interval velocity. This velocity correction is used to update the previous migration velocity and then migration is repeated until convergence is reached. To update the velocity function, a method for quantifying the deviation of events in a CIG from horizontal alignment is required. If the data were migrated with a constant velocity (V_m) which isn't equal to the true average velocity then the traveltime is expressed as:

$$t = \frac{2\sqrt{x^2 + z_m^2}}{V_m}, \tag{2.16}$$

where z_m is the depth of the migrated reflector and 'x' is the half source-receiver offset. However, if the true average velocity (V_{av}) is used then:

$$t = \frac{2\sqrt{x^2 + z^2}}{V_{av}}, \tag{2.17}$$

where 'z' is the true reflector depth. The traveltime should be the same in Equations (2.16) and (2.17) because it is an observed quantity. The ambiguity occurs between velocity and depth. Hence by eliminating 't' from these equations the following expression is obtained:

$$z_m = \sqrt{\gamma^2 z^2 + (\gamma^2 - 1)x^2}, \tag{2.18}$$

where $\gamma = V_m/V_{av}$ (Al-Yahya, 1989). The medium velocity can then be determined from:

$$V_{av} = \frac{V_m}{\gamma} \tag{2.19}$$

The method of determining which value of γ to use is based on semblance. At each depth, the data are summed along curved trajectories which represent different values of γ and the sum is largest for that value of γ that matches the actual curvature. The γ value that is determined for a layer is of course related to all γ values above that layer. For a depth-dependent velocity, the interval velocity can be calculated from the value of γ by a method similar to the Dix equation (Dix, 1955). This derivation is based on small offset, horizontal reflectors, and a laterally invariant velocity. The goal of driving all images in the CIG toward γ=1 at all depths is achieved by iteratively changing the interval velocity model, calculating γ for each event and remigrating until the process converges. The main advantage of the iterative method is that it promises to home in on the correct velocity in each iteration, which makes it more economical than the search method (Al-Yahya, 1989).

Other RCA methods include that developed by Deregowski (1990). This method was based on the fact that residual moveout (RMO) in common-offset migration is relatively independent of reflector dip (an early scheme of a similar nature was developed by Sattlegger et al. (1980)). This method is the commonly known "Deregowski loop" and involves the data being migrated and the resulting gathers subjected to RCA. The results from this analysis are used to update the interval velocity model. However, the presence of RMO in the migrated gathers indicates that the event being picked is located at the wrong spatial location. In addition, the velocity errors picked are inverted vertically using the Dix equation. To correctly update the model, the velocity error should be picked in its correct spatial location, and then used to update the velocity model by inverting along the normal to the reflector being updated. Liu and Bleistein (1992) derived a general RCA representation under the assumption of small offset and proved that RCA in common offset migration is insensitive to reflector dip for a depth dependent velocity. This conclusion implies that the velocity can be corrected without further iterations for a laterally invariant velocity. Lee and Zhang (1992) generalized Al-Yahya's (1989) residual NMO equation and proposed another residual NMO and depth restretching equation. They generalised the condition of horizontal reflector into small-angle dip by using the following relation:

$$z_m = \sqrt{\gamma^2 z^2 + (\gamma^2 - 1)(x_0^2 + (x - x_0)^2)}\ , \qquad (2.20)$$

where x_0 (Figure 2.5) is related to reflector dip, θ and is given by:

$$x_0 = z \tan\theta\ . \qquad (2.21)$$

However, this involves two unknown parameters (true velocity and reflector dip) at each imaged location which makes the approach less convenient than the determination of one single parameter. In addition, this method is still restricted by the assumptions of small dip angle and small offset compared to the migrated depth. To handle complex structures Lafond and Levander (1993) proposed an RCA method that was based on a layer stripping Kirchhoff algorithm with geometrical ray tracing in heterogeneous media. By using perturbation theory, Liu and Bleistein (1995) proposed an analytical formulation for residual moveout that is valid for any velocity distribution and any subsurface structure. This formulation can also be used to analyse the sensitivity of MVA. Tieman (1995) investigated the validity of the layer stripping approach and produced the following variation on Al-Yahya's (1989) approach in order to incorporate the effect of lateral velocity variations:

$$\tilde{z}(h,k) = \sqrt{\gamma^2 z^2 + (\gamma^2 - 1)\xi^2 x^2}\ , \qquad (2.22)$$

where 'k' is the horizontal wavenumber which is a measure of the rapidity with which an anomaly varies laterally, ξ is a correction factor that takes into account lateral velocity variations, and all other parameters are as before. If k=0 then ξ=1 and the resulting relationship is identical to Al-Yahya's (1989) formula. Liu (1997) found a relation between the perturbations of the reflector depth and the perturbations of the velocity field that could be exploited to update velocity. In this derivation there is no limitation imposed on offset, dip, or velocity distribution. However, this technique, successfully applied in a layer stripping approach, still requires picking and interpretation. Finally, Yan et al. (2001) developed an analytical equation which consists of dip-corrected residual NMO, curvature measurement, and stacking power. The dip-corrected residual NMO equation is derived by generalizing Al-Yahya's (1989) residual NMO equation and Lee and Zhang's (1992) residual NMO and depth restretching equations.

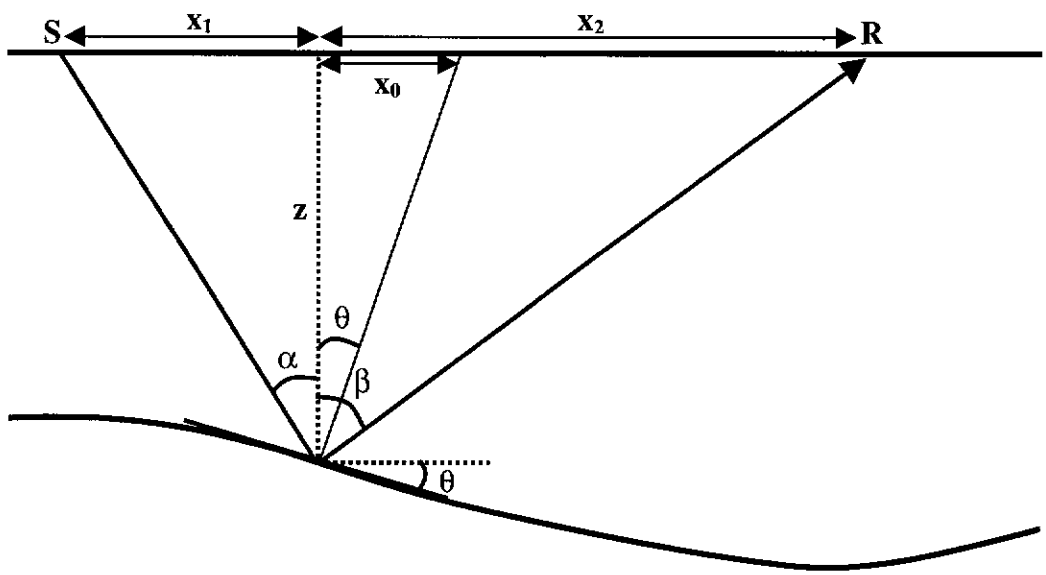

Figure 2.5: Common reflection point geometry for non-horizontal reflectors. The common reflection point is separated from the common midpoint by a distance x_0. For horizontal reflectors x_0 is equal to zero and $\alpha = \beta$ (after Lee and Zhang, 1992).

Reasonable velocity estimates may be achieved with only a few iterations for cases where residual moveouts are small (Yilmaz et al., 2001). However, sometimes a reasonable estimate is never converged upon even after quite a few iterations. This often occurs when the initial residual moveouts are caused largely by significant errors in the initial velocity-depth model. Therefore, if a good initial model could be found, an accurate velocity model might be achieved by using the RCA method. Although tomography and MVA are both used quite commonly in industry, it is the latter that will be targeted as an area of research here since it should be easily incorporated into a Kirchhoff implementation.

2.4 DEPTH IMAGING – WHERE TO FROM HERE?

PSDM is the preferred method of producing a depth image in complex geological regions. However, it is important that the depth migration process be constantly improved to enable imaging in even more complex regions. In Section 1.2, major deficiencies in the depth imaging method were cited:

(a) Computer run times (and hence costs) are excessively high;
(b) The success of depth migration is highly dependent upon the accuracy of the velocity model; and
(c) Seismic multiples obscure the primary reflection events representative of the subsurface geology.

The purpose of this chapter has been to identify elements of the depth imaging process that are associated with as many of these deficiencies as possible in order to target more specific areas that might ultimately lead to improvements in the quality and reduction in cost of the seismically determined depth section.

Initially, the PSDM component of depth imaging was considered and it was found that of the three methods presented, the Kirchhoff method appears the most attractive basis for this research. This decision was based on the fact that both finite-difference and full wave equation migration are not particularly attractive in a prestack mode due to the high run times and large amount of data needed to be stored in the computer memory. The Kirchhoff method is considered to be the workhorse in industry for prestack depth imaging. It is this common usage that designates the method as being the one that research should target for improvement. The Kirchhoff method is a simple

and flexible technique to implement in prestack mode and usually produces acceptable images at a small fraction of the cost of the other depth migration methods. However, when computing resources are insufficient, the costs are still too high and even Kirchhoff PSDM is considered to have significant run times. Decreasing the run time of Kirchhoff PSDM normally involves some form of trade-off with the amount of information that is to be used in the process. This ultimately leads to a reduction in the accuracy of depth section. However, the effect of this trade-off might be lessened by focussing on the traveltime component of Kirchhoff PSDM where a finite-difference traveltime solver is used. A finite-difference solution to the Eikonal equation is preferred over ray tracing due to the latter having the major disadvantage of providing inaccurate traveltimes in regions of complex velocity where PSDM is most often used. The finite-difference method is also preferred since it is a more convenient way to calculate traveltimes on a grid.

The second deficiency of prestack depth imaging refers to the accuracy required in the velocity model used for depth migration. Velocity estimation remains a fundamental imaging problem especially when the velocity of the subsurface varies laterally. In such situations, the migration problem becomes even more difficult since most velocity determination techniques assume minimal lateral variation (Fagin, 1998). Therefore, any new method that can be used to estimate velocity more accurately is of extreme importance as it should ultimately lead to higher quality depth images. In particular, a method that would reduce the number of iterations required to build the velocity model (and hence the time spent building the model), whilst still achieving a high degree of accuracy, is highly desirable. If this could be achieved then the cost and run time required to build the velocity model would be reduced. Although tomography and MVA are both used quite commonly in industry, it is the latter that will be targeted in this research since it is easily incorporated into a Kirchhoff PSDM algorithm. The research to be undertaken will target the RCA method as an area where improvements might be made. This method was chosen due to significant deficiencies in the other MVA methods. The stacking power method is too expensive as it requires PSDM with many different velocities in order to determine which velocity stacks with the highest power. In addition, the DFA method is conventionally based on finite-difference migration which is relatively

slow and dip limited. It is also based only on stacking power which can be an ambiguous measure of local velocity error. Alternatively, RCA has several ready made methods for quantifying the degree of residual moveout (Al-Yahya, 1989) in addition to updating velocity (Deregowski, 1990). Youn and Zhou (2001) have shown that by utilising information that is normally considered noise (i.e. multiples) in full wave equation migration, it is possible to improve the quality of the depth migrated section. Similar considerations in this research will be investigated. The possibility of using multiple energy as signal will be examined using the RCA technique to see if the velocity model accuracy can be improved using fewer PSDM iterations.

The third problem refers to the existence of multiple reflections in the depth image. An attempt is normally made to attenuate multiple energy as early as possible in the seismic processing sequence so that these events do not cause confusion in interpretation. It is often the case that several different multiple attenuation techniques will be combined in commercial processing to target a particular multiple problem. However, this can be an expensive exercise. In addition, most of these techniques rely on certain assumptions or prerequisites to perform optimally. Thus for particular cases they may or may not be good demultiple tools. As a result multiples remain a problem, motivating the search for new demultiple techniques which can function with less a priori information, fewer restrictions and unrealistic assumptions, and can target more than one multiple type. Following the investigation of using multiples as signal in the velocity model building process, they will then be considered as noise. The review of velocity model building procedures has presented MVA as a possible technique that should be investigated to attenuate problematic multiples. This possibility will be examined in the latter part of the thesis.

The goal of the depth imaging process is to produce a high quality depth section that is representative of the subsurface geology. If any one of the three possible research topics suggested proves to be successful, then the quality of the depth migrated section will have been improved.

CHAPTER 3

CALCULATION OF TRAVELTIMES

Kirchhoff PSDM maps events to their true subsurface locations using an assumed velocity model. Data are selected from shot gathers by computing traveltimes from source to receiver locations via scatterpoints located in the assumed model. The traveltime component of the Kirchhoff PSDM process is of great importance since if the technique used to calculate these traveltimes is not accurate, then inappropriate data will be selected and mapped to incorrect locations in the output depth section. This will result in a depth section with correspondingly limited accuracy. As stated in Section 2.2.2, the major problem with the finite-difference method of traveltime computation is the compromise that has to be made between accuracy and cost. Hence, this is an area in which research could be focussed in order to seek an alternative solution to this compromise. Several implementations of the finite-difference method are discussed in the literature, I have however chosen to concentrate on the method developed by Zhao (1996b). The challenge in Kirchhoff migration lies more in the traveltime computation than in the amplitude simulation and Zhao's (1996b) technique provides the ability to simulate wavefront propagation with both speed and accuracy. This technique has been implemented by Manuel (1998) and Manuel et al. (2001). A further investigation into this method will be performed in this chapter to see if improvements might be made to the traveltime computation procedure that is a key component in Kirchhoff PSDM.

3.1 IMPLEMENTATION OF THE FINITE-DIFFERENCE METHOD

As introduced in Section 2.2.2, the finite-difference method developed by Zhao (1996b) generalises the techniques of Podvin and Lecomte (1991) while also incorporating the curved wavefront approach of Schneider et al. (1992) in order to improve the accuracy of the traveltimes. The method allows for transmission, refraction, and diffraction of seismic waves with the arrival times being based on Fermat's principle of least time. However, the method does not consider wave amplitudes or wave shape, making it computationally very fast, and hence very cheap to run.

The method of Zhao (1996b) uses a nearest neighbour approximation to Huygens' principle for the traveltime calculation. This means that the time at each grid point is related to the traveltimes at its neighbouring points. Each of these neighbouring points acts as a secondary source emitting an impulse so it is not necessary for the location of the source to be known. The first arrival time at a grid point is obtained by choosing the minimum traveltime from its neighbouring Huygens' sources at neighbouring grid points. However, besides accounting for the traveltimes from the neighbouring grid points, one more approximation is needed because, in the actual medium, Huygens' sources are not just limited to the neighbouring grid points. Non-grid points are also used where necessary. This traveltime mapping procedure includes forward propagation which starts from a source and continues outward through the velocity model towards the model boundaries. It also includes propagation from the model boundaries back into the same medium. This accounts for headwaves which may develop along an interface exhibiting a suitable velocity contrast. By selecting the fastest arrival time at a grid point, headwaves can be mapped. The method of Zhao (1996b) only considers forward transmission, diffraction, and refraction – it does not cater for reflection.

Numerical simulation techniques are of limited use if they stop short of mapping seismic reflections. The Kirchhoff diffraction mapping method developed by Zhao et al. (1998) involves downward propagation from a source and downward propagation from a receiver (as if it were a source) to all scatterpoint positions using the above traveltime computation technique. The mapping technique then sums the times from the source and the receiver at each "diffraction point" in the subsurface. Using these times, data values are selected from the seismic record to create the resulting depth section. Zhao (1996b) adopted this approach to save computation time. It was faster than computing the traveltime from each scatterpoint individually to each source and receiver. Although Zhao et al. (1998) state that this method is able to handle diffractions and refractions in complex velocity models, this is not exactly the case. The adoption of this approach does have the potential to introduce a fidelity problem since diffraction is not a reversible wave phenomenon. For example, consider wave propagation from a point A to a point B. Then consider wave propagation from point B to point A. The diffractions produced in the first instance are not the same as those

produced in the second instance. It is preferable that the direction of wave propagation be honoured when traveltimes are being calculated. Therefore, it is important to develop the method further to be able to simulate seismic reflection more completely.

3.2 THE GENERALISED EXPLODING REFLECTOR METHOD

The ability to simulate seismic reflection was introduced to the method of Zhao (1996b) by Lambert (1996). This was done by incorporating a generalisation of the exploding reflector concept. However, before introducing this later development it is helpful to give a description of the original exploding reflector method (ERM) developed by Loewenthal et al. (1976).

3.2.1 METHOD DESCRIPTION

Loewenthal et al. (1976) developed the ERM to simulate a zero offset section. Imagine exploding sources to be located along the reflecting interfaces. In addition, consider one receiver located along the surface at each CMP location along the line. The sources explode in unison and send out waves that propagate upward to be recorded by the receivers at the surface (Figure 3.1). The seismic section that results from this exploding reflector model is largely equivalent to a zero offset section produced by CMP stacking, with one important distinction. A zero offset section is displayed as a function of two-way traveltime (from source to reflection point to receiver), while the ERM generates one-way traveltimes (from the exploding reflection points to the receivers). To make the sections compatible it is common place with the ERM to set the velocity of propagation to half the true medium velocity (an alternative is to double the traveltimes).

The exploding reflector concept is a powerful analogy to the zero offset recording configuration however, it has several serious shortcomings (Claerbout, 1985):

(a) At that point in time, no-one had figured out how to extend the concept to data recorded at non-zero offset. This is a necessary requirement since much data is recorded at rather large offsets.

(b) Figure 3.2 shows rays that are not predicted by the ERM but could be present in a zero offset section. Though implemented as wavefront propagation, the ERM

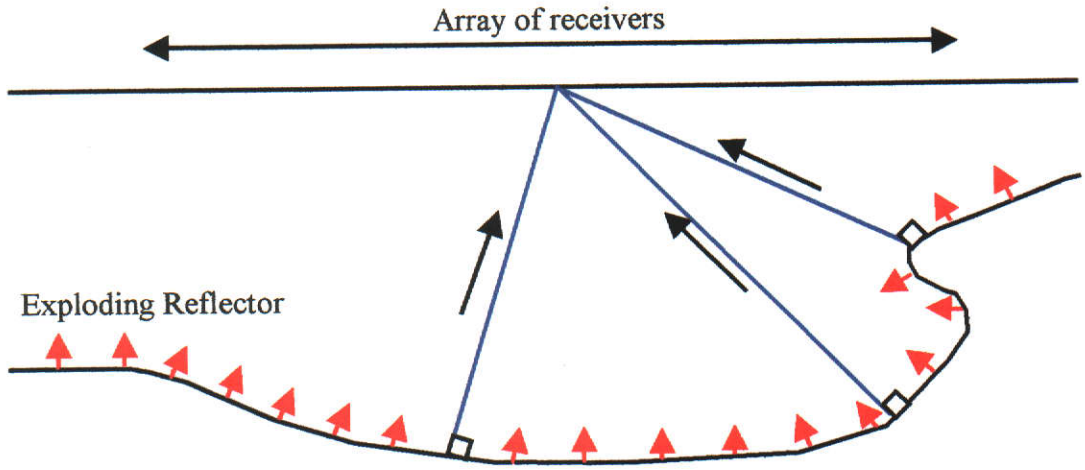

Figure 3.1: The exploding reflector method. Point sources along a reflector are exploded simultaneously at time zero and the wavefield is recorded at receivers located along the surface (Claerbout, 1985).

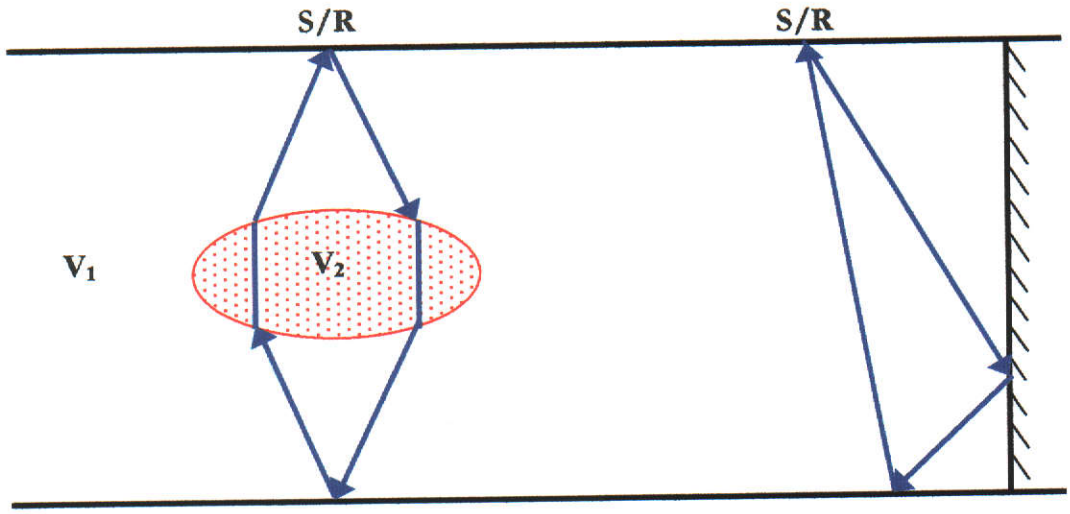

Figure 3.2: Two rays not predicted by the exploding reflector model. These would nevertheless be evidenced on a zero offset section. A lateral velocity variation is required to generate these waves (Claerbout, 1985). S/R indicates a coincident source and receiver.

virtually assumes that the raypath associated with downward propagation is the same as that associated with upward propagation (i.e. reflection occurs normal to the exploding reflector).

(c) The exploding reflector concept fails with multiple reflections. For a flat sea floor with a two-way traveltime t_1, multiple reflections would occur at times $2t_1$, $3t_1$, $4t_1$, etc. In the exploding reflector geometry the first multiple propagates from the reflector to the surface, then from the surface to the reflector, followed by propagation from the reflector to the surface again, for a total time of $3t_1$. Subsequent multiples would then occur at times $5t_1$, $7t_1$, etc. Obviously the multiple reflections generated on a CMP stacked section differ from those produced by the ERM.

(d) The final failing of the ERM occurs in situations where waves bounce from both sides of an interface. The ERM predicts the waves emitted by both sides to have the same polarity. However, the reflections from opposite sides of course have opposite polarities.

These failings, identified by Claerbout (1985), reduce the effectiveness of the ERM as a tool for modelling and migration hence an alternative method is required to counter them. The ERM propagates waveforms (i.e. amplitudes and phases). However, the method that will be investigated in this chapter propagates the wavefronts (traveltimes) required for Kirchhoff PSDM. Therefore, it is only relevant here to consider the issues (a) through to (c) above.

The generalised exploding reflector method (GERM) (Lambert, 1996; Manuel, 1998; Manuel et al., 2001) involves wavefront propagation and is a two step process. The first step involves exploding a point source at the surface and obtaining the traveltimes along a reflector (Figure 3.3(a)). The reflector is then exploded with each secondary point source along the reflector having a different initial time (equivalent to the arrival time from the point source located on the surface). These point sources are exploded systematically along the reflector as shown in Figure 3.3(b). *In this approach the traveltimes on the reflector are propagated both downward and upward. Polarities are not an issue since amplitudes are not being dealt with.*

Several distinct differences exist between the wavefront propagation characteristics

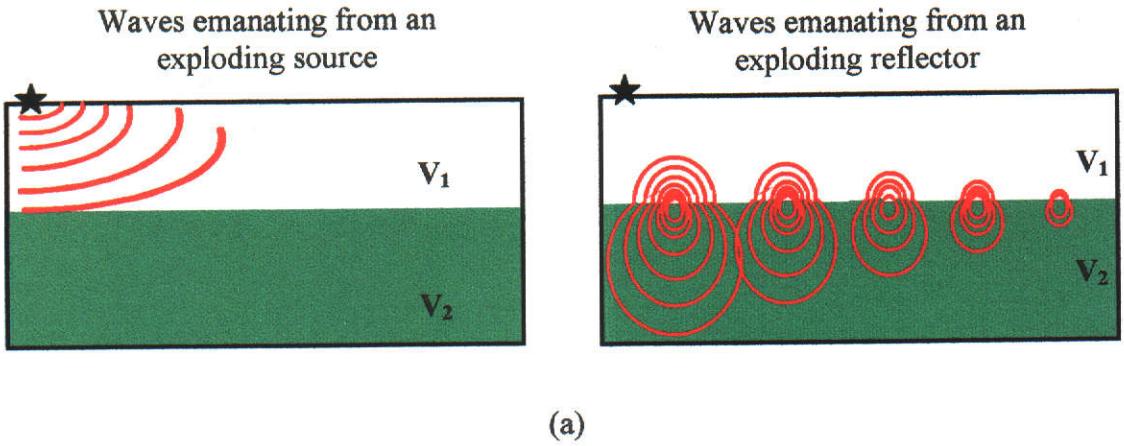

(a)

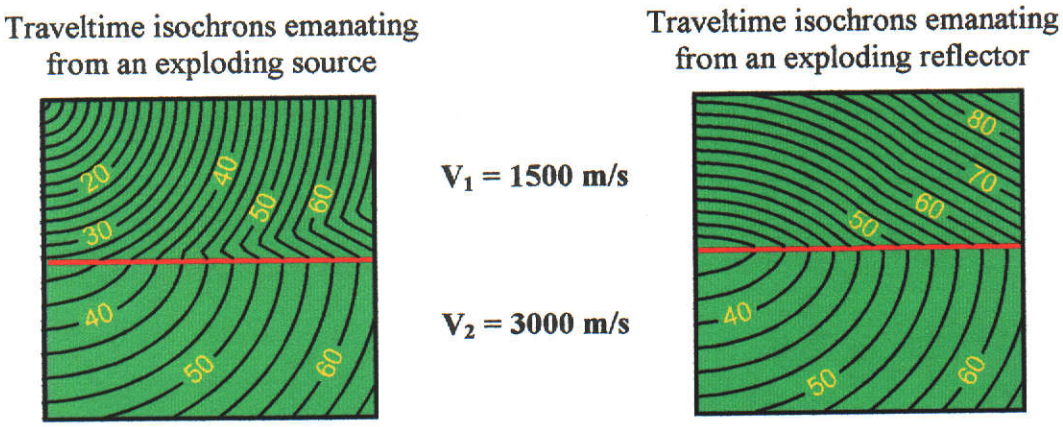

(b)

Figure 3.3: The generalised exploding reflector method.

(a) Wavefronts emanating from an exploding source and an exploding reflector (refracted waves not shown here).

(b) Traveltime isochrons emanating from an exploding source and an exploding reflector. Refracted waves are observed in the downward propagation and the upward propagation after implementation of the GERM (traveltimes are in msec).

of the GERM and the ERM:

(a) In the GERM the sources located along the exploding reflector do not explode simultaneously at time zero as in the ERM - they are exploded systematically along the reflector one at a time with the time at each source equivalent to the direct wave traveltime obtained along the reflector at each respective position.

(b) Since two-way traveltimes are used there is no need to halve the true medium velocity as must be done for the ERM.

(c) The calculated arrival times for each event are obtained at any offsets, not just zero offset.

Several applications can result from the development of this technique, two of which will be introduced here. One of these applications (covered in the next section) includes the ability to not only simulate a single reflection, but multiple reflections. Not only will reflections be faithfully reproduced but all wave types will be simulated as they should actually occur (i.e. diffractions and refractions). Converted wave traveltimes (not considered in this thesis) could also be computed with ease (Manuel, 1998).

3.2.2 SIMULATION OF SEISMIC MULTIPLES

Simulation of seismic multiples will aid in the identification of multiple events in Chapters 4 and 5 where their use will be examined in initially building the velocity model, followed by being targets for attenuation. When a boundary is exploded at depth, wavefront propagation occurs in both the upward and downward directions (Figure 3.3). The upward propagating wavefield (obtained after implementation of the GERM) will be used to simulate seismic primary reflections. Then, using the same approach, the surface boundary, and other geological boundaries may be exploded to simulate seismic multiples (Manuel, 1998). This capability enables true wave propagation direction to be honoured. *Hence diffraction and refraction will be faithfully simulated.*

Numerical simulation techniques are of limited use if they stop short of mapping seismic wave reflections. The diffraction mapping method of Zhao et al. (1998) involved downward propagation to compute diffracted traveltimes for depth

migration. However, this method did not incorporate the ability to map reflections. Therefore, there was the opportunity to develop it further to include reflections. The method of Zhao et al. (1998) incorporated Fermat's principle of least time which states that the seismic raypath between two points is that for which the traveltime is a minimum. Thus all traveltimes calculated by the program are consistent with this principle. Since seismic reflections are also governed by the same principle, this provided Lambert (1996) with the theoretical justification for the proposed modifications to the software initially developed by Zhao (1996a). Lambert (1996) was able to extend the method to simulate primary reflection by implementing the GERM. I will introduce a logical extension to this, involving the simulation of multiple reflections. This has previously been reported in a rudimentary form (Manuel, 1998).

Lambert (1996) was able to simulate primary reflections by implementing the GERM along a reflector located in the velocity model. The up-going wavefield propagated towards the surface where the arrival times were obtained at grid points representative of receiver locations. Traveltime isochron maps associated with the simulation of primary reflection from horizontal and rugose boundaries are presented in Figure 3.4. The first and second layer velocities are 1500m/s and 2000m/s respectively. These plots exhibit several phenomena. Firstly, the spreading of traveltime isochrons can be observed in the deeper layer which has a faster velocity. Secondly, the development of headwaves along each boundary can be observed in the down-going isochron map. However, these headwaves aren't very significant in this example since the velocity contrast between the two layers in both examples is only 500m/s. A third phenomenon can be observed especially in the isochron maps resulting from implementation of the GERM along the rugose boundary. This is wavefront healing which can be observed as the notching in the isochrons becomes less significant as the distance increases from the boundary where the GERM was implemented. The fact that these phenomena are being observed indicates that Lambert (1996) was successful in faithfully simulating wavefront propagation by implementation of the GERM. I confirm this by comparing the arrival times at the surface obtained from a standard numerical simulation package. This will be performed next in conjunction with numerical simulation of multiple reflections.

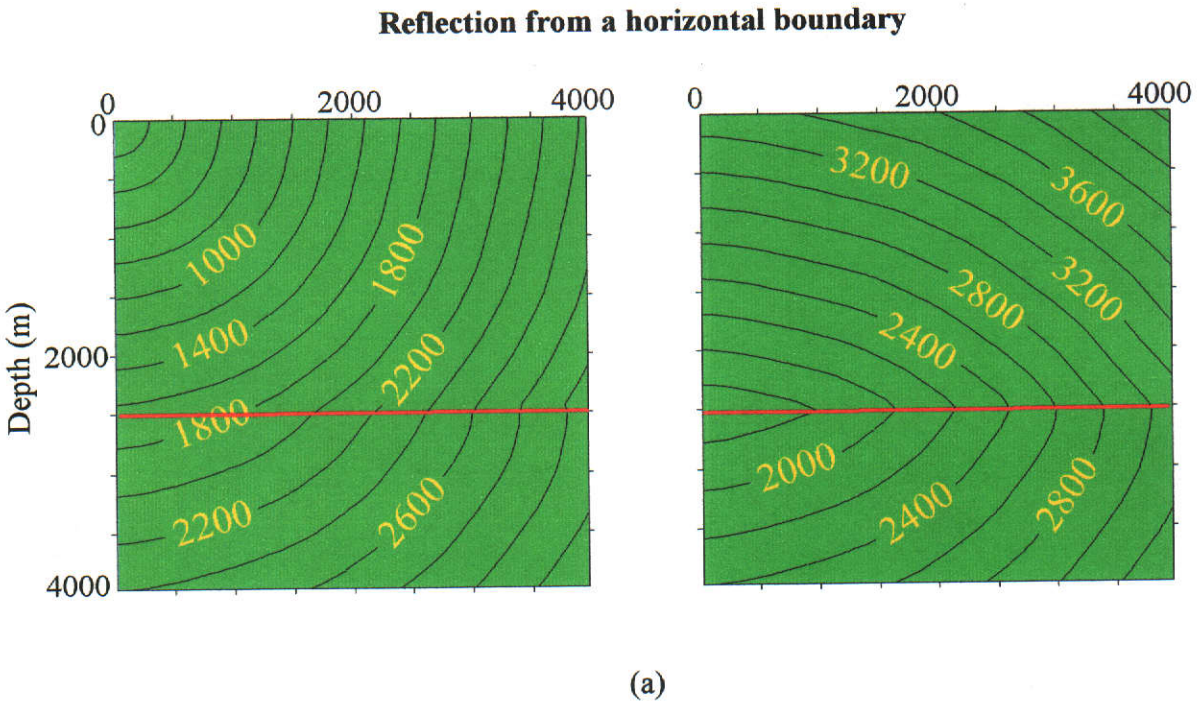

Figure 3.4: Implementation of the GERM to simulate primary reflection.

(a) Downward (left) and upward (right) wave propagation in the case of reflection from a horizontal boundary, and

(b) Downward (left) and upward (right) wave propagation in the case of reflection from a rugose boundary (traveltimes are in msec).

Extension of the method to simulate multiple reflections involves implementation of the GERM along boundaries where each bounce of the multiple occurs. For example the first order water-bottom multiple involves implementation of the GERM along the water-bottom, obtaining the arrival times along the surface and then implementing the GERM once again for the down-going reflection. Once again, arrival times may then be obtained along the water-bottom then the GERM may be executed a final time again to obtain the multiple. Arrival times may then be obtained at receiver locations at or near the surface to simulate the first order water-bottom multiple event.

Before presenting an example of this process I will describe the short hand event nomenclature presented by Levin and Shah (1977). This is best done with an example. An "S201R" event indicates that energy has propagated downward from a source (S), then reflected from the second boundary (indicated by interface 2), followed by reflection from the surface (interface 0), then reflection from the water-bottom (interface 1), and finally arrival of the energy at a receiver (R). Software that I wrote for generating the traveltimes contained in the following examples is presented in Appendix A1. Traveltime isochron maps associated with simulation of the S101R and S10101R events using the horizontal boundary model shown in Figure 3.4(a) are presented in Figure 3.5. The traveltime isochron maps associated with simulation of an interbed multiple (S212R) in a model with dipping layers can be seen in Figure 3.6. Simulation of the interbed multiple involves obtaining the arrival times along the second boundary and then implementing the GERM. Arrival times are then obtained along the first boundary and the GERM is implemented once again. A final implementation of the GERM occurs along the second boundary with the arrival times then being obtained at the surface for the S212R event.

To determine how the event arrival times obtained using the GERM compare with those from a standard numerical simulation package, the same velocity models were used in the finite-difference modelling package contained in Promax©. This finite-difference method in Promax© was developed by Vidale (1988) who, as mentioned in Section 2.2.2, proposed using the Eikonal equation to compute traveltime fields

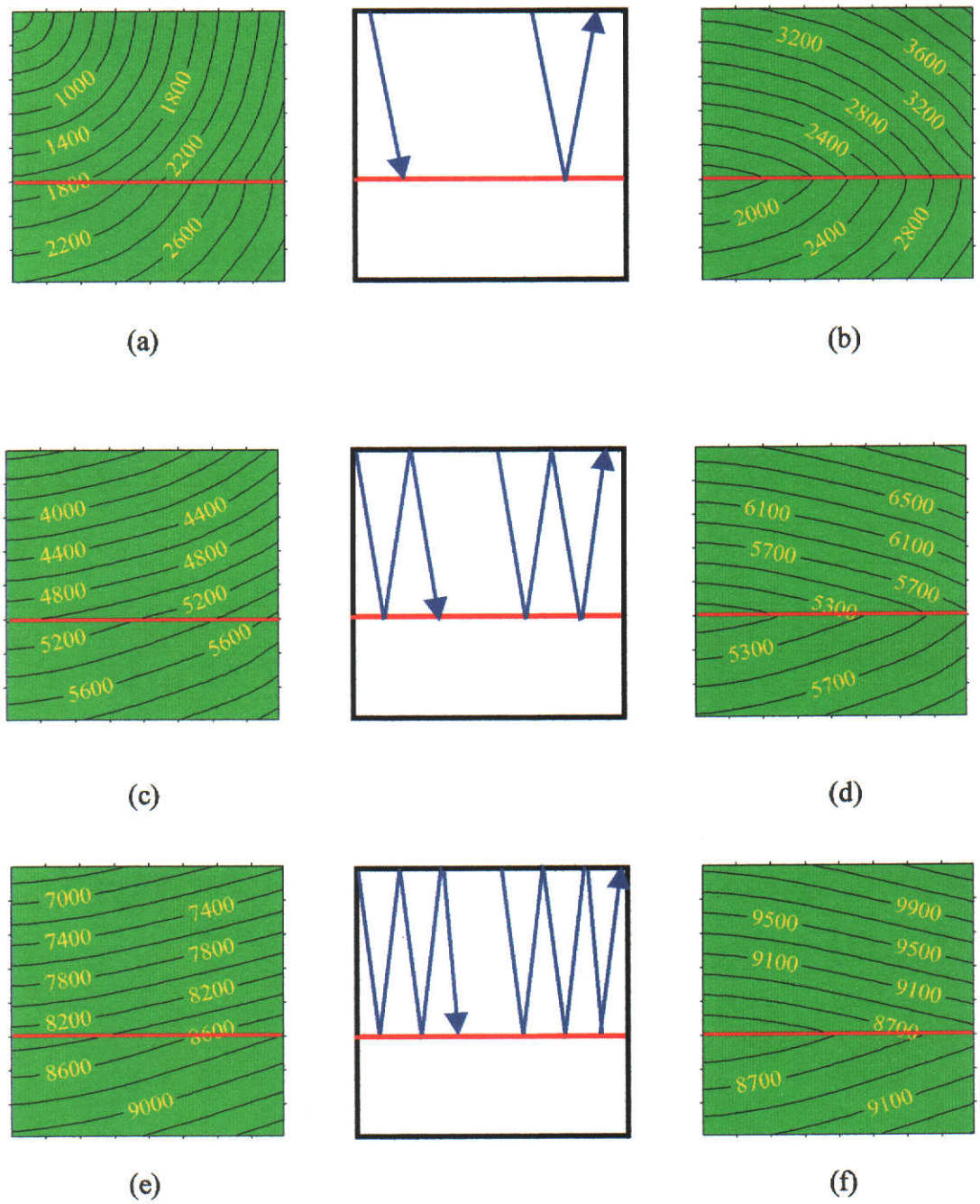

Figure 3.5: Traveltime isochron maps associated with implementation of the GERM to simulate water-bottom multiples in horizontally layered media. The S101R (a,b,c,d) and S10101R (a,b,c,d,e,f) events have been modelled. Raypaths indicate the stage of wave propagation (traveltimes are in msec).

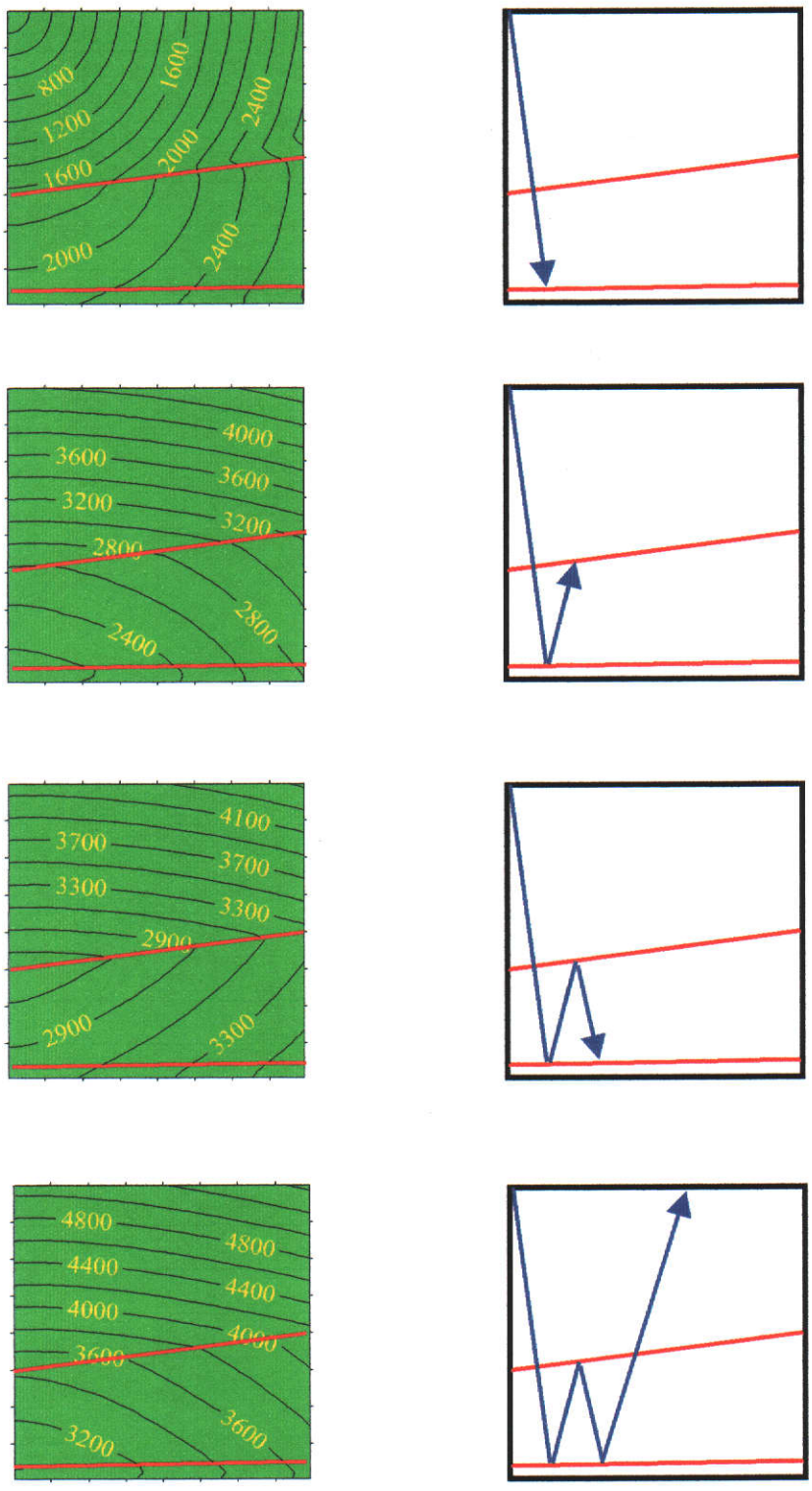

Figure 3.6: Traveltime isochron maps associated with implementation of the GERM to simulate a S212R event in dipping media. Simulation occurs in a model containing dipping layers. Raypaths indicate the stage of wave propagation (traveltimes are in msec).

directly on a regular grid. This was achieved by solving the Eikonal equation numerically, by a finite-difference approach, at each grid point. Although this method fails in the presence of high velocity contrasts, it can be used here for comparison since the velocity models here have relatively small velocity contrasts. The simulation involved the use of 400 receivers spaced 10m apart. An attempt was made to model most events in Promax© however, some were unable to be obtained due to limitations in the Promax© software. To simulate the same receiver spread using the GERM, the velocity model was divided into 400x400 cells of size 10x10m. This meant that arrival times were required at every grid cell node along the surface which made for a convenient comparison. The comparison between modelling packages when using the rugose boundary model is presented in Figure 3.7. For this example, only the S1R event was able to be compared due to the failure of Promax© to model other events. Both the whole shot gather and a zoom on the S1R event are shown here with good correlation observed between the modelled events. Figure 3.8 presents a suite of events modelled using both the GERM and Promax© for the three layer model with dipping boundaries used in Figure 3.6. The only event that was unable to be compared was the S212R event, once again due to the failure of Promax©. However, all other events compare well with very little difference (<5msec) being observed between the same events modelled using different packages. The times of each event were obtained much more quickly using the implementation of the GERM than Promax© since amplitudes didn't have to be considered with the former.

These examples have demonstrated the capacity of both the GERM and the Eikonal method to simulate seismic reflection equally well. The original ERM (Loewenthal et al., 1976) would not have been able to simulate the traveltimes produced here due to the source and receiver locations not being coincident. The adaptation to the simulation of seismic multiples has been successful with propagation direction having been honoured. This will aid in the identification of multiple events in the following chapters.

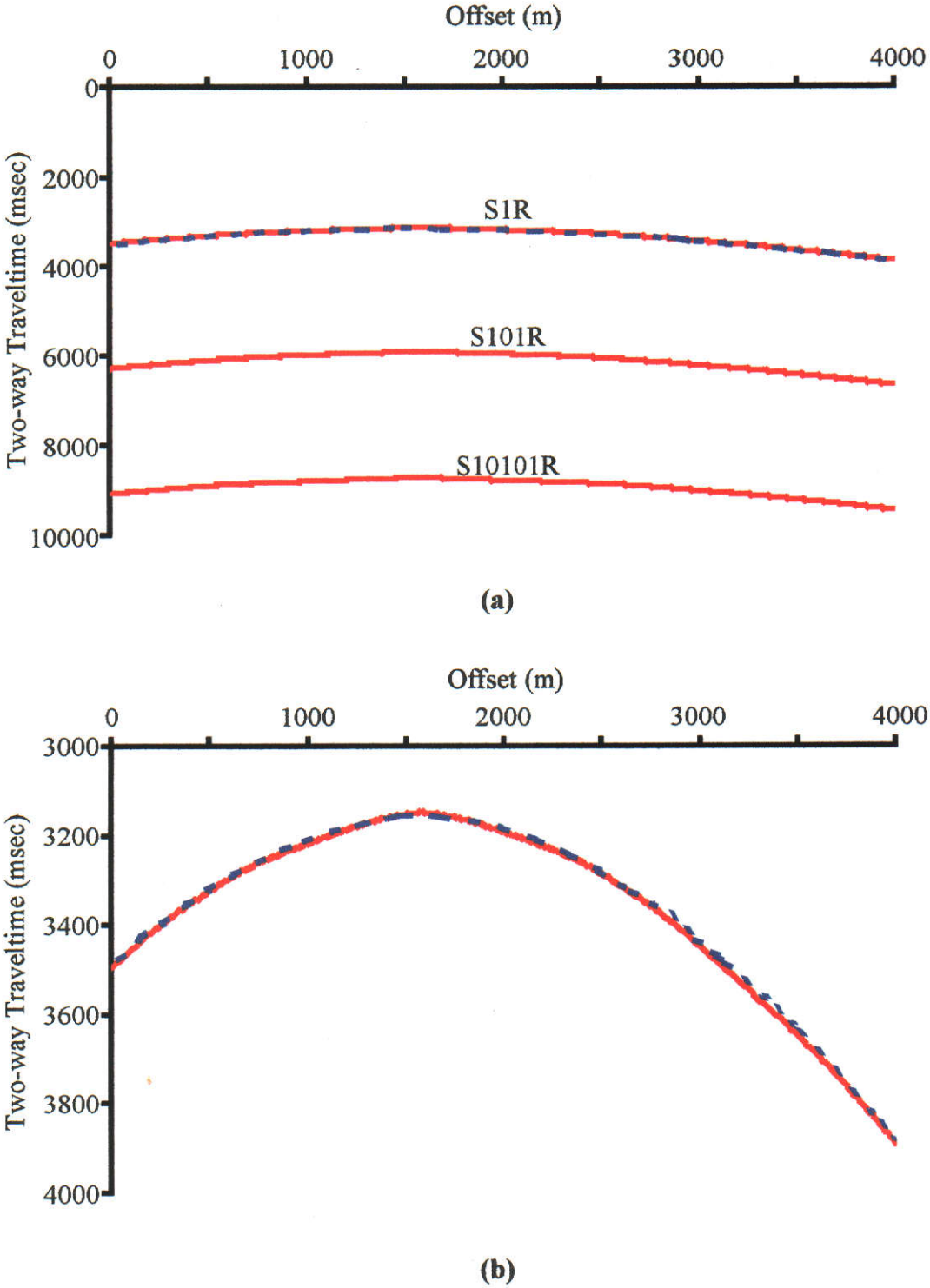

Figure 3.7: A comparison of event arrival times from using the rugose boundary model. Red events are those produced from the GERM while blue dashed events are those obtained from Promax© - (a) the whole shot gather, and (b) zoom of the S1R event.

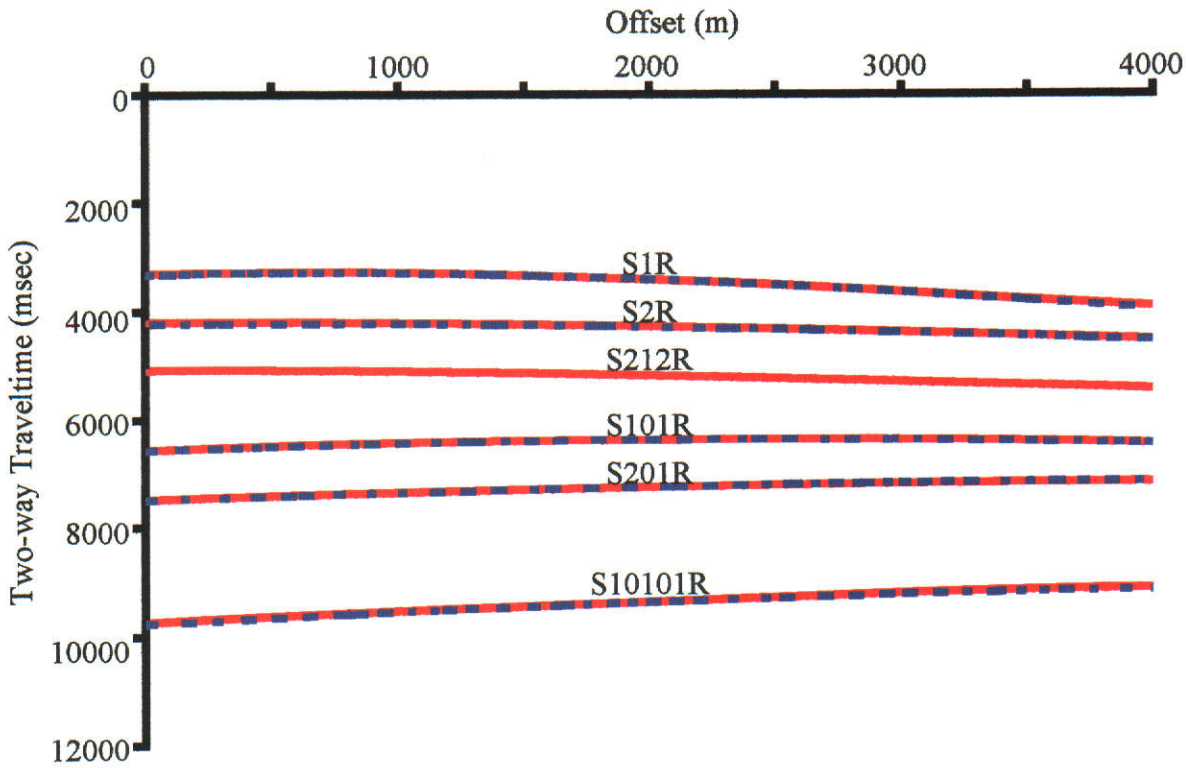

Figure 3.8: A comparison of event arrival times using the three layer model with dipping boundaries. Red events are those produced from the GERM while blue dashed events are those obtained from Promax©.

3.2.3 MULTIPLE GRID CELL SIZES

The finite-difference method for traveltime computation is restricted in accuracy by the grid cell size used in the computational scheme. When a continuous medium is approximated by a discrete grid, the calculated traveltimes will lose accuracy if the grid cell size is too large. Conversely, making the grid cell size smaller to reduce traveltime errors, becomes expensive. Therefore, in finite-difference methods which utilise one grid cell size, a compromise normally has to be made between traveltime accuracy and cost. It is important to keep this in mind when modelling more complex structures where many closely spaced events may be present.

Kirchhoff PSDM conventionally uses only one grid cell size in the traveltime computation. This means that the velocity model is divided into a number of grid cells, each of the same size, in which the velocity is constant. In these cases the square of the run time is inversely proportional to the grid cell size. For example, if the grid cell size is halved, then the run time for the traveltime component is quadrupled. If a velocity model consists of a region where the velocity varies significantly and another region where it doesn't vary much at all, then using a large grid cell size may suffice in the latter region but may cause problems in the former region. On the other hand, if a small grid cell size is used, accurate traveltimes will be obtained but it is not necessary to use such a small grid cell size in the region where the velocity variation is insignificant to achieve the required traveltime accuracy. This is where the GERM might be used to solve this problem whilst retaining accuracy in the traveltimes. Reducing run time and hence cost of the traveltime computation process might be performed by allowing more than one grid cell size to be used in the downward stage of wave propagation with the grid cell size being varied to suit the complexity of the velocity model. A smaller grid cell size could be used in those areas where the velocity variations are closely spaced while larger grid cell sizes could be used in areas where the velocities vary minimally. The decision as to what grid cell sizes to use, and in which regions, could be based on stacking velocities or other a priori knowledge.

Mechanics of Changing Grid Cell Size

The GERM involves exploding a reflector using the direct arrival times at each

"point source" along the reflector. Previously, it was used to simulate seismic reflection and subsequently simulation of seismic multiples. This involved the use of both the down-going and up-going traveltimes produced from implementation of the GERM along a reflector, and successfully honoured true wave propagation direction. In order to change grid cell sizes, the GERM will be implemented but just the down-going traveltimes will be utilised. If the grid cell size needs to be changed at a certain depth in the velocity model, the arrival times obtained at each point along a horizontal boundary at that depth would be interpolated to the new grid cell size. This boundary could then be exploded to continue downward propagation from these interpolated times. If the grid cell size were to be changed again deeper in the velocity model, then the process could be repeated. This could be done with either increasing or decreasing grid cell size any number of times. The horizontal boundary along which the GERM is implemented does not need to represent any geological boundary. It needs only be defined for the purposes of separating regions of differing velocity complexity and grid cell size. These regions can be defined from locations where significant frequency changes occur in the corresponding seismic data.

This procedure is illustrated in the schematic shown in Figure 3.9 where the velocity model has been separated into three regions based on the degree of velocity variation. The shallowest and deepest regions are assumed to contain minimal velocity variations whereas the central region contains significantly varying velocities thus requiring a smaller grid cell size. The shallowest region requires a square grid cell of width dh in order to adequately model the velocity variations. The direct arrivals along the horizontal boundary where the grid cell size is to be changed are obtained at locations separated by this distance. The central region is where the velocity varies most therefore a smaller grid cell size is required here for traveltime calculations. The square grid cell width is chosen in this illustration to be half that required in the shallowest region ($dh/2$). In order to change the grid cell size, the boundary needs to be exploded using point sources located at intervals of $dh/2$. Therefore, the times originally obtained at an interval of dh need to be interpolated to the new grid points midway between those already known. These times may be conveniently determined by using a simple linear interpolation or by implementing a Lagrange interpolation scheme. Once these times have been obtained, the boundary

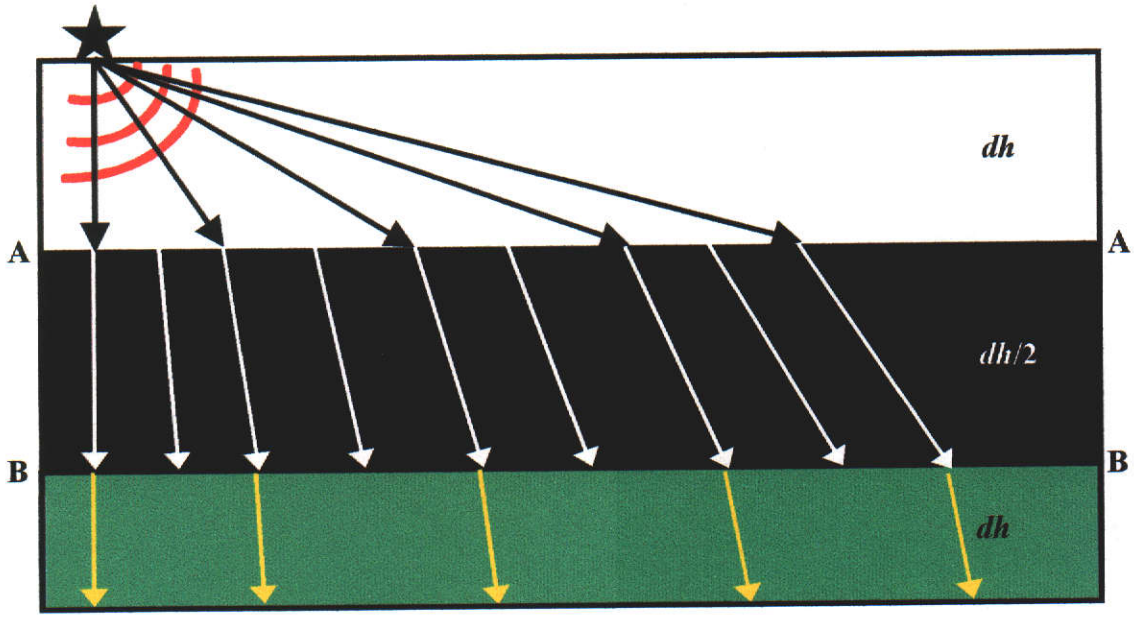

Figure 3.9: Application of the generalised exploding reflector method to change the grid cell size. The velocity model is divided into a grid containing square cells of width *dh* in the finite-difference traveltime technique. AA and BB are horizontal lines along which grid cell size is changed. These do not need to be representative of geological boundaries. Here, they separate regions of differing velocity complexity. Rays are drawn here merely to illustrate the concept. Ray tracing is not involved.

can be exploded with wavefront propagation continuing downward until the top of the third region where the velocity variation becomes less significant once again. Traveltimes could then be obtained along the boundary where the grid cell size needs to be changed. These times are then obtained at intervals of *dh* followed by the boundary being exploded and wavefront propagation continuing downward to the bottom of the velocity model. *Figure 3.9 uses raypaths purely to illustrate the concept of the technique. Ray tracing is not being used here to compute traveltimes.*

Two examples will be presented next to investigate the technique further. Initially the focus will be on examining traveltime differences with and without implementations of the GERM. This will be followed by an examination of the amplitude differences obtained by implementing the GERM in the traveltime component of a Kirchhoff PSDM algorithm. Finally, an analysis of the run times will be presented. Software that I developed for changing grid cell sizes by implementing the GERM is presented in Appendix A2.

Simple Field Example

Testing was performed to gauge the effectiveness of the method just introduced. Initially the accuracy of the traveltimes obtained from the method was tested, which required an interval velocity-depth model. Following this, it was necessary to see how the method performed when implemented in a Kirchhoff PSDM algorithm. Not only were traveltime and subsequently amplitude accuracies analysed, but it was also considered necessary to look at the run times of the method when implemented using different numbers and combinations of grid cell sizes. The run times obtained were compared with those obtained using conventional methods that utilise one grid cell size in the traveltime computation with a finite-difference traveltime solver.

The first example required an interval velocity-depth model to be built (Figure 3.10). The dataset that was used to create this model was originally acquired by Geophysical Services Incorporated for Minora Resources N.L. in the Carnarvon Basin situated on the North West Shelf of Western Australia. The geology along the line consists of slightly dipping (to the east) planar layers to a depth of 1500m where an unconformity is present. Below this unconformity is a series of planar layers of

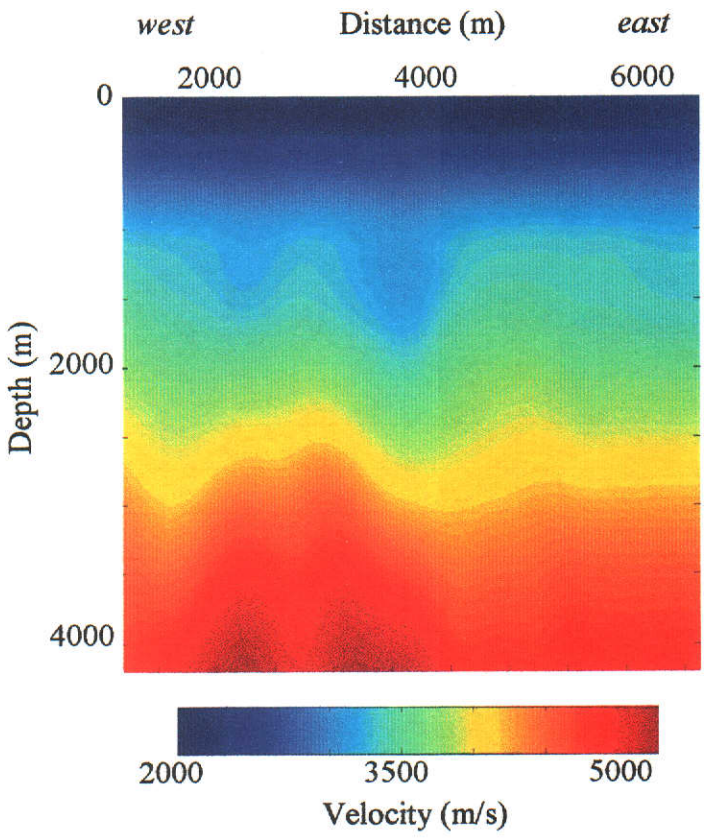

Figure 3.10: The field velocity model used for demonstrating how the GERM can be implemented with changing the grid cell size. The model was obtained by converting stacking velocities to interval velocities via the Dix transformation. The velocity variations exhibited in this model are reasonably simple.

even greater dip to the east. These layers are interrupted by a normal fault of limited throw and heave. The first and last shots were at positions 1000m and 6025m respectively from the western end of the line. Distance between shots (202 in total) was 25m with each shot being at a depth of 3.5m. The streamer (at 6.8m depth) was composed of 96 hydrophone groups, with the group spacing being 25m. Near and far offsets were 90m and 2465m respectively. Data was sampled at 4msec with a total of 5120msec of data being acquired per trace.

To produce the interval velocity-depth model, I processed the field data using the following sequence and Promax© software: initial pre-processing (trace editing and application of geometry); F-K filtering to remove spatial aliasing and linear coherent noise (mudroll); initial velocity analysis at locations every 250m along the line; dip moveout (DMO) processing to remove reflector point dispersal at non-zero offsets caused by dipping reflectors; repeated velocity analysis at locations every 250m along the line (the velocities obtained here proved to be more accurate since DMO had been applied); and application of a Dix transformation to convert the stacking velocities in time to interval velocities in depth. Since DMO had been applied, the stacking velocities were considered close enough to *rms* velocities hence a Dix transformation could be implemented successfully. These interval velocities were then smoothed with the resultant velocity model being presented in Figure 3.10.

Traveltime Analysis

A traveltime map was initially created using a small square grid cell size of width 12.5m to provide a basis for comparison (Figure 3.11). Several other traveltime maps were then generated with different grid cell sizes. For each traveltime map created in this set of comparisons, a point source was exploded on the surface at a position of 3500m along the line. Due to the traveltimes varying smoothly, subsequent tests with coarser grid dimensions were evaluated by interpolation of times to the finer grid cell size used in the base comparison. Alternatively, since the velocities varied smoothly, the traveltimes of the base comparison could have been sampled at the same grid cell size as that which is being used in a test. However, the finer grid was expected to produce a more thorough comparison. The difference between the two traveltime maps produced a *traveltime difference map*. As an example, a traveltime map was

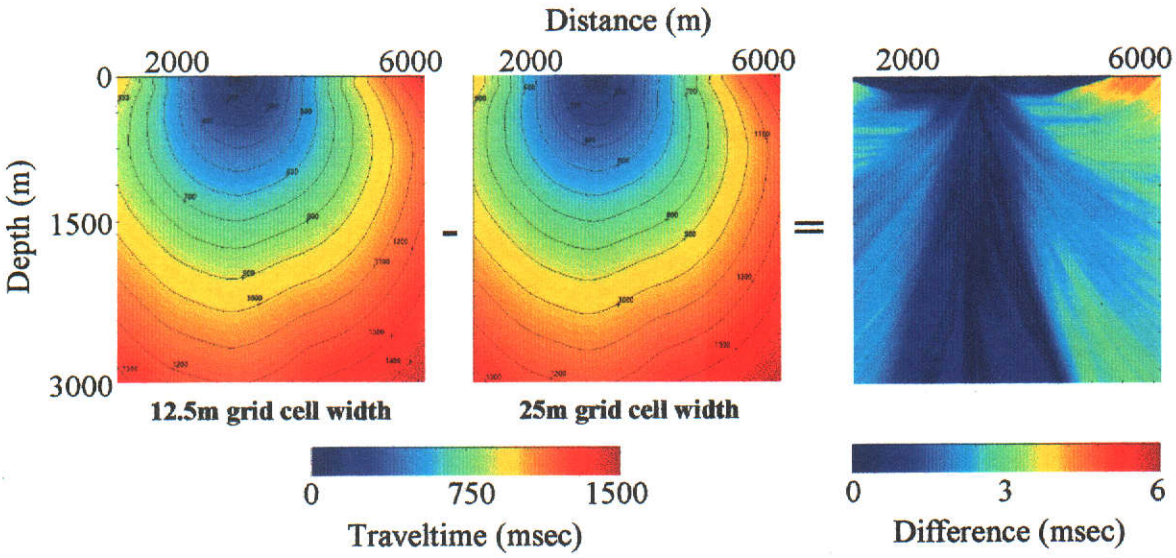

Figure 3.11: Quantitative analysis of differences in traveltime using the simple field velocity model. The traveltime map created using a square grid cell size of width 12.5m is used as the base comparison for this example. Traveltime differences of up to 5msec can be observed when using a square grid cell size of width 25m.

created using a square grid cell size of width 25m then subsequently linearly interpolated to the finer square grid cell size of width 12.5m. I then subtracted this map from the base comparison map to give the traveltime difference map shown in Figure 3.11. Examination of the difference map reveals that differences of up to 5msec have been introduced by the coarser grid cell.

To change the grid cell size, the GERM was implemented to compute traveltimes using the following square grid cell widths for different depth regions in the velocity model: 25m<800m, 800m≤12.5m<2000m, and 25m≥2000m. I then compared these times with those computed using the base comparison grid cell size. A traveltime difference map was obtained between the two traveltime maps and this is presented in Figure 3.12. In addition, the traveltime difference map from Figure 3.11 is shown alongside for comparison purposes. The central plot in this figure shows the average traveltime difference observed at each depth level in the model. Due to the velocities not varying greatly in this model, large differences in the traveltimes aren't observed with most of the differences from in both traveltime difference maps being less than 5msec. However, the traveltime difference map obtained by changing the grid cell size using the GERM has the majority of the differences in the order of 1msec as indicated by the graph of average difference with depth in Figure 3.12. The average difference exhibited when comparing the traveltime map created using a square grid cell size of width 25m is about 2msec. Therefore, the accuracy has been shown to increase to a small degree by using the smaller grid cell size in parts of the velocity model.

Kirchhoff PSDM Analysis

Having discussed the effect on the accuracy of traveltime mapping using the GERM to change grid cell sizes, it is pertinent to discuss the effect on the accuracy of depth sections created with Kirchhoff PSDM. I developed software for performing Kirchhoff PSDM (Appendix A3) in order to create the depth sections. This was done in order to be able to incorporate the traveltimes generated by using the GERM to change the grid cell size. However, to include reflected rays for this application, velocity boundaries and grid cell size zone boundaries must coincide with geological boundaries. Since this is not the case in this example, traveltimes were computed by

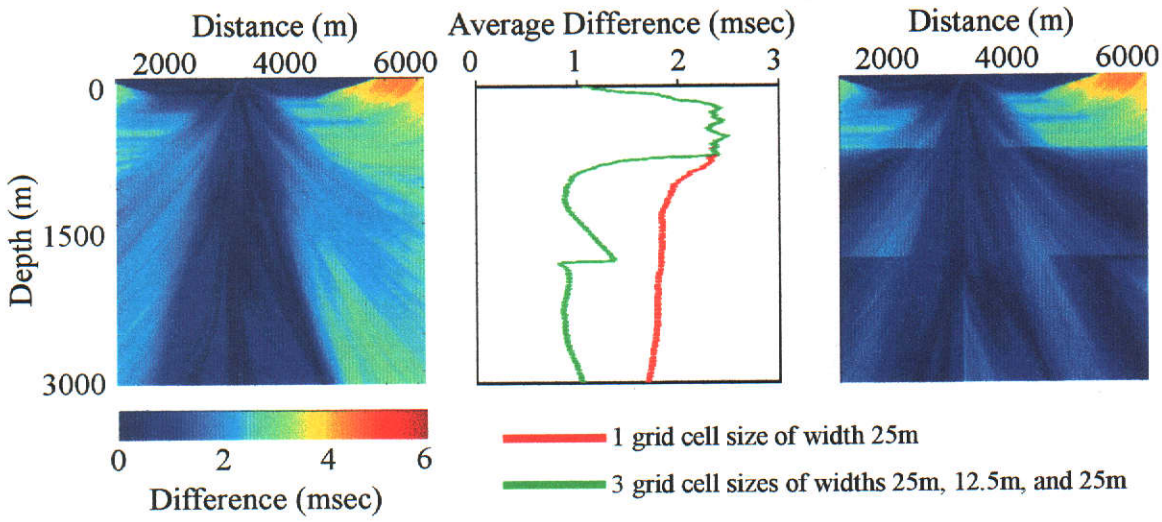

Figure 3.12: Traveltime difference analysis for the simple field velocity model. The traveltime difference map after using a square grid cell size of width 25m is shown on the left; the traveltime difference map after using the GERM to change the grid cell size is shown on the right; and the average traveltime difference with depth is shown in the centre. The differences produced by implementing the GERM to change the grid cell size are slightly less than which uses a single grid cell size in the traveltime computation.

downward propagation from sources and receivers. Hence, the Kirchhoff PSDM algorithm implemented is similar to that introduced by Zhao et al. (1998) with the difference being that I was able to change the grid cell size in the traveltime computation and only the first arrival times for diffraction mapping were considered (not later arrivals).

A square grid cell size of width 12.5m was once again used in a traveltime computation to form a depth section to be used as a base comparison. Then, a grid cell size of width 25m was used in the traveltime computation to produce another depth migrated section. This depth section was subsequently interpolated to the smaller base comparison grid cell size. Following subtraction of this interpolated depth section from the base comparison depth section, an amplitude difference map was obtained (Figure 3.13). I then employed a similar process when using the GERM in the traveltime computation with the following square grid cell widths being used in different depth regions: 25m<800m and 12.5m≥800m. The resultant amplitude difference map exhibits little difference between that with the 12.5m grid cell size width and that using a range of grid cell sizes. This is presumed to be due to there being little improvement in the traveltime accuracy due to there being a lack of substantial velocity variation in the velocity model.

Run time Analysis

The run times for a series of tests with and without changing the grid cell size using the GERM in the traveltime computation are presented in Figure 3.14. All five tests for this exercise were conducted on a Sun Ultra Enterprise 4000/250 server. Before discussing the results two points about this figure need to be made:

(a) Those bars in red represent the run times that are conventionally obtained using one grid cell size in the traveltime computation. It can be seen that by halving the grid cell size, the run time is approximately quadrupled. The blue bars represent the run times required for various implementations of the GERM to change grid cell sizes (where 3-D data is concerned, the run time will be increased by a factor of eight).

(b) On the left are the run times for each test in producing a traveltime map from one shot. These times are in seconds which may give the impression that a

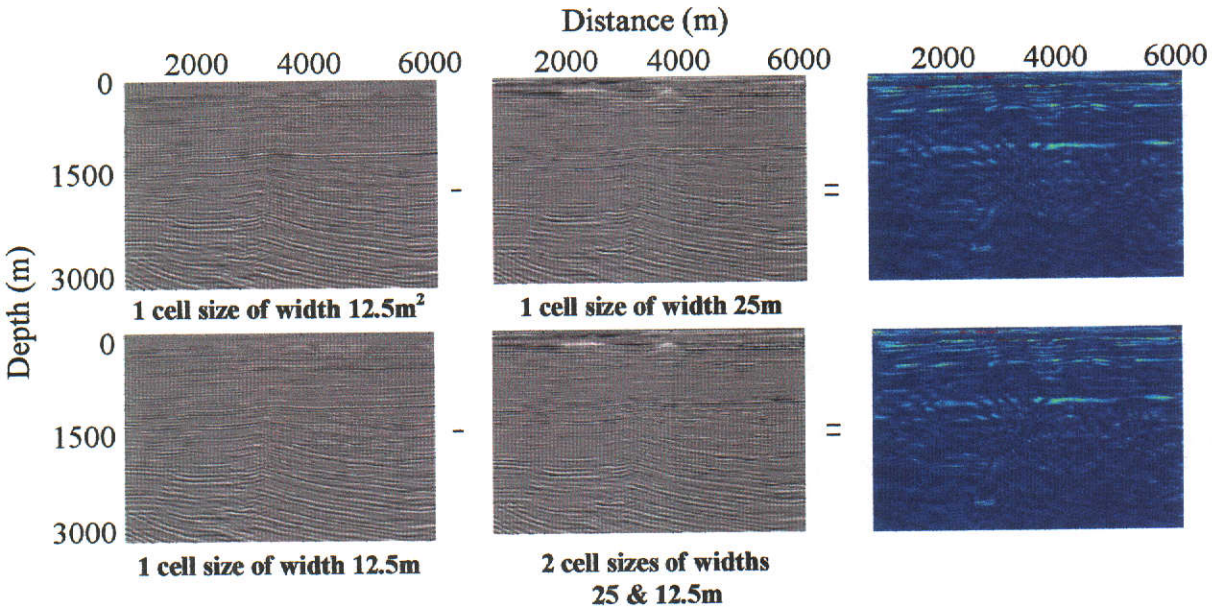

Figure 3.13: Implementation of the GERM in PSDM of the field dataset. The amplitude difference sections obtained with (bottom) and without (top) implementation of the GERM to change the grid cell size exhibit no significant differences presumably due to the lack of velocity variation not introducing any significant traveltime difference. Data courtesy of Minora Resources N.L. (1987).

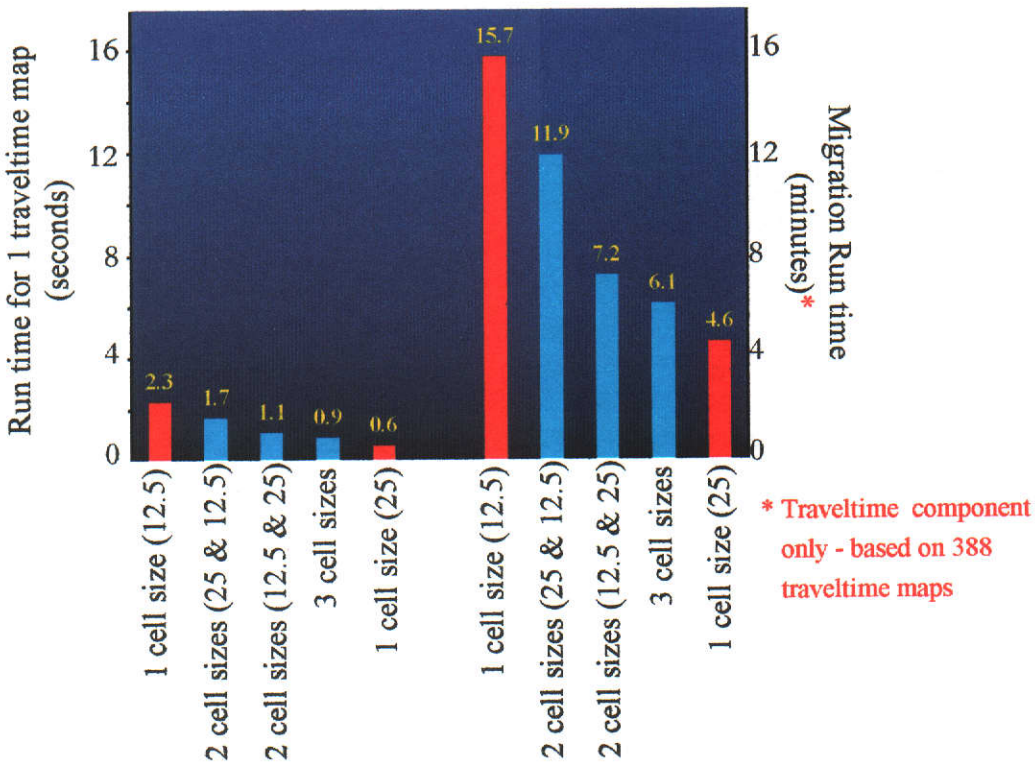

Figure 3.14: Run times for each test associated with the field dataset. Run times are associated with calculating one traveltime map (left) and calculating the 388 traveltime maps required for PSDM (right) of the field dataset. The square grid cell width is given in brackets.

difference of a few seconds in calculating one traveltime map is insignificant. However, when computing all of the traveltime maps required for Kirchhoff PSDM, the difference can convert into hours. On the right are the run times for each test in computing the 388 traveltime maps required for Kirchhoff PSDM using this velocity model and dataset. It must be kept in mind that the Kirchhoff PSDM consists of both traveltime computation and amplitude summation, however it is normally the former that comprises the majority of the run time.

An example selected from this figure shows that halving the square grid cell size from a width of 25m to 12.5m quadruples the run time from 0.6s to 2.3s to give one traveltime map. This translates to 4.6 minutes in calculating the 388 maps needed for the PSDM when using a square grid cell size of width 25m or 15.7 minutes when using a grid cell size of width 12.5m. The increase in run time doesn't improve the accuracy of the traveltimes (and consequently the depth migrated section) to any significant degree due to the lack of velocity variation in the model. Therefore, the increase in run time by decreasing the cell size seems unwarranted. However, when using the three different grid cell sizes (the same as those used in Figure 3.12) to obtain a traveltime map, the average traveltime difference from that of the base comparison traveltime map was 1msec. The production of the 388 traveltime maps needed for Kirchhoff PSDM required 6.1 minutes. The run time for producing the traveltime maps required when using the base comparison grid cell size of 12.5m was 15.7 minutes. Therefore, a sacrifice of 1msec in traveltime accuracy could be made to achieve a run time saving of 9.6 minutes (15.7 - 6.1 minutes). To determine the situations where changing grid cell sizes might be of more use it was decided to perform tests on a model where significant velocity variations were observed.

Complex Synthetic Example – Marmousi Model

A velocity model that exhibits the significant velocity variations required for further testing is the *Marmousi model.* Based on a detailed geological 2-D cross section of the Cuanza basin in Angola, the Marmousi interval velocity-depth model (Figure 3.15) was generated by the Institut Francais du Petrole (IFP) and was released to the seismic industry for the purpose of testing migration and velocity estimation techniques (European Association of Geoscientists and Engineers, 1989). The model is structurally complex, with many very thin layers broken by several major faults and an

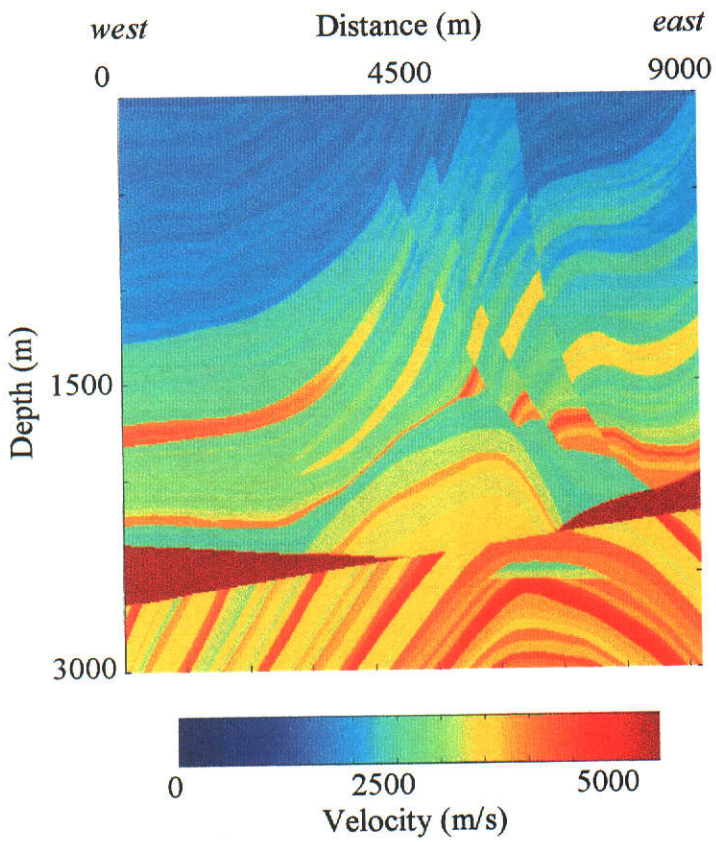

Figure 3.15: The synthetic Marmousi velocity model generated by the Institut Francais du Petrole (IFP) (European Association of Geoscientists and Engineers, 1989). This velocity model was used for demonstrating how the GERM can be implemented in changing the grid cell size.

unconformity surface. This extremely complex data set continues to be used as a test bed for migration and velocity estimation methods (Versteeg, 1994).

Traveltime Analysis

As in the previous example, I initially created a traveltime map using a small grid cell size to provide a basis for comparison. For each traveltime map created in this test, a point source was exploded on the surface at a position of 4500m along the line. Figure 3.16 presents a base comparison traveltime map which was created using a square grid cell size with a width of 4m. A traveltime map was also created using a uniform square grid cell size of width 16m. This map was subsequently interpolated to the finer square grid cell size of width 4m and subtracted from the base comparison traveltime map to give a traveltime difference map. Examination of the difference map reveals that differences of up to 20msec occurred when the coarser grid cell was used in the traveltime computations.

I then implemented the GERM to create the following square grid cell widths for different depth regions in the velocity model: 8m≤2000m, 2000m<16m≤2600m, and 32m>2600m. A traveltime difference map using the initial 4m square grid cell width for comparison was subsequently obtained and compared with the traveltime difference map presented in Figure 3.16. Both of these traveltime difference maps are shown in Figure 3.17. By using the three different grid cell sizes in the traveltime computation the effectiveness of applying the GERM to change grid cell sizes is illustrated as the traveltime difference is reduced to less than 7msec difference with an average of 4msec difference being observed. As stated previously, the traveltime difference map created using the square grid cell size of width 16m exhibits considerable differences of up to 20msec in large regions of the model with the average difference being about 12msec.

Implementing the GERM to enable the traveltime computation to occur using three grid cell sizes has reduced the traveltime difference significantly. The discrepancy between the maximum differences observed in each case being 13msec (the discrepancy in average traveltime differences is in the order of 8msec). A significant

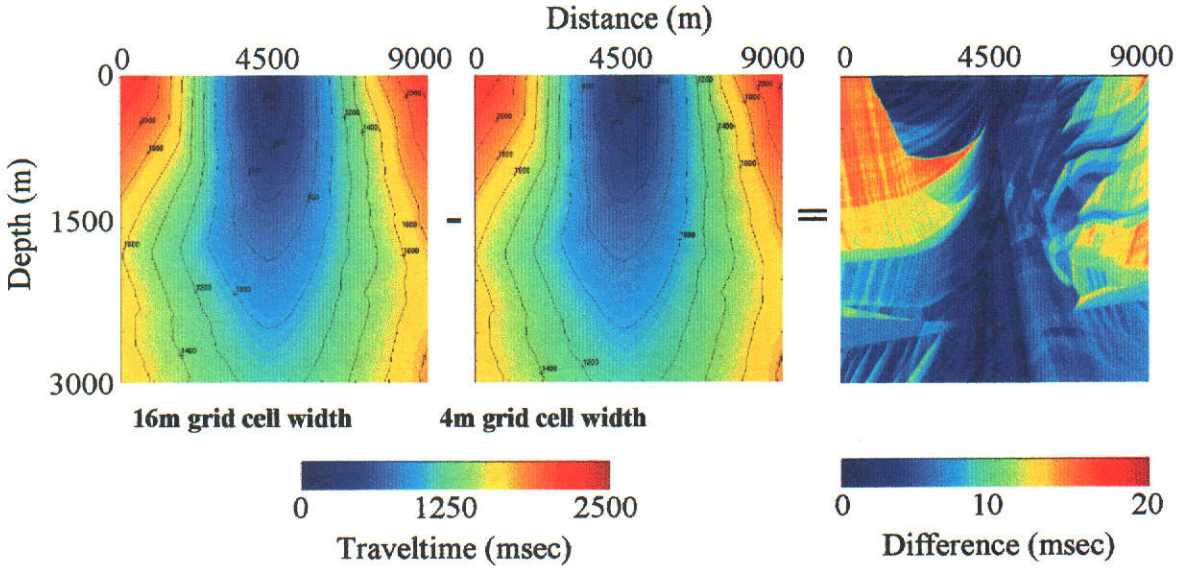

Figure 3.16: Quantitative analysis of differences in traveltime using the Marmousi velocity model. The traveltime map created using a square grid cell size of width 4m was used as the base comparison for this example. Traveltime differences of up to 20msec can be observed when using a square grid cell size of width 16m.

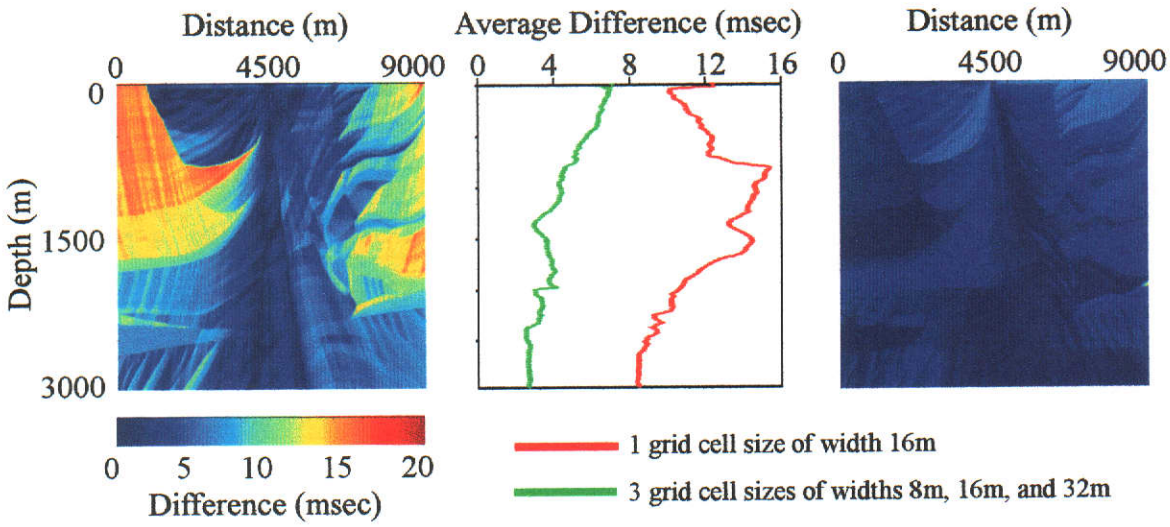

Figure 3.17: Traveltime difference analysis for the Marmousi model. The traveltime difference map after using a square grid cell size of width 16m is shown on the left; the traveltime difference map after using the GERM to change the square grid cell size is shown on the right; and average traveltime difference with depth is shown in the centre. The differences produced by implementing the GERM are considerably smaller.

increase in accuracy has been achieved by using zoned grid cell sizes compared with a uniform coarse grid. A single smaller square grid cell size can still be used, however it will result in a waste of computing time in areas where the velocity doesn't vary rapidly. A larger grid cell size should be employed in these areas to achieve the same accuracy. This indicates that there are run time issues that need to be considered and these will be discussed shortly.

Kirchhoff PSDM Analysis

Once again, an analysis was made of the effects of implementing variable grid cell sizes in the traveltime component of Kirchhoff PSDM. Not only was an interval velocity-depth model required, but a prestack dataset was also necessary. The Marmousi interval velocity-depth model was used for the generation of a synthetic dataset created by using 2-D acoustic wave propagation software which incorporated a second order (both in space and time) finite-difference scheme. Third order absorbing boundary conditions were used to reduce unwanted edge effects (Versteeg, 1994). This dataset, along with the velocity model, was obtained from IFP for use with the GERM method in Kirchhoff PSDM.

The line was acquired from west to east with the first and last shot points being 3000m and 8975m respectively from the western edge of the model. The distance between each of the 240 shots acquired was 25m with each source consisting of six water guns (each at a depth of 8m) with an array length of 40m and an 8m interval between individual guns. The shot position was located in the middle of the source array. The streamer (at 12m depth) was composed of 96 hydrophone groups, each consisting of five hydrophones spaced 4m apart. The trace for each group was obtained by summing the five hydrophone traces with the distance between two consecutive groups being 25m. The near offset for each shot was 200m while the far offset was 2575m. The data was sampled at 4msec with a total of 751 samples per trace being generated (Versteeg, 1994).

Due to the computational time required for PSDM, I used a square grid cell size of width 16m (rather than 4m) in a traveltime computation to form a depth section for a base comparison. Then a square grid cell size of width 32m was used in the

traveltime component of Kirchhoff PSDM to produce another depth section. This was subsequently interpolated and subtracted from the base comparison depth section to give the amplitude difference section shown in Figure 3.18. A similar process was then used when implementing the GERM to change the grid cell sizes within the model in the traveltime computation. The following square grid cell widths were used in different depth regions: 16m<1000m and 32m≥1000m. Following interpolation and subtraction of the depth section from the base comparison depth section, another amplitude difference map was obtained. This exhibits considerable differences from that created when a single grid cell size width of 32m was used. Significant areas where these differences did occur are denoted by A, B, C, and D in Figure 3.18. These differences are the result of using a different grid cell size in the traveltime computation. In addition, the larger grid cell size introduced aliasing into the depth migrated section as indicated by E in Figure 3.18 where the dipping reflector appears stippled. However, by implementing the GERM, the smaller cell size used in the first 1000m of the model doesn't allow as much difference to accumulate in the deeper regions resulting in less aliasing and thus a lower amplitude difference. In this instance, the amplitudes that are mapped in the Kirchhoff PSDM process when using the GERM to change the grid cell size are closer to those mapped when using the square grid cell size of width 16m (the base comparison grid cell size) throughout the whole velocity model.

The depth section I obtained when using the GERM to change the grid cell size does prove to be nearly as accurate as that obtained when using a smaller grid cell size throughout. In addition, from the traveltime difference analysis presented in Figure 3.17, an average traveltime difference of 12msec was observed between using single grid cell widths of 16m and 4m. On the other hand, by implementing the GERM to change the grid cell size, an average traveltime difference of 4msec was achieved. Taking into consideration that the Marmousi dataset was sampled at 4msec, these traveltime differences represent differences of four samples and one sample respectively. A difference of four samples is significant when performing Kirchhoff PSDM especially when using a dataset acquired over a complex geological area such as the Marmousi dataset. Amplitudes can vary widely within the space of four samples therefore structural information may be mapped to incorrect positions in the

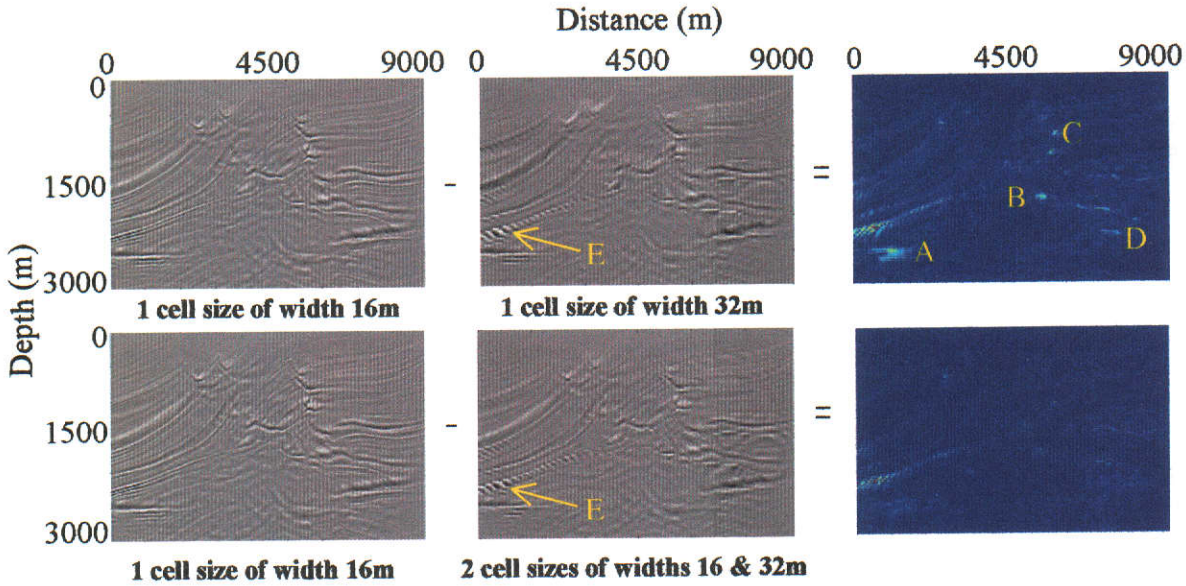

Figure 3.18: Implementation of the GERM in PSDM of the Marmousi dataset. The amplitude difference sections obtained with (bottom) and without (top) implementation of the GERM exhibit considerable differences (identified in regions A, B, C, and D) presumably due to the large velocity variations introducing significant traveltime differences. Aliasing is identified by E.

depth section. A difference of one sample will not introduce as much error into the depth migrated section. Hence by implementing the GERM to change the grid cell size in the traveltime component of Kirchhoff PSDM, amplitude differences can be reduced thus resulting in more accurate depth migrated sections. Grid cell sizes may be increased in regions where the velocity doesn't vary as much, without sacrificing significant accuracy.

Run time Analysis

Similar to the earlier example, I obtained the run times for a series of tests with and without changing the grid cell size using the GERM in the traveltime computation and these are presented in Figure 3.19. Run times have been presented for producing a single traveltime map and for producing the required number of traveltime maps (in this case 478) for the traveltime component of Kirchhoff PSDM. With respect to the run time for calculating the 478 traveltime maps required for the Kirchhoff PSDM, these results indicate a large run time difference of 45 minutes between using square grid cell sizes having widths of 16m and 8m in the traveltime component of the PSDM. If the PSDM were to be performed using a square grid cell size of width 4m, the approximate run time to calculate the 478 traveltime maps would have been 4 hours and 15 minutes, a difference of 3.5 hours. This result demonstrates that by implementing the GERM to change the grid cell size, a reduction in run time could be achieved without a substantial loss of accuracy. In this example, using the GERM to change the grid cell size (to accommodate the regions defined in Figure 3.17) allows run times to be cut from 65.3 minutes to 45.3 minutes whilst introducing an average traveltime difference of only 4msec. This corresponds to a run time saving of 25%.

A significant increase in accuracy has been achieved by using zoned grid cell sizes compared with a uniform coarse grid. As stated earlier in the traveltime comparison, the employment of a single square grid cell size such as that having a width of 12m can still be used to decrease run time and provide an alternative to using a width of 8m. However, accuracy cannot always be guaranteed since a 12m width will not be small enough in certain regions of the velocity model. On the other hand, it will result in a waste of computing time in areas where the velocity doesn't vary to any

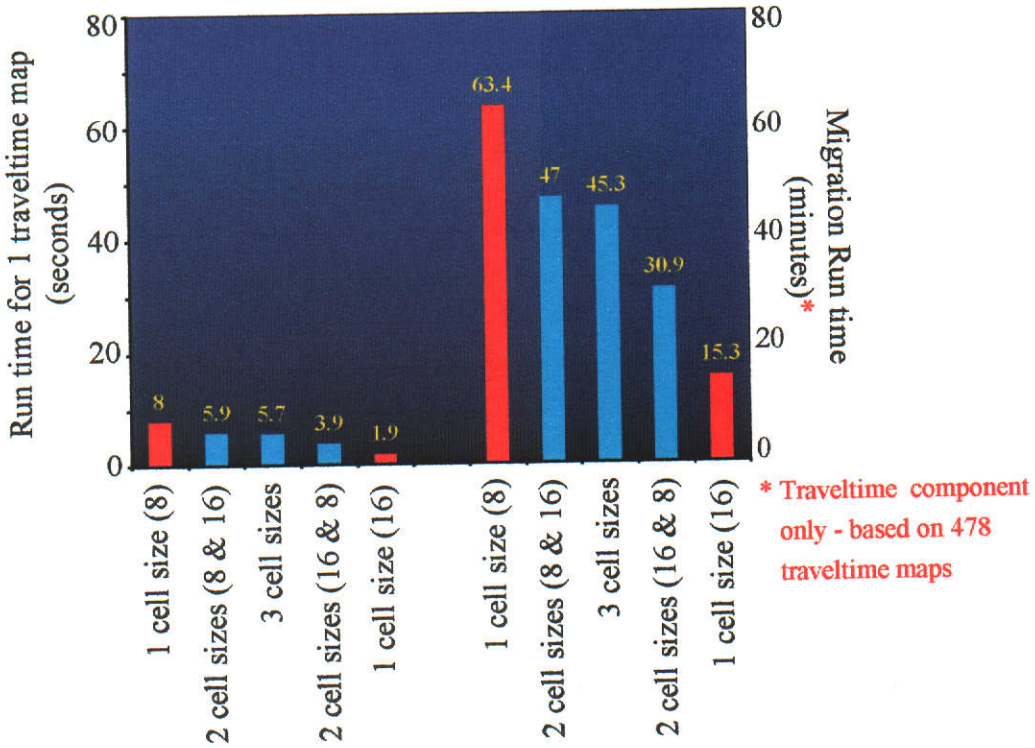

Figure 3.19: Run times for each test associated with the Marmousi dataset. Run times are associated with calculating one traveltime map (left) and calculating the 478 traveltime maps required for PSDM (right) of the field dataset. The square grid cell width is given in brackets.

significant degree and a larger grid cell size could be used to achieve similar accuracy. Hence a traveltime computation that incorporates *both* square grid cell widths of 16m and 8m in regions appropriate to the velocity complexity, would be more efficient than more efficient than a method that just utilises one grid cell size of width 16m *or* 8m. *The advantage of using the GERM is that it can be employed to change the grid cell size according to the degree of velocity variation in the model to save run time without a significant loss of accuracy.*

Implementing the GERM to change the grid cell size in the traveltime component of Kirchhoff PSDM has been shown that it is possible to produce a depth section that possesses similar accuracy to a depth section obtained using a single smaller grid cell size. In addition, the depth section in the example shown was produced in less run time than that required when using the single smaller grid cell size. The application of this technique for changing grid cell size in the traveltime computation component of Kirchhoff PSDM is naturally very example specific. This research has shown that when applied judiciously, carefully considered changes to grid cell sizes may make a significant decrease in run time. As mentioned in Section 1.2, Kirchhoff PSDM is commonly used to produce a depth section with traveltime computations comprising a significant proportion of the run time in this process. Conventionally, there is often a trade-off between run time and accuracy. If run time is to be decreased then accuracy must often be sacrificed in the depth image. The innovation introduced in this chapter would be expected to have a significant impact on commercial Kirchhoff depth imaging since significant decreases in run time can be obtained for only small losses in accuracy.

A fast, accurate, and efficient method for calculating the traveltimes required for Kirchhoff depth imaging has been presented. However, not only is traveltime accuracy paramount for a high quality depth section, but accuracy in the interval velocity model is too. Without an accurate interval velocity model, traveltimes will be computed that will not map amplitudes accurately from the prestack data to the output depth section. The next chapter deals with this issue by investigating whether a technique can be developed to create an accurate interval velocity model.

CHAPTER 4

MIGRATION VELOCITY ANALYSIS USING SEISMIC MULTIPLES

Pre-stack depth migration, which can handle both dipping reflections and lateral velocity variations, is a very attractive tool for velocity estimation in geologically complex regions because of its high sensitivity to the velocity model (Liu, 1997). Conventionally, only primary events are utilised for velocity analysis with multiples being considered as noise. Attempts are normally made to remove multiples before final velocity analysis. This chapter however, will investigate the possibility of incorporating multiples into a velocity analysis procedure by treating them as signal rather than noise. Specifically, I will investigate whether or not multiple events are more sensitive to changes in velocity than primary events. If this can be established, then the MVA technique discussed in Section 2.3 will be examined to see if improvements in the accuracy of the velocity model might be made using the information content of multiple reflections.

4.1 SENSITIVITY OF MULTIPLES TO CHANGES IN VELOCITY

Velocity model building typically requires many iterations of computationally intensive PSDM which can be costly in terms of time and money. As mentioned in Section 2.3, the frequent inability of PSDM to predict accurate target locations in practice does not represent an inherent failure of the method, but rather a shortcoming in the ability to perform velocity estimation. Therefore, other methods or other sources of information must be found to improve the velocity model. I will consider information in the seismic record that is normally made redundant to see if any velocity information can be gleaned from it. In other words, the sensitivity of multiple events to changes in interval velocity will be investigated.

Consider the propagation of a reflected wave at the correct velocity for a given medium. The reflected wavefront is shown arriving back at the surface in Figure 4.1(a). Now compare this arriving wavefront with that propagated for the same time in the same medium, but at a lower velocity than the correct velocity. For the same traveltime the second wavefront will not reach the surface. The further the waves

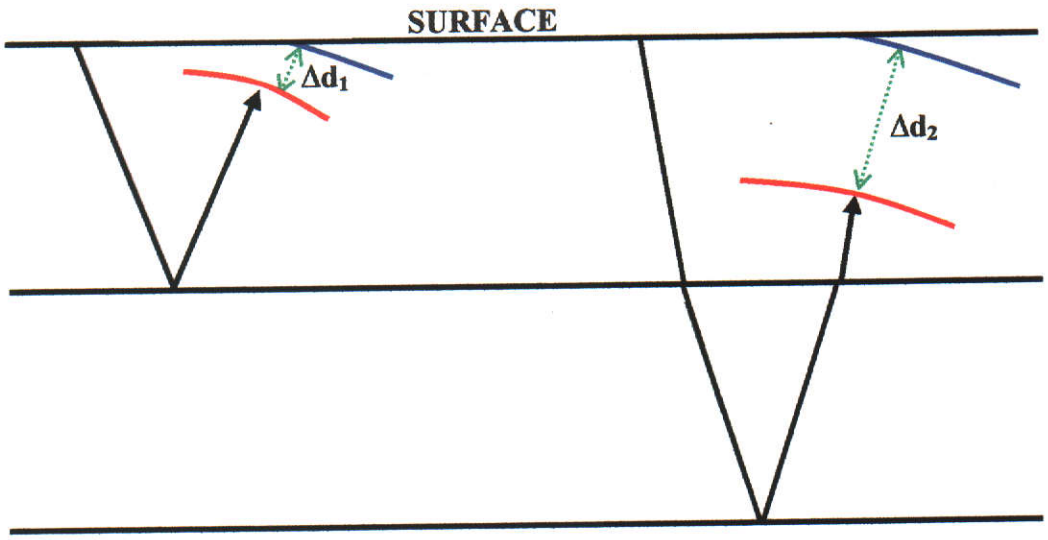

(a)

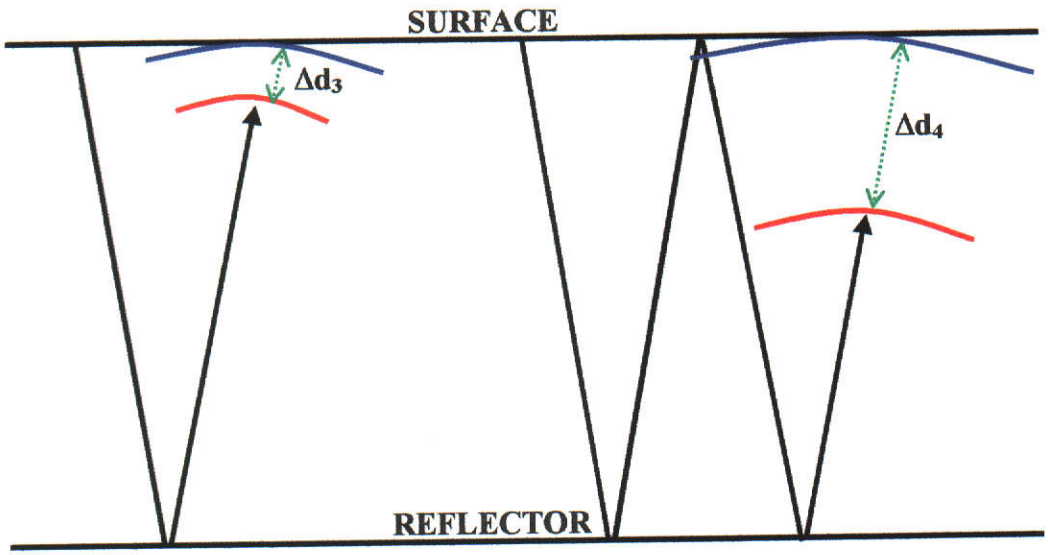

wavefront position at propagation velocity < true medium velocity

wavefront position at propagation velocity = true medium velocity

(b)

Figure 4.1: Error in velocity is compounded as the distance of propagation increases. (a) Difference in propagation distances involved with two primary events ($\Delta d_2 > \Delta d_1$) and (b) Difference in propagation distances involved with a multiple event and a corresponding primary event ($\Delta d_4 > \Delta d_3$). A greater traveltime difference is associated with the multiple when compared to the corresponding primary.

travel through the Earth, the greater the distance between the two wavefronts. Figure 4.1(a) also shows a greater difference when reflection occurs from a deeper interface. Hence, when performing velocity analysis, it should be much easier to distinguish between correct and incorrect velocities based on an event involving a greater propagation distance. This *does not* imply that velocity analysis based on deeper events is more accurate than that at earlier reflection times (conventional velocity analysis is based on normal moveout (NMO) which decreases as the ratio of receiver offset to reflector depth decreases). Furthermore, this does not refer to the greater moveout of multiples when compared to primary reflections at the same arrival time in the seismic record. The concept is that the moveout of multiples should be greater than that of the corresponding primaries at earlier times. For example, the S201R multiple will have greater moveout than the S2R primary. Velocity differences are compounded in the multiple event. This is illustrated in Figure 4.1(b) by the difference between the two wavefronts in the multiple event propagated at different velocities. This shows different distances travelled in the same time with the difference between wavefronts being greater with the multiple than with the corresponding primary. Following this line of reasoning, with the greater traveltime difference to the surface being observed between the multiple and the primary wavefronts, it might be concluded that multiples are more sensitive than primaries to changes in the velocity model.

To utilise the greater traveltime discriminating power of multiples, a new approach to velocity analysis might be beneficial. The technique that will be examined in this chapter is migration velocity analysis (MVA) since this can be used to build a velocity model in complex regions as described in Section 2.3. Based on the assumption of a higher traveltime discriminating power of multiples, an investigation will be performed into whether multiples can be used to provide more accurate interval parameters (velocity and thickness) information than primary events. Specifically, I will be looking into whether or not the average velocity of a primary can be obtained from the average velocity of a multiple generated off the same primary event (i.e. its corresponding primary). If this were possible, then two purposes might be served:

1) A more accurate average velocity may be found for the primary event; and

2) The multiple could be used to provide an alternative means for velocity analysis when the corresponding primary is obscured by noise or shallower multiple events.

4.2 DETERMINATION OF INTERVAL VELOCITY FROM MULTIPLES

Provided that no multiple attenuation has taken place, a common image gather (CIG) will contain both primary and multiple events. The initial reflection in a multiple event can be considered to be the primary component with the remainder being the multiple reverberation. Therefore, the average velocity of the multiple must be related to the average velocity of the corresponding primary in some way. A velocity analysis technique that utilises multiples will be examined to see if the *multiple reverberation component* can be removed to leave a *primary* component that can subsequently be used to obtain interval parameter information.

Residual curvature analysis (RCA) is a form of migration velocity analysis (MVA) that utilises differences in imaged depth in CIGs to provide information for iteratively updating the velocity. The RCA approach of Al-Yahya (1989) that was discussed in Section 2.3 involves the prestack data being migrated with a constant velocity to obtain an estimated residual average velocity for each event. This is then converted to a residual interval velocity which is used to update the previous migration velocity. The migration is then repeated until convergence is reached. To update the velocity function, a method for quantifying the deviation of events in a CIG from horizontal alignment is required. Al-Yahya (1989) introduced the γ parameter which is the ratio of the migration velocity to the average velocity of a particular event. After selecting a γ value for each event in the CIG based on the event curvature, the average velocity of each event can be found since the migration velocity is a known quantity:

$$V_{av} = \frac{V_m}{\gamma}, \tag{4.1}$$

where V_m is the migration velocity and V_{av} is the average velocity to a particular event. Conventionally, the next step involves solving for the interval thicknesses beginning with the shallowest layer and working through to the deepest layer:

$$d = \sum x_n = (\sum t_n) V_{av} \,, \tag{4.2}$$

where 'd' is the depth to the reflector, and x_n and t_n are the interval thickness and one-way interval traveltimes respectively for the n^{th} layer. Alternatively,

$$x_n = (t_1 + t_2 + t_3 + ... + t_n) V_{av} - (x_1 + x_2 + x_3 + ... + x_{n-1}) . \tag{4.3}$$

The interval velocity for the n^{th} layer is then determined as such:

$$V_{int(n)} = \frac{x_n}{t_n} . \tag{4.4}$$

Equations (4.1) through to (4.4) define the basis of the method of interval velocity determination when utilising primary events. This is the method that is conventionally employed when using the residual curvature analysis technique (RCA) (Al-Yahya, 1989; Deregowski, 1990; Liu and Bleistein, 1992; Lee and Zhang, 1992) to build an interval velocity model. It is nownecessary to investigate how multiples could be incorporated into the RCA technique.

Equation (4.2) assumes the use of primary events only. If it were used for determining the interval thickness where the average velocity was determined from a multiple event, then an incorrect velocity structure would be obtained at the MVA location. Treating the multiple as a primary would have resulted in extra ficticious layers being interpreted. I have postulated that a multiple event can be considered as the sum of a primary event plus a multiple reverberation component (Figure 4.2). This can be represented mathematically by:

$$D_m = D_p + (\sum D_m^*) = T_m \, V_{av(m)} \,, \tag{4.5}$$

where $\sum D_m^*$ is the sum of the distances contributing to the multiple reverberation, D_p is the distance travelled by the corresponding primary, and D_m, T_m, and $V_{av(m)}$ are the propagation distance, two-way time, and average velocity respectively of the multiple event. The difference in average velocity between the multiple and its corresponding primary is due to the multiple reverberation component. A link is required between the average velocity of the multiple and the average velocity of its corresponding primary in order to remove the effects of the multiple reverberation. Rearranging Equation (4.5) gives:

$$X_p = T_m \, V_{av(m)} - (\sum D_m^*) . \tag{4.6}$$

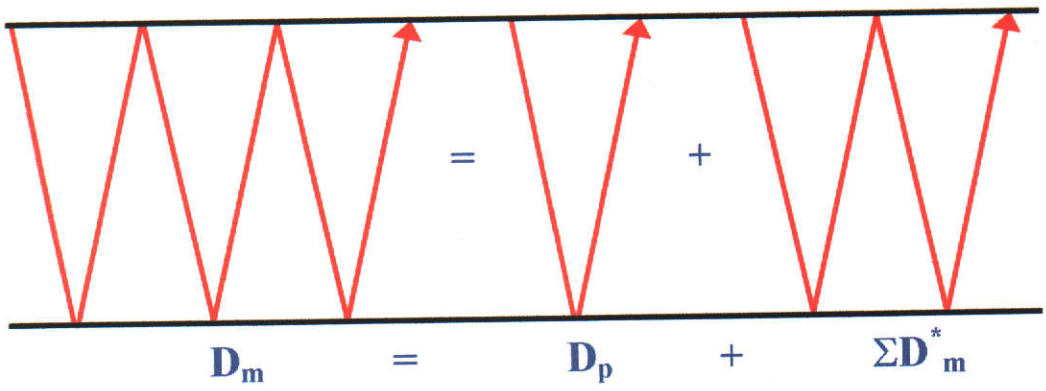

(a)

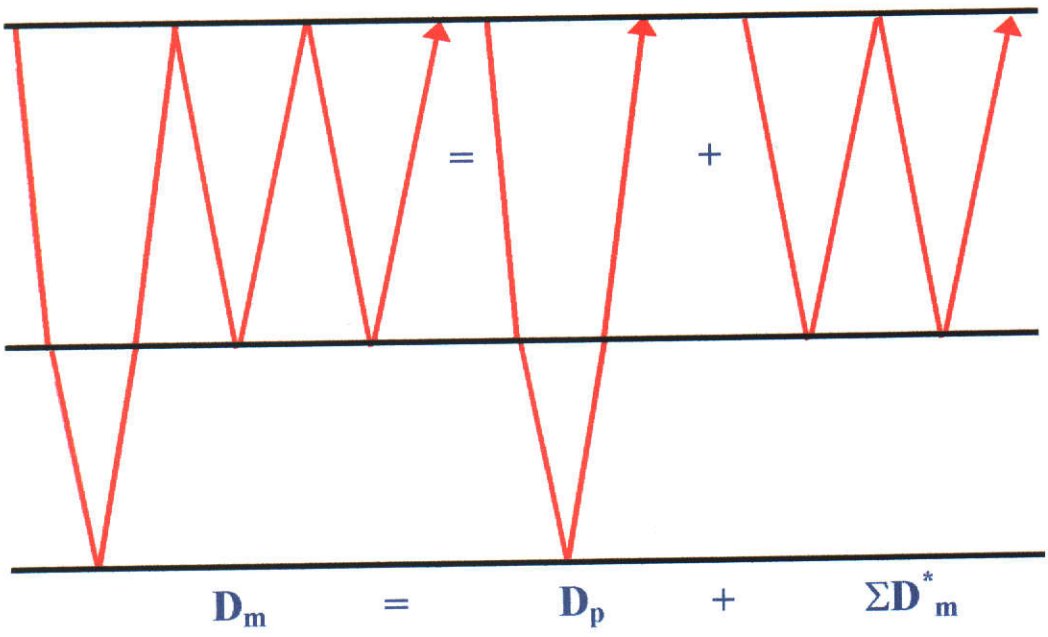

(b)

Figure 4.2: Multiple reverberation in a layered situation. The distance travelled by a multiple event consists of a primary component plus a multiple reverberation component. (a) water-bottom multiples and (b) surface peg-leg multiples.

Dividing both sides by the two-way time of the primary event results in:

$$\frac{D_p}{T_p} = \frac{T_m V_{av(m)} - \left(\sum D_m^*\right)}{T_p}. \tag{4.7}$$

In other words:

$$V_{av(p)} = \frac{T_m V_{av(m)} - \left(\sum D_m^*\right)}{T_p}. \tag{4.8}$$

Equation (4.8) enables the average velocity of a primary event to be obtained from the average velocity of a multiple generated from it by removing the impact of the multiple reverberation. Determination of interval thicknesses and interval velocities will then follow the conventional method given by Equations (4.3) and (4.4). Having postulated earlier that multiples should exhibit a higher traveltime discriminating power than corresponding primaries, Equation (4.8) will now be utilised in synthetic testing to determine whether multiples can be used to provide more accurate interval parameter information than primary events.

Specifically, the synthetic testing to follow will examine the use of Equation (4.8) in different geological scenarios. Examples will be presented to look into:

(a) The effectiveness of different types of multiples in MVA;

(b) The velocity information that can be obtained when there is a high amplitude multiple which interferes with primary events; and

(c) The effect of geological dip on the accuracy of velocities obtained from with the use of multiple events.

The γ-semblance method of Al-Yahya (1989) for determination of interval velocities and thicknesses is based on the assumption of horizontal layers. However, since the effect of geological dip will also be examined (in item (c) above), the γ-semblance method of Lee and Zhang (1992) will be considered. This method is based on the assumption of small dips and could be of more use in studying the application of Equation (4.8) in dipping geological settings.

4.3 SYNTHETIC DATA TESTING

The synthetic datasets used in the following examples were created using a new 3-D seismic modelling program (Hartley, 2002a). This software uses computer algebra to

symbolically calculate expressions for traveltimes and offsets for a variety of raypaths through a three-layer Earth model with planar interfaces. Correct amplitude values are calculated (according to the angles of incidence) using formulations of the Zoeppritz equations, also generated by computer algebra. Geometric spreading is determined using Jacobian terms output from the computer algebra computations. The following events are available for modelling with this software: S1R, S101R, S10101R, S1010101R, S2R, S201R, S20101R, S2010101R, S212R, S21212R, S202R, S3R, S10102R, S10201R, S102R, S1010102R, S1010201R, S1020101R, S21201R, and S10212R. Events appropriate for demonstrating the particular purpose of the following examples were selected from this suite. The synthetic datasets generated consisted of 200 shot gathers located at 20m intervals. A fixed receiver spread was used with receivers also located at 20m intervals. A source Ricker wavelet with a frequency of 30Hz was used to generate each synthetic dataset. MVA was performed at a surface location of 2000m in each model. PSDM with a constant velocity (equal to the first layer velocity) was performed on 99 synthetic shot gathers surrounding this location in order to form a CIG to be used in γ-semblance analysis. The software that I wrote for performing the MVA and the γ-semblance analysis are presented in Appendices A4 and A5 respectively. The velocity models used in each of the following examples will be described in each case.

4.3.1 THE EFFECT OF MULTIPLE PERIODICITY IN MVA

The important distinction between multiple types is whether they are long-period or short-period. A long-period multiple arrives as a distinct event whereas a short-period multiple arrives so soon after the primary that it merely adds tail to the primary (Sheriff, 1994). In the testing of the effect of multiple periodicity on the results obtained from MVA, surface peg-leg multiples will be used to see if longer-period multiples might provide greater accuracy in determining the interval parameters than shorter-period multiples.

Figure 4.3 presents four velocity models with the difference between them being the thickness of the first layer which was varied between 50m and 1000m to change the periodicity of the multiple reverberation. These velocity models were used to

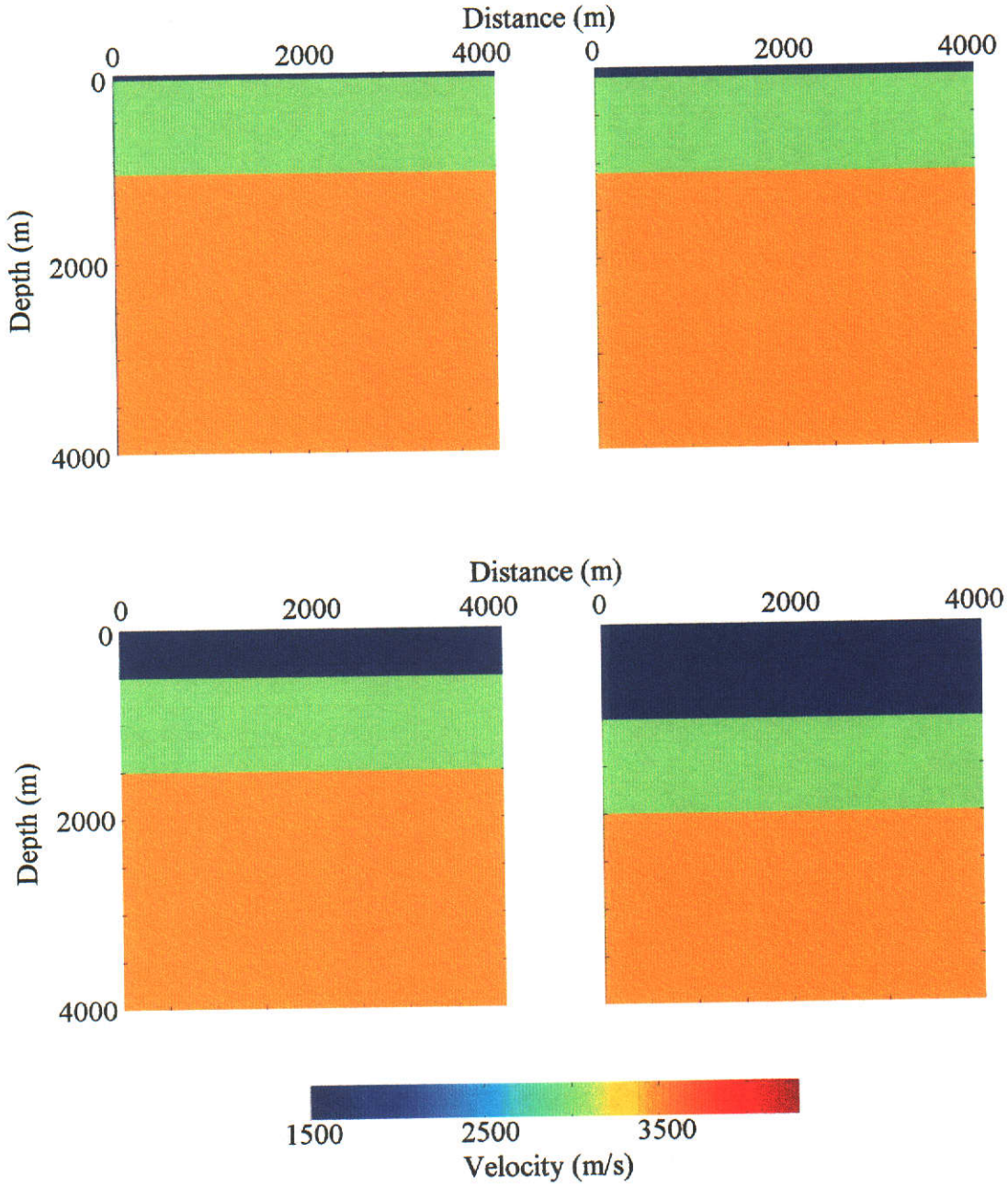

Figure 4.3: Velocity models used for generating short-period and long-period surface peg-leg multiples. The thickness of the first layer was varied from 50m through to 1000m while the second layer thickness was kept constant at 1000m. The interval velocities of the three layers from shallowest to deepest are 1500m/s, 3000m/s, and 5000m/s.

generate 200 shot gathers containing the events: S1R, S2R, S201R, S20101R, and S2010101R. The hundredth shot in each dataset is shown in Figure 4.4. As expected, the shot record produced from the velocity model with a first layer thickness of 50m showed little discrimination between the various surface peg-leg events generated off the second interface. Looking at this shot record on a trace-by-trace basis, the tail of S2R event is actually overlapped by the beginning of the response of the S201R event. A similar situation can be observed with the S20101R and S2010101R events. This is a classic example of short-period multiples. As the thickness of the first layer was increased, the events became more separated

After migrating with the first layer velocity, the 99 shot records surrounding the MVA location at 2020m along the line, a CIG was formed for each of the four models. These are presented in Figure 4.5. The next step was to implement Equation (2.18) in order to produce a set of γ-semblance plots (Figure 4.6). Amplitudes in each CIG were summed along curves defined by different values of γ with the largest semblance defining the best value of γ for a particular event. Note that the vertical axis in each γ-semblance plot in Figure 4.6 is expressed in terms of the product of γ and depth. This was done to impose a limit on all combinations of γ and depth that produced the same migration depth to the same level (Al-Yahya, 1986). As was observed in the shot records, when the periodicity of the multiples becomes shorter, the events became harder to differentiate in the CIGs and γ-semblance plots.

Calculation of Interval Parameters

The use of Equation (4.8) for determining the interval parameters can be demonstrated by working through an example step by step. The example chosen for this purpose was the longest-period multiple. The γ values selected from the associated γ-semblance plot for each event (Figure 4.6) were: S1R=0.987; S2R=0.8; S201R=0.863; S20101R=0.887; and S2010101R=0.904. The constant migration velocity (1500m/s) was divided by each of these γ values to give the following average velocities for each event: S1R=1520m/s; S2R=1875m/s; S201R=1738m/s; S20101R=1691m/s; and S2010101R=1659m/s. The next step was to determine the interval thicknesses and subsequently the interval velocities starting with the

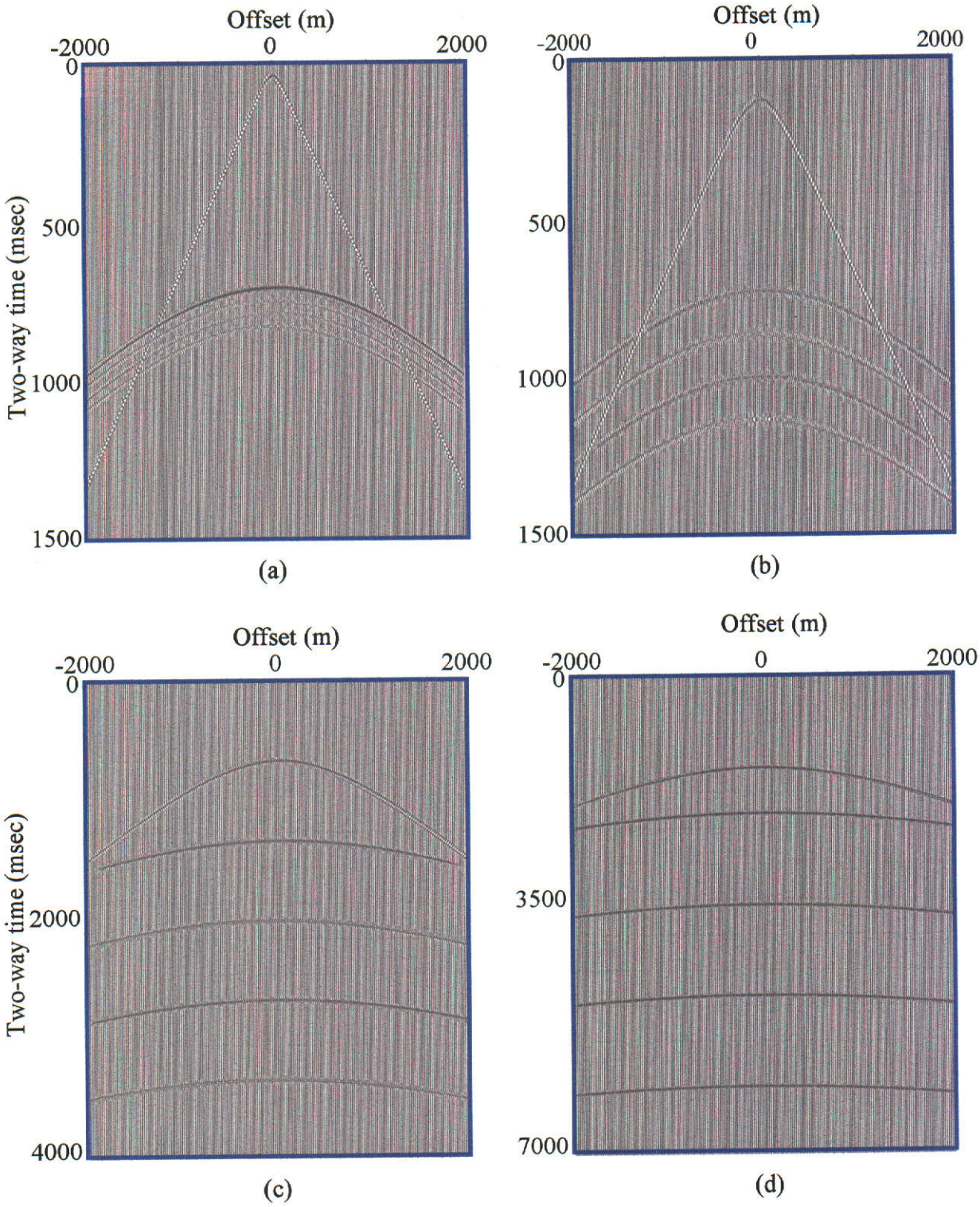

Figure 4.4: Shot 100 from each dataset created using different first layer thicknesses to vary the multiple periodicity. First layer thicknesses of (a) 50m, (b) 100m, (c) 500m, and (d) 1000m were employed. Events in order of arrival are S1R, S2R, S201R, S20101R, and S2010101R.

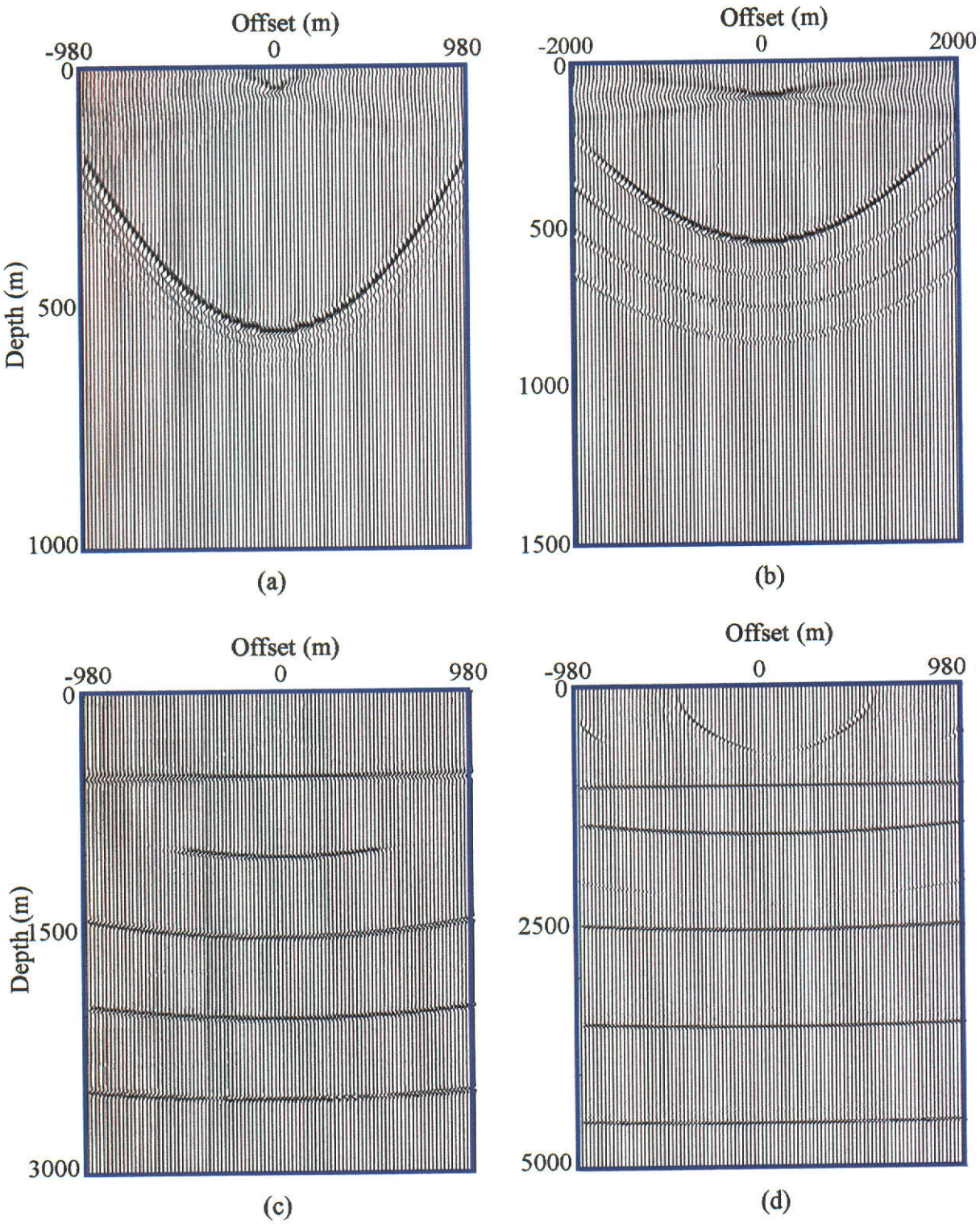

Figure 4.5: Common image gathers formed as a result of migrating a suite of shots from each dataset: First layer thicknesses are (a) 50m, (b) 100m, (c) 500m, and (d) 1000m. Events in order of increasing depth are S1R, S2R, S201R, S20101R, and S2010101R. When the periodicity of the multiples became shorter, the events became harder to discriminate in the CIGs.

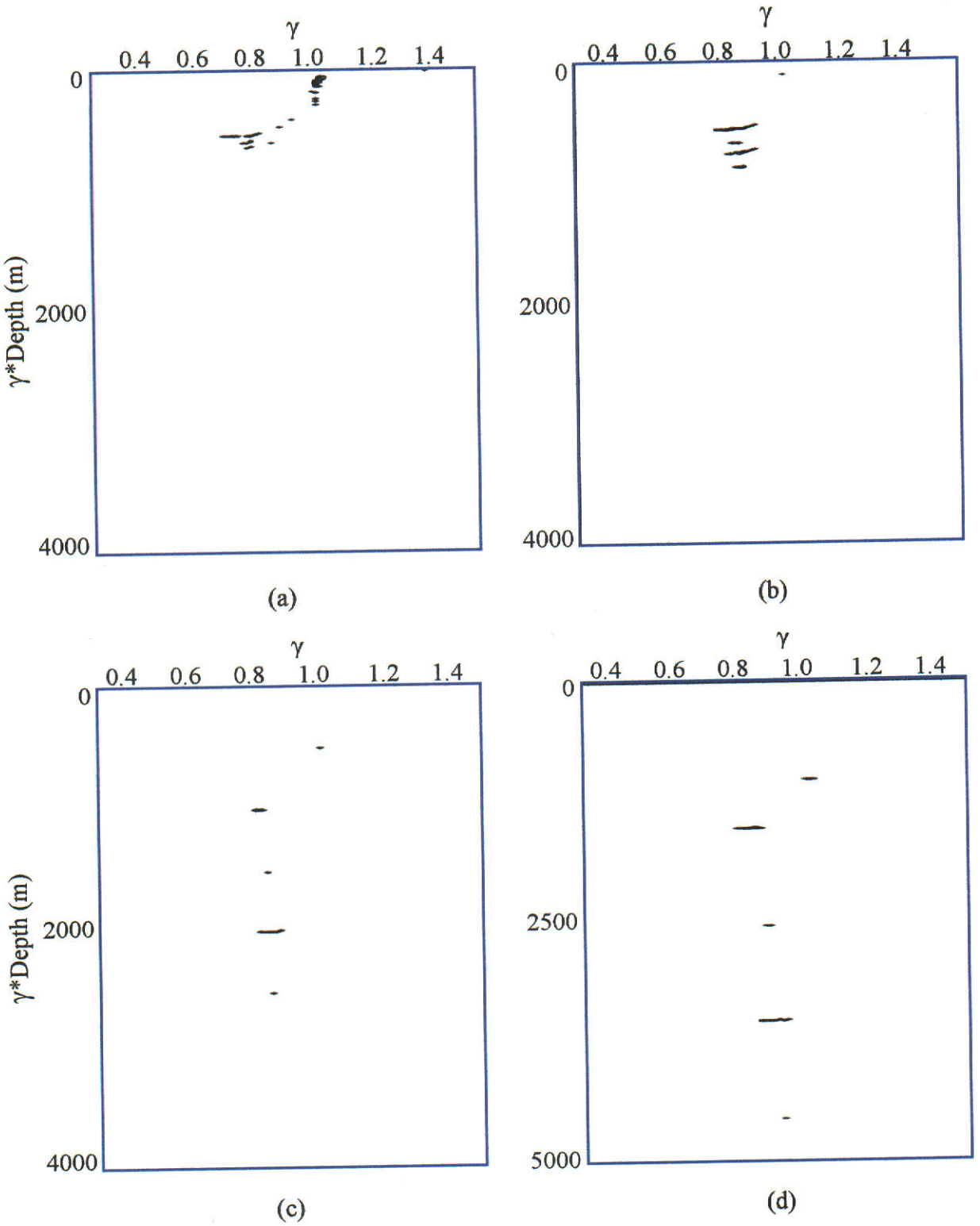

Figure 4.6: γ-semblance analysis for each example obtained using Equation (2.18). First layer thicknesses are (a) 50m, (b) 100m, (c) 500m, and (d) 1000m. Events in order of arrival are S1R, S2R, S201R, S20101R, and S2010101R. As the periodicity of the multiples decreased, the events became harder to discriminate in the γ-semblance plots.

shallowest layer. For the purposes of this example the exact first layer thickness was used so that no error was introduced from the first layer when considering the deeper events. This was done so that any phenomenon observed could be presumed to be solely due to the effect of varying the multiple periodicity. The thickness of the second layer was determined by implementing Equation (4.8) using the following calculation:

$$x_{2(S2R)} = V_{av(S2R)} T_{S2R} - x_{1(S1R)} = [(1875)(2)]/2\text{-}1000 = 875\text{m},$$

where $x_{2(S2R)}$ is the interval thickness of the second layer as determined using the S2R event. Division by two was necessary since two-way times were used and it was a one-way entity that was being determined (i.e. interval thickness).

When the S201R event was used to determine the interval thickness the following calculations were made:

$$x_{2(S201R)} = V_{av(S2R)} T_{S2R} - x_{1(S1R)}$$

$$V_{av(S2R)} = [T_{S201R} V_{av(S201R)} - \Sigma D^*_{S201R}]/T_{S2R}$$

$$\Rightarrow x_{2(S201R)} = [[T_{S201R} V_{av(S201R)} - \Sigma D^*_{S201R}]/T_{S2R}] T_{S2R} - x_1$$

$$\Rightarrow x_{2(S201R)} = [[(3.33)(1738) - (2)(1000)]/2] - 1000$$

$$\Rightarrow x_{2(S201R)} = 897\text{m},$$

where $x_{2(S201R)}$ is the interval thickness of the second layer as determined using the S201R event.

Similar calculations for the S20101R and S2010101R events were also made to obtain a thickness for the second layer. These were found to be: $x_{2(S20101R)} = 946$m and $x_{2(S2010101R)} = 977$m. The interval velocity was then found from the following calculations:

$$V_{2(S2R)} = x_{2(S2R)}/(T_2\text{-}T_1) = 875/[(2\text{-}1.33)/2] = 2625\text{m/s}$$

$$V_{2(S201R)} = x_{2(S201R)}/(T_2\text{-}T_1) = 897/[(2\text{-}1.33)/2] = 2690\text{m/s}$$

$$V_{2(S20101R)} = x_{2(S20101R)}/(T_2\text{-}T_1) = 946/[(2\text{-}1.33)/2] = 2837\text{m/s}$$

$$V_{2(S2010101R)} = x_{2(S2010101R)}/(T_2\text{-}T_1) = 977/[(2\text{-}1.33)/2] = 2931\text{m/s},$$

where $V_{2(S2R)}$, $V_{2(S201R)}$, $V_{2(S20101R)}$, and $V_{2(S2010101R)}$ are the interval velocities determined using information from the S2R, S201R, S20101R, and S2010101R

events respectively. An error analysis was then performed by using the following relation:

$$\%\text{Error} = \frac{|\text{calculated} - \text{true}|}{\text{true}} * 100\%, \tag{4.9}$$

where 'calculated' is the interval parameter obtained from the analysis just presented and 'true' is the correct interval parameter. The error obtained from a comparison of the true and calculated interval thicknesses is basically the same as that obtained when interval velocities are compared. These parameters are related by the common parameter of traveltime therefore the term interval parameter is used to describe both.

The results obtained from velocity analysis are presented in Table 4.1(a). A similar analysis was performed using the data obtained from the velocity models with first layer thicknesses of 500m and 100m respectively. These results are presented in Tables 4.1(b) and (c). No results were obtained for the case where the first layer thickness was 50m due to difficulty in determining γ values for each event in the γ-semblance plot.

To enable an easier interpretation of these results, Figure 4.7 presents a graphical representation of the error analysis. Focussing on the errors in interval velocity obtained from the S2R and surface peg-leg events, it is observed that as the order of the multiple increases in each test, the error between the calculated and true parameter values decreases. This supports my contention that as the distance of propagation increases, the sensitivity of an event to any error in velocity increases. Further examination of these results shows that the interval parameters obtained were most accurate where the traveltimes were greatest. Interpreting the results from the perspective of multiple periodicity, we see that as the period of multiple reverberation becomes less, the accuracy of the interval parameters obtained from the MVA also becomes less. This is because the events associated with the shorter-period of reverberation haven't travelled as far through the Earth as those associated with the longer-period. This is why the sensitivity of these events to any error in velocity is lower.

Event	γ	$V_{av(calc)}$	$V_{av(true)}$	$x_{int(calc)}$	$x_{int(true)}$	$V_{int(calc)}$	$V_{int(true)}$	% Error
S1R	0.987	1520	1500	1013	1000	1520	1500	1.3
S2R	0.8	1875	2000	875	1000	2625	3000	12.5
S201R	0.863	1738	1800	897	1000	2690	3000	10.3
S20101R	0.887	1691	1714	946	1000	2837	3000	5.4
S2010101R	0.904	1659	1667	977	1000	2931	3000	2.3

(a)

Event	γ	$V_{av(calc)}$	$V_{av(true)}$	$x_{int(calc)}$	$x_{int(true)}$	$V_{int(calc)}$	$V_{int(true)}$	% Error
S1R	0.984	1524	1500	508	500	1524	1500	1.6
S2R	0.8	1875	2250	750	1000	2250	3000	25
S201R	0.825	1977	2000	818	1000	2454	3000	18.2
S20101R	0.85	2136	1875	924	1000	2772	3000	7.6
S2010101R	0.852	2153	1800	935	1000	2805	3000	6.5

(b)

Event	γ	$V_{av(calc)}$	$V_{av(true)}$	$x_{int(calc)}$	$x_{int(true)}$	$V_{int(calc)}$	$V_{int(true)}$	% Error
S1R	0.95	1579	1500	105	100	1579	1500	5.3
S2R	0.775	1935	2750	645	1000	1935	3000	35.5
S201R	0.787	1906	2571	741	1000	2223	3000	25.9
S20101R	0.787	1906	2438	847	1000	2541	3000	15.3
S2010101R	0.812	1847	2333	923	1000	2770	3000	7.7

(c)

Table 4.1: Interval velocity and thickness summary based on MVA for long- and short-period multiples. First layer thicknesses of (a) 1000m, (b) 500m, and (c) 100m were utilised to vary the multiple periodicity. Parameters in red represent true values. As the multiple reverberation periodicity increases, interval parameter error decreases.

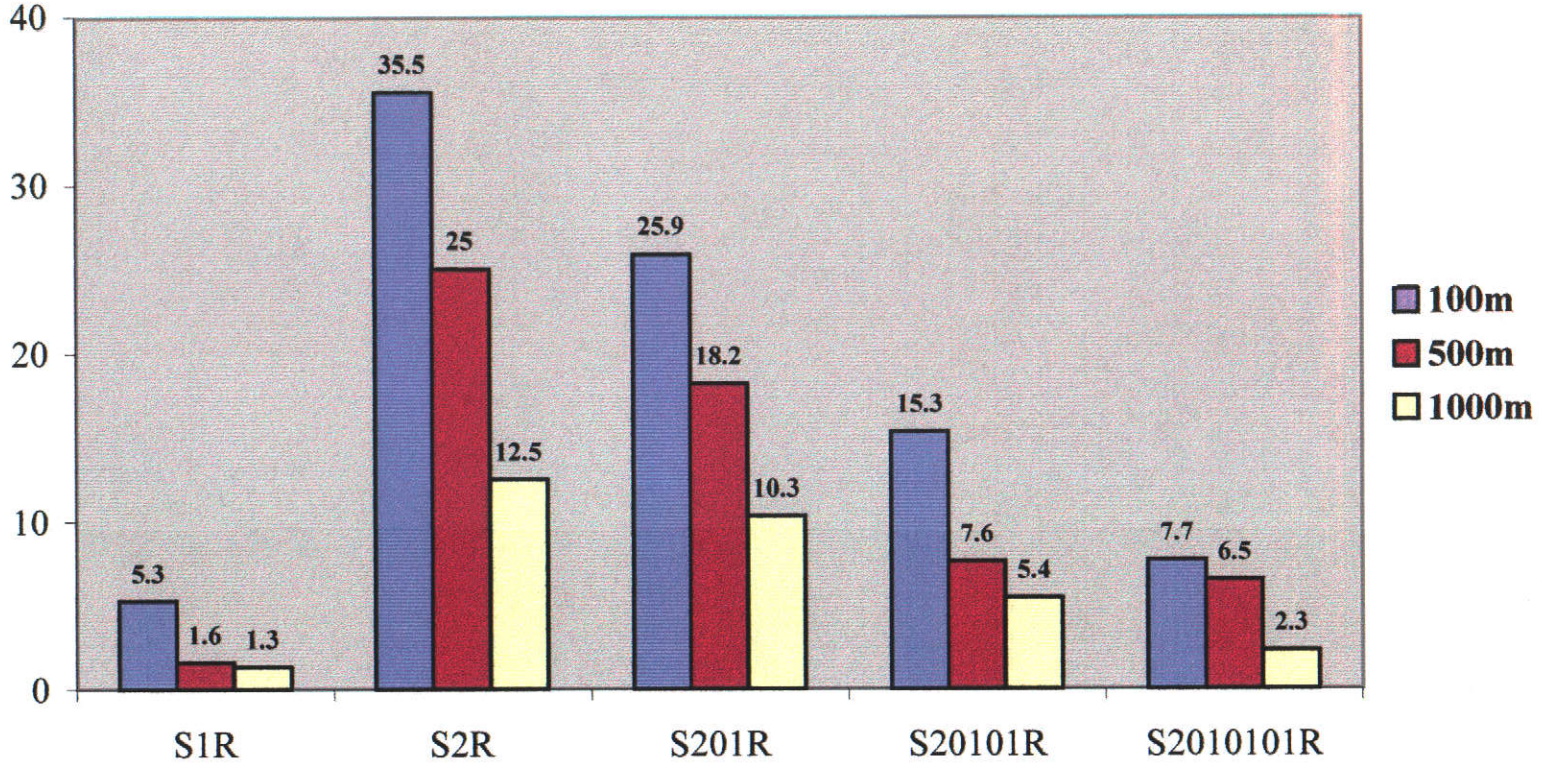

Figure 4.7: Interval parameter errors obtained when examining multiple periodicity in MVA. The legend key indicates the thickness of the first layer in which the multiple reverberation occurred.

4.3.2 MVA USING WATER-BOTTOM MULTIPLES

The next synthetic example will examine the use of water-bottom multiples in MVA. Figure 4.8 presents a velocity model used to generate a series of water-bottom multiples, a resultant shot gather, the CIG obtained after migrating with the water velocity, and a γ-semblance plot. The γ-semblance plot has had automatic gain control (AGC) applied to it therefore some events stand out more than others.

After migrating with the water velocity, the water-bottom primary and water-bottom multiples appear flat in the CIG. This means that the γ values obtained for each event are close to unity. The reason that all events appear flat is due to the interval velocity being equal to the average velocity in this case. This is not so for deeper layers since the average velocity will have been affected by shallower velocity variations. The water-bottom multiples represent a special case since Equation (4.8) doesn't need to be implemented to obtain the interval velocity. In order to obtain the interval thicknesses from each event, it is just a matter of obtaining the average velocity of each event and dividing it by the two-way traveltime of the primary water-bottom reflection. Table 4.2 summarises the results.

As expected, the γ-semblance plot shows the multiple events plotting closer to γ=1 since the distance of propagation through the Earth is larger thereby increasing the sensitivity of these events to any error in velocity. These events are expected to provide increasing accuracy in the interval parameters of the water layer. However, a point to note is that the water layer parameters are normally accurate enough when provided by the water-bottom primary. In addition, water column information can normally be obtained by using other methods therefore, it is not expected that MVA using water-bottom multiples will be very worth while.

4.3.3 MVA USING INTERBED MULTIPLES

Another type of multiple that needs to be examined as a potential interval parameter determination tool, when using MVA, is the interbed multiple. Figure 4.9 presents the velocity model that was used to generate a synthetic dataset containing interbed multiples. It also displays a shot gather from this synthetic dataset, the CIG obtained

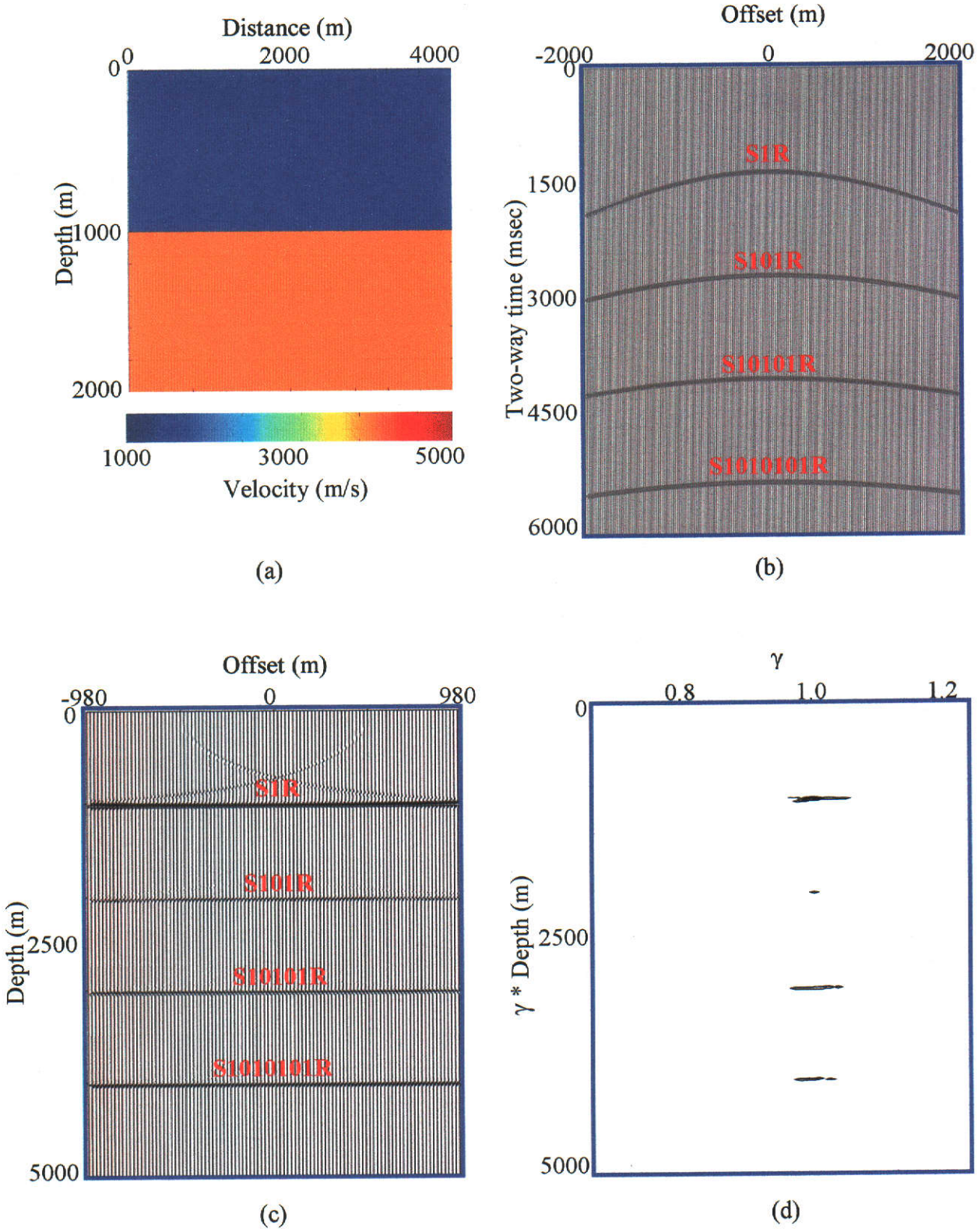

Figure 4.8: MVA using water-bottom multiples. (a) Velocity model, (b) shot gather, (c) CIG, and (d) γ-semblance analysis. First and second layer interval velocities are 1500m/s and 4000m/s respectively. The first layer thickness is 500m.

Event	γ	$V_{av(calc)}$	$V_{av(true)}$	$x_{int(calc)}$	$x_{int(true)}$	% Error
S1R	0.987	1520	1500	1013	1000	1.3
S101R	1	1500	1500	1000	1000	0
S10101R	1	1500	1500	1000	1000	0
S1010101R	1	1500	1500	1000	1000	0

Table 4.2: Results of MVA after using water-bottom multiples for interval parameter determination. The average velocity is equal to the interval velocity when dealing with the water-bottom primary and multiple events. Parameters in red represent true values. The water-bottom multiple events provide more accuracy in interval parameter determination.

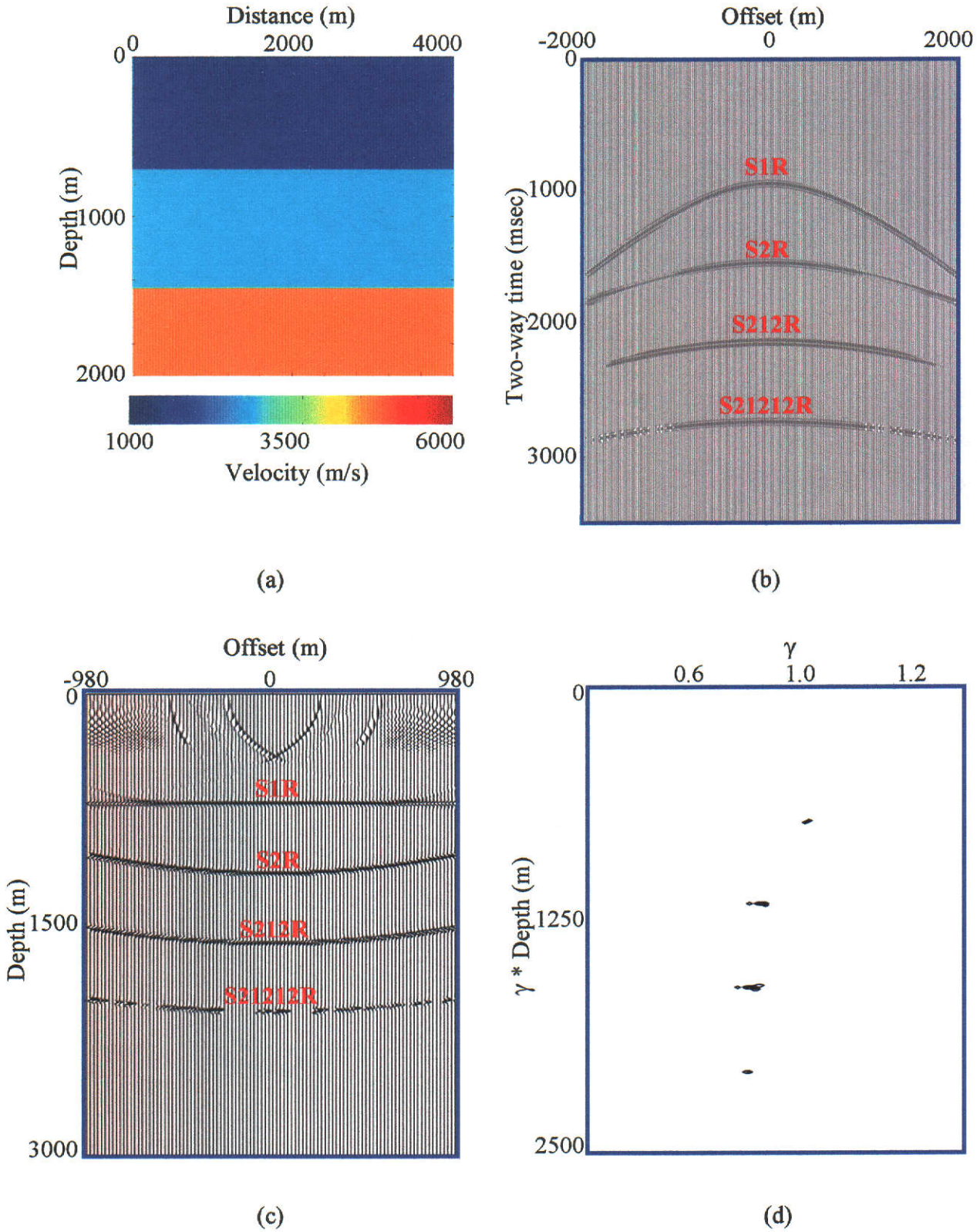

Figure 4.9: MVA using interbed multiples: (a) velocity model, (b) shot gather, (c) CIG, and (d) γ-semblance analysis. The interval velocities and thicknesses of the three layers were: 1500m/s and 700m; 2000m/s and 750m; and 5000m/s respectively. As the order of the multiple increases, the interval parameter error decreases.

after migrating with the water velocity, and a γ-semblance plot. Missing data on some traces within the shot gather may be observed around the location of the S21212R event. This was due to certain incident angles exceeding the critical angle when using the synthetic generation program (Hartley, 2002b). However, this does not detract from the results obtained since a γ value was still able to be obtained that was representative of the curvature of this event in the CIG.

The mathematical analysis presented here will concentrate on the S212R and S21212R events with the water layer velocity and thickness of 1500m/s and 700m assumed to be already known. The average velocities for the interbed multiples were larger than that of the S2R primary event due to the extra travelpath(s) in the higher velocity second layer. This is reflected in the γ-semblance plot where decreasing γ values are observed as the depth increases. A second layer thickness of 653m was obtained using the Dix equation applied to the S2R event. This was used to remove the multiple reverberation component associated with the S212R and S21212R events as detailed below. With the subscripts S2R, S212R, and S21212R being used to indicate the event information being utilised, these calculations were as follows:

$$\Rightarrow x_{2(S212R)} = [T_{S212R}\, V_{av(S212R)} - \Sigma D^{*}_{S212R}] - x_{2(S2R)}$$

$$\Rightarrow x_{2(S212R)} = [(2.133)(1870) - (2)(653)]/2 - 653$$

$$\Rightarrow x_{2(S212R)} = 689\text{m}.$$

$$\Rightarrow x_{2(S21212R)} = [T_{S21212R}\, V_{av(S21212R)} - \Sigma D^{*}_{S21212R}] - x_{2(S2R)}$$

$$\Rightarrow x_{2(S21212R)} = [(2.733)(1948) - (4)(653)]/2 - 653$$

$$\Rightarrow x_{2(S21212R)} = 703\text{m}.$$

The results from this analysis (Table 4.3) indicate interval parameter errors of 14.8%, 9.4%, and 7.2% obtained from the events S2R, S212R, and S21212R respectively. This illustrates that as the order of the multiple increases, the interval parameter error decreases. In other words, as the propagation distance increases, the accuracy of the interval parameter determination also increases. However, since the multiple reverberation was within the layer where interval parameters were being determined, an estimate of this thickness must be known beforehand so that those effects can be

Event	γ	$V_{av(calc)}$	$V_{av(true)}$	$x_{int(calc)}$	$x_{int(true)}$	$V_{int(calc)}$	$V_{int(true)}$	% Error
S1R	1	1500	1500	700	700	1500	1500	0
S2R	0.85	1765	1891	653	750	2177	2500	14.8
S212R	0.802	1870	2063	689	750	2296	2500	9.4
S21212R	0.77	1948	2159	703	750	2344	2500	7.2

Table 4.3: Results of MVA after using interbed multiples for interval parameter determination. Parameters in red represent true values. As the order of the multiple increased the accuracy of the interval velocity and thicknesses determined also increases.

removed, and the interval parameters determined. In this example, the only way that this estimate can be made is by using the information provided by the S2R event. This event provided interval parameters with an error of 14.8% which was subsequently propagated through to the calculations involving the multiple events. Therefore, the errors obtained for the interval parameters provided by the interbed multiples can be in part due to the error introduced from the estimate of second layer thickness provided by the S2R event.

It was demonstrated in Section 4.3.1 that surface peg-leg multiples could provide increasing accuracy in the second layer interval parameters with increasing order of multiple. In those cases the multiple bounce occurred in a layer above that for which the interval parameters were being determined. Therefore, to reduce the error propagated into the calculations involving the interbed multiples as occurred in the results shown, we need to use a more accurate estimate such as that provided by a surface peg-leg multiple.

4.3.4 MVA WHERE MULTIPLES INTERFERE WITH PRIMARIES

The next stage of the analysis involved examining whether multiples could be used as a source of interval velocity information when they interfered with primary events. The goal was to determine the interval parameters at a specific location without having to remove the multiples beforehand. Figure 4.10 presents the velocity model and a representative shot gather for this example. The events generated were: S1R, S101R, S10101R, S1010101R, S2R, S201R, S20101R, S2010101R, and S3R. The shot gather shows the S2R event being obscured at short offsets by the S101R event and at far offsets by the S1R event. The S3R event is also obscured at the far offsets by the same two events. In addition the surface peg-leg multiples were overlapped by the water-bottom multiples. This could potentially reduce the ability of the former events in determining the interval parameters of the second layer. After migration with the first layer velocity, a CIG was formed and a γ-semblance plot was produced (Figure 4.10). The CIG illustrates that better discrimination is present between all events at the far offsets but at the near offsets there is still considerable overlap. However, each event exhibits a different curvature as evident in the γ-semblance plot

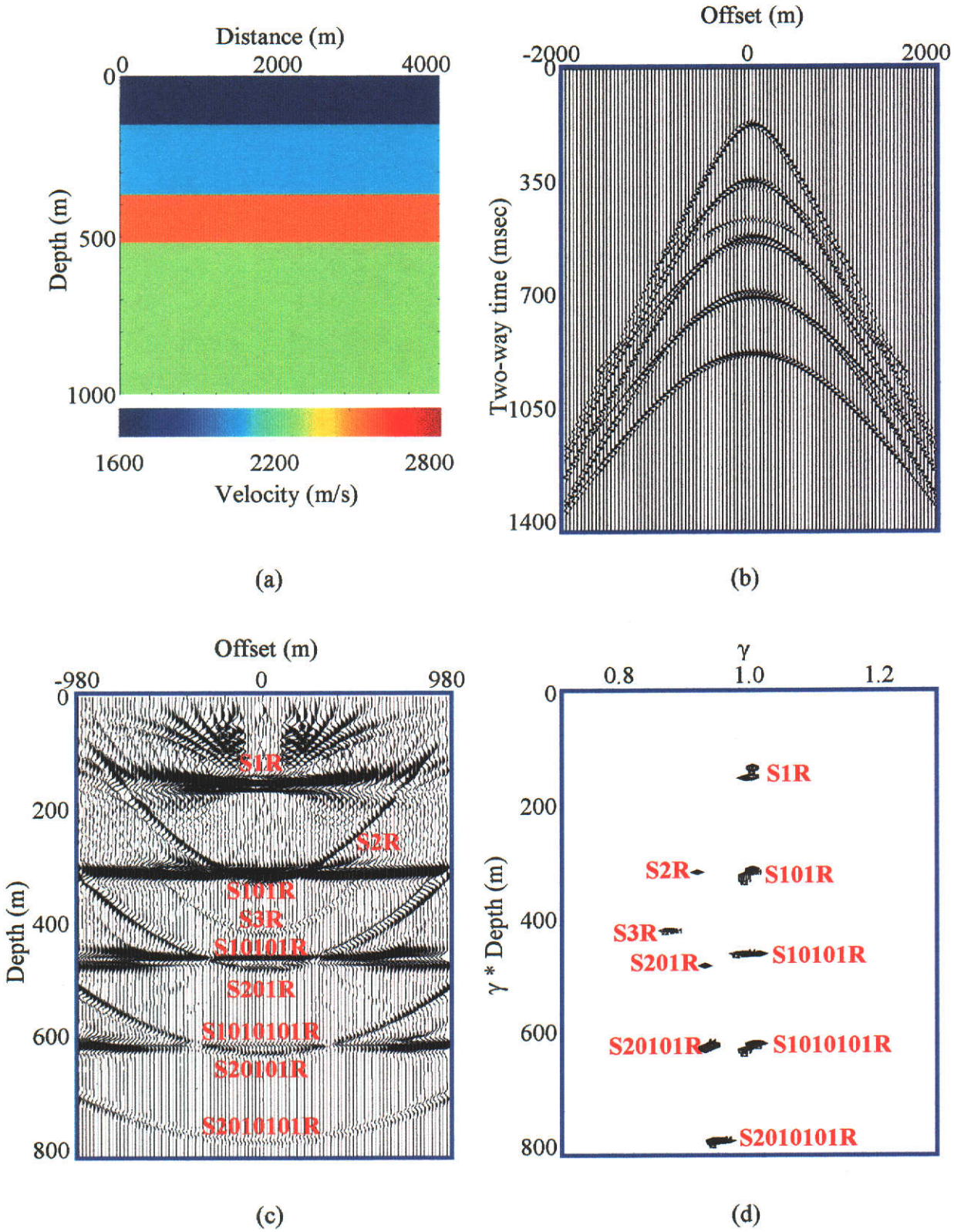

Figure 4.10: MVA where multiples and primary events interfere: (a) velocity model, (b) shot gather, (c) CIG, and (d) γ-semblance analysis. The interval velocities and thicknesses of the four layers were: 1500m/s and 150m; 2000m/s and 220m; 2500m/s and 150m; and 2200m/s respectively. Multiples are able to be discriminated from other events to enable velocity analysis.

where excellent discrimination was made.

After the γ values were selected from the γ-semblance plot, the interval parameters were determined using Equation (4.8). A similar procedure to that described in Section 4.3.1 for surface peg-leg multiples and in Section 4.3.2 for water-bottom multiples was used for the calculations. However, since this is a four layer example, the third interval thickness was able to be calculated a number of different ways. This was due the existence of a number of thickness estimates being available for the first and second intervals to use in the calculation of the third interval thickness. To calculate the third layer thickness, two different thicknesses were used for the second layer - one calculated using the S2R event only, and the other calculated using S2010101R information. These thicknesses were designated $x_{3(S3R\text{-}P)}$ and $x_{3(S3R\text{-}M)}$ respectively:

$$\Rightarrow x_{3(S3R\text{-}P)} = T_{S3R}\, V_{av(S3R)} - x_{1(S1R)} - x_{2(S2R)}$$

$$\Rightarrow x_{3(S3R\text{-}P)} = [(0.54)(1740)/2] - 150 - 189$$

$$\Rightarrow x_{3(S3R\text{-}P)} = 131\text{m}$$

$$\Rightarrow x_{3(S3R\text{-}M)} = T_{S3R}\, V_{av(S3R)} - x_{1(S1R)} - x_{2(S2010101R)}$$

$$\Rightarrow x_{3(S3R\text{-}M)} = [(0.54)(1740)/2] - 150 - 219$$

$$\Rightarrow x_{3(S3R\text{-}M)} = 101\text{m}$$

The third interval velocity was then found using each of these two thicknesses. The results obtained from this velocity analysis are presented in Table 4.4 along with an error analysis for the determined interval velocities by use of Equation (4.9). The S1R event provided an interval thickness that was in error by 2 metres. When using the water-bottom multiple events to determine the first layer thickness and velocity, this error was reduced since it was known that the average velocity of a water-bottom event is equal to the interval velocity. Hence no information from the primary event was needed to remove the effects of the multiple bounce(s) (refer to Section 4.3.2). This meant that the error associated with the first layer derived from using the water-bottom primary was not carried through to calculations involving deeper events. The

Event	γ	$V_{av(calc)}$	$V_{av(true)}$	$x_{int(calc)}$	$x_{int(true)}$	$V_{int(calc)}$	$V_{int(true)}$	% Error
S1R	0.987	1520	1500	152	150	1520	1500	1.3
S101R	1	1500	1500	150	150	1500	1500	0
S10101R	1	1500	1500	150	150	1500	1500	0
S1010101R	1	1500	1500	150	150	1500	1500	0
S2R	0.925	1622	1762	189	220	1718	2000	14.1
S201R	0.925	1622	1677	199	220	1809	2000	9.6
S20101R	0.925	1622	1634	209	220	1900	2000	5
S2010101R	0.937	1601	1608	219	220	1991	2000	0.4
$S3R_P$	0.862	1740	1926	131	150	2150	2500	12.7
$S3R_M$	0.862	1740	1926	101	150	1650	2500	32.7

Table 4.4: Results of MVA for the case where surface peg-leg multiples are interfering with primary events. Parameters in red represent true values. $S3R_P$ indicates that the results were obtained from using S1R and S2R information only while $S3R_M$ indicates the S1010101R and S2010101R events were used.

events developed off the second interface provide a classic example of how higher order multiples can provide more accurate interval information for the second layer. This can be seen in the error analysis in Table 4.4 where the S2R event provides interval parameters that exhibit 14.1% error. On the other hand, the S201R, S20101R, and S2010101R events provide increasingly more accurate interval parameters with respective errors of 9.6%, 5%, and 0.4% being observed in this example. Even though the S2R event was somewhat obscured by the S101R event, the interval parameters of the second layer were still able to be determined with a higher order of accuracy by using the multiple events generated by reflection from the second boundary.

The interval parameters obtained for the third layer show that by using multiple information it may seem as though the result has more error than that obtained from analysis based on primary information alone. However, this is not the case for the error originating from the use of the S3R event. The interval parameters obtained by utilising the information provided by the S1010101R and S2010101R events are in error by 0% and 0.45% for the first and second layers respectively. Whereas the interval parameters obtained by using the S1R and S2R events produced errors of 1.3% and 14.1%. The error of 14.1% is significant when analysing deeper layers. Hence the error observed when determining the interval parameters of the third layer using the multiple events cannot be attributed to the S1010101R and S2010101R events - it must be due to the error from using the S3R event.

4.3.5 MVA USING MULTIPLES IN THE PRESENCE OF DIP

The examples presented thus far have examined the use of multiples as a tool for determining interval parameter information in horizontally layered situations. These examinations utilised the γ-semblance method of Al-Yahya (1989) which assumes horizontal layers. It was then considered necessary to investigate the extent to which multiples can be used when reflectors are dipping. For this I will use the γ-semblance method of Lee and Zhang (1992) which is able to handle small dips (Section 2.3). γ-semblance analysis for horizontally layered situations involves scanning over a range of γ values to determine which value provides the highest stacking power for each

event in a γ-semblance plot. The method presented by Lee and Zhang (1992) scans over a range of both γ values and dip values. The correct combination of both γ and dip for each event provides the highest stacking power. For my purposes it was proposed to use their method to see if multiples could be used reliably for velocity analysis in the presence of dip.

A Comparison of γ-Semblance Methods

It is worthwhile to illustrate what would happen if the γ-semblance method of Al-Yahya (1989) were utilised when MVA is performed in the presence of dip. Figure 4.11 illustrates a three-layered velocity model with interval velocities of 1500m/s, 2500m/s, and 5000m/s for the first second and third layers respectively. The thickness of the first layer was 500m while the thickness of the second layer at the MVA location in the middle of the model was 325m. The boundary between the second and third layers was given a dip of 5°. A shot record generated using the software of Hartley (2002a) is also shown along with a CIG formed by migrating 99 shot records with the first layer velocity. This CIG exhibits differences from those that have been presented previously (c.f. Figure 4.5(d)). Although the S1R, S101R, and S10101R events all appear flat (since the first boundary is horizontal and migration has occurred with the velocity of the first layer), the events generated from the second boundary (S2R, S201R, and S20101R) exhibit a tilt due to the dip of the second reflector boundary.

The next step in this illustration was to perform γ-semblance analysis on the CIG. Figure 4.12(a) presents the γ-semblance analysis performed on the CIG based on Al-Yahya's (1989) relation (Equation (2.18)) which assumes horizontal layers. For the purpose of comparison the same CIG was then analysed using the γ-semblance method of Lee and Zhang (1992). Their relation (Equation (2.20)), which is able to handle small dips, produced the γ-semblance plot in Figure 4.12(b). After the γ values were selected from the γ-semblance plot, the interval parameters were determined using Equation (4.8). Once again, a procedure similar to that described in Section 4.3.1 for surface peg-leg multiples and in Section 4.3.2 for water-bottom multiples was used for the calculations. The results from the analysis based on the

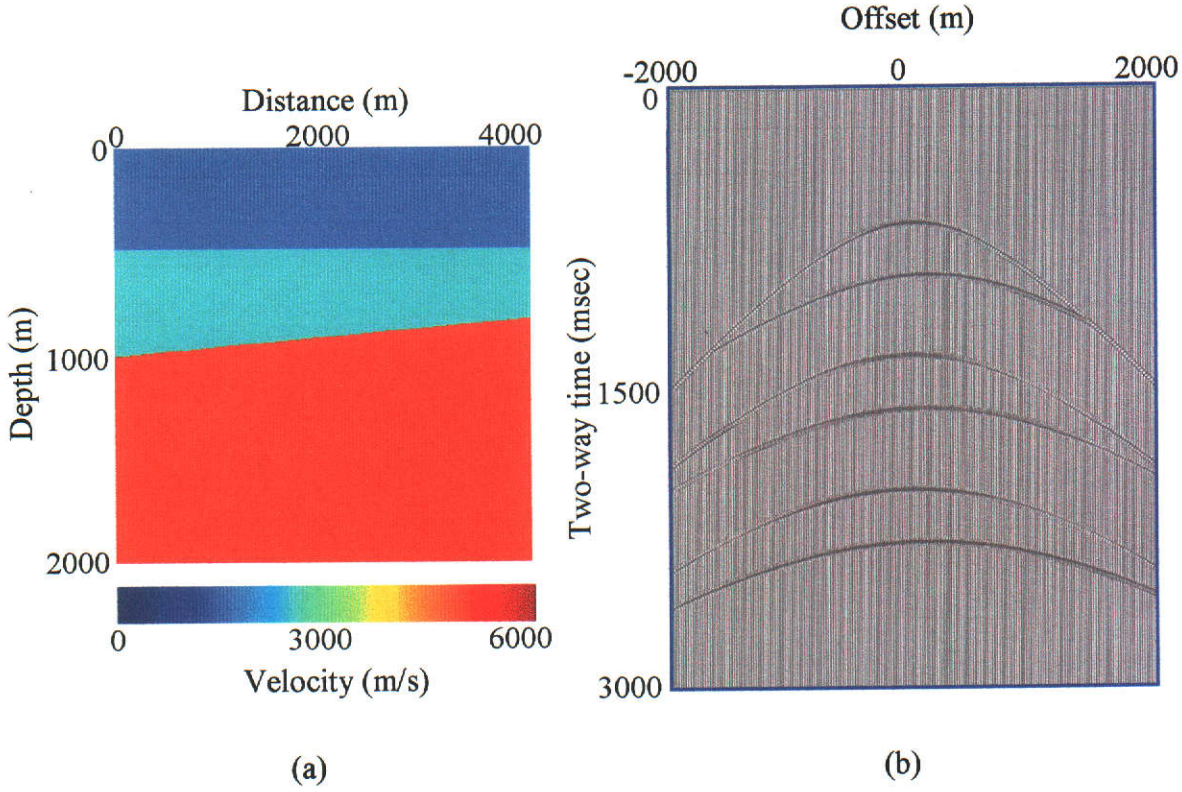

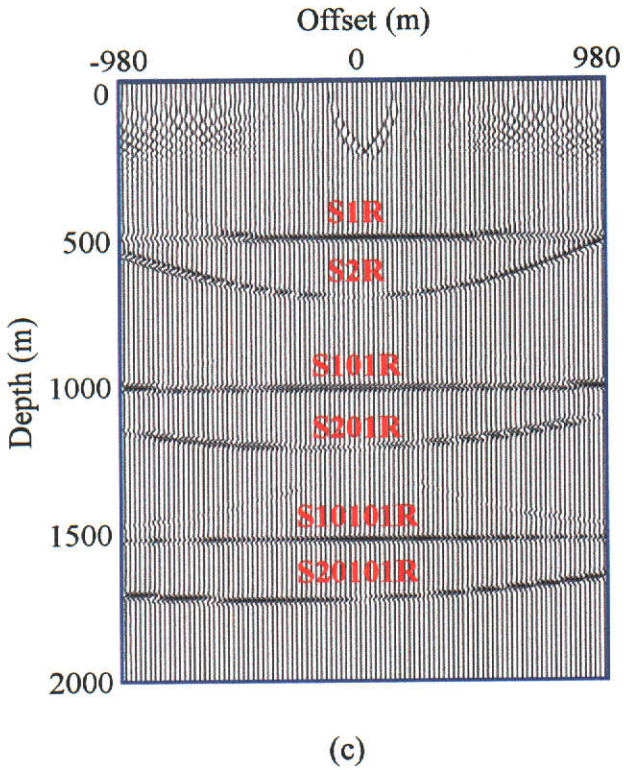

Figure 4.11: MVA in the presence of dip. (a) Velocity model, (b) shot gather, and (c) CIG. The interval velocities and thicknesses of the three layers at the MVA location were: 1500m/s and 500m; 2500m/s and 825m; and 5000m/s respectively. Events in the CIG off the second boundary are tilted due to this boundary having dip.

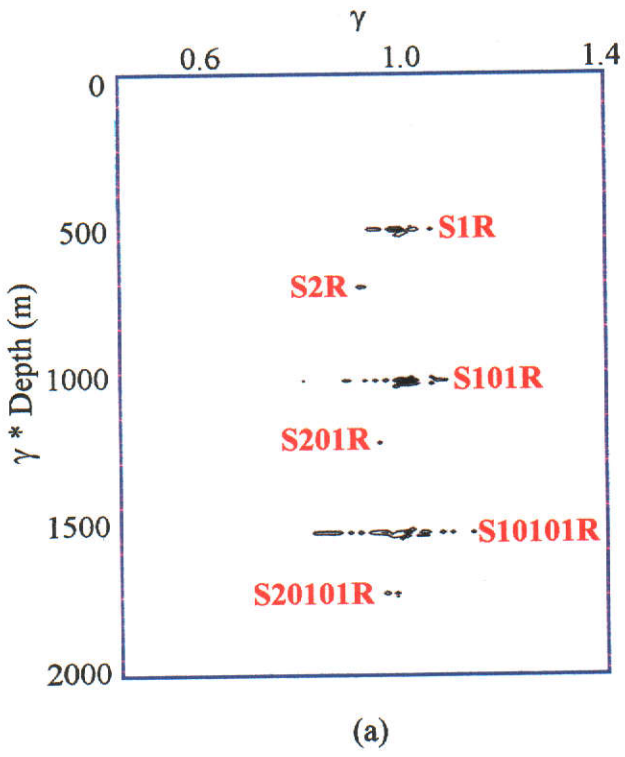

(a)

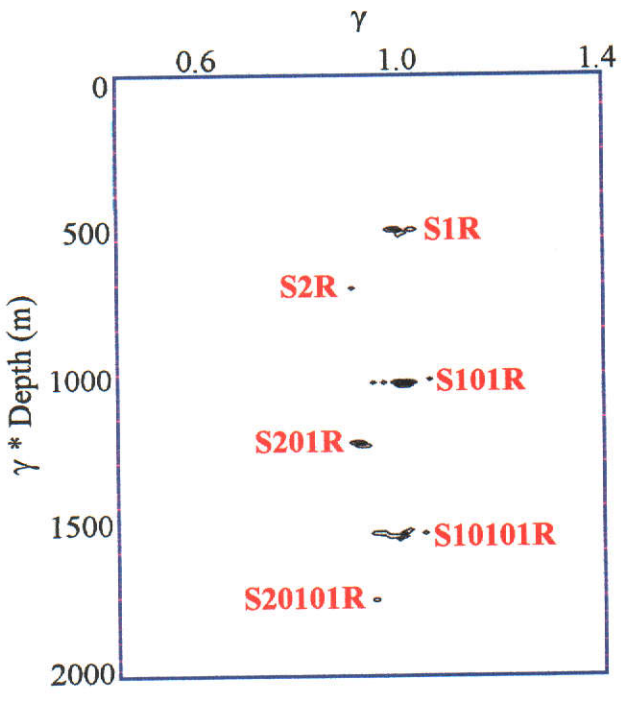

(b)

Figure 4.12: A comparison of γ-semblance methods. γ-semblance analysis using the method by (a) Al-Yahya (1989) and (b) Lee and Zhang (1992). The latter method provides more accurate γ values in the presence of dip.

γ-semblance method of Al-Yahya (1989) are presented in Table 4.5(a) while those obtained using the γ-semblance method of Lee and Zhang (1992) are presented in Table 4.5(b). Tables 4.5(a) and (b) only focus on the S2R, S201R, and S20101R events. It was presumed that most variation between results obtained by using the two different γ-semblance methods would be associated with events generated off the dipping boundary.

The interval velocities obtained for the second layer by using the γ-semblance method of Al-Yahya (1989) and the S2R, S201R, and S20101R events were 2134m/s, 2193m/s, and 2260m/s respectively. By use of Equation (4.9), these values were in error by 14.6%, 12.3%, and 9.6% for the S2R, S201R, and S20101R events respectively. On the other hand, the interval velocities obtained for the second layer by using the γ-semblance method of Lee and Zhang (1992) and the S2R, S201R, and S20101R events were 2271m/s, 2672m/s, and 2635m/s respectively. By use of Equation (4.9), these values were in error by 9.1%, 6.9%, and 5.4% for the S2R, S201R, and S20101R events respectively. From this analysis, the errors obtained by implementing Lee and Zhang's (1992) γ-semblance method have proven to be lower than those obtained using Al-Yahya's (1989) method. This is due to the former method providing for the existence of small dip.

γ-semblance analysis involves the determination of a "best-fit γ-semblance curve" for a particular event in the CIG with each curve being defined by a different value of γ (Al-Yahya, 1989) or γ and dip (Lee and Zhang, 1992). Amplitudes are then summed along this curve to provide a maximum "γ-semblance value". It is the maximum γ-semblance value that enables the correct value of γ to be determined for a particular event from such a γ-semblance plot. The results just presented can be investigated further by examining the best-fit γ-semblance curves obtained using the two different methods. This was done for the S2R event which was initially picked off the CIG presented in Figure 4.11(c). By using Equations (2.18) and (2.20) (which are the basis for respective γ-semblance methods of Al-Yahya (1989) and Lee and Zhang (1992), and the respective γ values obtained from each of the γ-semblance analyses, theoretical γ-semblance curves used to best-fit the S2R event picked off the CIG can

Event	γ	$V_{av(calc)}$	$V_{av(true)}$	$x_{int(calc)}$	$x_{int(true)}$	$V_{int(calc)}$	$V_{int(true)}$	% Error
S2R	0.894	1678	2159	277	325	2134	2500	14.6
S201R	0.93	1613	1883	285	325	2193	2500	12.3
S20101R	0.945	1587	1770	293	325	2260	2500	9.6

(a)

Event	γ	$V_{av(calc)}$	$V_{av(true)}$	$x_{int(calc)}$	$x_{int(true)}$	$V_{int(calc)}$	$V_{int(true)}$	% Error
S2R	0.874	1716	1781	295	325	2271	2500	9.1
S201R	0.887	1691	1664	347	325	2672	2500	6.9
S20101R	0.92	1630	1615	342	325	2635	2500	5.4

(b)

Table 4.5: Results of MVA when two different γ-semblance methods were used for determining interval velocity and thickness. γ-semblance analysis using the method by (a) Al-Yahya (1989) and (b) Lee and Zhang (1992). Parameters in red represent true values. The interval velocity and thickness obtained for the second layer are more accurate when derived by using the relation of Lee and Zhang (1992).

be calculated. These two theoretical best-fit γ-semblance trajectories and the S2R event picked off the CIG are compared in Figure 4.13. It can be seen that the best fit obtained using the method of Al-Yahya (1989) does not provide as good a fit as that provided by the method of Lee and Zhang (1992). This is because the former method cannot account for the shifting of the apex in the γ-semblance curve that occurs both laterally and vertically when dip is present. Therefore, for best results, dip must be taken into account when performing γ-semblance analysis for MVA.

Uniform Multiple Reverberation

It has been established that it is necessary to utilise the γ-semblance method of Lee and Zhang (1992) for MVA in regions where dip is present. It will now be investigated whether multiples could be a reliable source of interval parameter information in such regions by utlising this γ-semblance method. For both the following examples, synthetic datasets containing the S1R, S2R, S201R, S20101R, and S2010101R events were generated using the software of Hartley (2002a). The models (with varying structures) used to generate each dataset are specified below. Each dataset created contained 200 shot gathers with sources spaced 20m apart. In addition, a fixed receiver spread containing 200 receivers spaced 20m apart was used.

The example that follows involved the first interface being kept horizontal with the second interface being allowed to dip. This allowed all multiple reverberations to occur within a uniform horizontal layer. For this reason I use the term *uniform multiple reverberation*. The investigation then involved varying the dip of the interface from -20° to +20° at 2° increments. In all, 21 tests were performed for which 21 different datasets were synthesised and 21 runs of MVA were completed in order to obtain the 21 CIGs required for γ-semblance analysis using the relation of Lee and Zhang (1992). The interval velocities for each of the 21 velocity models were 1500m/s, 3000m/s, and 5000m/s for the first, second, and third layers respectively. The first layer thickness was 500m while the second layer thickness varied with the dip. Figure 4.14 presents three of the velocity models utilised in this series of tests. A representative shot record from each of the synthetic datasets

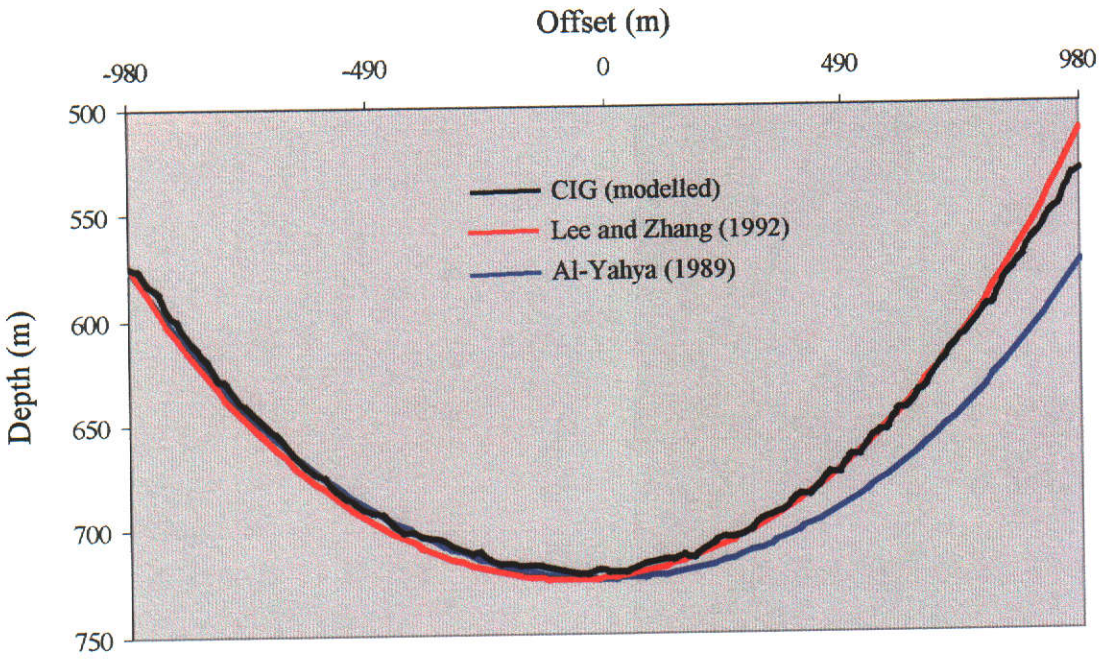

Figure 4.13: Trajectories on a CIG of the semblance analysis curves defined by the methods of Al-Yahya (1989) and Lee and Zhang (1992). γ-semblance computation trajectories using optimum γ values found by the methods of Al-Yahya (1989) and Lee and Zhang (1992) are shown for the S2R event. The method of Lee and Zhang (1992) provides a better fit to the data in the CIG than does the method of Al-Yahya (1989).

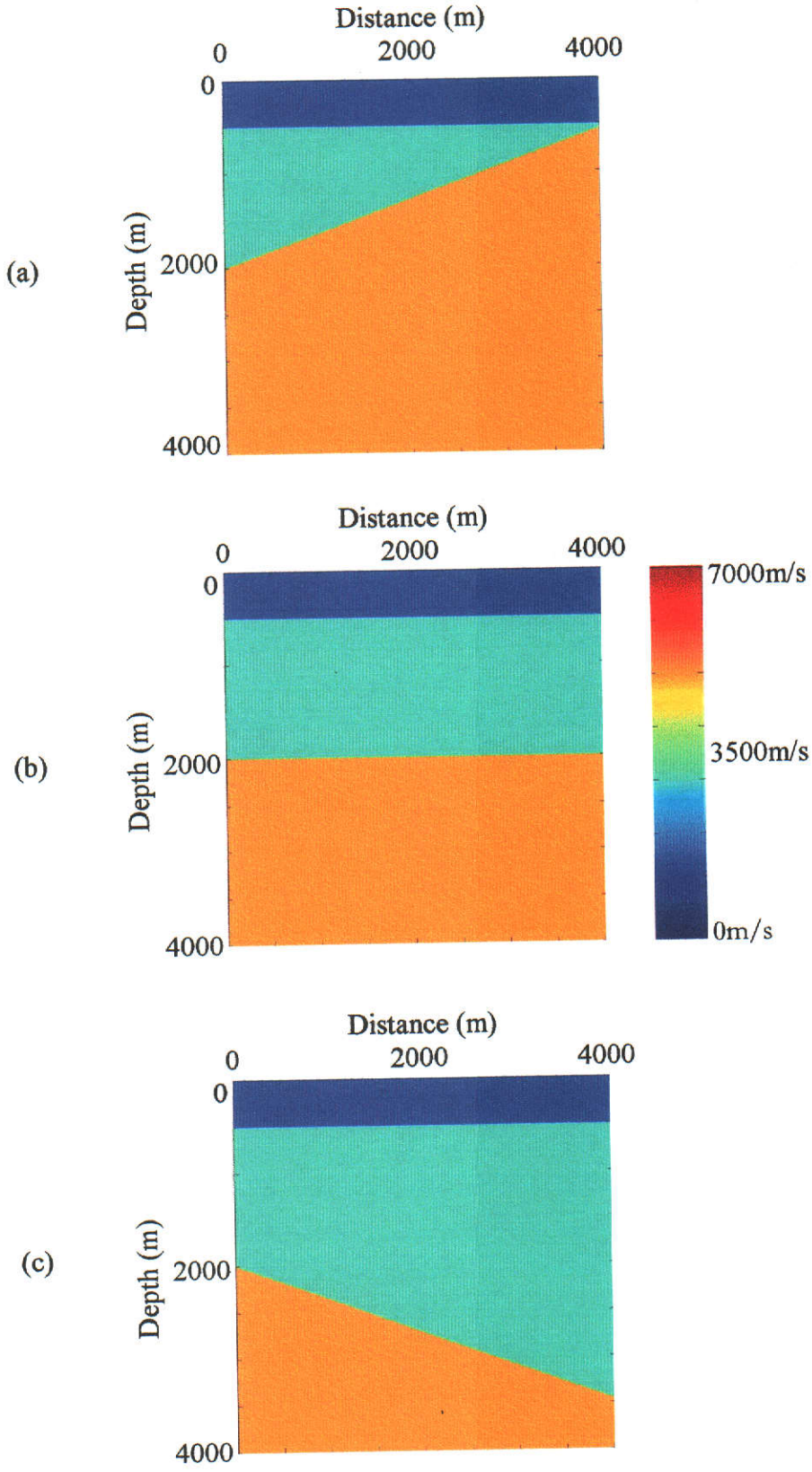

Figure 4.14: Three velocity models used for generating synthetic data where the multiple reverberations occur in a horizontal layer and the second layer was allowed to dip. Dip was varied between (a) -20°, (b) 0°, and (c) +20° at 2° increments. Interval velocities were 1500m/s, 3000m/s, and 5000m/s for the first, second, and third intervals respectively.

created using dips of 20°, 0°, and -20° is shown in Figure 4.15. Also shown in this figure are CIGs formed by migrating 99 shot records from each dataset with the velocity of the first layer (1500m/s). γ-semblance plots created by implementing Equation (2.20) for the tests using dips of -20°, 0°, and 20° can be observed in Figure 4.16. After the γ values were selected from the γ-semblance plot, the interval parameters were determined using Equation (4.8) as before. In order to remove the reverberation component of the multiples to determine the average velocity of the primary event representative of its first bounce, I used the known constant thickness of the first layer (1000m). The results from performing MVA are presented in Table 4.6.

An analysis of the results presented in Table 4.6 indicated two trends. The first trend was that as the order of the multiple increased, interval parameter accuracy also increased. This was observed for all 21 tests performed. For example, in the case of a dip of -10°, the error decreased from 33.5% obtained using the S2R event, 26% using the S201R event, 24.2% using the S20101R event, and finally to 18% obtained using the S2010101R event. As mentioned in Section 4.1, this can be explained by the fact that as the propagation distance increased, the sensitivity to any error in any interval parameter increased. The second trend indicated that as the dip increased, the interval parameter errors generally increased for all events considered. For example, results from the S2R event showed interval parameter errors of 42.3%, 33.5%, 29.2%, 35%, and 38.4%, for dips of -20°, -10°, 0°, 10°, and 20° respectively. Similar trends are observed with other events. The explanation for this phenomenon lies in the underlying assumption on which the γ-semblance relationship of Lee and Zhang (1992) is based. As the dip becomes larger, the assumption of small dip angle is increasingly violated. However, even in the presence of larger dips where this assumption is clearly violated, multiples of increasing order can still be observed to give more accurate interval parameters than those obtained from the corresponding primary event. Therefore, for a uniform multiple reverberation, even though accuracy decreases with increasing dip, multiples can still be seen to give greater accuracy in interval parameters than the corresponding primary event for a given dip.

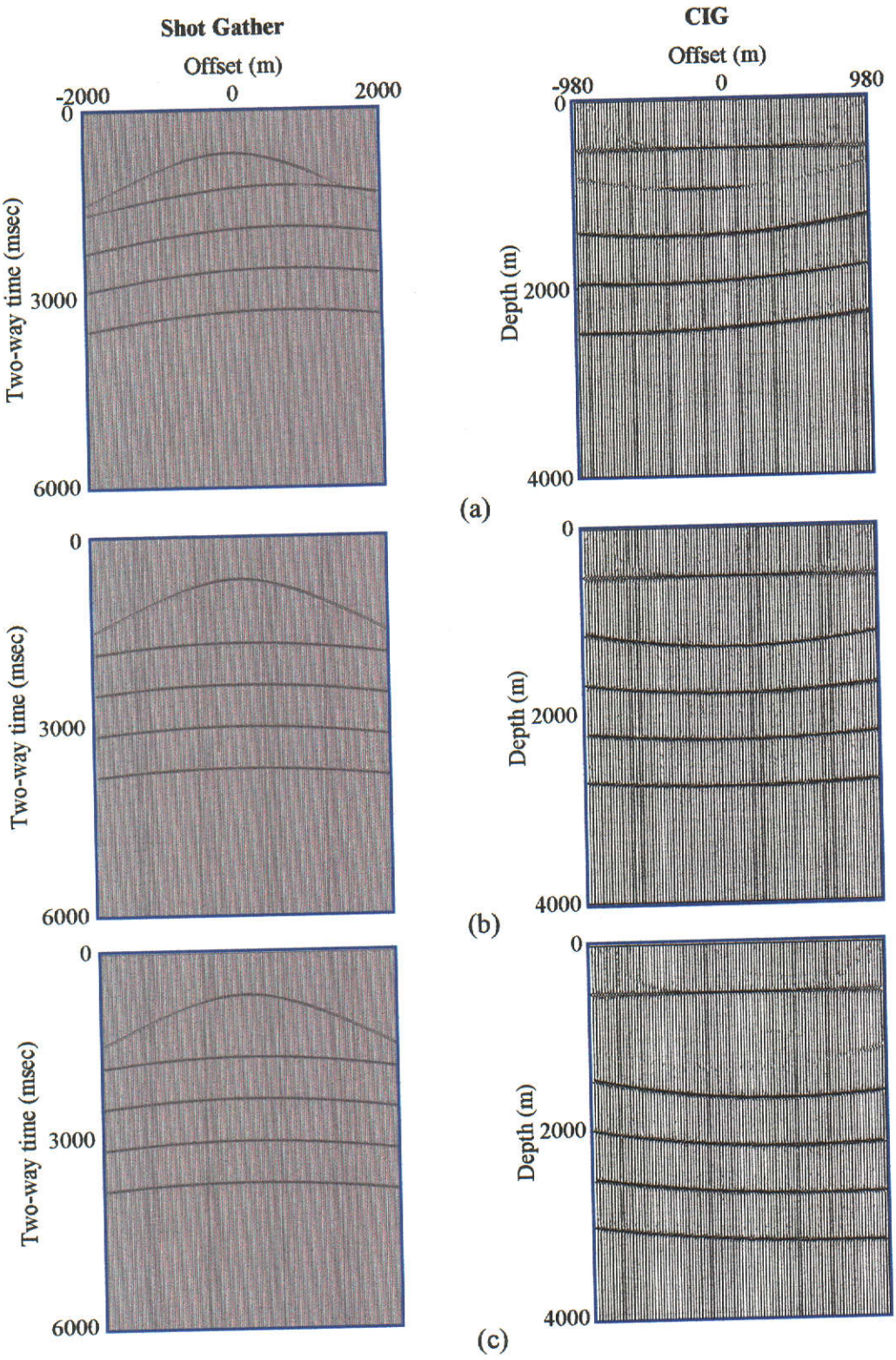

Figure 4.15: Shot gathers and CIGs obtained where the second layer dip varied. The shot gathers and the CIGs were created using a second layer dip of (a) -20°, (b) 0°, and (c) +20° in the velocity model. Events in order of arrival are S1R, S2R, S201R, S20101R, and S2010101R. The events generated off the second boundary change in appearance according to the dip of this reflector.

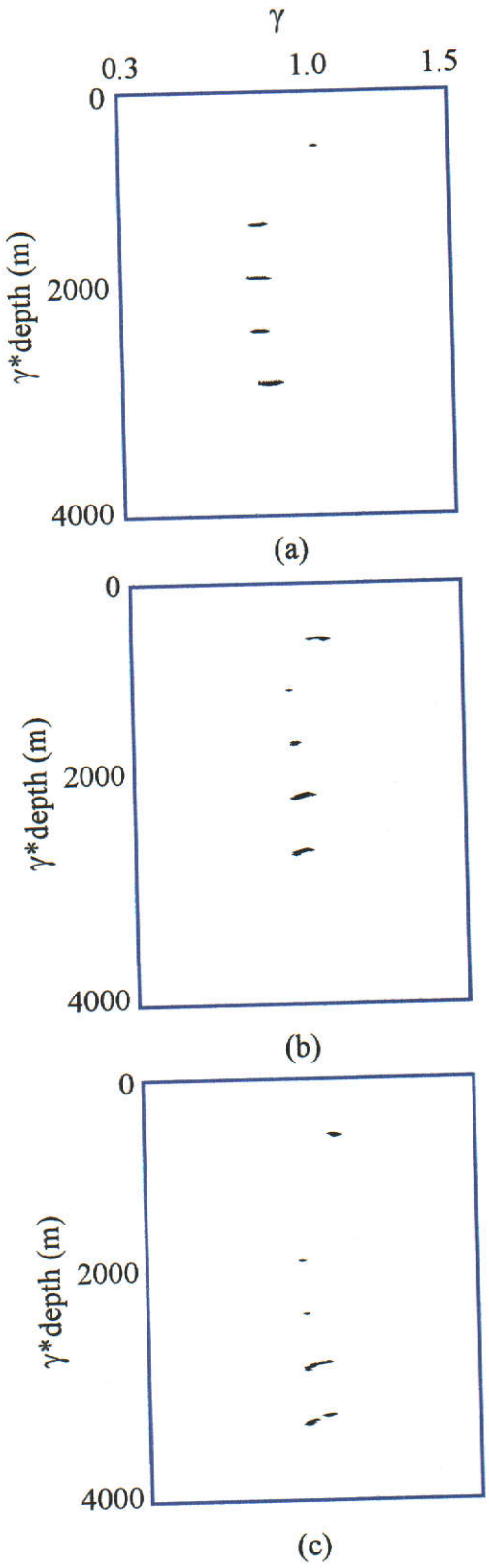

Figure 4.16: γ-semblance analysis using Equation (2.20) where the second layer dip varied. The results shown used dips of (a) -20°, (b) 0°, and (c) +20° in the second layer. Events in order of arrival are S1R, S2R, S201R, S20101R, and S2010101R. The γ values associated with each event change according to the dip of the second boundary.

Dip	Event	γ	$V_{av(calc)}$	$V_{av(true)}$	$x_{int(calc)}$	$x_{int(true)}$	$V_{int(calc)}$	% Error
-20°	S2R	0.937	1601	2154	446	772	1731	42.3
	S201R	0.875	1714	1918	584	772	2269	24.4
	S20101R	0.887	1691	1807	626	772	2434	18.9
	S2010101R	0.898	1670	1743	657	772	2553	14.9
-10°	S2R	0.85	1765	2301	763	1147	1995	33.5
	S201R	0.851	1763	2047	849	1147	2220	26.0
	S20101R	0.875	1714	1915	870	1147	2275	24.2
	S2010101R	0.875	1714	1834	941	1147	2461	18.0
0°	S2R	0.8	1875	2400	1063	1500	2125	29.2
	S201R	0.812	1847	2143	1155	1500	2310	23.0
	S20101R	0.813	1845	2000	1268	1500	2535	15.5
	S2010101R	0.819	1832	1909	1358	1500	2716	9.5
10°	S2R	0.837	1792	2474	1204	1853	1950	35.0
	S201R	0.862	1740	2221	1235	1853	1999	33.4
	S20101R	0.875	1714	2073	1273	1853	2061	31.3
	S2010101R	0.888	1689	1975	1295	1853	2098	30.1
20°	S2R	0.862	1740	2535	1372	2228	1848	38.4
	S201R	0.875	1714	2290	1416	2228	1907	36.4
	S20101R	0.874	1716	2139	1491	2228	2007	33.1
	S2010101R	0.888	1689	2037	1507	2228	2029	32.4

Table 4.6: Results of MVA using multiples where the multiple reverberations occurred in a horizontal layer but the second layer was allowed to dip. True interval velocity of the second layer is 3000m/s. As the order of the multiple increases, the interval velocity and thickness become more accurate.

Non-Uniform Multiple Reverberation

Having investigated the utilisation of multiples in MVA when the peg-leg reverberation occurs in a layer which is horizontal but where the deeper bounce occurs on a dipping interface, it is now necessary to investigate a more complicated scenario. The example to follow involved examining the use of multiples in MVA when the multiple reverberations occurred within a layer which had a dipping lower surface This is called *non-uniform multiple reverberation.* In order to determine the interval parameters of the second layer at the location of the MVA, the interval parameters of the first layer had to be known at the MVA location as well. However, removing the multiple reverberation component using Equation (4.8) involved knowing the thickness of the interval in which this reverberation occurs. If the reverberation occurs in a dipping layer, the effective thickness will be different at the location of each bounce. It is proposed to see if interval parameters can still be obtained with any degree of accuracy using such multiples.

The investigation here involved allowing the second layer to dip from -10° to +6° at 2° increments. Three of the velocity models used are shown in Figure 4.17. The creation of datasets using larger dips in the velocity model was not possible due to the offset ranges involved. However, these dip extents were considered sufficient for this test. Therefore, nine tests were performed which once again meant that nine different datasets had to be synthesised. MVA then had to be performed nine times in order to obtain the nine CIGs required for γ-semblance analysis. The interval velocities for each of the nine velocity models were 2000m/s, 5000m/s, and 8000m/s for the first, second, and third layers respectively. The first layer thickness was varied depending on the dip however, the second layer thickness was kept constant at 1000m.

Representative shot records from each of the synthetic datasets created, using dips of -4°, 0°, and 4°, and their corresponding CIGs are shown in Figure 4.18. γ-semblance plots for these three tests are shown in Figure 4.19. Once again, after the γ values were selected from the γ-semblance plot, the interval parameters were able to be determined using Equation (4.8). The use of Equation (4.8) involves the removal of

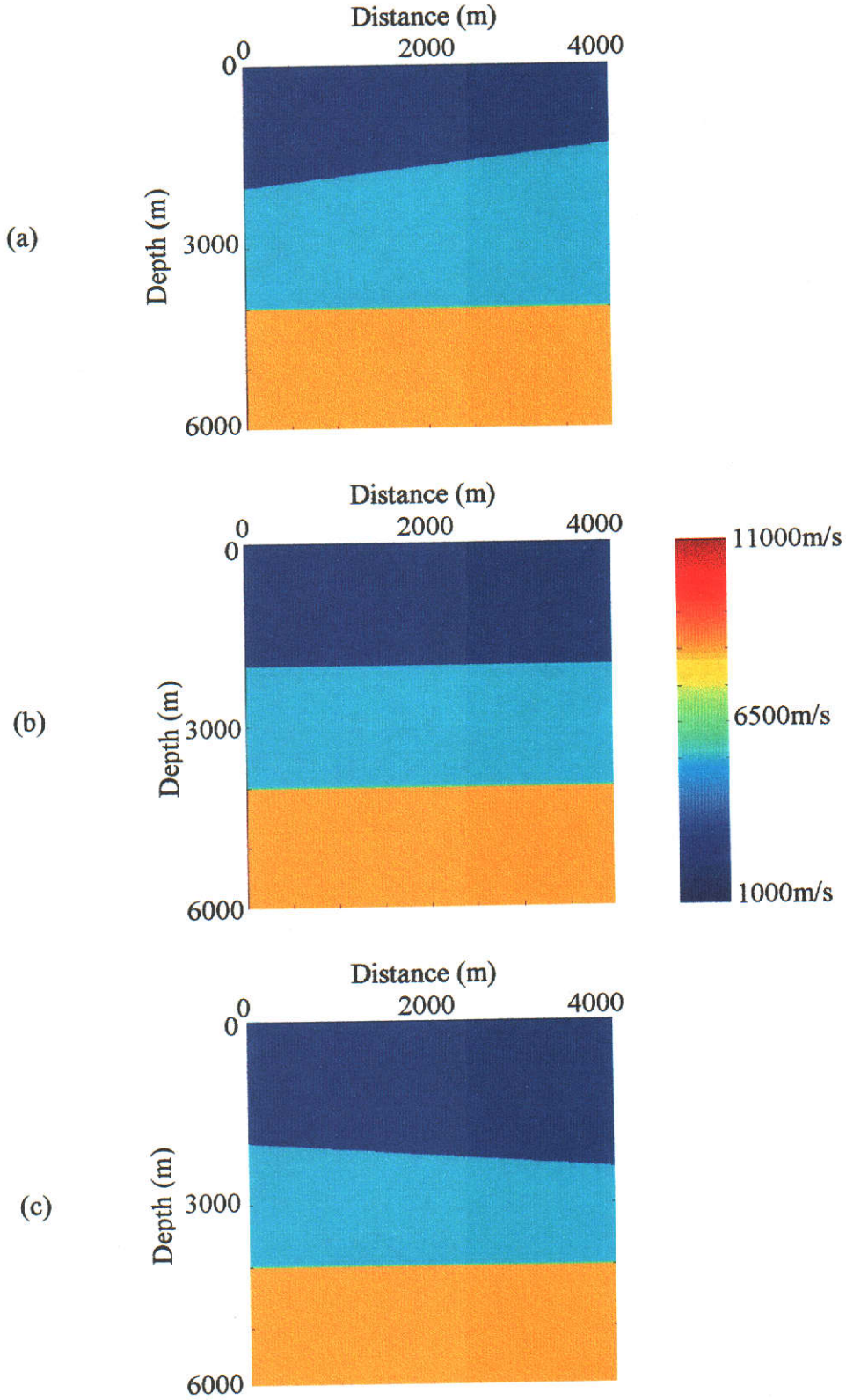

Figure 4.17: Three velocity models used for generating synthetic data where the multiple reverberations occur within a dipping layer. Dip was varied between (a) -10°, (b) 0°, and (c) +6° at 2° increments. Interval velocities were 2000m/s, 5000m/s, and 8000m/s for the first, second, and third intervals respectively.

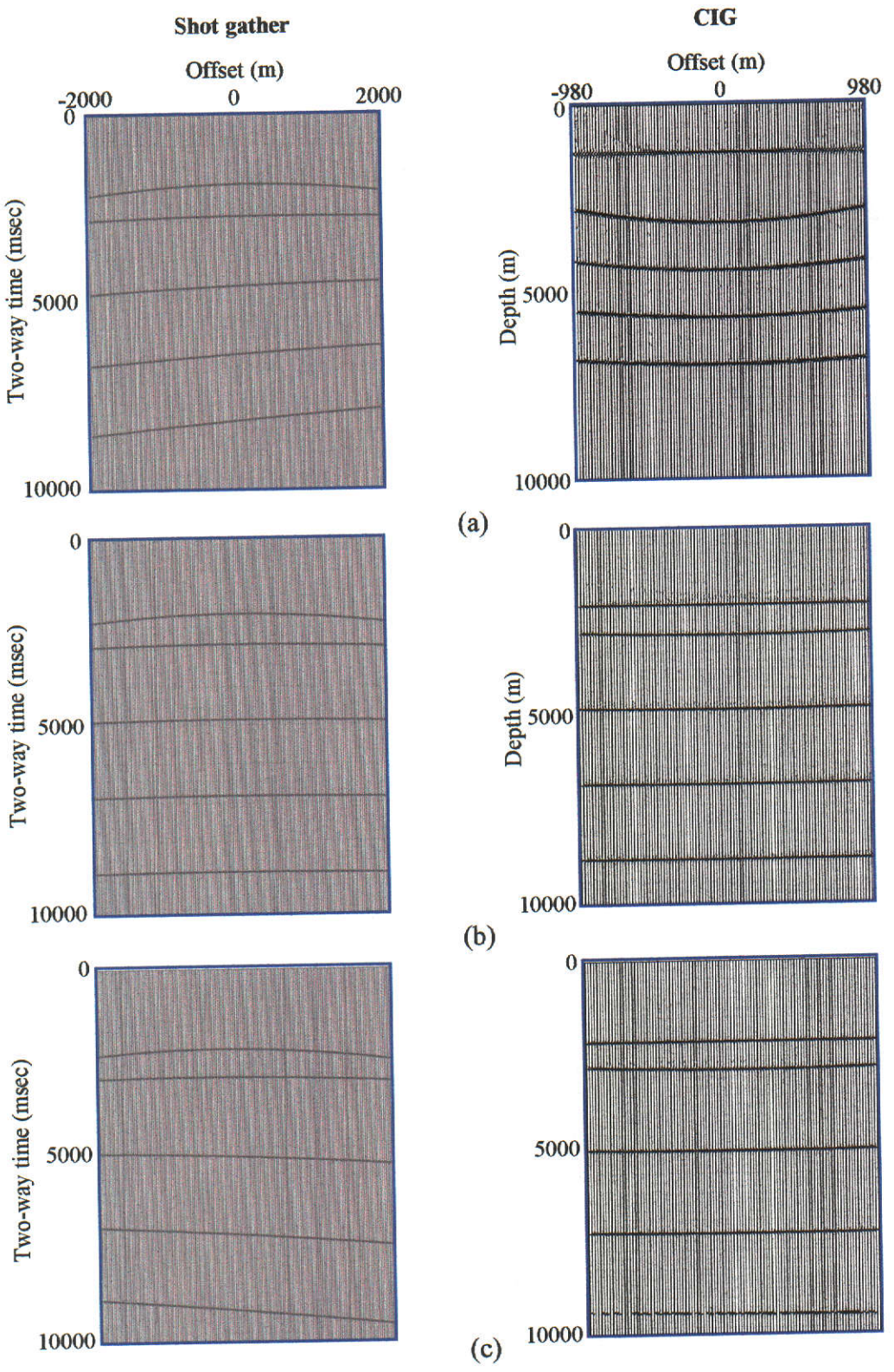

Figure 4.18: Shot gathers and CIGs obtained where the first layer dip varied. The shot gathers (left) and the CIGs (right) were created using a first layer dip of (a) -4°, (b) 0°, and (c) +4°. Events in order of arrival are S1R, S2R, S201R, S20101R, and S2010101R. The events generated off the second boundary change in appearance according to the dip of the first reflector.

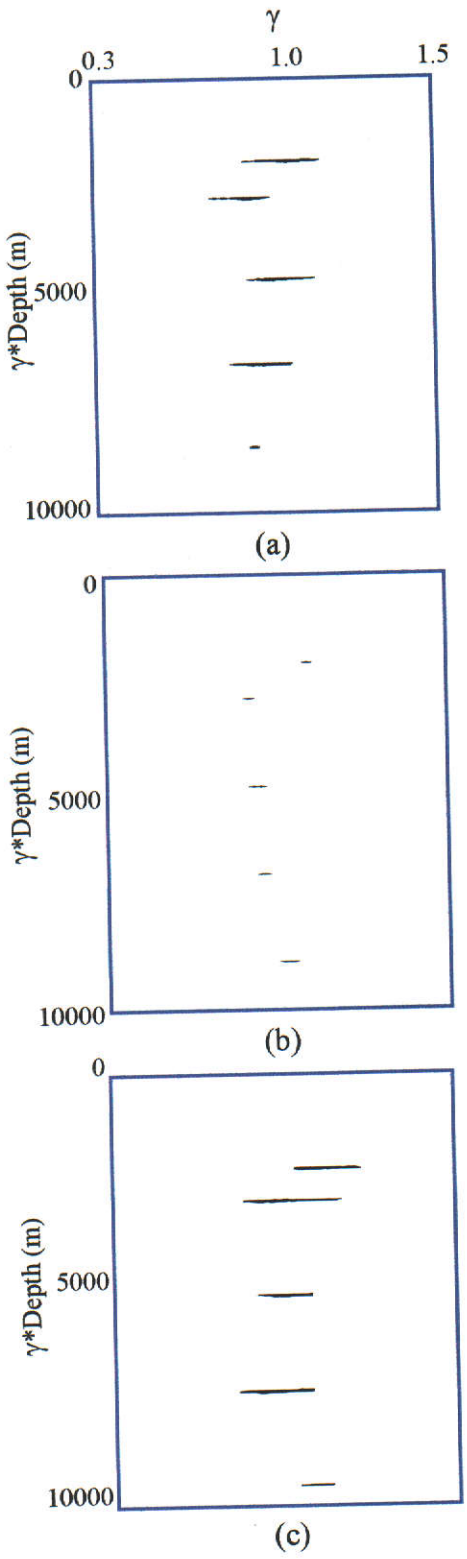

Figure 4.19: γ-semblance analysis using Equation (2.20) where the first layer dip varied. The results shown used dips of (a) -4°, (b) 0°, and (c) +4° in the second layer. Events in order of arrival are S1R, S2R, S201R, S20101R, and S2010101R. The γ values associated with each event change according to the dip of the first boundary.

an estimated multiple reverberation distance. This involves knowing the thickness of the first layer at the position of each multiple bounce. However, for the tests performed in this example, the thickness actually used was that determined at the MVA location.

The results of these tests are summarised in Table 4.7. These were obtained using a similar procedure to that used in Section 4.3.1. Focussing on the analysis for the second layer, as the dip increased, considerable errors were found as expected for the interval parameters using both primaries and multiples. This occurred more so than when the multiple reverberation was uniform. For large dips the errors obtained from utilising multiples in the analysis were actually larger than the errors obtained from using the S2R event. A general observation was made that as the dip became increasingly negative, the γ values *decreased* for higher orders of the surface peg-leg multiples. For example, in the case of a dip of -6°, the γ values for the S201R, S20101R, and S2010101R events were 0.912, 0.86, and 0.857 respectively. Decreasing γ with increasing multiple order indicates that the average velocity is increasing due to more of the propagation occurring in the higher velocity second layer. This can be accounted for by the multiple reverberations occurring in a decreasing thickness of the lower velocity first layer. That is, updip from the MVA location. On the other hand, in the case of a dip greater than or equal to zero, γ values *increased* with the order of the multiple. For example, for a dip of 2° the γ values for the S201R, S20101R, and S2010101R events were 0.86, 0.892, and 0.918 respectively. This fact suggests that the average velocity is decreasing due to more of the propagation occurring in the first layer. This can be accounted for by the multiple reverberations occurring in an increasing thickness of the first layer. That is, downdip from the MVA location.

Similar to the case where the multiple reverberation was uniform, another phenomenon that was observed was related to the interval parameter errors. As the order of the multiple increased, the interval parameter error generally decreased. Once again, the general trend of the interval parameter error was to increase with increasing positive or negative dips. This is probably due to the γ-semblance relation

Dip	Event	γ	$V_{av(calc)}$	$V_{av(true)}$	$x_{int(calc)}$	$x_{int(true)}$	$V_{int(calc)}$	% Error
-6°	S1R	1	2000	2000	1895	1895	2000	0
	S2R	0.85	2353	2923	1220	2000	2898	42
	S201R	0.912	2193	2545	1079	2000	2562	48.8
	S20101R	0.86	2326	2387	1589	2000	3775	24.5
	S2010101R	0.857	2326	2300	1793	2000	4258	14.8
-2°	S1R	1	2000	2000	1965	1965	2000	0
	S2R	0.87	2299	2879	1194	2000	2935	41.3
	S201R	0.9	2222	2515	1271	2000	3124	37.5
	S20101R	0.9	2222	2364	1455	2000	3574	28.5
	S2010101R	0.88	2273	2282	1857	2000	4563	8.7
0°	S1R	1	2000	2000	2000	2000	2000	0
	S2R	0.8	2500	2857	1500	2000	3750	25
	S201R	0.837	2389	2500	1735	2000	4337	13.3
	S20101R	0.844	2370	2353	2057	2000	5142	2.8
	S2010101R	0.878	2278	2273	2023	2000	5057	1.1
2°	S1R	1	2000	2000	2035	2035	2000	0
	S2R	0.813	2460	2836	1470	2000	3740	25.2
	S201R	0.86	2326	2486	1646	2000	4189	16.2
	S20101R	0.892	2242	2342	1725	2000	4389	12.2
	S2010101R	0.918	2179	2264	1723	2000	4384	12.3
6°	S1R	1	2000	2000	2105	2105	2000	0
	S2R	0.874	2288	2794	1276	2000	3355	32.7
	S201R	0.946	2114	2458	1252	2000	3303	33.9
	S20101R	0.96	2083	2321	1368	2000	3610	27.8

Table 4.7: Results of MVA using multiples where the multiple reverberations occur within a dipping layer. True interval velocity of the second layer is 5000m/s. Considerable errors can be observed. However, as the order of the multiple increases, the interval velocity and thickness still become more accurate.

of Lee and Zhang (1992) not being able to handle larger dips. This trend can be observed in Figure 4.20 where a graphical representation of the results is presented.

Another trend revealed in Figure 4.20 is that as the dip becomes increasingly positive or negative, the interval parameter errors obtained when utilising the first order surface peg-leg multiple begin to exceed the errors obtained using the S2R event. This occurs at dips equal to ±4°. A review of this phenomenon will now be made in conjunction with Figure 4.21 which presents schematics of multiple reverberations within a layer of small dip compared with reverberations in a layer of steep dip.

In Figure 4.21, as the order of the multiple increases, the thickness of the first layer observed at the position of the multiple bounce decreases compared with that observed at the MVA location (i.e. $x_{1a} < x_{1b} < x_{1c} < x_{1d}$ in Figure 4.21). This decrease in thickness becomes larger with increasing dip (i.e. $x_{1a} << x_{1b} << x_{1c} << x_{1d}$). This indicates that if the thickness observed at the MVA location were used to remove the multiple reverberation component of the multiple, there would be a difference between the true distance of propagation of the multiple and the calculated distance at the MVA location. This will introduce increasing error into the calculations when using multiples. Consider the following simplification of Equation (4.8) to obtain the second interval thickness:

$$x_2 = T_m V_{av(m)} - \sum D_m^* - x_1 \qquad (4.10)$$

where x_1 and x_2 are the first and second interval thicknesses and the other parameters are as described in Section 4.2. The increase in interval parameter accuracy is derived from the $T_m V_{av(m)}$ component of Equation (4.10) since this represents the total distance of propagation (as the distance of propagation increases, the sensitivity to any changes in interval parameter increases). Therefore, any error that is introduced by dip is going to be associated with the $\sum D_m^*$ component - the distance of propagation of the multiple reverberations. Therefore, there will be a *dip limit* beyond which the error introduced by the propagation distance of the multiple reverberations will outweigh the accuracy gained by utilising the multiple event in the MVA. A dip greater than this limit will result in the introduced error being greater than the improvement in accuracy achieved by utilising the multiple event in

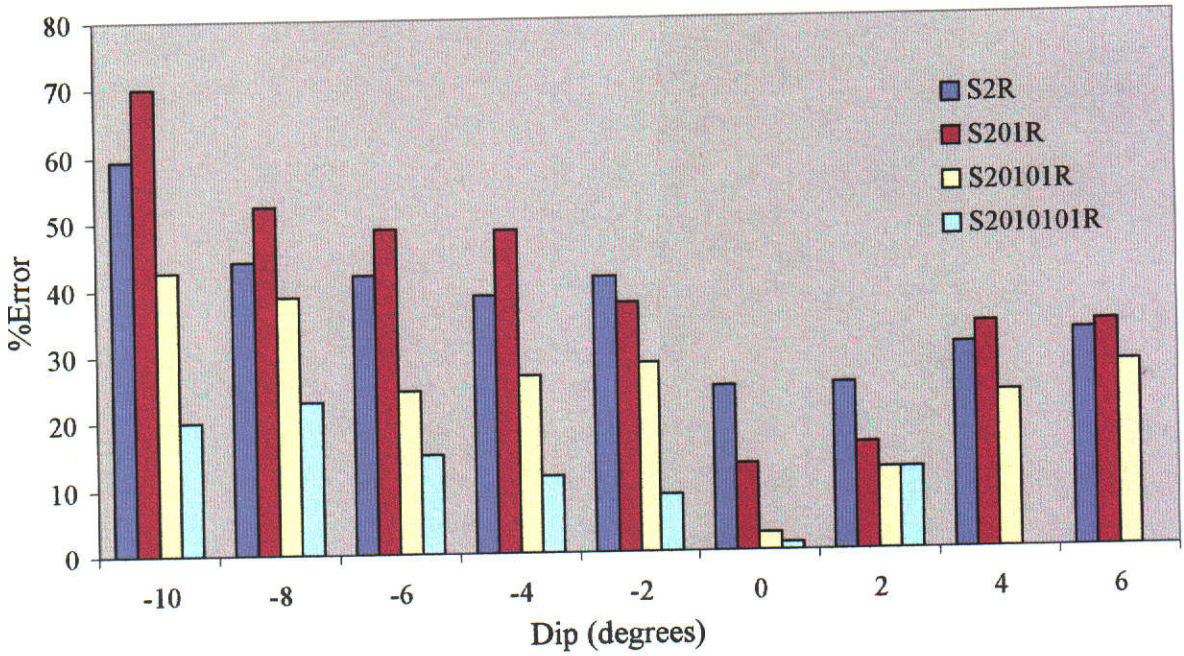

Figure 4.20: Error analysis from performing MVA using multiples where the multiple reverberation occurs within a dipping layer. The dip limit for the S201R event is the dip at which the interval parameter error provided by the S201R event begins to exceed that provided by the S2R event. Here it is ±4°.

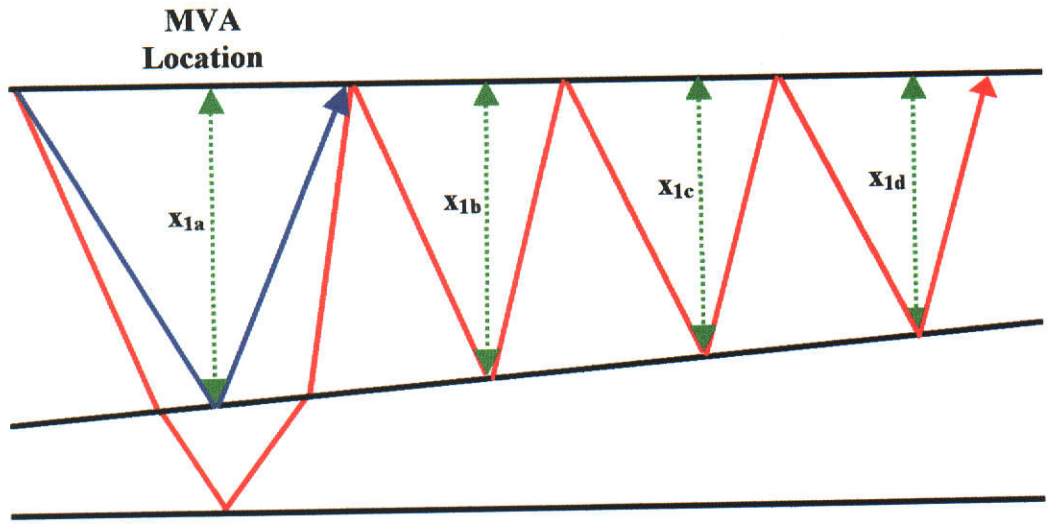

(a)

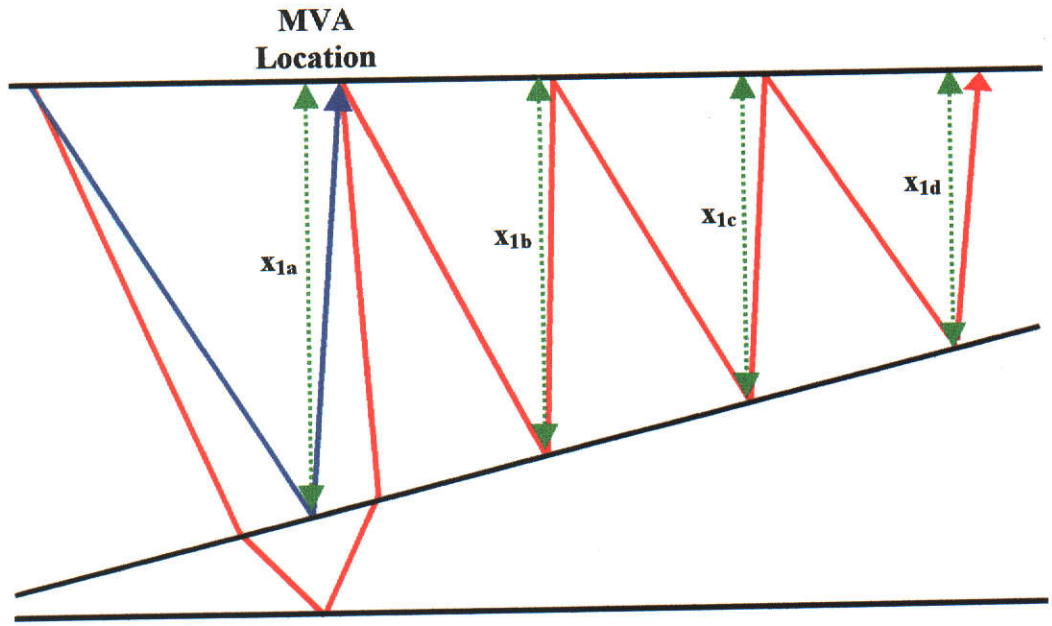

(b)

Figure 4.21: Multiple reverberation within a layer of differing dips. As the order of the multiple increases, the thickness of the first layer observed at the position of the multiple bounce decreases compared with that observed at the MVA location. This decrease in thickness becomes larger with increasing dip: (a) small dip and (b) large dip.

the MVA. This dip limit will also be dependent on the order of the multiple. In the example just presented, the dip limit for the S201R event is ±4° (this can be observed in Figure 4.20). This means that at dips greater than ±4°, the S2R event will provide greater interval parameter accuracy for the second layer than the S201R event. However, the higher order multiples can still be used to provide even more accurate interval parameters since the dip limit for these events will be greater than for the lower order multiples.

4.4 SUMMARY

These synthetic tests enable the following conclusions to be drawn regarding the use of multiples in MVA:

(a) All multiple types can be utilised for determining interval parameters. However, long-period multiples provide better accuracy and although water-bottom multiples can be used, the benefits of doing so are limited.

(b) Multiples can be used to provide interval parameter information when primary events are obscured.

(c) Multiples *can* be used to determine interval parameters in the presence of geological dip. However, the method is more effective when the multiple reverberations occur within a layer that is horizontal. That is, when the multiple reverberations are uniform. If the layer in which the reverberation occurs is dipping then the benefits of the use of a particular order of multiple will decrease as the dip increases. The method tested here relies on the γ-semblance relation provided by Lee and Zhang (1992) which assumes small dips and small offsets relative to the migration depth.

(d) Only when a multiple is visible will it have any benefit in contributing to the velocity analysis.

Conventionally, only primary events are employed for velocity analysis with multiples being considered as noise. Attempts are usually made to remove them beforehand. Here they have been treated as signal and successfully incorporated into a migration velocity analysis (MVA) procedure known as residual curvature analysis (RCA). By utilising multiple events in MVA, a higher order of accuracy can be

obtained in interval parameters. Multiples are events that have travelled farther through the Earth than their corresponding primaries. As the distance of propagation increases, the time sensitivity to velocity increases, which makes these events more appropriate to use in obtaining accurate interval parameters. Multiples can not only provide a more accurate average velocity than their corresponding primaries, but they can also be used to provide an alternative means for MVA when primaries are obscured by noise or shallower multiple events. The use of multiple events in MVA should also reduce the number of migration iterations conventionally required in building an interval velocity model for PSDM. This would be due to the average velocities for primary events, obtained by stripping off the effect of multiples, being more accurate initially. This has implications for reducing the time and hence cost of the MVA process. With a more accurate interval velocity model, corresponding improvements in the quality of the depth sections created using Kirchhoff PSDM should follow.

Two issues associated with Kirchhoff depth imaging have now been examined – traveltime computation and velocity model building. The latter considered multiple events as signal in the determination of interval velocities and thicknesses. However, multiple events will eventually have to be considered as noise and removed from the data to ensure that they won't hinder interpretation of the depth section obtained from prestack depth migration (PSDM). This issue will be examined in the following chapter.

CHAPTER 5

MULTIPLE ATTENUATION USING MIGRATION VELOCITY ANALYSIS

As mentioned in Chapter 1, developments in mature technology more often than not occur as a result of the culmination of *incremental* advancements. Thus far I have presented two incremental advancements to aid in the improvement in the quality of the depth section obtained from Kirchhoff PSDM. Initially I used the "generalised exploding reflector method" in a finite-difference traveltime computation procedure to reduce run time whilst retaining significant accuracy in the calculated traveltimes. Secondly, I used multiples to improve the accuracy of the velocity model. However, these multiples will eventually need to be considered as noise and removed from the data.

By continuing with the same philosophy, this chapter is concerned with investigating whether an incremental advancement can be made in the field of multiple attenuation. Conventionally, most multiples are attenuated by using a combination of different methods. Therefore, I will be examining whether another method can be found to add to the multiple attenuation armoury. I will investigate migration velocity analysis (MVA) as a tool for removing multiples from the seismic record so that they won't hinder interpretation of the depth section obtained with prestack depth migration (PSDM).

There are currently five popular means of suppressing multiples contaminating prestack data: (1) multi-trace multiple prediction and subtraction; (2) frequency-wavenumber (F-K) demultiple; (3) parabolic or hyperbolic discrete Radon transforms of normal moveout (NMO) corrected common midpoint (CMP) gathers (Hampson, 1986; Foster and Mosher, 1994); (4) surface-generated multiple elimination by 2-D deconvolution (Verschuur et al., 1992); and (5) model driven multiple suppression via downward continuation (Berryhill, 1979). With regard to the methods that are based on a degree of velocity discrimination between primary and multiple events, most are less effective in areas of strong lateral velocity variations since the NMO correction that separates primary and multiple events is normally based on

hyperbolic assumptions. This operation could be replaced by PSDM since PSDM can account for non-hyperbolic moveout in the CMP gather. It is proposed to investigate whether the velocity information obtained from multiple events from MVA (which uses PSDM) can be used as a basis for their attenuation.

5.1 MULTIPLE ATTENUATION IN THE PRESTACK DEPTH DOMAIN

In conventional seismic data processing, an attempt is normally made to attenuate multiple energy as early as possible in the seismic processing sequence, so that these events do not cause confusion in interpretation. However, it is often the case that several different techniques need to be applied to remove a particular multiple. This can be an expensive exercise. In addition these techniques may also rely on certain assumptions and the provision of a priori information. For example: the geology may need to be horizontally layered; there may need to be a certain amount of velocity discrimination; or a method may be limited to certain offsets. Hence, to improve the quality of results obtained from 2-D Kirchhoff prestack depth imaging, it is worthwhile to find a demultiple technique that doesn't have as many restrictions, and can target more than one multiple type. This chapter will investigate whether a multiple attenuation technique can be developed based on information derived from the MVA process.

5.1.1 THE NEED FOR MULTIPLE ATTENUATION IN DEPTH IMAGING

A depth section needs to contain as little multiple content as possible for optimal interpretation to occur. If multiples remain in the section they may be interpreted as being representative of actual geology or they may obscure lower amplitude, more subtle primary events.

Yilmaz (2001) illustrated the effect of water-bottom and surface peg-leg multiples on the results obtained when imaging beneath volcanics in the West Shetlands near the Atlantic Margin. This region has undergone extensional tectonism allowing salt diapiric structures to form. Common structural targets in the area are the Permian sands of the Rotliegendes and Carboniferous substrata below the Zechstein diapiric formation. In the West Shetlands survey area, an accurate depth structure map was required at the top of the Rotliegendes formation. This required an estimate of the

velocity-depth model above the salt and removal of its deleterious effect (i.e. multiples) on the underlying targets (Yilmaz, 2001).

Without multiple attenuation, PSDM yields the image gathers presented in Figure 5.1(a). These gathers show flat primary events (in blue) having been migrated with an accurate velocity model. Events associated with multiples (in red) have significant residual moveout since they remain undermigrated. When these image gathers are stacked to produce the depth migrated section, these multiples could contaminate the section to the point where a successful interpretation could not be made. In addition, Yilmaz (2001) states that multiples dominated the image gathers so much that conventional residual moveout analysis could not have been conducted using this data without multiple attenuation. In contrast, the image gathers which have had the multiples attenuated using Radon demultiple, are presented in Figure 5.1(b). Note that the majority of events are flat since most are primaries and have been migrated with an accurate velocity model. These gathers would stack to produce a depth migrated section where interpretation could proceed without the hindrance of multiple events.

This example has shown that multiples can make analysis of image gathers for residual moveout a difficult task using conventional methods. In addition they may also result in false interpretations being made on the depth section obtained after PSDM. There is a need to remove them before PSDM so that these consequences do not occur.

5.1.2 RECENT DEVELOPMENTS FOR MULTIPLE ATTENUATION IN THE PRESTACK DEPTH DOMAIN

Duquet and Marfurt (1999) developed a technique for multiple attenuation in the prestack depth domain by using the following processing sequence:

(a) Interval velocity model development;
(b) Transformation of the CMP time gathers to the prestack depth domain using PSDM;
(c) Transformation of the data in the prestack depth domain to another domain where multiple attenuation could take place;

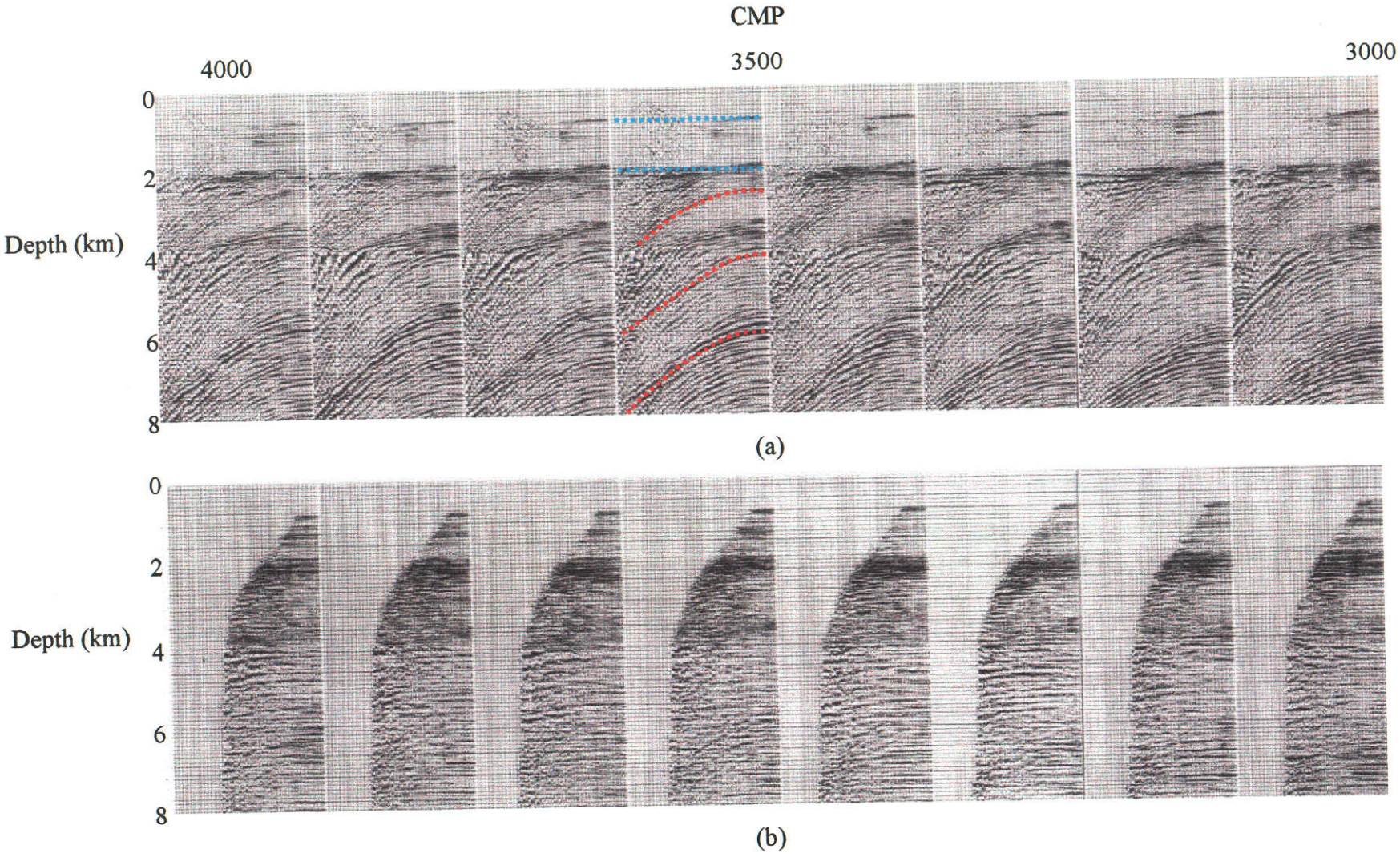

Figure 5.1: The West Shetlands line – selected image gathers. (a) Before and (b) after Radon-transform multiple attenuation (after Yilmaz, 2001). Representative primary events are shown in blue while multiples are shown in red.

(d) Attenuation of multiples;

(e) Inverse transformation of the remaining data to the prestack depth domain;

(f) Inverse transformation to from the prestack depth domain to CMP time gathers.

This process can be thought of as a double transform, (b) and (c), followed by filtering, (d), followed by an inverse double transform, (e) and (f).

To provide the basis for discrimination against multiples with their method, an estimate of the true interval velocity model was developed using the input data (i.e. step (a)). They then reduced these velocities by a factor of 20% to ensure that all primary energy would be overmigrated. It was envisaged that this would retain some of the steeply dipping multiple energy that was too steep to be migrated using the true estimate of the velocity model. They considered it more important to retain all signal and remove most noise, than to remove all noise and risk losing some signal. The CMP time gathers were then transformed to the prestack depth domain by using Kirchhoff PSDM (i.e. step (b)). The common image gathers (CIGs) that were obtained consisted of undermigrated multiple events, and primary events that were overmigrated. Duquet and Marfurt (1999) then employed a new Radon transform that parameterised differential moveout in the CIG using Al-Yahya's (1989) γ curves. This was known as the γ-curve transform (i.e. step (c)). This was in contrast to using the conventional hyperbolic or parabolic transformations. Undermigrated energy (i.e. multiples) in the CIG corresponded to $\gamma<1$ values in the γ-curve transform domain. On the other hand, overmigrated energy (i.e. primary energy) corresponded to $\gamma>1$ values in the γ-curve transform domain. The energy corresponding to values of $\gamma<1$ was subsequently muted in this transform domain (i.e. step (d)). The remaining energy then underwent an inverse γ-curve transform to recover the filtered data in the prestack depth domain (i.e. step (e)). The final step that Duquet and Marfurt (1999) employed involved modelling filtered CMP time gathers based on information from the filtered CIGs and the velocity model used for the initial Kirchhoff PSDM (i.e. step (f)). This was performed by using the conjugate gradient method developed by Duquet et al. (1998). This processing sequence was applied with a reasonable degree of success with considerable multiple energy being

suppressed. However, the method does not operate without limitations and these will be discussed next.

Duquet and Marfurt (1999) estimated the true interval velocity model and then reduced the velocities by a factor of 20%. This allowed the effects of complex wave propagation in the traveltime mapping stage to be reduced to the point where the γ-curve transform could accurately parameterise the residual moveout of each event. However, they stated that in the presence of strong velocity contrasts their Kirchhoff PSDM algorithm produced traveltime tables, and hence CIGs, that appeared to be broken rather than continuous. This was due to the introduction of undesired and unspecified complex wave phenomena. Hence it was necessary to smooth the velocity model before PSDM so these issues could be avoided. Another limitation of the method of Duquet and Marfurt (1999) was in regard to the conjugate gradient algorithm they used to recover the filtered CMP time gathers. This algorithm normally required 3-5 iterations to converge on the best solution. It also proved to be 6-10 times more expensive than conventional Kirchhoff PSDM. In addition, there was a lack of event resolution in the γ-curve transform domain which resulted in subsequent "leakage" of signal into the rejection band. Hence some signal was lost during the process. A final issue was to do with Al-Yahya's (1989) method only being accurate for 1-D media. Therefore, for significant lateral velocity variations, the more efficient parabolic Radon transform was suggested to possibly provide the same level of moveout discrimination. With such limits and expense associated with a depth varying velocity filter technique, it is imperative that a less expensive technique be found that is based on less a priori information.

5.1.3 AN ALTERNATIVE PROCESSING FLOW FOR MULTIPLE ATTENUATION IN THE PRESTACK DEPTH DOMAIN

I propose to investigate a similar, but somewhat different, processing sequence to that presented by Duquet and Marfurt (1999) in order to target specific multiple energy. That is, to find a suitable velocity model that will enable discrimination between primary and multiple events, perform a double forward transform, filter the data, and perform an inverse double transform to obtain the filtered data in the

prestack time domain. Performance will be judged by differencing the filtered and original records in the prestack time domain.

Initially I will examine the use of Kirchhoff PSDM in transforming the data from the prestack time domain to the prestack depth domain. Following this I will examine the use of the τ-p and wavelet transforms to assess their capacities for isolating specific multiple energy when applied to data in the prestack depth domain. If successful, I will then inverse transform the isolated multiple energy back to the prestack depth domain. A method will then be investigated to transform the multiple energy from the prestack depth domain to the prestack time domain by removing the effects of Kirchhoff PSDM. This multiple energy will then be subtracted from the original data in the x-t domain to possibly remove the presence of the specific multiple. This proposed processing flow is presented in Figure 5.2.

5.2 TREATING MULTIPLES AS NOISE IN MVA

Previously, multiple events were considered as signal in the MVA process in Chapter 4. However, these events eventually have to be removed from the data so that they won't hinder interpretation of the depth section obtained with PSDM. I will now analyse each step in the processing sequence presented in Figure 5.2 to see if specific multiple energy can be isolated and then see if it can be removed from the data as proposed.

5.2.1 THE ROLE OF AVERAGE VELOCITY

Kirchhoff PSDM requires an interval velocity model for traveltime mapping purposes so that energy in the prestack time domain can be mapped to the correct locations in the depth domain. Duquet and Marfurt (1999) initially obtained an estimate of the true interval velocity model. These velocities were then reduced by a factor of 20% to ensure that all primary energy would be overmigrated. In the approach I present next, I will build on my earlier initiatives. I propose to use a constant interval velocity model which is based on information derived from the MVA procedure. If successful, this would remove the need for providing a detailed estimate of the velocity model as was required in the technique of Duquet and Marfurt (1999).

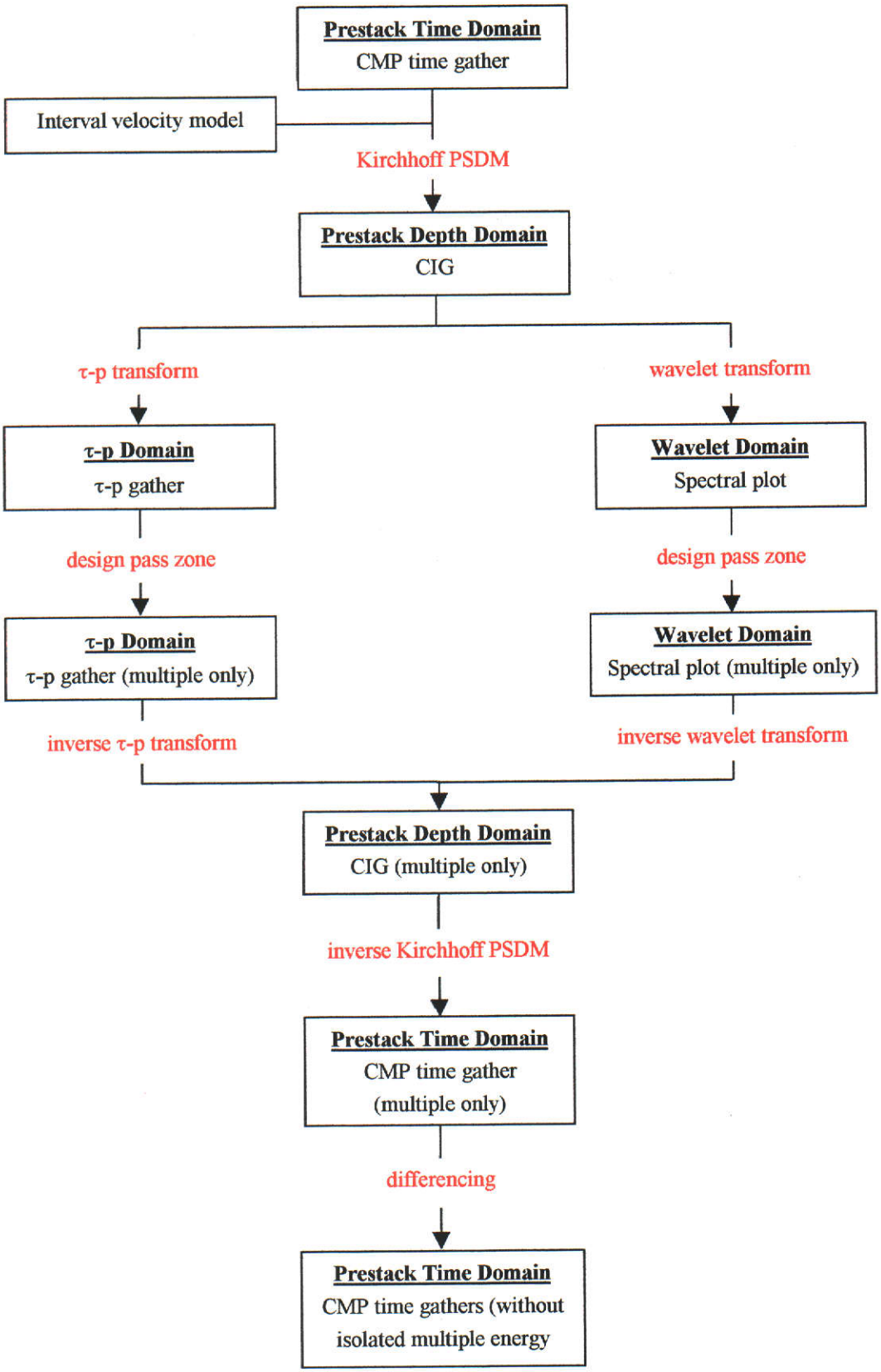

Figure 5.2: A proposed processing flow for multiple attenuation in the depth domain. Red captions indicate a transform process while black captions indicate a transform domain.

Theory

The importance of average velocity was indicated in Chapter 4 where it was used to determine interval thicknesses and velocities. Average velocity is defined as the ratio of the distance along a certain path to the time required for a wave to traverse that path. Conventionally, this type of velocity is used to convert directly from time to corresponding points in depth. While it strictly has meaning only with respect to a particular path, it is mainly valid for vertical velocity variations only and should not be used for any type of time to depth mapping when structures have significant lateral velocity variations. When lateral velocity variations are present, image ray conversions should be used (Bancroft, 1997). In Section 4.2, the average velocity to a particular reflector was determined from the associated value of γ which was selected from a γ-semblance plot. Recall that γ was defined as the ratio of the average velocity to a reflector, to the constant velocity at which Kirchhoff PSDM was performed (i.e. the migration velocity). This ratio effectively defined the degree of curvature that an event exhibits in a CIG. Lines et al. (1993) suggested that if an event curves upwards, the migration velocity used was too slow and the depth imaging would yield depths that are too shallow. Conversely, if an event curves downwards, the migration velocity used was too fast and the depth imaging would yield depths that are too deep. Al-Yahya's (1989) quantitative measure for this phenomenon was $\gamma<1$ values for the former case and $\gamma>1$ values for the latter case. If $\gamma=1$ then the event is flat in a CIG since the average velocity to the event would be equal to the migration velocity.

I propose to examine the curvature difference evident in a CIG as a potential method for discriminating between primaries and multiples. Performing migration with the average velocity of a multiple should flatten this event in a CIG. If other events surrounding the depth of this multiple exhibit a curvature that allows a degree of discrimination, then this could lead to a method for isolating and subsequently attenuating the multiple. I will illustrate my idea with an example.

Example

The dataset utilised in this process was created using the new 3-D seismic modelling

program developed by Hartley (2002a). The velocity model used for the synthetic data generation is shown in Figure 5.3(a) while a representative shot gather that was created is shown in Figure 5.3(b). The interval velocities and thicknesses for the first, second and third layers were 1500m/s and 750m, 2000m/s and 700m, and 5000m/s respectively. Events that were modelled included the S1R, S101R, S2R, S212R, and the S201R events. The synthetic dataset generated consisted of 100 shot gathers located at 20m intervals. A fixed receiver spread was used with receivers also located at 20m intervals. A source wavelet with a frequency of 30Hz was also used. The average velocity of each event in the shot gather was determined using MVA as described previously in Section 4.2. Essentially, Kirchhoff PSDM was carried out with the velocity of the first layer, a CIG was formed, and γ-semblance analysis was performed using this CIG. The average velocities were subsequently found to be S1R = S101R = 1500m/s; S2R = 1706m/s; S212R = 1792m/s; and S201R = 1630m/s.

Three different implementations of constant velocity Kirchhoff PSDM were then performed, each one using the average velocity of a specific multiple as the migration velocity. The resultant CIGs that were formed at an MVA location situated in the middle of the velocity model are presented in Figure 5.4. Each CIG exhibits migration noise in the form of "spiders legs" above and below each event in the CIG. This form of noise results from truncation of the summation curve (diffraction hyperbola defined by traveltime mapping) at the edge of each shot record (Bancroft, 2000).

In each CIG, the flat event was the event which had an average velocity equal to the migration velocity. All other events curved upwards or downwards to varying degrees depending on whether their average velocity was less than or greater than the migration velocity. For example, when PSDM was performed with a velocity equal to the average velocity of the S201R multiple (Figure 5.4(b)), the S1R and S101R events both exhibited downward curvature since they had been overmigrated. On the other hand, the S2R and S212R events exhibited upward curvature since they had been undermigrated. The S201R event appeared flat since the migration velocity was equal to the average velocity of this event. Another observation made from Figure 5.4(b) was that the S2R event appeared flatter than the S212R event. This is logical

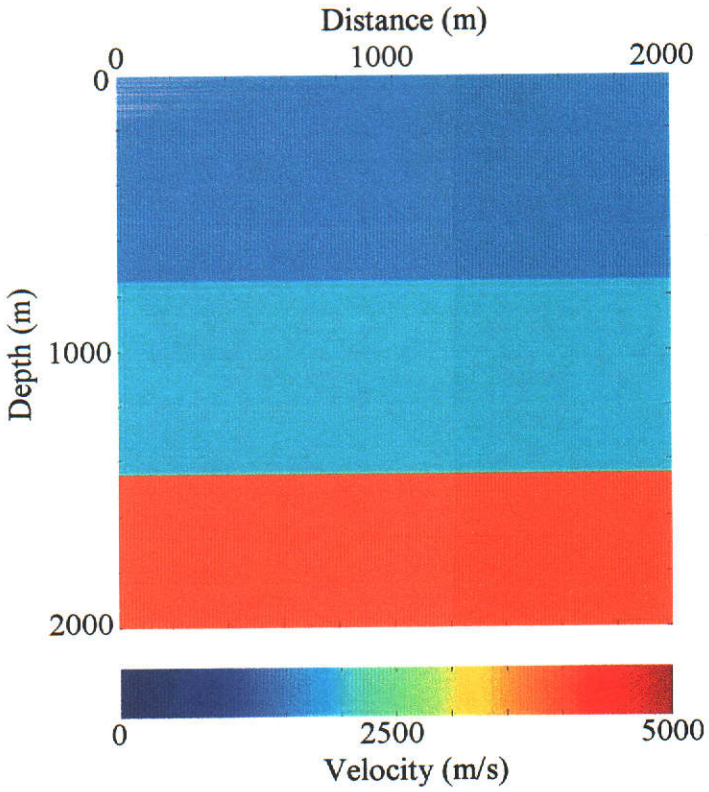

(a)

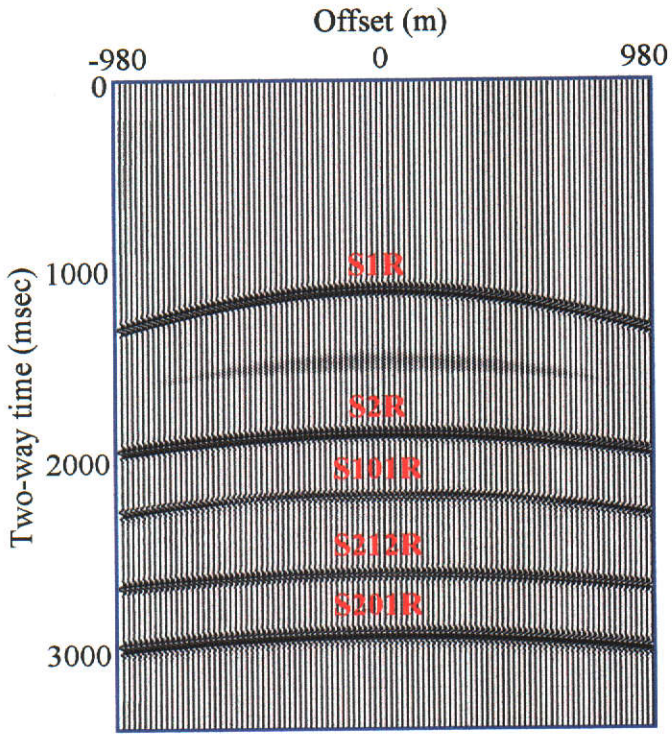

(b)

Figure 5.3: Velocity model used to generate synthetic data for testing the proposed processing flow. (a) Velocity model and (b) a representative shot record. The interval parameters for the first, second and third layers are 1500m/s and 750m, 2000m/s and 700m, and 5000m/s respectively.

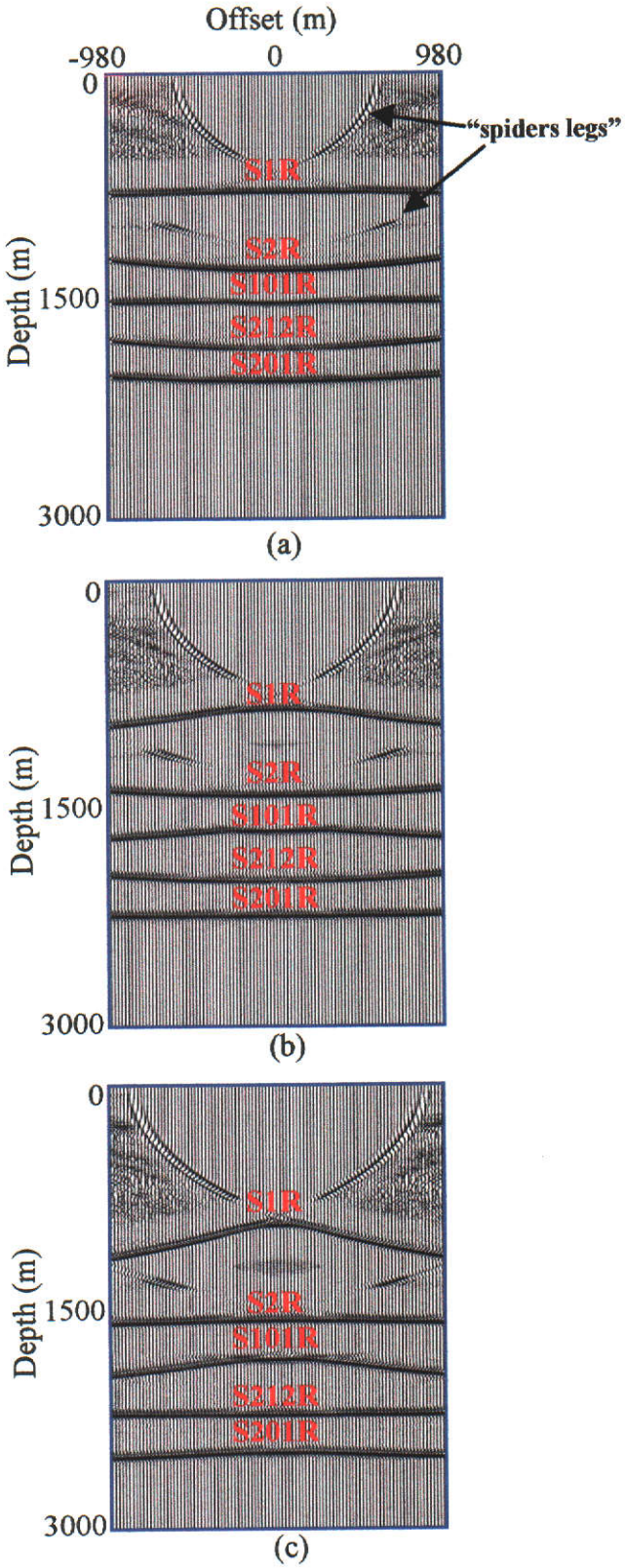

Figure 5.4: CIGs obtained in the prestack depth domain after performing Kirchhoff PSDM with the average velocity of specific multiples. PSDM was executed with the average velocity of the (a) S101R, (b) S201R, and (c) S212R events. The "spiders legs" that result from truncation of the diffraction hyperbolae used in amplitude summation are shown.

since the average velocity of the S2R event was closer to the average velocity of the S201R event - the migration velocity.

The phenomenon just observed could provide a basis for discrimination between a specific multiple and all other energy in the prestack depth domain dataset. Therefore, it is worthwhile for the investigation to proceed to the next phase where I will see whether a transform can be applied to the CIG to isolate the specific multiple energy being targeted.

5.2.2 SEPARATION OF MULTIPLE AND PRIMARY ENERGY IN A CIG

Having suggested that Kirchhoff PSDM be performed using a constant velocity equal to the average velocity of a specific multiple, I will now examine two possible transform domains in which the possible discrimination could be exploited. Two separate transforms will be applied to the CIG in order to do this: the slant-stack transform and the wavelet transform.

The Slant-Stack Transform

Forward transform

Plane-wave decomposition of a wavefield (such as a shot gather), can be achieved by applying linear moveout and summing amplitudes over the offset axis in the prestack time or depth domain. This procedure is known as *slant-stacking* and it replaces the offset axis with the ray parameter axis (i.e. slowness). A gather in the time or depth domain that has undergone the slant-stack transformation is known as a slant-stack gather. Alternatively it is referred to as a τ-p gather where 'τ' is the intercept and 'p' is the slowness (Taner, 1977; Stoffa et al., 1981; Stoffa, 1989). Reflection hyperbolas in the pre-transform domain will plot as ellipses in the τ-p domain and linear events will plot as points.

Based on the fact that linear events map to points and hyperbolic events map to ellipses in the τ-p domain, it will be investigated whether the CIG obtained by migrating with the average velocity of a multiple will exhibit the same phenomena. That is, will the flattened multiple plot as a point, and the events exhibiting curvature

plot as ellipses (or some other coherent event) in the τ-p domain? I expect that since the multiple is flat in the CIG, it should *always* plot as a point in the τ-p domain. If this transform is successful, it may allow the multiple to be discriminated from other events and permit further processing to be performed.

Inverse Transform

Inverse mapping from the τ-p domain involves applying a filter beforehand to enable proper restoration of amplitudes in the pre-transform domain. This is accomplished by multiplying the amplitude spectrum of each τ-p trace by the absolute value of the frequency (Yilmaz, 2001). Even so, it is logical that the less information that has to undergo the inverse operation, the fewer artifacts that will be introduced by the inverse transform. Hence, I will examine whether a pass zone can be designed that includes only the multiple energy related to the flat event in a CIG. The character of other events in the transform domain then becomes less important. This energy could then be inverse transformed to reconstruct the multiple event in the CIG.

Example

The τ-p transform was used to target the S101R, S212R and S201R multiples in the CIGs presented in Figure 5.4. I defined the intercept axis in each transformation as the right hand side of each CIG. The τ-p transforms of the CIGs obtained by performing constant velocity Kirchhoff PSDM with the average velocity of the S101R, S201R, and S212R events are shown in Figures 5.5(a), (b), and (c) respectively. The migration noise observed earlier in the CIGs, also transforms to undesirable events in the τ-p domain. However, most of this noise is associated with the larger amplitude primary events.

The appearance of events in the τ-p domain depends on the difference between the average velocity of the event and the migration velocity. When migration was carried out with the velocity of the S212R event, the S212R event appeared in a localised region around the p=0 axis due to this event being flat in the CIG (Figure 5.5(c)). Since all other events were "frowns" in the CIG, they all appeared with a degree of curvature and smearing across the τ-p plane depending on the velocity discrimination

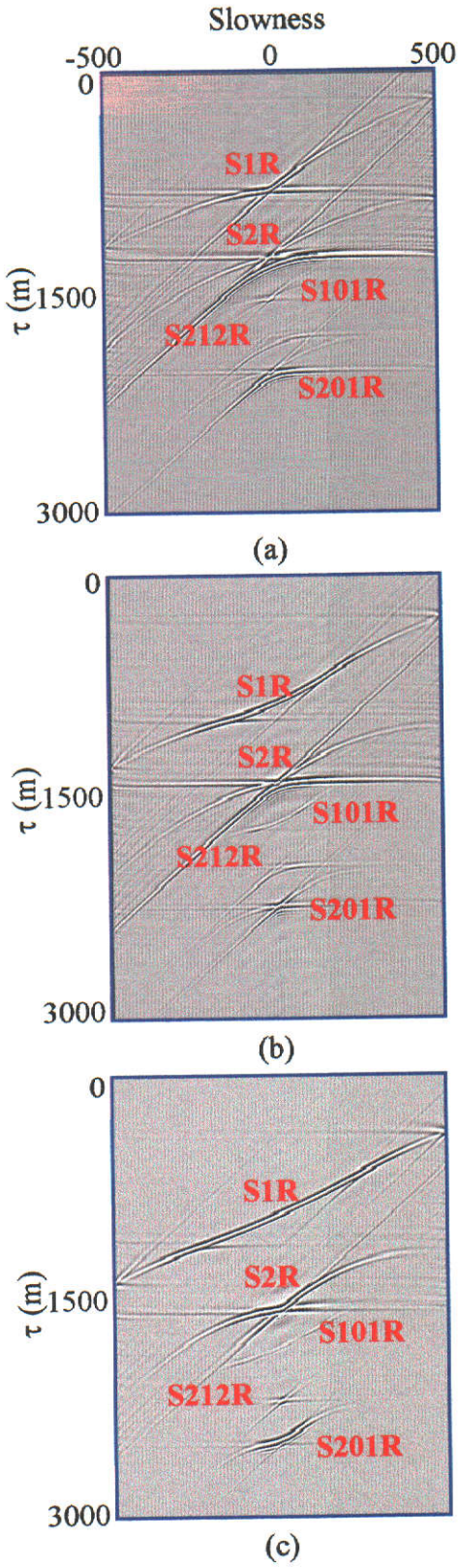

Figure 5.5: Results of performing τ-p transforms on the CIGs obtained after migrating with the average velocity of a specific multiple. Migration was carried out with the average velocity of the (a) S101R, (b) S201R, and (c) S212R events.

between their respective average velocity and the migration velocity. The amount of smearing in the τ-p domain was also dependent upon the relative amplitude strength of the event. When the migration velocity was equal to the average velocity of the S1R and S101R events these events appeared flat in the CIG and all other events exhibited "smiles". The representation of these "smiles" in the τ-p domain is evidence once again of a degree of curvature and smearing (Figure 5.5(a)). The S101R event transformed to a local position around the p=0 axis and so did the S1R event although the latter event was somewhat obscured by the representation of the migration noise in the τ-p domain. The S1R event also appeared to be localised in a larger region than the S101R event because of the difference in amplitude strength between the two events.

The characteristics of each event in the τ-p domain changed depending on the velocity at which Kirchhoff PSDM was originally performed. For example, when migration was carried out with the velocity of the S1R and S101R events, the S201R event curved downwards in the τ-p domain (Figure 5.5(a)) since the average velocity of the S201R event was larger. However, when migration occurred with the average velocity of the S212R event, the S201R event curved upwards in the τ-p domain (Figure 5.5(c)) since the average velocity was less than that of the S201R event. When the migration velocity was equal to that of the S201R event, this event congregated around the p=0 axis (Figure 5.5(b)).

The next step was to design a pass zone around each of the multiples which had been localised around the p=0 axis. This was a simple process since each multiple had discrimination in depth. An inverse τ-p transform was then performed on the isolated multiple energy to obtain its representation as a CIG in the prestack depth domain. The multiple energy retained in the τ-p domain and the reconstructed CIG in the prestack depth domain for the S101R, S201R, and S212R events are presented in Figures 5.6(a), (b), and (c) respectively. Top and bottom mutes were applied to these reconstructed CIGs since the inverse τ-p transform introduced some noise above and below each respective multiple.

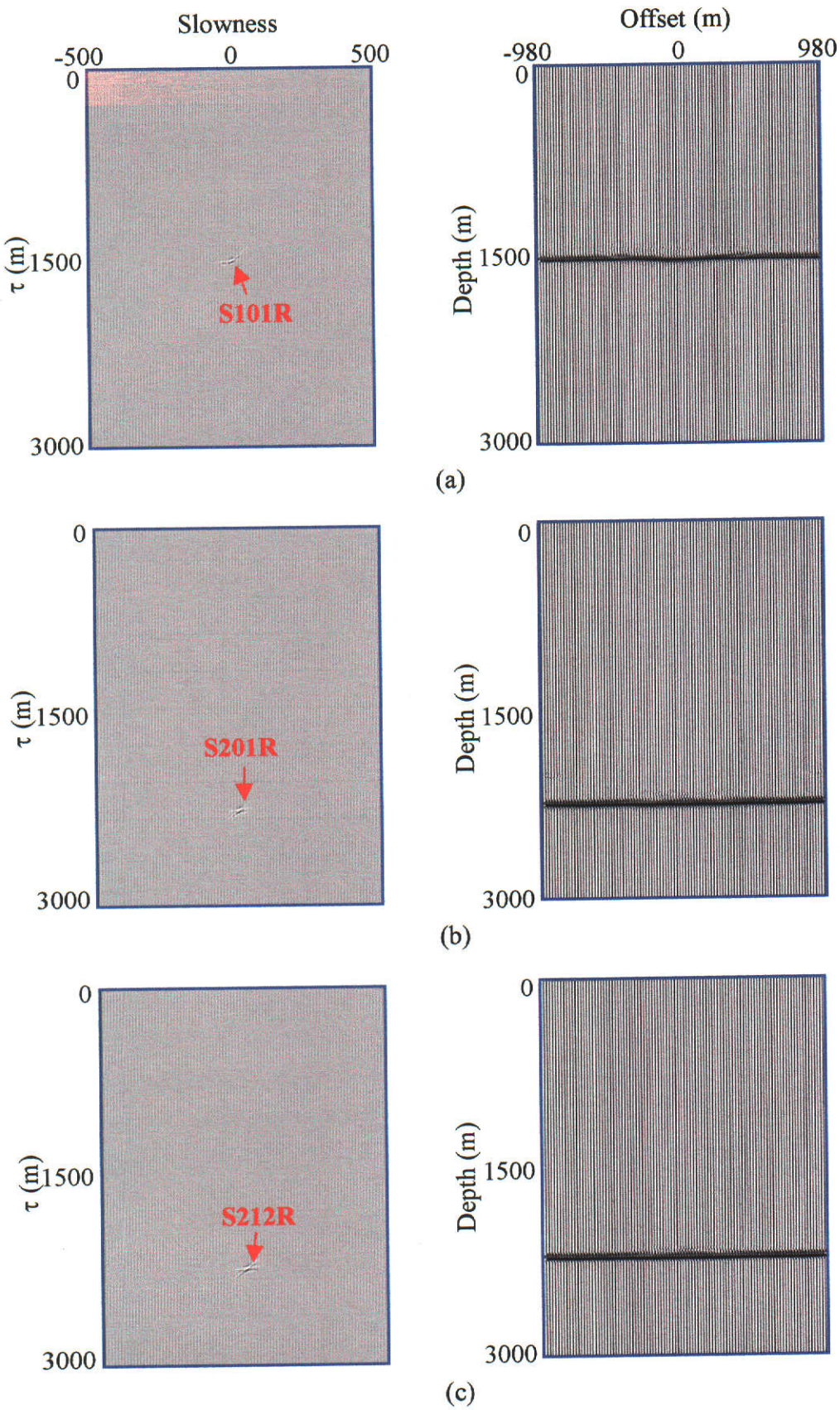

Figure 5.6: τ-p transforms and reconstructed CIGs after rejecting all energy but the targeted multiple. Migration occurred with the average velocity of the (a) S101R, (b) S201R, and (c) S212R events. The multiple energy has been isolated successfully.

A visual comparison of the CIGs in Figure 5.4 and the filtered CIGs in Figure 5.6 confirms that considerable multiple energy has been isolated. This energy will now need to be used in the next phase of processing which involves the removal of the Kirchhoff PSDM operator applied previously. However, before investigating this removal operation, another transform that is available for isolating specific multiple energy will be described.

The Wavelet Transform

Another method that could exploit the property of an event being flat in a CIG is *wavelet analysis* (the practical representation of this is the *wavelet transform*). The widespread use of wavelet analysis began with the formalisation of multi-resolution by Mallat (1999). With respect to geophysics, an excellent review paper on this subject is given by Kumar and Foufoula-Georgiou (1997). Before investigating the possibility of using wavelet analysis to exploit the moveout evident in a CIG, it is necessary to briefly describe how the wavelet transform operates.

Theory

In Fourier analysis, a waveform may be shown to be composed of a series of sinusoids. In wavelet analysis, a wavelet basis (or wavelet dictionary) is a series of wavelets that enables representation of a signal as a linear combination of wavelets. For example, consider a signal S, and a wavelet basis containing the wavelets w_1, w_2, w_3, w_4, w_5, and w_6. The signal can be represented as such:

$$S=c_1w_1+ c_2w_2+ c_3w_3+ c_4w_4+ c_5w_5+ c_6w_6, \qquad (5.1)$$

where constants c_1 through to c_6 represent the proportion of each wavelet (w_1 through to w_6 respectively) used to constitute the signal. These constants are known as "wavelet coefficients". One particular wavelet basis is the Haar basis which starts with a scaling function (father wavelet) that is used to generate the so called mother wavelet. The mother wavelet then acts as a prototype for defining all other wavelets in the basis. Figure 5.7(a) presents a series of Haar wavelets which constitute a wavelet basis for discrete analysis of a signal (the scaling function is not shown). These wavelets are made up of *translations* and *dyadic dilations* of the mother wavelet. The finest scale corresponds to a wavelet that is defined over two samples (it is known from sampling theory this is the highest frequency that can be recorded)

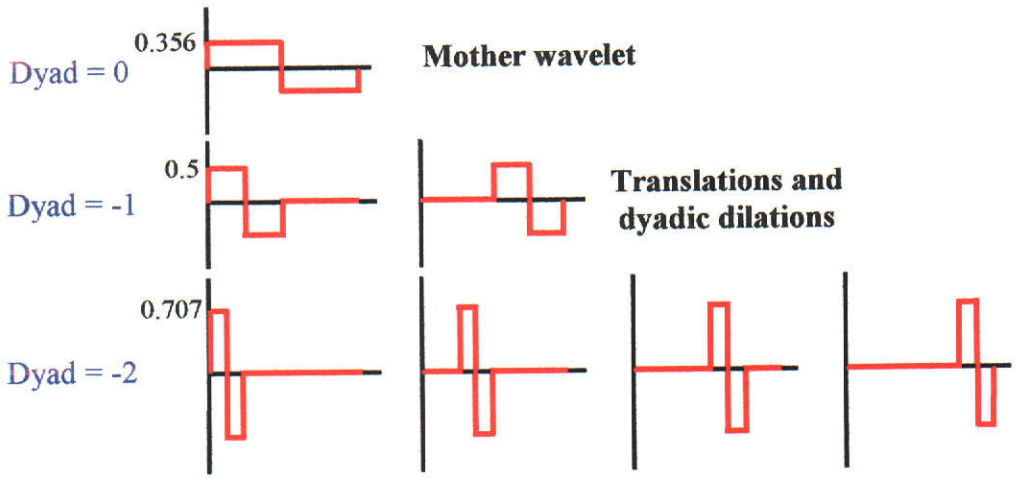

(a)

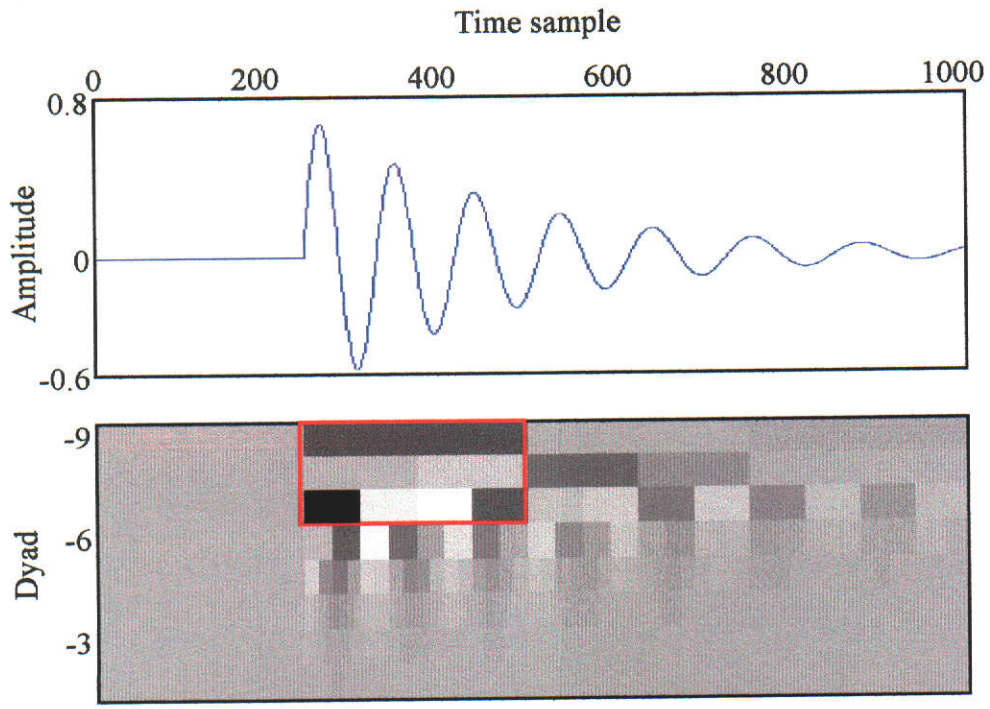

(b)

Figure 5.7: The wavelet transform. (a) The Haar basis illustrating seven wavelets and (b) an example of wavelet analysis using the Haar wavelet basis performed on a signal with decaying amplitudes and frequencies over time. The position of the red box in the spectral plot indicates where the majority of the signal lies - in the high frequencies between samples 256 and 512.

while the coarsest scale is measured by the father wavelet which measures the average (or DC component) of the signal. The dyad gives the fractional width of the wavelet. For example a dyad of -2 means the wavelet is one quarter (2^{-2}) of the entire signal in width.

Essentially, the process of wavelet analysis involves a series of high and low pass filters being convolved with the input signal. The high pass filter is the wavelet function and the low pass filter is the scaling function. In a multi-resolution approach, the signal is high and low pass filtered with the low pass component being used again in another high and low pass filter pair. In the second, and successive steps, the wavelet function is dilated and translated along the time series so that the wavelet function analyses successive levels, or scales, of details in the original time series. The end result is that wavelet analysis produces approximation information with the scaling functions, and detailed information with the wavelet functions (Leblanc and Morris, 2001). An example of wavelet analysis is presented in Figure 5.7(b) where a signal with decaying amplitude and frequency over time has been analysed. Black or white rectangles in the spectral plot below the signal indicates significant energy from the signal being associated with a particular time and dyad. It is clear that most of the energy is contained in the high frequencies (large negative dyad values) located between samples 256 and 512 (indicated by the red box).

Previous Application to Multiple Attenuation

Due to the very nature of their design, wavelets are a powerful tool for characterising similar behaviour and recognising patterns over a range of time and offset scales. Thompson and Hartley (2002) described a multiple suppression technique based on the fact that there is a correlation between related multiple events. The wavelet transform was performed by Thompson and Hartley (2002) on a trace-by-trace basis and involved decomposing a zone surrounding the targeted multiple on each trace. This zone included the target multiple and a reference event which was defined as the target multiple on adjacent traces. A sliding window was then moved over the target and reference zones to create two decompositions that described their respective time-frequency properties. Their next step involved performing a correlation in the decomposition domain between the target and reference zones.

This corrected for any misalignment of the coefficients as a result of errors in the locations of the reference and targeted multiple picks. The two zones were then compared on a coefficient-by-coefficient basis to obtain a prediction of the target multiple based on the reference.

Thompson and Hartley (2002) decomposed a reference zone on a trace (or number of traces) either side of the trace containing the target zone. Predicted multiples from each reference zone were then averaged to minimise the removal of energy other than that associated with the target. The only input required for the technique was knowledge of the location of the multiple to be targeted. If this location were known, the decomposition zone could be centred around it. Generally, water-bottom multiples are predictable in time, hence these were targeted by Thompson and Hartley (2002).

In my research it was shown (Figure 5.4(a)) that water-bottom multiples appear flat in a CIG formed by performing Kirchhoff PSDM with the water velocity. The depth to the water-bottom is known from velocity analysis (and other means) hence water-bottom multiples are also predictable in depth. Locations of interbed and peg-leg multiples could also be inferred during MVA.

Application of the Wavelet Transform to Multiple Prediction in a CIG

It is proposed to investigate whether the wavelet transform can be used as a tool for isolating specific multiple energy contained in a CIG obtained after performing constant velocity Kirchhoff PSDM with the average velocity of the specific multiple. The possible advantage of operating in the prestack depth domain is that due to the multiple being flat, the decomposition window associated with the wavelet transform could be positioned horizontally. PSDM will ensure that an event will appear flat in a CIG regardless of whether the moveout is hyperbolic or non-hyperbolic. Hence, a horizontal window could possibly be used for wavelet decomposition around a particular multiple in *all* scenarios.

Similar to the τ-p transform, if the multiple energy being targeted can be isolated using the wavelet transform, an inverse wavelet transform will need to be

implemented to reconstruct the multiple energy in the prestack depth domain. If this can be done, the processing sequence could be completed by investigating how to remove the effects of the Kirchhoff PSDM operator so that the data can be recovered in the prestack time domain.

Example

The wavelet transform was used to isolate water-bottom multiple energy in the CIG shown previously in Figure 5.4(a). Figure 5.8(a) illustrates this CIG once again. The S1R and S101R events both appear flat however, all other events curve upwards to differing degrees. Wavelet decompositions were performed in a window that slid over the position of the water-bottom multiple. The wavelet representative of the S101R event was predicted on a certain trace by averaging the wavelet decompositions of traces located on either side. Upon transformation back to the prestack depth domain, the CIG containing the isolated S101R energy was obtained. This is presented in Figure 5.8(b). A visual inspection of Figures 5.8(a) and (b) reveals that the targeted multiple has been isolated with reasonable success.

The targeted multiple energy has now been isolated in the prestack depth domain by using either the τ-p transform or the wavelet transform. After differencing the isolated multiple energy from the original CIG, a visual inspection reveals that the former was more successful in achieving isolation of the multiple energy. Thus the τ-p derived data will be used for this task in the remainder of the flow chart presented previously in Figure 5.2. The next step in the processing sequence is to remove the effects of Kirchhoff PSDM. If successful, this will enable the isolated multiple energy to be recovered in the prestack time domain.

5.2.3 INVERSE KIRCHHOFF PSDM – HOW IS IT PERFORMED?

It will be necessary to find a way to remove the effects of the constant velocity Kirchhoff PSDM. This will enable:

(a) other multiples to be targeted at the same location; or

(b) a CIG to be analysed at another location for multiples to be attenuated; or

(c) PSDM to be performed with the correct interval velocity model to produce a

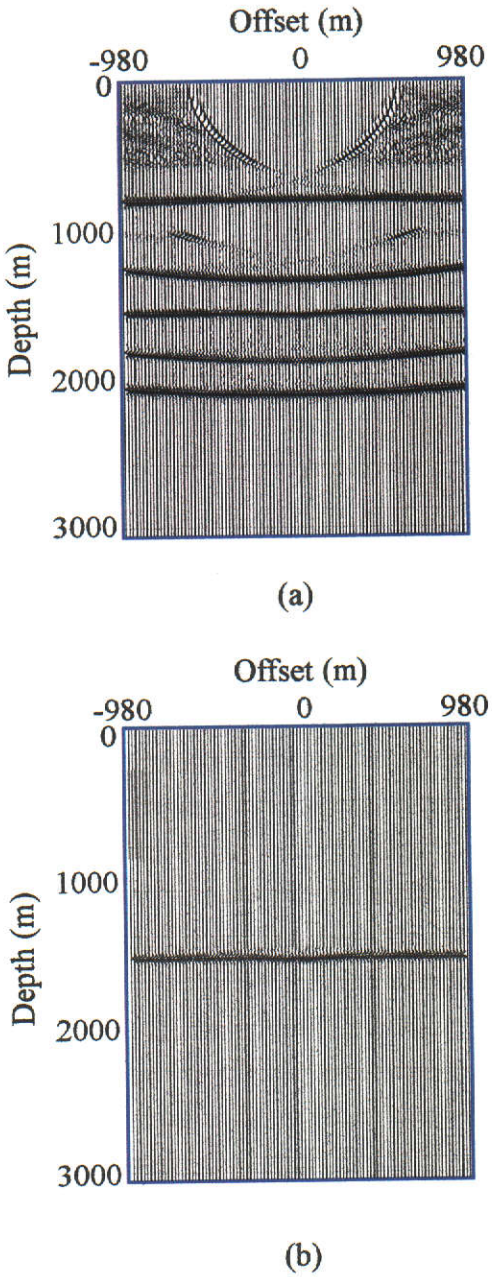

Figure 5.8: Using the wavelet transform to predict multiple energy in a CIG. (a) The CIG obtained by performing Kirchhoff PSDM with the water velocity and (b) the predicted S101R energy by utilising the wavelet transform. The multiple energy associated with the S101R event has been isolated with a reasonable degree of success.

final depth migrated section.

The common term for the process of inverse migration is "demigration" (or modelling). This operation is not yet available in most conventional processing software therefore it was necessary to develop it for the purposes of this research.

To understand how demigration might be performed, it is necessary to understand how Kirchhoff PSDM operates. In essence, Kirchhoff PSDM involves summation of amplitudes from different traces along diffraction hyperbolae defined by traveltime mapping. However, prior to summation, each amplitude also has an obliquity, scaling and wavelet shaping factor applied to it. The result of summing these modified amplitudes is then output to the depth section. In the formation of a CIG, several shot gathers undergo Kirchhoff PSDM and the trace in each migrated shot gather nearest the MVA location is retained to form a CIG. Therefore, in the formation of one trace in a CIG, the amplitude summation only occurs over a single shot gather in the prestack time domain.

Demigration will involve recovering the amplitude at a certain sample on a trace in the shot gather situated nearest the MVA location, from the associated trace in the CIG. This will require knowledge of the amplitude contribution at that sample to the resultant amplitude situated on the CIG trace. I define this contribution as the "amplitude ratio". In addition, it will require knowledge of the obliquity, scaling, and wavelet shaping factors applied to that particular amplitude before it was summed. I propose to develop a method for demigration based on two stages: demigration in depth followed by demigration in time.

Demigration in Depth

Demigration in depth will involve converting the CIG in the prestack depth domain to a *demigrated* CIG in the prestack depth domain. Each sample on each trace in the CIG will be multiplied by the amplitude ratio followed by removal of the obliquity and scaling factors associated with each amplitude. These three pieces of information will need to be stored in memory during Kirchhoff PSDM and retrieved when required for the demigration. It may be noticed that I have not considered the wavelet

shaping factor that is associated with Kirchhoff migration which is explained as follows. Most commercial Kirchhoff PSDM algorithms incorporate some form of "cost-cutting" procedure. Methods for cost saving include controlling the migration aperture, resampling the input data, increasing the size of the grid cell size in the velocity model, or eliminating the wavelet shaping factor (Urosevic, 2000). The algorithm that I wrote for performing the demigration (presented in Appendix A6) reduced run time and hence costs by not accounting for the wavelet shaping factor.

Demigration in Time

Following the above procedure it will be necessary to convert the demigrated CIG in depth to the prestack time domain. If successful, the result will be analogous to a CMP gather. This process will involve relocating amplitudes on the traces in the demigrated CIG (in depth) to corresponding positions on traces located in time. It is envisaged that this will not just be a simple matter of dividing the position in depth by the constant velocity at which migration was originally performed. This is due to each trace in the CIG originating from a different migrated shot gather. Therefore, offset will also need to be considered in the calculations.

Specifically, demigration of the CIG in time will involve the determination of the total distance from a source located near the surface at an offset from the MVA location, to a receiver also located near the surface but at the MVA location, via a scatterpoint positioned at depth on the CIG trace. This is illustrated in Figure 5.9 where the source position is defined by the coordinates (S_x,S_z), the receiver position is located at (R_x,R_z), and the scatterpoint position is defined by (R_x,P_z). The total distance is given by D_T. It is necessary to determine where the amplitude at a sample on the demigrated trace in time originated from in depth. Therefore, the goal is to determine P_z. From Figure 5.9, the total distance, D_T is defined by:

$$D_T = D_{SP} + D_{PR}. \tag{5.2}$$

Expanding Equation (5.2) gives:

$$D_T = \sqrt{(S_x - R_x)^2 + (P_z - S_z)^2} + (P_z - R_z). \tag{5.3}$$

Squaring both sides and rearranging gives:

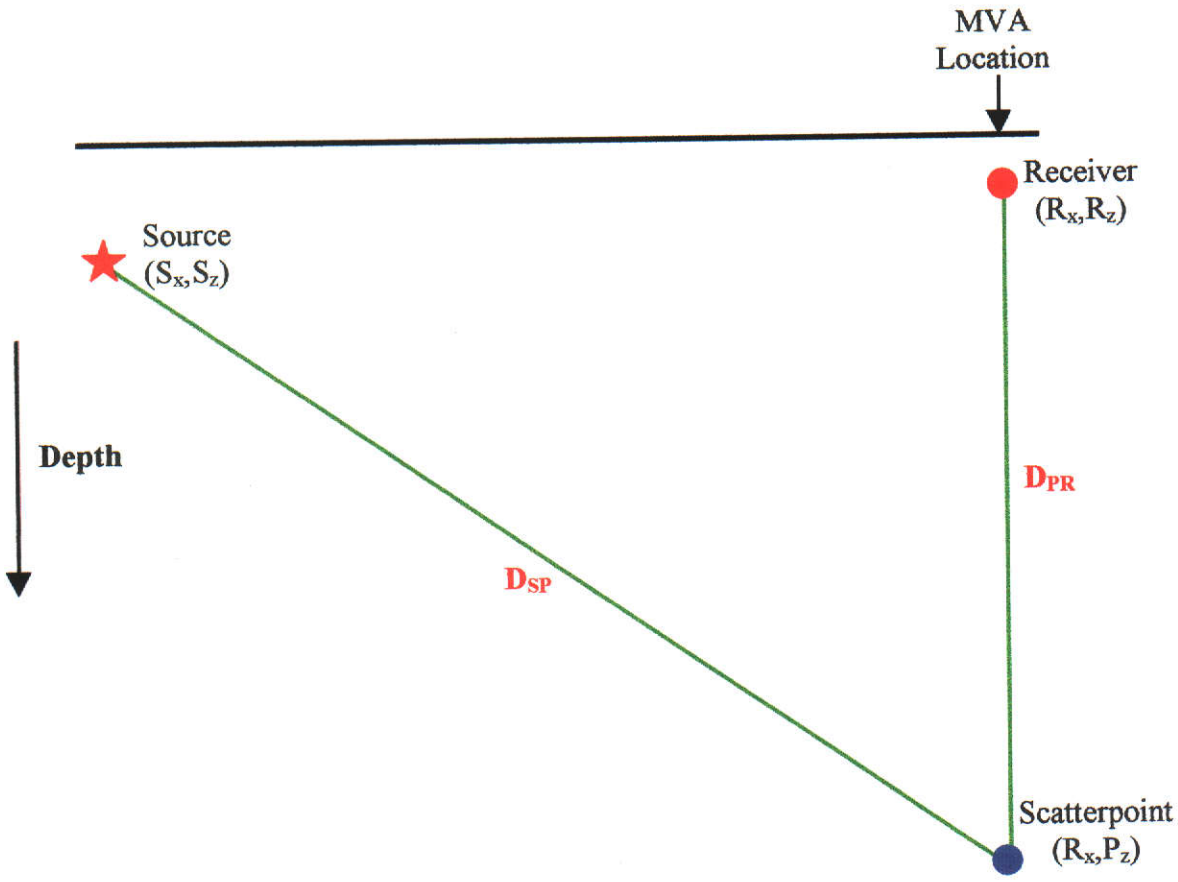

Figure 5.9: Determination of the total distance required for demigration in time. D_T represents the distance from a source to a scatterpoint located at the MVA location (D_{SP}) plus the distance from the scatterpoint to a receiver also located at the MVA location (D_{PR}).

$$[D_T - (P_z - R_z)]^2 = (S_x - R_x)^2 + (P_z - S_z)^2. \quad (5.4)$$

Expanding all terms gives:

$$D_T^2 - 2D_T P_z + 2D_T R_z + P_z^2 - 2P_z R_z + R_z^2 = (S_x - R_x)^2 + P_z^2 - 2P_z S_z + S_z^2. \quad (5.5)$$

Finally, simplifying and solving for P_z gives:

$$P_z = \frac{(D_T + R_z)^2 - S_z^2 - (S_x - R_x)^2}{2(D_T + R_z - S_z)}. \quad (5.6)$$

For a certain time sample on a particular trace in a demigrated CIG in time, Equation (5.6) will allow an amplitude to be relocated from the equivalent trace in the demigrated CIG in depth, from a depth, P_z. If the depth calculated does not equate to an exact sample, a four point Lagrange interpolation routine will be used to provide a more accurate amplitude to be mapped to the trace in time rather than using a simple linear interpolation routine.

Demigration in depth followed by demigration in time should allow the CIG in the prestack depth domain to be transformed to a CMP gather in the prestack time domain. If successful, then differencing between the original CMP traces and the demigrated traces can be performed to obtain CMP traces without the targeted multiple energy. In practice, where a large number of image gathers would require demigration, only the CIGs containing the isolated multiple energy would necessitate demigration in order to reduce run time. However, for the purposes of the following example, it was considered necessary to not only demigrate the CIG containing the isolated multiple energy in the prestack depth domain, but to also demigrate the original CIG. By utilising data that had not been modified (except by the forward transformation of Kirchhoff PSDM) the demigration procedure itself could be gauged for accuracy. The usefulness of this technique will now be demonstrated with an example.

Demigration using the Isolated Multiple Energy From the τ-p Domain

Initially, the multiple energy isolated earlier by using the τ-p transform was demigrated. The results of the former transform are presented in Figure 5.6(a), (b), and (c) for the S101R, S201R, and S212R events respectively. Figures 5.10 and 5.11 present the results of demigrating in depth and time respectively of the original CIGs

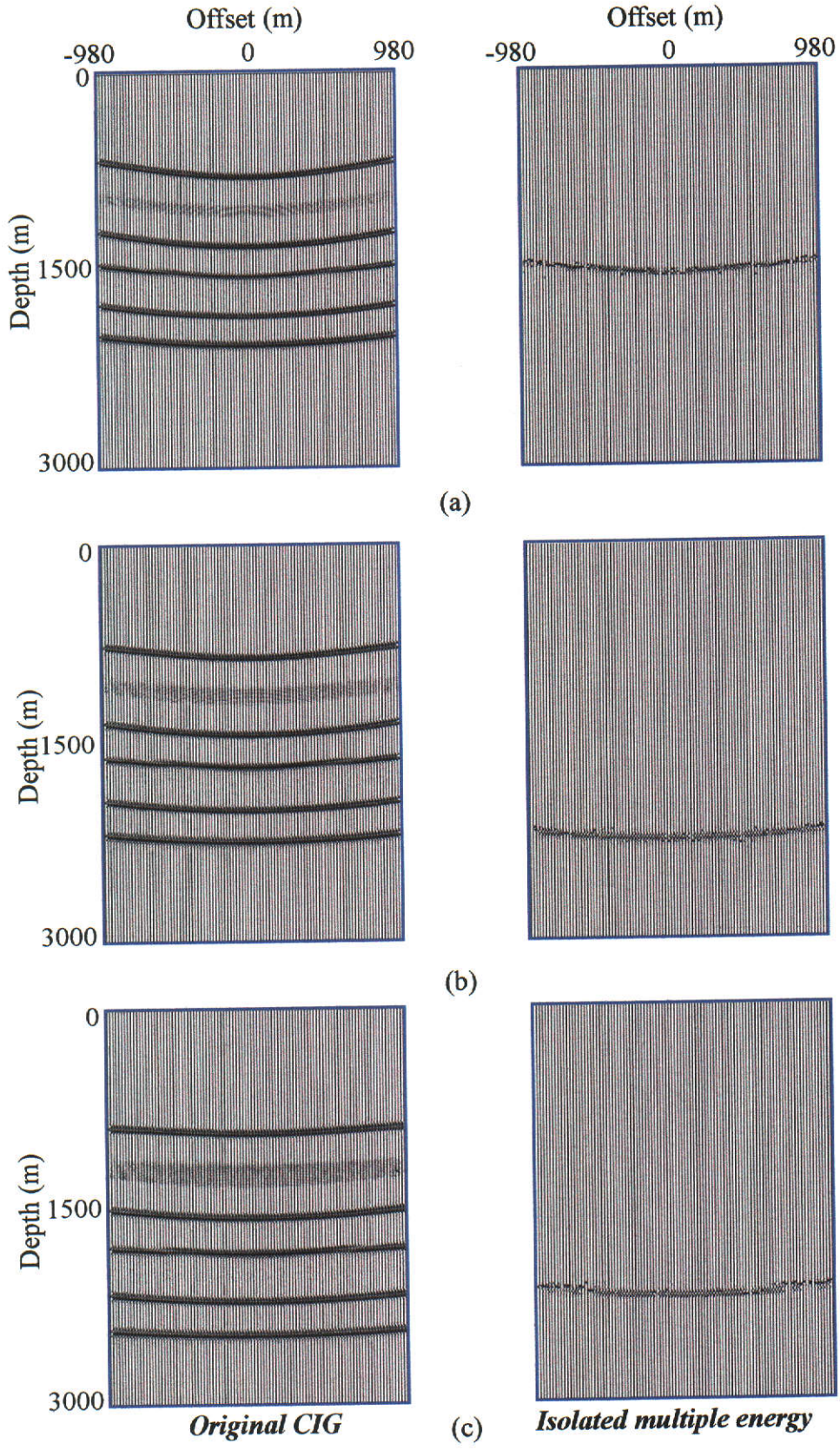

Figure 5.10: Demigration in depth of the original CIGs and the CIG containing the isolated multiple energy from the τ-p transform. PSDM was originally carried out with the average velocity of the (a) S101R, (b) S201R, and (c) S212R events.

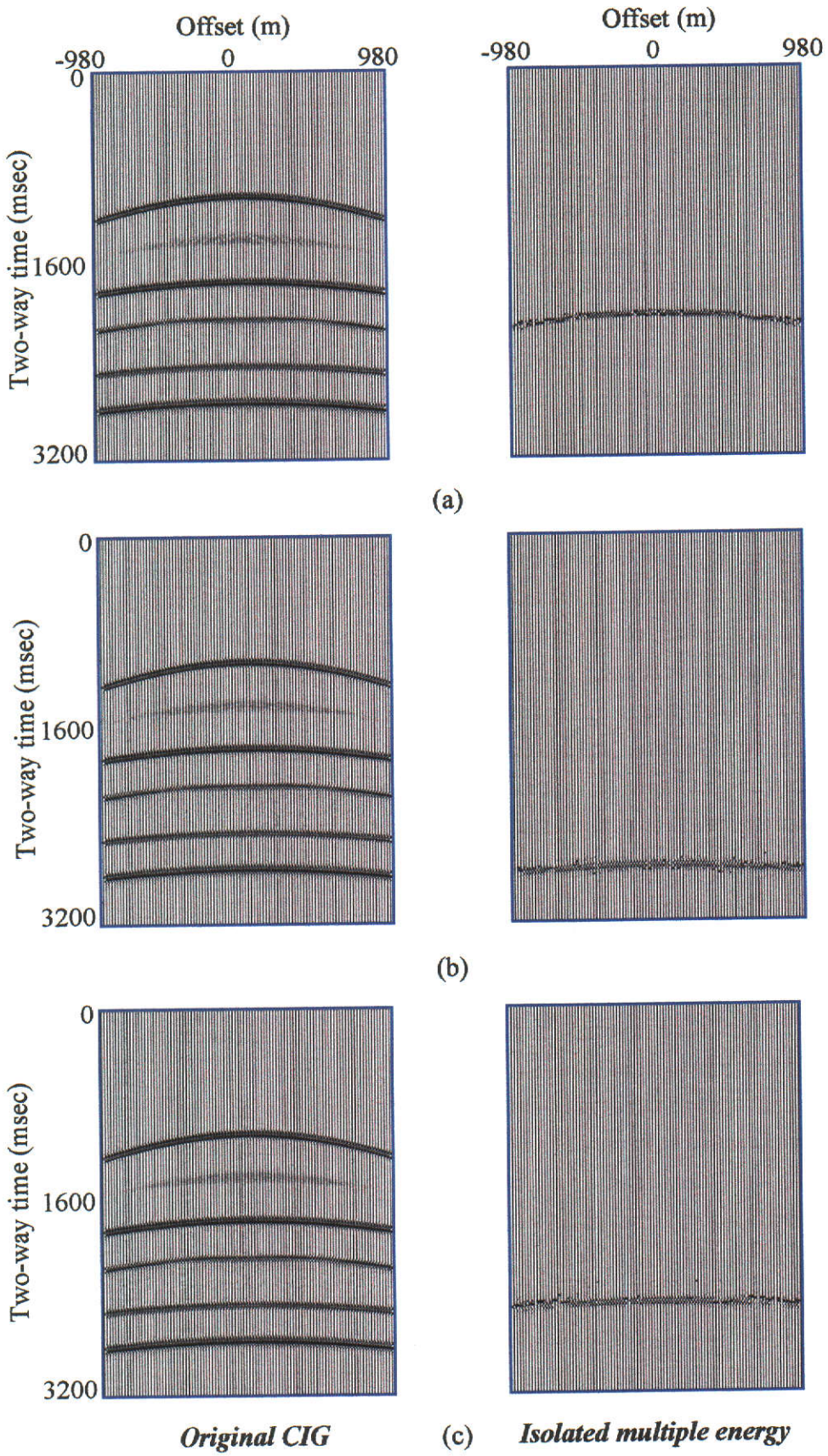

Figure 5.11: Demigration in time of the demigrated sections in depth. PSDM was originally carried out with the average velocity of the (a) S101R, (b) S201R, and (c) S212R events.

and the CIGs containing the isolated multiple energy. The ability of the technique to demigrate the original CIGs was observed to be highly successful with minimal artefacts introduced by the process. For example, consider the zero offset trace taken from an unmigrated CMP gather located at the MVA location. This trace would be equivalent to the zero offset trace obtained from the CMP gather obtained after demigration of either of the three examples presented in Figure 5.11. The trace compared here was taken from the demigrated CIG which was originally formed by Kirchhoff PSDM using a constant velocity of 1500m/s. A comparison of these traces is shown in Figure 5.12 which indicates that the demigration process I developed was quite accurate. Excellent matches were made between all events on the pre-migrated and demigrated traces. However, very slight differences were observed, particularly with the wavelets associated with the larger amplitude S1R and S2R events. These can be attributed to the wavelet shaping factor in Kirchhoff PSDM not being accounted for here. The demigration technique is also very fast with demigration of one CIG containing 99 traces and 600 samples per trace requiring 1.95 secs on a Sun Ultra Enterprise 4000/250 server.

On the other hand, demigration of the reconstructed CIGs containing just the isolated multiples did introduce some noise around the location of the event. Since the multiple energy was localised around the p=0 axis in the τ-p domain, it was assumed that most of the energy was retained when removing all other information from the τ-p gather. Thus, the introduction of noise into the demigration process most likely resulted from the inability of the inverse τ-p transform to successfully reconstruct the original amplitudes of the multiple event accurately. In addition, demigration parameters such as the obliquity and scaling factors were based on data prior to the τ-p transform. Therefore, if the amplitudes of the multiple event within the reconstructed CIG were different (from the amplitudes of the multiple event in the CIG before transformation to the τ-p domain), the demigration process could possibly have amplified these differences.

The final step in the processing sequence was to subtract the processed CMP gather (i.e. demigrated CIG containing the isolated multiple energy) from an original CMP

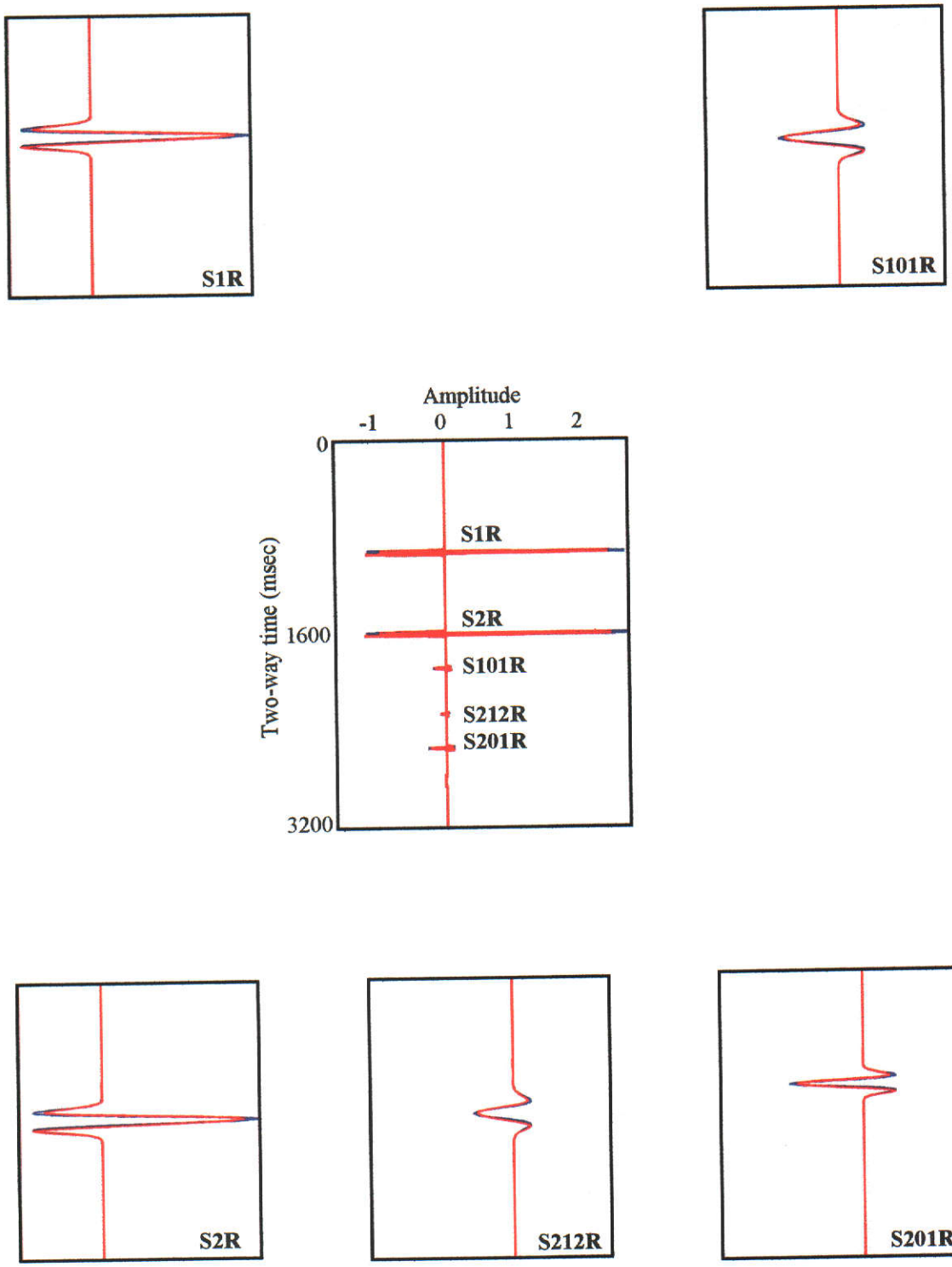

Figure 5.12: A comparison of pre-migrated and demigrated zero offset traces. A comparison of each trace is shown in the central plot while a zoom of each event is shown in the surrounds. The pre-migrated trace is shown in blue while the demigrated trace is shown in red. Small differences in wavelet shape were observed with the larger amplitude events.

gather. Figure 5.13 shows the results for this step after using a CMP gather with zero offset located at the MVA location, as the comparison gather. The resultant gathers show that for each multiple targeted, a considerable amount of the multiple energy has been removed. This is with the exception of multiple energy located at far offsets. It is at these locations that the multiple energy still exists and this phenomenon could be attributed to two causes:

(a) The inverse τ-p transform not returning exact amplitudes; or

(b) The existence of slight curvature at the far offsets of the event in the CIG. This means that some energy may have been located outside the pass zone in the τ-p domain.

The reduced effectiveness at the far offsets is most likely a result of contributions from both possible causes. The fact that the multiple energy is removed at the near offsets as opposed to the far offsets is interesting. Most multiple attenuation techniques based on a degree of velocity discrimination have trouble at near offsets due to similar moveouts existing between primary and multiple events at these locations. However, it is observed after using my technique that beneficial multiple attenuation does occur at the near offsets. However, it must be kept in mind that no interfering events were present therefore, this is an issue that needs to be examined. If desired, the traces in the processed CMP gather could be sorted into the respective shot gathers from whence they came to replace the original traces. The fact that the far offset traces in the CMP gather obtained here still exhibit multiple energy, means that there is no point sorting them back into their respective shot gathers. However, the near offset traces show little multiple energy and can in fact replace the original traces within the respective shot gathers. As an example, consider the zero offset trace taken from a shot gather located at the MVA location. This trace would be equivalent to the zero offset trace taken from the processed CMP gather. Figure 5.14 presents comparisons between these traces before and after the S212R and S201R events were targeted. A zoom has been employed to emphasise the attenuation of each multiple. Although the amplitude of the S212R event is relatively small, it has still undergone significant attenuation on this trace. On the other hand, the S201R event is a much more problematic multiple and can be observed to have been attenuated quite well. This indicates that the amplitude of the multiple doesn't

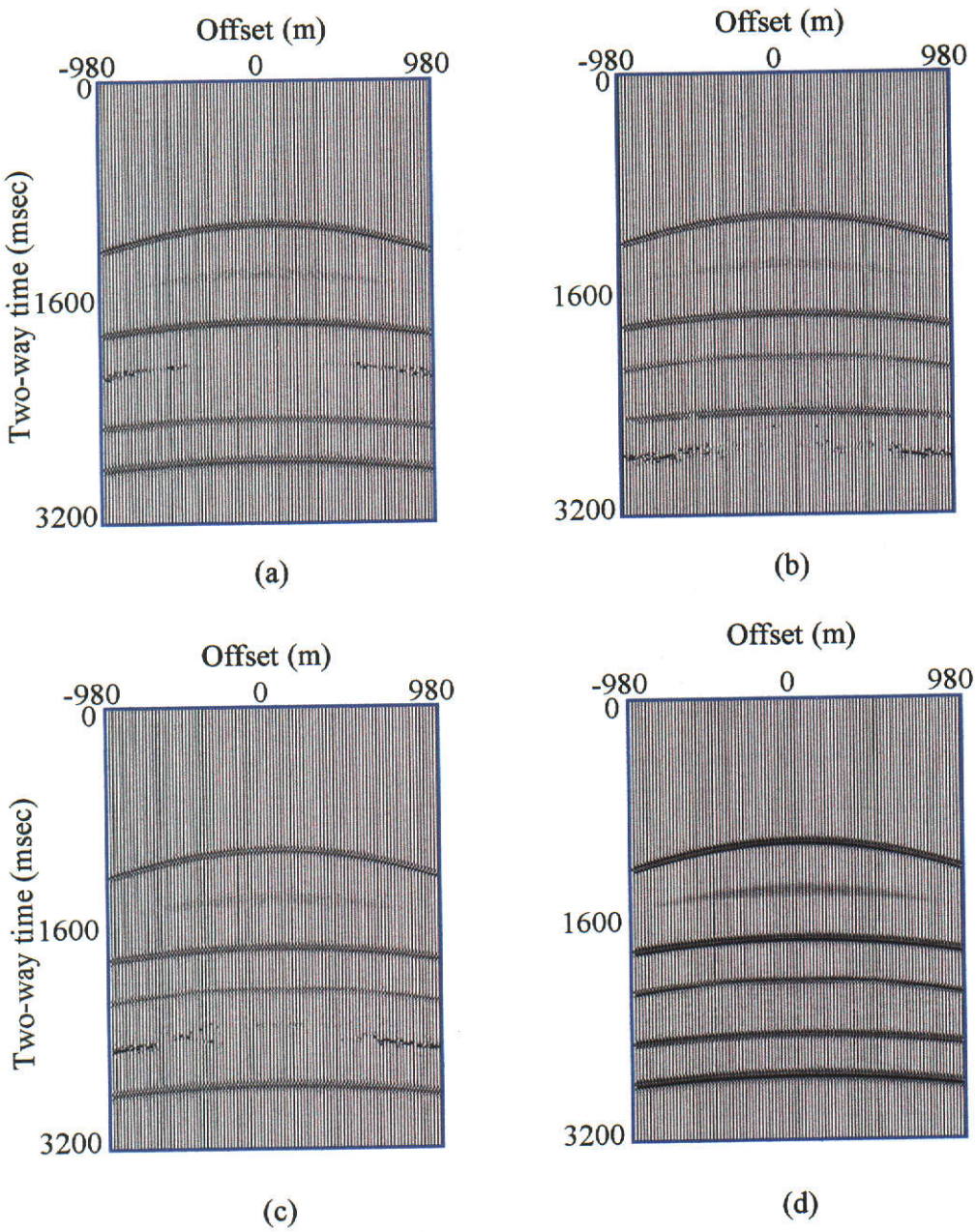

Figure 5.13: Resultant CMP gathers after subtracting the demigrated isolated multiple energy from a CMP gather located at the MVA location. PSDM occurred with the average velocity of the (a) S101R, (b) S201R, and (c) S212R events. The original CMP gather is shown in (d). The differenced gathers show that considerable multiple energy has been removed.

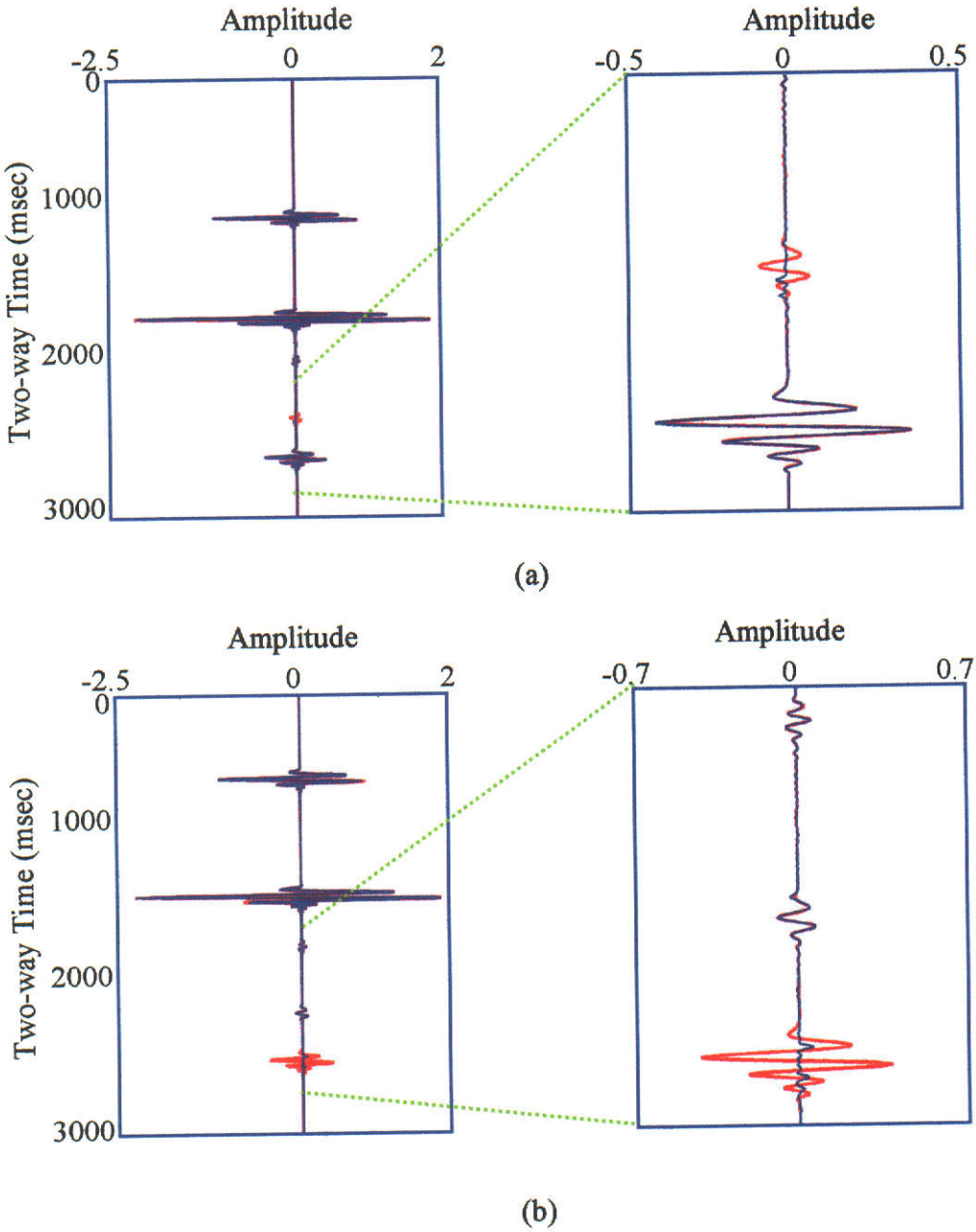

Figure 5.14: A comparison of zero offset traces from an original CMP gather located at the MVA location and the processed CMP gathers. Migration was carried out with the average velocity of the (a) S212R, and the (b) S201R events. The trace from the original CMP gather is shown in red while the trace from the processed CMP gather is shown in blue. Successful multiple attenuation was achieved in each instance.

impose limits on the technique since the majority of the energy will be localised around the p=0 axis in the τ-p domain.

The process for multiple attenuation in the prestack depth domain just described was implemented successfully using data in which the primaries could be discriminated from multiples. However, the method was found to be highly dependent on the ability of the τ-p transform to isolate the multiple energy. This processing sequence will now be applied to data in which events interfere in the prestack time domain.

5.3 MULTIPLE ATTENUATION WHERE EVENTS INTERFERE

Previously, during the development of the multiple attenuation processing sequence, I demonstrated that multiples could be attenuated at near offsets. However, this occurred when events were able to be discriminated from each other. The following example will investigate whether the technique is able to attenuate a the S201R multiple when it is interfered with by another event at near offsets. The synthetic dataset generated for the following example consisted of 200 shot gathers located at 20m intervals. A fixed receiver spread was used with receivers also located at 20m intervals. A source wavelet with a frequency of 40Hz was used to generate the synthetic dataset. MVA was performed at a surface location of 2000m in the model. PSDM with a constant velocity (equal to the first layer velocity) was performed on 199 synthetic shot gathers surrounding this location in order to form a CIG to be used in the multiple attenuation processing sequence.

Figure 5.15(a) presents the velocity model used for the synthetic data generation while a representative shot gather that was created is shown in Figure 5.15(b). The interval velocities and thicknesses for the first, second, third, and fourth layers were 1500m/s and 600m, 3000m/s and 900m, 4500m/s and 1800m, and 7000m/s respectively. Events that were modelled included the S1R, S101R, S2R, S201R, and the S3R events. The S3R event is obscured at near offsets by the S201R event. The average velocity of each event in the shot gather was determined by using MVA which was described previously in Section 4.2. Essentially, Kirchhoff PSDM was carried out with the velocity of the first layer, a CIG was formed, and γ-semblance

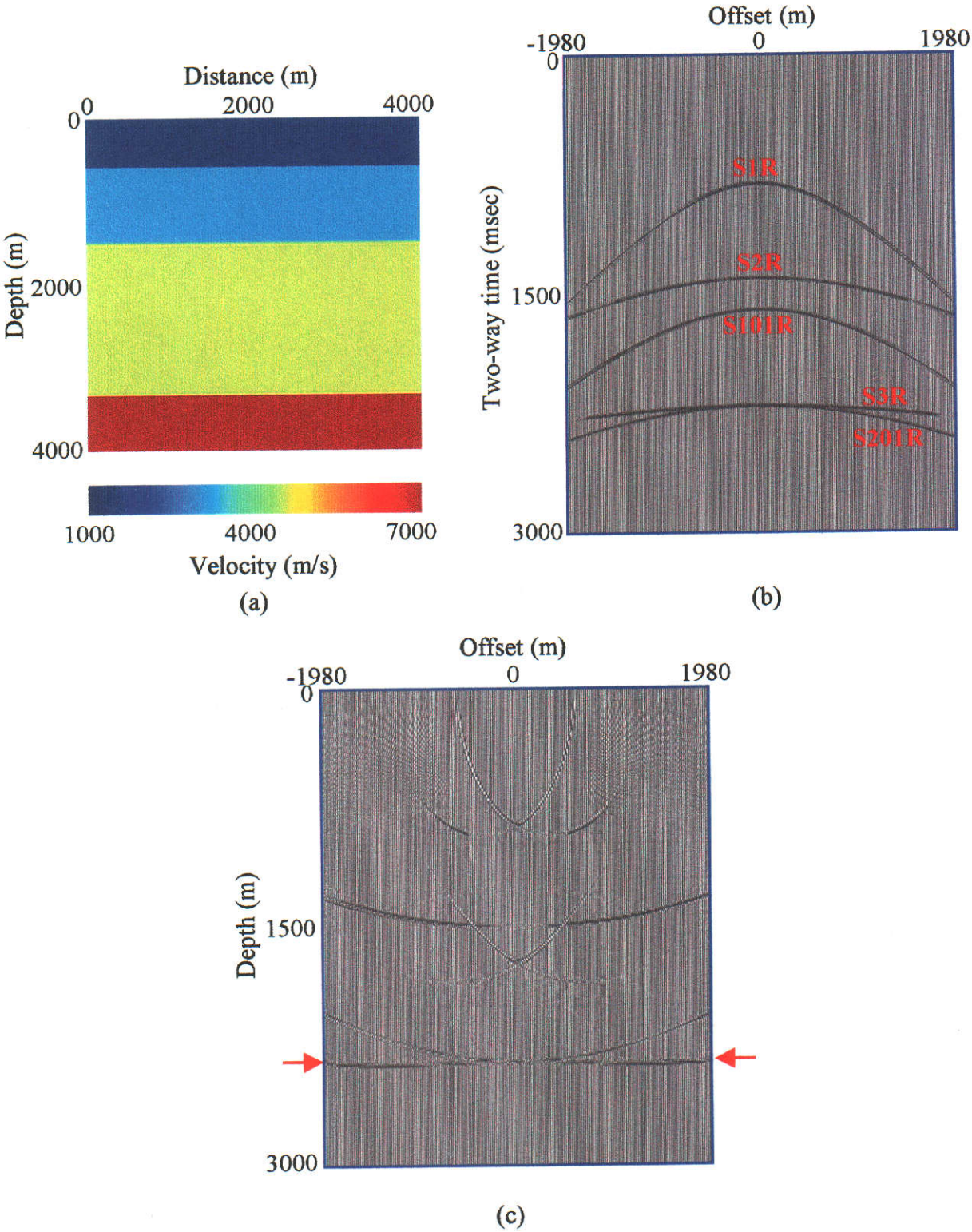

Figure 5.15: Velocity model used to generate synthetic data containing events that interfere. (a) Velocity model, (b) a representative shot record, and (c) a CIG formed after migrating with the average velocity of the S201R event (1910m/s). The interval velocities and thicknesses for the first, second, third, and fourth layers were 1500m/s and 600m, 3000m/s and 900m, 4500m/s and 1800m, and 7000m/s respectively. The flattened S201R event is identified in the CIG.

analysis was performed using this CIG. Since the S201R multiple was being targeted for attenuation, it is this average velocity that was required. This was found to be 1910m/s.

The next step involved migrating a suite of shots surrounding the MVA location with the average velocity of the targeted multiple. The CIG that was formed is presented in Figure 5.15(c). Having migrated with the average velocity of the S201R event, the S1R and S101R events curve downwards since their average velocities are less than the migration velocity. On the other hand, the S2R and S3R events curve upwards since the average velocities of these events are greater than the migration velocity.

Significant "spiders legs" are present in the CIG associated with the larger amplitude events. A point to note about the overmigrated events (S1R and S101R) is that they could be interpreted as upward curving events. Bancroft (2000) explains this phenomenon as follows. When the migration velocity is too fast (as is observed with the S1R and S101R events) the moveout component of the NMO (normal moveout) equation becomes too large. That is:

$$T_x^2 - T_0^2 << \frac{4x^2}{v^2}, \tag{5.7}$$

where T_x is the two-way time at an offset, 'x'; T_0 is the two-way time at zero-offset; and 'v' is the migration velocity. Hence, one may be led to believe that the events will be overcorrected and curve downwards. However, the opposite is also true. In these situations, the migration summation operator is narrower than the diffraction. Therefore, when the summation operator gathers energy, it can only collect tangential energy from the diffraction. This will only occur when the summation operator is below the diffraction. The result is that the event appears undermigrated. In any case, an important observation is made around the location of the S201R and S3R events in the CIG. These events actually exhibit more discrimination in the CIG than in the shot gather (Figure 5.15(b)). An attempt was made to exploit this fact by isolating the S201R event in the τ-p domain. This is examined next.

Figure 5.16(a) presents the τ-p gather formed by performing a τ-p transformation on

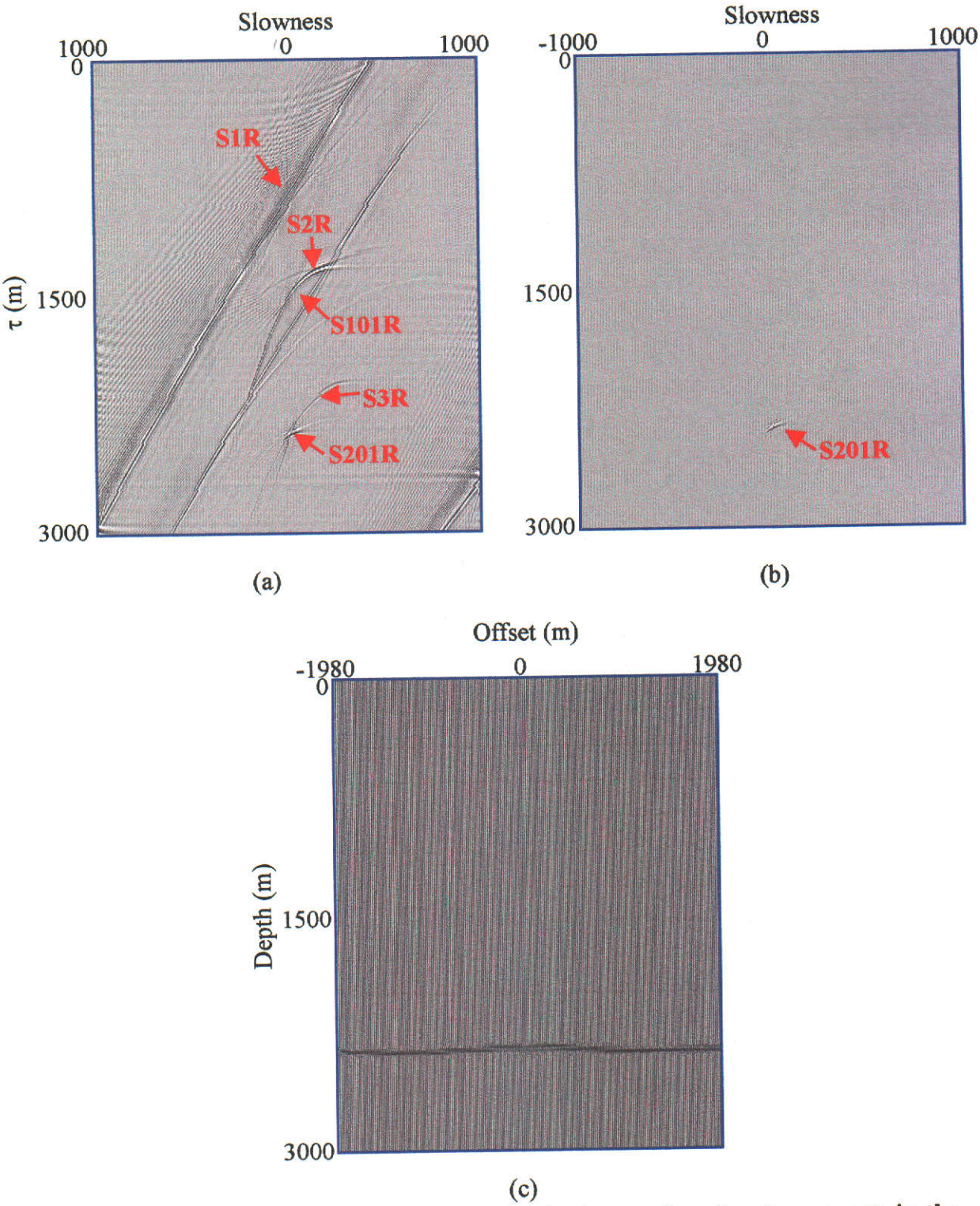

Figure 5.16: Isolation of the S201R event in the τ-p domain where events in the CIG interfere. (a) τ-p gather illustrating all events evident in the CIG shown previously (Figure 5.16(c)), (b) the isolated S201R event in the τ-p domain, and (c) the isolated S201R event in a CIG after performing an inverse τ-p transform.

the CIG presented in Figure 5.15(c). With regard to the region that corresponds to the location of the S201R and S3R events, these events both cross the p=0 axis at the same intercept. However, depending on the difference between their respective average velocity and the migration velocity, and their relative amplitude, these events smear over the τ-p domain differently. The S201R event is localised since the migration velocity is equal to the average velocity for this event. The S3R event plots over a larger region since a difference exists between the average velocity of the S3R event (3000m/s) and the migration velocity (1910m/s). Having determined that the targeted multiple plots locally around the p=0 vent, it was then isolated in the τ-p domain by applying a pass zone around just this event. The result is shown in Figure 5.16(b). This filtered τ-p gather was then subject to an inverse τ-p transformation to produce the CIG containing just the S201R energy. Top and bottom mutes were applied around the isolated event to remove undesirable noise introduced by the inverse τ-p transformation. The result is presented in Figure 5.16(c). A visual comparison with the original CIG reveals that most of the S201R energy has been isolated. However, it will not be known how successful this isolation has been until the event has been transformed back to the prestack time domain and compared with an original CMP gather. This was performed next by using the process of demigration.

Figures 5.17(a) and (b) present the CIG obtained after demigration in depth and time respectively. These results indicate that the demigration process is positioning the S201R events in the correct position. However, the amplitudes at each offset do appear to be distorted. The result of subtracting the demigrated CIG in time from an original CMP gather is shown in Figure 5.17(c). A comparison can be made with an original CMP gather which is presented in Figure 5.17(d). The result indicates that minimal S201R energy has been attenuated. This is due to the distorted amplitudes in the filtered gather not differencing accurately with the original event. The demigration technique I developed was proven earlier (Figure 5.12) to be very accurate with only slight difference in wave shape evident before and after the process. Therefore, the results obtained in this example can only be attributed to the inverse τ-p transform being unable to reconstruct accurate amplitudes. This affected

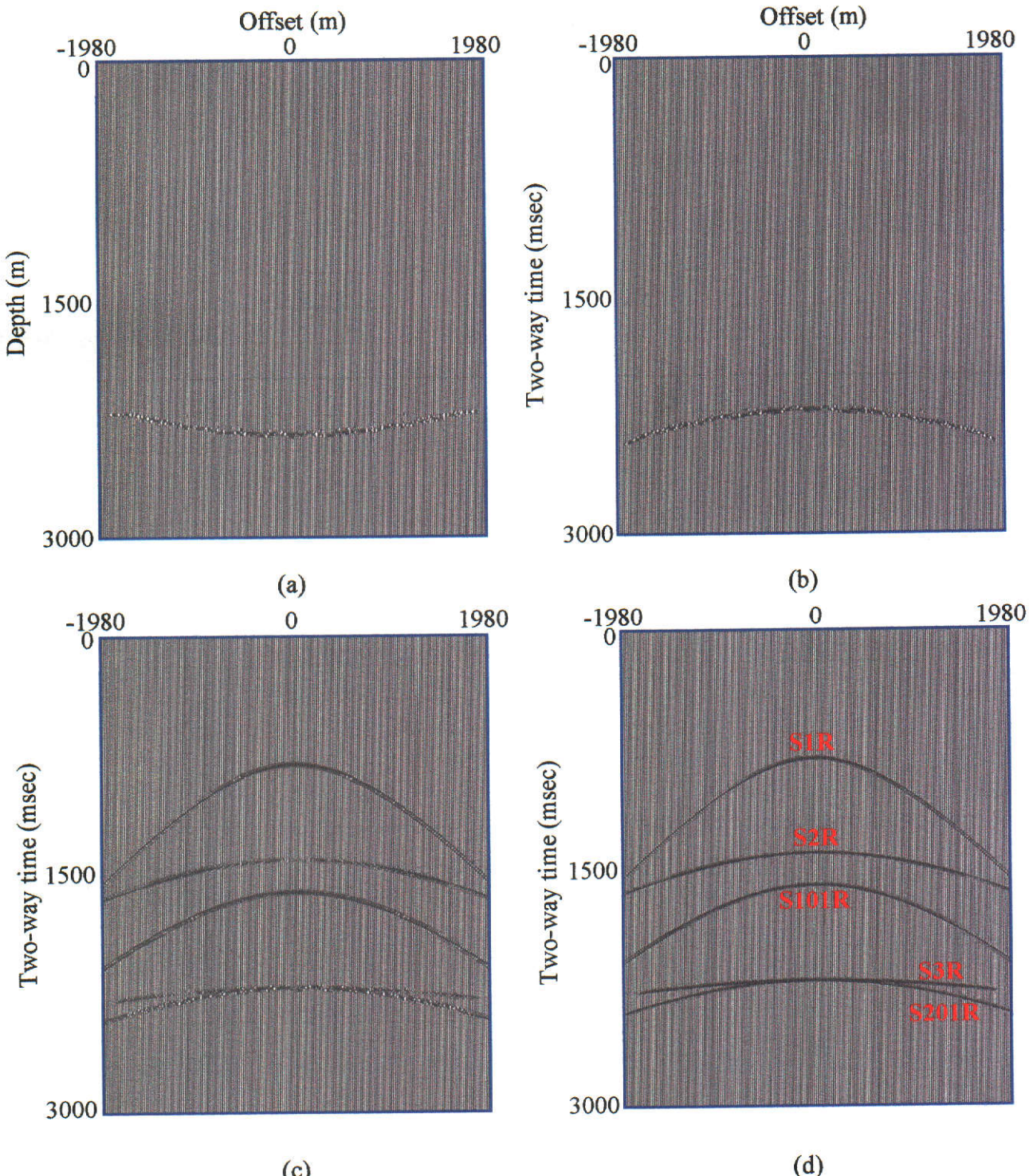

Figure 5.17: Demigration of the filtered CIG in the case where the problematic multiple interferes with other events. (a) Demigration of the filtered CIG in depth; (b) demigration in time; (c) The result of differencing with the original CMP gather; and (d) the original CMP gather. The S201R event is still quite prominent due to the inability of the inverse τ-p transform to reconstruct accurate amplitudes.

the result at all offsets since any discrepancy between the amplitudes before and after τ-p filtering will have been exaggerated in the demigration process.

Multiple attenuation processes that predict or isolate multiple energy, then remove it from the original record, find difficulty in wavelet matching. Where waveforms have been shifted slightly in time, or whose phase content has been modified, there will be a degree of mismatch with the original data. This will become more apparent after differencing. The solution to this general problem in multiple attenuation methods will probably lie in the use of *matched filters*. Through this process, differencing after wavelet adjustment should be more effective. The issue of matched filtering is wider than just being applicable in this research. Hence, for practical reasons of time, this issue will not be pursued further in this research.

5.4 SUMMARY

The synthetic tests conducted in this chapter enable the following conclusions to be drawn regarding the processing flow presented for multiple attenuation in the prestack depth domain:

(a) The success at which the multiple attenuation occurred was highly dependent on the method used to isolate the multiple in the prestack depth domain. The τ-p transform was not an ideal method to do this since the inverse transform couldn't recover exact amplitudes. The demigration process exaggerated these amplitude errors. If amplitude preservation were possible then the multiple attenuation flow might have been more successful.

(b) The results have shown that an event migrated with its average velocity will flatten it in a CIG and localise it around the p=0 axis in the τ-p domain. This overcomes the limitation of the method of Duquet and Marfurt (1999) that relies on an estimate of the true interval velocity model. In addition, the necessity to smooth the velocity model was removed since a constant velocity model was utilised.

(c) The technique is very fast with the majority of the run time being devoted to computing the traveltime maps required for Kirchhoff PSDM. My demigration algorithm gives results in a much lower run time than the conjugate gradient

method of Duquet and Marfurt (1999). Their method normally required 3-5 iterations to converge on the best solution and it proved to be 6-10 times more expensive than conventional Kirchhoff PSDM.

(d) As with all velocity based multiple attenuation techniques, event discrimination is a necessary requirement. If a multiple has a similar average velocity to a primary event, then these events will both be reasonably flat in a CIG after PSDM with the average velocity of the multiple. Both events will then be localised around the p=0 axis in the τ-p domain at very similar depths. This makes isolation of the multiple very difficult. Hence, this is a limitation of the method.

(e) The proposed processing sequence may have more success if the *hyperbolic* τ-p transform is implemented. Using this method (in conjunction with adequate tapering of amplitudes) may focus events to smaller energy locations thus allowing for better discrimination. This is left for future research.

CHAPTER 6

CONCLUSIONS AND RECOMMENDATIONS

This goal of this thesis was to develop a suite of methods for improving the quality of the depth section obtained with Kirchhoff prestack depth imaging. I have achieved this by developing three methods that will improve each step of the depth imaging process.

During the development of the techniques, I have provided alternative solutions to well-known problems that exist in Kirchhoff prestack depth imaging. These problems include: (a) the inefficiency and accuracy with which traveltimes are calculated; (b) the inaccuracy of the interval velocity model; and (c) the presence of multiple reflections which are detrimental to interpretation of the resultant depth section. I have provided solutions to these problems by developing:

- Applications for the generalised exploding reflector method (GERM). This has been introduced with a dual purpose: (a) to simulate seismic multiples, while honouring true wave propagation direction; and (b) allowing the grid cell size to be changed in the calculation of one traveltime map.
- A new interval velocity model building technique. This treats multiple energy as signal and uses the information contained within these events to produce more accurate interval velocities and thicknesses than can be obtained using primary events alone.
- A new processing sequence for the attenuation of multiple events. This occurs after utilising the multiple events in the previous development and it allows attenuation in the prestack depth domain.

By combining all three new methods, improved accuracy in the depth image can be obtained. Each method has been tested on various numerical models with the GERM also being tested on the well-known Marmousi velocity model and dataset in addition to a velocity model and dataset acquired from the North West Shelf of Western Australia. The suite of techniques that I have developed can be applied

separately or combined in a whole new processing sequence. As a result I have provided alternative solutions for the problems associated with Kirchhoff depth imaging that were set out in the introduction:

- Multiple events can be identified by modelling using a finite-difference traveltime computation technique that incorporates the GERM.
- Computer run times (and hence costs) have been reduced without any significant reduction in accuracy. This has been made possible by development of the GERM and implementation in a finite-difference traveltime solver.
- The accuracy of the velocity model (which is of upmost importance to the success of Kirchhoff depth imaging) has been improved by treating multiple events as signal and utilising the information carried by these events. It has been found that all multiple types can be used for this purpose. It was also found that as the order of the multiple increased, the accuracy of the specific interval velocity being determined also increased.
- A new processing flow for attenuating seismic multiples (which often obscure the primary reflection events representative of the subsurface geology) has been developed and tested. The isolation of specific multiple energy is made easier in the prestack depth domain since non-hyperbolic moveout is not an issue as is the case when performing velocity analysis in the prestack time domain. My method also requires less a priori information than other methods with only the average velocity of the multiple being targeted needing to be known. However, it is important to utilise an accurate forward and inverse transform pair in the prestack depth domain to exploit the property of the multiple appearing flat in a CIG. The inverse τ-p transform did experience some difficulty in reconstructing accurate amplitudes after the targeted multiple had been isolated.

These new techniques for Kirchhoff depth imaging are capable of producing a depth section with improved accuracy, and with increased efficiency, that will aid in the process of seismic interpretation. However, further work is suggested such as the extension to testing using appropriate field data and to implementing a wavelet matching technique in the multiple attenuation technique described in Chapter 5. These recommendations will require substantial effort and are left for future projects.

REFERENCES

Abma, R., Sun, J., and Bernitsas, N., 1999, Antialiasing methods in Kirchhoff: Geophysics, 64, 1783-1792.

Alford, R.M., Kelly, K.R. and Boore, D.M., 1974, Accuracy of finite-difference modeling of the acoustic wave equation: Geophysics, 39, 834-842.

Al-Yahya, K., 1986, Velocity analysis by prestack migration: Stanford Exploration Project Report No. 48, Stanford University.

Al-Yahya, K., 1989, Velocity analysis by iterative profile migration: Geophysics, 54, 718-729.

Audebert, F., Nichols, D., Rekdal, T., Biondi, B., Lumley, D.E., and Urdaneta, H., 1997, Imaging complex geologic structure with single-arrival Kirchhoff prestack depth migration: Geophysics, 62, 1533-1543.

Australian Petroleum Production and Exploration Association Limited, 2001, Industry Facts and Figures [Online], Available: http://www.appea.com.au/statistics/index.html [2001, Nov. 10].

Bancroft, J. C., 1997, A pracical understanding of pre- and poststack migrations (Vol 1&2), *in* Young, R. A., (Ed.), A practical understanding of pre- and poststack migrations: Course Notes Series, No. 7, Soc. of Expl. Geophys.

Bancroft, J.C., 2000, *Migration Velocity Analysis*, E-mail to author (bancroft@geo.ucalgary.ca), [2000, Dec. 8th].

Baysal, E., Kosloff, D.D., and Sherwood, J.W.C., 1983, Reverse time migration: Geophysics, 48, 1514- 1524.

Berkhout, A.J., 1985, Seismic migration - Imaging of acoustic energy by wavefield extrapolation, Theoretical aspects: Elsevier.

Berkhout, A.J., 1996, Seismic processing between two focusing steps: 66th Ann. Internat. Mtg Soc. of Expl. Geophys., 403-406.

Berkhout, A.J., 1997a, Pushing the limits of seismic imaging, part I: Prestack migration in terms of double dynamic focusing: Geophysics, 62, 937-953.

Berkhout, A.J., 1997b, Pushing the limits of seismic imaging, part II: Integration of prestack migration, velocity, estimation, and AVO analysis: Geophysics, 62, 954-969.

Berkhout, A.J. and Van Wulfften Palthe, D.W., 1979, Migration in terms of spatial deconvolution: Geophysical Prospecting, 27, 261-291.

Berkhout, A.J. and Rietveld, W.E.A., 1994, Determination of macro models for prestack migration: Part 1 - estimation of macro velocities: 64th Ann. Internat. Mtg Soc. of Expl. Geophys. 1330-1333.

Berryhill, J., 1979, Wave-equation datuming: Geophysics, 44, 1329-1344.

Bevc, D., 1997, Imaging complex structures with semi-recursive Kirchhoff migration: Geophysics, 62, 577- 588.

Beylkin, G., 1985, Imaging of discontinuities in the inverse scattering problem by inversion of a causal generalised Radon transform: J. Math. Phys., 26, 99-108.

Bishop, T.N., Bube, K.P., Cutler, R.T., Langan, R.T., Love, P.L., Resnick, I.R., Shuey, R.T., Spindler, D.A., and Wyld, H.W., 1985, Tomographic determination of velocity and depth in laterally varying media: Geophysics, 50, 903-923.

Bleistein, N., 1987, On the imaging of reflectors in the earth: Geophysics, 52, 931-942.

Bleistein, N., Cohen, J.K., and Hagin, F.G., 1985, Computational and asymptotic aspects of velocity inversion: Geophysics, 50, 1253-1265.

Bleistein, N., Cohen, J.K., and Hagin, F.G., 1987, Two-and-one-half dimensional Born inversion with an arbitrary reference: Geophysics, 52, 26-36.

Boore, D.M., 1972, Finite-difference methods for seismic wave propagation in heterogeneous materials; *In* Alder, B., Fernbach, S. and Rotenburg, M. (Eds.), Methods in computational physics, Volume 2: Academic Press, New York, 21-22.

Cao, S. and Greenhalgh, S., 1994, Finite-difference solution of the Eikonal equation using an efficient, first-arrival, wavefront tracking scheme: Geophysics, 59, 632-643.

Cerveny, V., 1972, Seismic rays and ray intensities in inhomogeneous anisotropic media: Geophys. J., 28, 1972, 1-13.

Chang, W.F., and McMechan, G.A., 1986, Reverse-time migration of offset vertical seismic profiling data using the excitation-time imaging condition: Geophysics, 51, 67-84.

Claerbout, J.F., 1971, Toward a unified theory of reflector mapping: Geophysics, 36, 467-481.

Claerbout, J.F., 1976, Fundamentals of geophysical data processing: McGraw-Hill Inc.

Claerbout, J.F., 1985, Imaging the Earth's interior: Blackwell Scientific Publications.

Clayton, R.W., 1978, Common midpoint migration: Stanford Expl. Proj., Rep. No. 14, Stanford University.

Clayton, R.W. and Stolt, R.H., 1981, A Born WKBJ inversion method for acoustic reflection data: Geophysics, 46, 1559-1568.

Cohen, J.K., Hagin, F.G. and Bleistein, N., 1986, Three-dimensional Born inversion with an arbitrary reference velocity: Geophysics, 51, 1552-1558.

da Costa, C.A., Raz, S. and Kosloff, D., 1989, Gaussian beam migration: 59th Ann. Internat. Mtg Soc. of Expl. Geophys. 1169.

Department of Minerals and Energy , 2001, Statistics Digest 2000 [Online], Available: http://www.dme.wa.gov.au/statistics/resourcefocus2000 [2001, Apr. 23].

De Pledge, D.R., 1993, Deterministic Multiple Attenuation: M.Sc. thesis, Curtin University of Technology.

Deregowski, S.M., 1990, Common-offset migrations and velocity analysis: First Break, 8, 225-234.

Dix, C.H., 1955, Seismic velocities from surface measurements: Geophysics, 20, 68-86.

Doherty, S.M. and Claerbout, J.F., 1976, Structure independent velocity estimation: Geophysics, 41, 850-881.

Duquet, B., Marfurt, K.J., and Dellinger, J. 1998, Efficient estimates of subsurface illumination for Kirchhoff depth migration: 67th Ann. Internat. Mtg Soc. of Expl. Geophys. 1116-1119.

Duquet, B. and Marfurt, K.J., 1999, Filtering coherent noise during prestack depth migration: Geophysics, 64, 1054-1066.

European Association of Geoscientists and Engineers, 1989, Practical Aspects of Seismic Inversion: European Association of Geoscientists and Engineers.

Etgen, J., 1990, Residual prestack migration and interval velocity estimation: Stanford Exploration Project Report No. 68, Stanford University.

Fagin, S., 1998, Model-Based Depth Imaging: Course Notes Series, No. 10, Young, R.A. (Ed.), Society of Exploration Geophysicists.

Foster, D.J. and Mosher, C.C., 1994, Suppression of multiple reflectors using the Radon transform: Geophysics, 56, 386-395.

Fowler, P.J., 1984, Velocity independent imaging of seismic reflectors: 54th Ann. Internat. Mtg Soc. of Expl. Geophys., Session: S1.8.

Fowler, P.J., 1988, Seismic velocity estimation using prestack time migration: Ph.D thesis, Stanford University.

Gardner, G.H.F., French, W.S. and Matzuk, T., 1974, Elements of migration and velocity analysis: Geophysics, 39, 811-825.

Gazdag, J., 1978, Wave equation migration with the phase-shift method: Geophysics, 43, 1342-1351.

Gerritsma, P. H. A., 1977, Time-to-depth conversion in the presence of structure: Geophysics, 42, 760-772.

Golub, G.H. and Ortega, J. M., 1992, Scientific computing and differential equations: Academic press, Inc. Harcourt Brace Jovanovich, Publishers, Boston.

Gray, S.H., 1992, Frequency-selective design of the Kirchhoff migration operator: Geophys. Prosp., 40, 565- 571.

Gray, S. H., 1999, Speed and accuracy of seismic migration methods, Depth imaging of foothills seismic data: Soc. of Expl. Geophys.

Gray, S.H., 2001, Seismic Imaging: Geophysics, 66, 15-17.

Gray, S.H. and May, W.P., 1994, Kirchhoff migration using Eikonal equation traveltimes: Geophysics, 59, 810-817.

Gray, S.H., Etgen, J., Dellinger, J. and Whitmore, D., 2001, Seismic migration problems and solutions: Geophysics, 66, 1622-1640.

Hale, D., 1991, Stable explicit depth extrapolation of seismic wavefields: Geophysics, 56, 1770-1777.

Hampson, D., 1986, Inverse velocity stacking for multiple elimination: J. Can. Soc. Expl. Geophys., 22, 44-55.

Hartley, B.M., 2002a, A 3-D seismic modelling system for simple Earth models using computer algebra: Accepted for the 64th Mtg. Eur. Assn. Geosci. Eng.

Hartley, B.M., 2002b, Associate Professor of Geophysics at Curtin University of Technology, Conversation with the author, 13th Jan.

Hill, N.R., 1990, Gaussian beam migration: Geophysics, 55, 1416-1428.

Hill, N.R., 2001, Prestack Gaussian-beam depth migration: Geophysics, 66, 1240-1250.

Hill, S., Dragoset, B. and Weglein, A., 1999, An introduction to this special section - The new world of multiple attenuation: The Leading Edge, 18, 38.

Holberg, O., 1988, Towards optimum one-way wave propagation: Geophys. Prosp., 36, 99-114.

Jeannot, J.P., Faye, J.P. and Dennelle, E., 1986, Prestack migration velocities from depth-focusing analysis: 56th Ann. Internat. Mtg Soc. of Expl. Geophys., 438-440.

Kabir, M.M.N. and Verschuur, D.J., 1996, Macro model estimation using the common focus point technology: 58th Mtg. Eur. Assn. Geosci. Eng., Session:P139.

Kabir, M.M.N. and Verschuur, D.J., 2000, A constrained parametric inversion for velocity analysis based on CFP technology: Geophysics, 65, 1210-1222.

Kelly, K.R., Ward, R.W., Treitel, S. and Alford, R.M., 1976, Synthetic Seismograms - A Finite-Difference Approach: Geophysics, 41, 2-27.

Kim, Y.C. and Gonzalez, R., 1991, Migration velocity analysis with the Kirchhoff integral: Geophysics, 56, 365-370.

Kim, Y.C., Samuelsen, C.M., and Hauge, T.A., 1996, Efficient velocity model building for prestack depth migration: The Leading Edge, 15, 751-753

Kitchenside, P., Albertin, U., Chang, W., Kostov, C., Kleitz, A., Moldoveanu, N., Sugavanum, A., Yingst, D., 2001, Comparing finite-difference and Kirchhoff pre-stack depth migration: 71st Ann. Internat. Mtg Soc. of Expl. Geophys., 917-920.

Kosloff, D. and Baysal, E., 1983, Migration with the full acoustic wave equation: Geophysics 48, 677-687.

Kumar, P. and Foufoula-Georgiou, E., 1997, Wavelet analysis for geophysical applications: Reviews of Geophysics, 35, 385-412.

Lafond, C.F. and Levander, A.R., 1993, Migration moveout analysis and depth focusing: Geophysics, 58, 91-100.

Lambert, G., 1996, A Method for the Numerical Simulation of Seismic Wave Propagation and Reflection: B.Sc. (Hons) thesis, Curtin University of Technology.

Landa, E., Thore, P., Sorin, V. and Koren, Z., 1991, Interpretation of velocity estimates from coherency inversion: Geophysics, 56, 1377-1383.

Landmark Graphics Corporation, 1999, Promax© User Manual - 1998.1 Release Notes: Landmark Graphics Corporation.

Langan, R.T., Lerche, I., and Cutler, R.T., 1985, Tracing of rays through heterogeneous media – An accurate and efficient procedure: Geophysics, 50, 1456-1465.

Lazaratos, S. K. and Harris, J. M., 1990, Radon transform/Gaussian beam migration: 60th Ann. Internat. Mtg Soc. of Expl. Geophys. 1314-1317.

Leblanc, G.E. and Morris, W.A., 2001, Denoising of aeromagnetic data via the wavelet transform: Geophysics, 66, 1793-1804.

Lee, W. and Zhang, L., 1992, Residual shot profile migration: Geophysics, 57, 815-822.

Levin, S.A., 1984, Principles of reverse-time migration: Geophysics, 49, 581-583.

Levin, F.K. and Shah, P.M., 1977, Peg-leg multiples and dipping reflectors: Geophysics, 42, 957-981.

Lines, L., Rahzmian, F. and Kelly, K., 1993, A model-based comparison of modern velocity analysis methods: The Leading Edge, 12, 750-754.

Liu, Z., 1997, An analytical approach to migration velocity analysis: Geophysics, 62, 1238-1249.

Liu, Z. and Bleistein, N., 1992, Velocity analysis by residual moveout: 62nd Ann. Internat. Mtg Soc. of Expl. Geophys., 888-891.

Liu, Z. and Bleistein, N., 1995, Migration velocity analysis: Theory and an iterative algorithm: Geophysics, 60, 142-153.

Loewenthal, D., Lu, L., Roberson, R. and Sherwood, J., 1976, The Wave Equation Applied to Migration: Geophys. Prosp., 24, 380-399.

Loewenthal, D. and Mufti, I.R., 1983, Reverse-time migration in the spatial frequency domain: Geophysics, 48, 627-635.

Loewenthal, D., Stoffa, P. and Faria, E.L., 1987, Suppressing the unwanted reflections of the full wave equation: Geophysics, 52, 1007-1012.

Loewenthal, D. and Hu, L.Z, 1991, Two methods for computing the imaging condition for common-shot prestack migration: Geophysics, 56, 378-381.

Lumley, D., Claerbout, J., and Bevc, D., 1994, Anti-aliased Kirchhoff 3-D migration: 64th Ann. Internat. Mtg Soc. of Expl. Geophys., 1282-1285.

MacKay, S. and Abma, R., 1989, Refining prestack depth migration images without remigration: 59th Ann. Internat. Mtg Soc. of Expl. Geophys., 1258.

MacKay, S. and Abma, R., 1992, Imaging and velocity estimation with depth-focusing analysis: Geophysics, 57, 1608-1622.

MacKay, S. and Abma, R., 1993, Depth-focusing analysis using a wavefront-curvature criterion: Geophysics, 58, 1148-1156.

Mallat, S., 1999, A wavelet tour of signal processing (2nd Ed.): Academic Press.

Manuel, C.D., 1998, Numerical Simulation of Seismic Multiples: MSc thesis, Curtin University of Technology.

Manuel, C.D., Uren, N.F., and Lambert, G., 2001, The Generalised Exploding Reflector Method: 71st Ann. Internat. Mtg Soc. of Expl. Geophys., 1167-1170.

McMechan, G.A., 1983, Migration by extrapolation of time-dependent boundary values: Geophys. Prosp., 131, 413-420.

Minora Resources N.L., 1987, Whalebone Marine Seismic Survey – Permit EP-325: Acquired by Geophysical Services Incorporated.

Nautiyal. A., Gray, S.H., Whitmore, N.D., and Garing, J.D., 1993, Stability versus accuracy for an explicit wavefield extrapolation operator: Geophysics, 58, 277-283.

Petroleum Exploration Society of Australia, 2002, Petroleum Asset Opportunities - EP 325, Offshore Carnarvon Basin, North West Shelf, Western Australia [Online], Available: http://www.pesa.com.au/ [2002, Feb. 3].

Podvin, P. and Lecomte, I., 1991, Finite-difference computation of traveltimes in very contrasted velocity models - a massively parallel approach and its associated tools: Geophys. J. Int., 105, 271-284.

Qin, F., Luo, Y, Olsen, K.B., Cai, W. and Schuster, G.T., 1992, Finite-difference solution of the Eikonal equation along expanding wavefronts: Geophysics, 57, 478-487.

Ramsden, C.R.T., Hobson, M.R. and Cooper, R., 1988, The Geophysicists' Bane - Multiple Suppression on the North West Shelf: *In* Purcell, P.G. and R.R. (Eds.), The North West Shelf. Proceedings of Petroleum Exploration Society of Australia Symposium, Perth, Western Australia, 97-114.

Reshef, M. and Kosloff, D., 1986, Migration of common-shot gathers: Geophysics, 51, 324-331.

Sattlegger, J.W., 1975, Migration velocity determination - Part 1 - Philosophy: Geophysics, 40, 1-5.

Sattlegger, J.W., Stiller, P.K., Echterhoff, J.A. and Hentschke, M.K., 1980, Common offset plane migration (COPMIG): Geophys. Prosp., 28, 859-871.

Schleicher, K.L., Grygier, D.J. and Brzostowski, M.A., 1991, Migration velocity analysis: A comparison of two approaches: 61st Ann. Internat. Mtg Soc. of Expl. Geophys., 1237-1238.

Schneider, W.A., 1978, Integral formulation for migration in two and three dimensions: Geophysics, 43, 49-76.

Schneider Jr., W.A., Ranzinger, K.A., Balch, A.H., Kruse, C., 1992, A dynamic programming approach to first arrival traveltime computation in media with arbitrarily distributed velocities: Geophysics, 57, 39-50.

Schultz, P., 1998, The Seismic Velocity Model as an Interpretation Asset: Distinguished Instructor Series No. 2, Society of Exploration Geophysicists.

Sheriff, R.E., 1994, Encyclopedia Dictionary of Exploration Geophysics: (3rd Ed.), Society of Exploration Geophysicists, Tulsa, Oklahoma.

Sherwood, J., Chen, K.C. and Wood, M., 1986, Depths and interval velocities from seismic reflection data for low relief structures: 56th Ann. Internat. Mtg Soc. of Expl. Geophys., Session: S13.5.

Shurtleff, R.N., 1984, An F-K procedure for prestack migration and migration velocity analysis: Presented at 46th Mtg. Eur. Assn. Geosci. Eng.

Stoffa, P.L., 1989, Tau-p - An alternative domain for filtering, velocity analysis, and imaging, 59th Ann. Internat. Mtg: Soc. of Expl. Geophys., 551.

Stoffa, P.L., Buhl, P., Diebold, J.B. and Wenzel, F., 1981, Direct mapping of seismic data to the domain of intercept time and ray parameter - A plane-wave decomposition: Geophysics, 46, 255-267.

Stolt, R.H., 1978, Migration by Fourier transform: Geophysics, 43, 23-48.

Stork, C., 1992, Reflection tomography in the postmigrated domain: Geophysics, 57,680-692.

Sun, R. and McMechan, G.A., 1986, Pre-stack reverse-time migration for elastic waves with application to synthetic offset vertical seismic profiles: Proc. Inst. Electr. and Electron. Eng., 74, 457-465.

Taner, M.T. and Koehler, F., 1969, Velocity spectra - Digital computer derivation and applications of velocity functions: Geophysics, 34, 859-881.

Taner, M.T., 1977, Simplan – plane-wave stacking: 37th Mtg. Eur. Assn. Geosci. Eng.

Thompson, T.A. and Hartley, B.M., 2002, Adaptive Approximations for Multiple Suppression: Accepted for the 64th Mtg. Eur. Assn. Geosci. Eng.

Thorbecke, J. and Morton, S., 1997, Properties of common focus point gathers: 59th Mtg. Eur. Assn. Geosci. Eng., Session: A004.

Thurber, C.H., and Ellsworth, W.L., 1980, Rapid solution of ray tracing problems in heterogeneous media: Bull. Seis. Soc. Am., 70, 1137-1148.

Tieman, H.J., 1994, Investigating the velocity-depth ambiguity of reflection traveltimes: Geophysics, 59, 1763-1773.

Tieman, H.J., 1995, Migration velocity analysis: Accounting for the effects of lateral velocity variations: Geophysics, 60, 164-175.

Toldi, 1989, Velocity analysis without picking: Geophysics, 54, 191-199.

Urosevic, M., 2000, Senior Research Fellow at Curtin University of Technology, Conversation with the author, 28th Nov.

van der Made, P.M. and van Riel, P., 1988, Estimating complex velocity models for depth migration: 58th Ann. Internat. Mtg Soc. of Expl. Geophys., Session: S9.1

Verschuur, D. J., Berkhout, A.J., and Wapenaar, C.P.A., 1992, Adaptive surface-related multiple elimination: Geophysics, 57, 1166-1177.

Versteeg, R.J., 1993, Sensitivity of prestack depth migration to the velocity model: Geophysics, 58, 873-882.

Versteeg, R., 1994, The Marmousi experience: Velocity model determination on a synthetic complex data set: The Leading Edge, 13, 927-936.

Vidale, J., 1988, Finite-difference calculation of traveltimes: Bull. Seis. Soc. Am., 78, 2062-2076.

Vidale, J., 1990, Finite-difference calculation of traveltimes in three dimensions: Geophysics, 55, 521-526.

Whitmore, N.D., 1983, Iterative depth migration by backward time propagation: 53rd Ann. Internat. Mtg Soc. of Expl. Geophys., Session: S10.1.

Yan, L., Lines, L., and Lawton, D., 2001, Migration velocity analysis by curvature measurement and stacking power: 72nd Ann. Internat. Mtg Soc. of Expl. Geophys., 873-876.

Yilmaz, O., 1987, Seismic Data Processing: Society of Exploration Geophysicists, Tulsa, Oklahoma.

Yilmaz, O., 2001, Seismic Data Processing: Society of Exploration Geophysicists, Tulsa, Oklahoma.

Yilmaz, O. and Claerbout, J.F., 1980, Pre-stack partial migration: Geophysics, 45, 1753-1779.

Yilmaz, O. and Chambers, R.E., 1984, Migration velocity analysis by wave-field extrapolation: Geophysics, 49, 1664-1674.

Yilmaz, O., Tanir, I. and Gregory, C., 2001, A unified 3-D seismic workflow: 71st Ann. Internat. Mtg Soc. of Expl. Geophys., 499-502.

Youn, O.K. and Zhou, H., 2001, Depth imaging with multiples: Geophysics, 66, 246-255.

Zhao, P., 1996a, Techniques for Broad Spectrum Inversion of High Resolution Seismic Imaging: Ph.D. thesis, Curtin University of Technology.

Zhao, P., 1996b, An efficient computer program for wavefront calculation by the finite-difference method: Computers and Geosciences, 22, 239-251.

Zhao, P., Uren, N.F., Wenzel, F., Hatherly, P.J., and McDonald, J.A., 1998, Kirchhoff diffraction mapping in media with large velocity contrasts: Geophysics, 63, 2072-2081.

Zijlstra, D.M., can der Made, P.M., Bussemaker, F., and van Riel, P., 1992, Effective depth conversion: A North Sea Case Study: *In* Fagin, S.W. (Ed.), Seismic Modelling of Geologic Structures.

APPENDIX

SOFTWARE DEVELOPED IN THE THESIS

A1 Numerical simulation of seismic multiples using the GERM 197

A2 Implementation of multiple grid cell sizes using the GERM 213

A3 Kirchhoff PSDM incorporating the GERM 229

A4 Migration velocity analysis – residual curvature method 237

A5 Coherency for residual curvature method 247

A6 Demigration for multiple attenuation 251

Note: At the author's request, the appendices (p.197-256) of this thesis have not been reproduced.

(Co-ordinator, ADT Project (Bibliographic Services), Curtin University of Technology, 12/08/03)